12-2011

COMPUTATIONAL APPROACHES TO UNDERSTAND PHENOTYPIC STRUCTURE AND CONSTITUTIVE MECHANICS RELATIONSHIPS OF SINGLE CELLS

Scott Wood
Clemson University, scott.t.wood@gmail.com

COMPUTATIONAL APPROACHES TO UNDERSTAND PHENOTYPIC STRUCTURE AND CONSTITUTIVE MECHANICS RELATIONSHIPS OF SINGLE CELLS

A Dissertation
Presented to
the Graduate School of
Clemson University

In Partial Fulfillment
of the Requirements for the Degree
Doctor of Philosophy
Bioengineering

by
Scott Tyler Wood
December 2011

Accepted by:
Dr. Delphine Dean, Committee Chair
Dr. Jiro Nagatomi
Dr. John DesJardins
Dr. Brian Dean

ABSTRACT

The goal of this work is to better understand the relationship between the structure and function of biological cells by simulating their nonlinear mechanical behavior under static and dynamic loading using image structure-based finite element modeling (FEM). Vascular smooth muscle cells (VSMCs) are chosen for this study due to the strong correlation of the geometric arrangement of their structural components on their mechanical behavior and the implications of that behavior on diseases such as atherosclerosis.

VSMCs are modeled here using a linear elastic material model together with truss elements, which simulate the cytoskeletal fiber network that provides the cells with much of their internal structural support. Geometric characterization of single VSMCs of two physiologically relevant phenotypes in 2D cell culture is achieved using confocal microscopy in conjunction with novel image processing techniques. These computer vision techniques use image segmentation, 2D frequency analysis, and linear programming approaches to create representative 3D model structures consisting of the cell nucleus, cytoplasm, and actin stress fiber network of each cell. These structures are then imported into MSC Patran for structural analysis with Marc. Mechanical characterization is achieved using atomic force microscopy (AFM) indentation. Material properties for each VSMC model are input based on values individually obtained through experimentation, and the results of each model are compared against those experimental values. This study is believed to be a significant step towards the viability of finite

element models in the field of cellular mechanics because the geometries of the cells in

the model are based on confocal microscopy images of actual cells and thus, the results of

the model can be compared against experimental data for those same cells.

DEDICATION

This work is dedicated to my wonderful family. To my incredible wife Allison, whose unending encouragement, support, and distraction have bolstered me throughout the process of obtaining my doctoral degree. To my parents, Phil and Eileen, who taught me the value of education, hard work, and perseverance, and have always encouraged me to cling to my love of learning with wide-eyed-wonder all the answers to the perpetual question: "*How does that work?*." To my siblings, Kristin and Shane, who have provided a sympathetic ear and a competitive fire under my heels throughout my academic career. And to my grandparents, Dr. John and Helen Wood, Donald Anderson, and Lois Killian who each in their own unique way laid the foundation upon which the curiosity and determination that drove this work is built. I would not be where I am today without the support each of you has given me through the years – thank you all. I love each of you dearly.

ACKNOWLEDGEMENTS

First and foremost, I would like to thank my advisor, Dr. Delphine Dean, for giving me the opportunity to earn my Ph.D. under her tutelage. The guidance, support, insight, knowledge and encouragement she has so freely given me have proven absolutely indispensable for the past four-and-a-half years and have prepared me well for whatever upcoming adventures my career holds in store for the future. I would also like to thank my committee members, Dr. Jiro Nagatomi, Dr. John DesJardins, and Dr. Brian Dean for the guidance and thought-provoking questions they have provided to direct the course of my research. I would especially like to thank Dr. Brian Dean for all of the patience, effort, and long hours spent teaching and assisting me with the computer programming aspects of my research.

In addition, I would like to thank Dr. Jason Hemmer, whose doctoral research laid the foundation for my own as well as Dr. Shekhar Kanetkar and Dr. Zhong Qin of MSC.Software Corporation for their expert advice regarding the use of Patran and Marc. I would also like to extend a special thank you to Sandy Deitch, Will McAllister, Elliot Mappus, and all the other past and present members of the Multiscale Bioelectromechanics Lab who have provided assistance with cell culture, AFM expertise, and day-to-day lab work.

TABLE OF CONTENTS

Table of Contents (Continued)

Table of Contents (Continued)

LIST OF TABLES

Table   Page

LIST OF FIGURES

Figure   Page

CHAPTER 1

INTRODUCTION

1.1. SIGNIFICANCE OF CELLULAR MECHANICS MODELING IN MEDICAL RESEARCH

The ability to model the mechanical responses of cells of physical stimuli presents many opportunities to the world of medical research. Chief among these is the ability to further our understanding of the ætiology of many diseases [1, 2]. There are a wide variety of diseases whose ætiology or clinical presentation are either known or suspected to be related to abnormal cellular mechanics, alteration of cellular mechanotransduction processes, or changes in tissue structure [2]. Because physical distortion can affect cell growth, differentiation, contractility, motility, and apoptotic tendency [2], the ability to predict the mechanical behavior of cells in response to pathological conditions and medical treatments may be critical to prevention and treatment of many of these diseases [2-6].

1.2. COMMONLY MODELED CELLULAR MECHANICS TESTING INSTRUMENTATION

There are many methods of probing the mechanical responses of cells to applied stimuli [4], several of which are commonly modeled. One of the most commonly modeled methods for subcellular region probing is AFM, a form of cytoindentation. As its name implies, cytoindentation involves indenting a region of a cell with a small probe

and can be used to perform indentation force measurement and creep experiments [7, 8], which provide information that can be used to calculate the elastic modulus, viscosity, and hysteresis of a cell.

1.3. SINGLE CELL MECHANICS MODELS

For as long as there have been observations of the mechanical properties of cells, there have been models put forth to attempt to describe those observations. At the most basic level, there are two categories of these models: continuum and structure-based. The first models of cellular mechanics as a "balloon full of molasses" [9] were continuum models which by definition lack internal structure [10]. Despite the overwhelming evidence in support of structural elements within cells, these types of models remain popular with bioengineers due to their relative simplicity and similarity with the earliest mechanical principles taught to young engineers. Structure-based models, on the other hand, are comprised of one or more networks of discrete structural elements which work in harmony to explain the mechanical responses of cells. These models have many benefits, but can quickly become computationally expensive. In order to become widely accepted by the scientific community, any complete model of cellular mechanics must likely take into account aspects of both models, namely the viscoelastic, nonlinear and heterogenic mechanical responses of cells as well as their numerous structural components and their ability to actively remodel those components in response to applied stresses.

1.3.1 The Hertz Model

The most frequently used model of single-cell mechanics for analysis of atomic force
microscopy (AFM) nanoindentation [11], the Hertzian linear elastic solid analytical
model [12], is widely recognized as oversimplified because it cannot account for the
viscoelastic, nonlinear, and nonheterogeneous properties of the cell, as well as its
compound structure and ability to actively remodel itself [10, 11, 13]. In addition, for
standard AFM pyramidal tips, the model does not accurately represent the tip geometry
[14]. However, the Hertzian model's frequency and ease of use make it an important tool
for the purpose of comparison [14-16]. Eq. (1) shows the relationship between force and
elastic modulus as described by the Hertz model for indentation of a semi-infinite
substrate with a spherical indenter [17-19]:

$$(1) \qquad F = \frac{4}{3} \frac{E}{(1-v^2)} R^{\frac{1}{2}} \delta^{\frac{3}{2}}$$

Where F is measured force, E is elastic modulus, v is Poisson's ratio, R is spherical
indenter radius, and d is indentation depth. In this model the contact radius, a, is
calculated as:

$$(2) \qquad a = \left(\frac{3FR}{4E_R}\right)^{\frac{1}{3}}$$

Where E_R is the reduced elastic given by:

$$(3) \qquad \frac{1}{E_R} = \frac{\left(1-v_{indenter}^2\right)}{E_{indenter}} + \frac{\left(1-v_{sample}^2\right)}{E_{sample}}$$

1.3.2. Viscoelastic Models

Viscoelastic models are also commonly used for analysis of cell mechanics experiments. Although viscoelasticity is also a continuum model, and cannot therefore explicitly take into account the compound structure of cells, it also provides valuable data about the mechanical behavior of cells. The Kelvin model (also frequently referred to as the Standard Linear Solid (SLS) model of viscoelasticity) is the most frequently used model in the literature due to its relative simplicity, however it has been shown to be among the least accurate models of viscoelasticity for the representation of cellular mechanics [18, 20-24]. Other commonly used models of viscoelasticity include the Quasilinear Viscoelastic (QLV) model, the Generalized Maxwell or Weichert model, and the Power Law relaxation model [20, 21, 25-27]. The Kelvin element can be represented by a spring in parallel with a Maxwell element (a spring and dashpot in series), the QLV model is represented by an infinite series of Kelvin bodies, and the Generalized Maxwell model behaves similarly to the QLV model [27] and is represented by a spring in parallel with an infinite series of Maxwell elements. The Power Law relaxation model has no time constants, springs, or dashpots; it is a purely mathematical tool for fitting a relaxation curve. Each of these models is capable of describing experimental data from cell mechanics experiments with a reasonable degree of accuracy. Which model is selected appears in the literature to be based on the structural complexity of the cell being analyzed and the extent to which each researcher is willing to perform complex analytical techniques.

1.3.3. Tensegrity

Tensegrity is a theory of cell mechanics that appears to be followed by a small but dedicated few researchers. It is based on the idea that structures can stabilize their shape by continuous tension, or 'tensional integrity,' (like a tent) rather than by continuous compression (like a stone arch) – a building principle which has been utilized to varying degrees since the day man first used rope to hold flint axe heads and spear tips in place on a stick but was not described as a single cohesive theory of mechanics until R. Buckminster Fuller coined the term 'tensegrity' in 1961 [28]. Fuller initially described two broad classes of structures as falling within the definition of tensegrity: geodesic and prestressed networks. Geodesic structures are composed of triangular structural members oriented along geodesics (minimal paths) to constrain movement, while prestressed structures constrain movement through the use of pre-existing tensile stress of isometric tension ('prestress'). The definition of tensegrity has since been broadened and is now considered to include tensed networks that resist shape distortion and self-stabilize by incorporating other support elements that resist compression. All of these structures would fail to maintain their shape when mechanically stressed without continuous transmission of tensional forces [28-30]. There is a great deal of evidence of the principles of tensegrity at work within the cell, however the extent to which tensegrity plays a role in the mechanical behavior of cells remains a source of debate within the literature [10, 31-37].

1.4. SINGLE CELL FINITE ELEMENT MODELS

There has been much effort put into characterizing the behavior of cells using the models discussed above throughout the years, however there has not been quite as much effort put into utilizing those models in one of the most powerful analytical tools available to the engineer: the finite element model. This is largely due to the highly nonlinear geometric and material nonlinearity exhibited by cells which until recently was more computationally expensive than was feasible on the average personal computer [38]. There have been attempts to create 2D finite element models of cells since computing power began increasing in the 1990s [1, 8, 38, 39]; however, despite the ever-growing availability of sufficient computing power for more complex models, only two full 3D confocal-based models have been published [1, 40]. Furthermore, of those models that have been published, only one has employed large deformations [1], only one utilizes a compound structure [1], neither is based on accurate geometries capable of representing an entire cellular phenotype, and neither model is validated by comparing its predictions against experimental data. If the aims of this application are achieved, finite element analysis may finally be able to become a mainstream tool within the field of cellular mechanics. The work proposed in this study could also eventually be incorporated into multiscale models, providing a key link between the prediction of mechanical responses to pathological conditions and medical treatments from the tissue level down to the molecular level.

1.5. DOCUMENT OUTLINE

The content of each chapter will be as follows. Chapter 2 will state the aims of the current research. Chapter 3 will present the background and review the current literature related to the topics required to fulfill the aims stated in Chapter 2. Chapter 4 will present research fulfilling Aim 1 in which a 2D axisymmetric finite element model is established to investigate the relationship between geometry and mechanical properties. Chapter 5 will present research fulfilling Aim 2 in which an algorithm is established which is capable of analyzing confocal image stacks of cells and automatically generating geometric meshes fit for use in a finite element model. Chapter 6 will present research fulfilling Aim 3 in which a 3D finite element model is constructed based on geometries of actual cells and their structural subcellular features and the model is validated against experimental data. Chapter 7 will present the overarching conclusions for the present study and outline the recommendations for future work.

1.6. REFERENCES

1.   Slomka, N. and A. Gefen, Confocal microscopy-based three-dimensional cell-specific modeling for large deformation analyses in cellular mechanics. Journal of Biomechanics, 2010. 43(9): p. 1806-1816.

2.   Ingber, D.E., Mechanobiology and diseases of mechanotransduction. Annals of Medicine, 2003. 35(8): p. 564-577.

3.   Li, C. and Q. Xu, Mechanical stress-initiated signal transduction in vascular smooth muscle cells in vitro and in vivo. Cellular Signalling, 2007. 19(5): p. 881-891.

4.   Suresh, S., Biomechanics and biophysics of cancer cells. Acta Materialia, 2007. 55(12): p. 3989-4014.

5.   Lammi, M.J. Current perspectives on cartilage and chondrocyte mechanobiology. 2004. Ios Press.

6.   Li, Q.S., et al., AFM Indentation Study of Breast Cancer Cells. Biochemical and Biophysical Research Communications, 2008. 374(4): p. 609-613.

7.   Shieh, A.C. and K.A. Athanasiou, Biomechanics of single zonal chondrocytes. Journal of Biomechanics, 2006. 39(9): p. 1595-1602.

8.   Peeters, E.A.G., et al., Mechanical and failure properties of single attached cells under compression. Journal of Biomechanics, 2005. 38(8): p. 1685-1693.

9.   Li, B., et al., Development of micropost force sensor array with culture experiments for determination of cell traction forces. Cell Motility and the Cytoskeleton, 2007. 64(7): p. 509-518.

10.   Ingber, D.E., Tensegrity I. Cell structure and hierarchical systems biology. Journal of Cell Science, 2003. 116(7): p. 1157-1173.

11.   Costa, K.D., A.J. Sim, and F.C.P. Yin, Non-Hertzian approach to analyzing mechanical properties of endothelial cells probed by atomic force microscopy. Journal of Biomechanical Engineering-Transactions of the Asme, 2006. 128(2): p. 176-184.

12.   Hertz, H., Über die Berührung Fester Elastischer Körper (On the Contact of Elastic Solids). J. Reine Angew. Math., 1882. 92: p. 156-171.

13.   Dintwa, E., E. Tijskens, and H. Ramon, On the accuracy of the Hertz model to describe the normal contact of soft elastic spheres. Granular Matter, 2008. 10: p. 209-221.

14.   Costa, K.D. and F.C.P. Yin, Analysis of Indentation: Implications for Measuring Mechanical Properties With Atomic Force Microscopy. Journal of Biomechanical Engineering, 1999. 121(5): p. 462-471.

15.   Kuznetsova, T.G., et al., Atomic force microscopy probing of cell elasticity. Micron, 2007. 38(8): p. 824-833.

16.   Pillarisetti, A., et al. Mechanical Characterization of Mouse Embryonic Stem Cells. in IEEE Engineering in Medicine and Biology Society. 2009. Minneapolis, MN.

17.   Mofrad, M.R.K. and R.D. Kamm, eds. Cytoskeletal Mechanics. 2006, Cambridge University Press: New York, NY. 244.

18. Darling, E.M., S. Zauscher, and F. Guilak, Viscoelastic properties of zonal articular chondrocytes measured by atomic force microscopy. Osteoarthritis and Cartilage, 2006. 14(6): p. 571-579.

19. Hemmer J.D., D.D., Vertegel A., Langan E. III, LaBerge M., Effects of serum deprivation on the mechanical properties of adherent vascular smooth muscle cells. Proc Inst Mech Eng [H], 2008. 222(5): p. 761-72.

20. Hemmer, J.D., et al., Role of Cytoskeletal Components in Stress-Relaxation Behavior of Adherent Vascular Smooth Muscle Cells. Journal of Biomechanical Engineering-Transactions of the Asme, 2009. 131(4): p. 9.

21. Lim, C.T., E.H. Zhou, and S.T. Quek, Mechanical models for living cells--a review. Journal of Biomechanics, 2006. 39(2): p. 195-216.

22. Leipzig, N.D. and K.A. Athanasiou, Unconfined creep compression of chondrocytes. Journal of Biomechanics, 2005. 38(1): p. 77-85.

23. Merryman, W.D., et al., Viscoelastic Properties of the Aortic Valve Interstitial Cell. Journal of Biomechanical Engineering-Transactions of the Asme, 2009. 131(4).

24. Liao, D., et al., Viscoelastic properties of isolated rat colon smooth muscle cells. Cell Biology International, 2006. 30(10): p. 854-858.

25. Fung, Y.C., Biomechanics: Mechanical Properties of Living Tissues. Second ed1993, New York, NY: Springer-Verlag New York, Inc. 568.

26. Roylance, D., Engineering Viscoelasticity, 2001, Department of Materials Science and Engineering at Massachusetts Institute of Technology. p. 37.

27. Nekouzadeh, A., et al., A simplified approach to quasi-linear viscoelastic modeling. Journal of Biomechanics, 2007. 40(14): p. 3070-3078.

28. Fuller, R.B., Tensegrity. Portfolio Artnews Annual, 1961. 4: p. 112-127.

29. Fuller, R.B. and L.C. Keat, Synergetics. Portfolio1979, Philadelphia & Singapore.

30. Ingber, D.E., The architecture of life. Scientific American, 1998. 278(1): p. 48-57.

31. Brookes, M., Hard cell, soft cell. New Scientist, 1999. 164(2206): p. 42-46.

32. Banerjee, S.D., R.H. Cohn, and M.R. Bernfield, Basal lamina of embryonic salivary epithelia. Production by the epithelium and role in maintaining lobular morphology. J. Cell Biol., 1977. 2: p. 445-463.

33.   Wang, N., et al., Mechanical behavior in living cells consistent with the tensegrity model. Proc. Natl. Acad. Sci., 2001. 98: p. 7765-7770.

34.   Kumar, S., et al., Viscoelastic retraction of single living stress fibers and its impact on cell shape, cytoskeletal organization, and extracellular matrix mechanics. Biophys. J., 2006. 90: p. 3762-3773.

35.   Heidemann, S.R., et al., Direct observations of the mechanical behaviors of the cytoskeleton in living fibroblasts. J. Cell Biol., 1999. 145: p. 109-122.

36.   Heidemann, S.R., et al., Opposing views on tensegrity as a structural framework for understanding cell mechanics. Journal of Applied Physiology, 2000. 89(4): p. 1670-1678.

37.   Forgacs, G., On the possible role of cytoskeletal filamentous networks in intracellular signaling: an approach based on percolation. J. Cell Sci., 1995. 108: p. 2131-2143.

38.   When f =/= Ku, MSC.Software, Editor 2009. p. 2-11.

39.   Unnikrishnan, G.U., V.U. Unnikirishnan, and J.N. Reddy, Constitutive material modeling of cell: a micromechanics approach. Journal of Biomechanical Engineering-Transactions of the Asme, 2007. 129(3): p. 315-323.

40.   Dailey, H.L., et al., Image-based finite element modeling of alveolar epithelial cell injury during airway reopening. Journal of Applied Physiology, 2009. 106(1): p. 221-232.

CHAPTER 2

RESEARCH AIMS

The goal of this proposed research plan is to build a model composed of structural elements representative of those within cells which can be used to accurately predict the mechanical behavior of cells as measured by atomic force microscopy (AFM) measurements of cells on a 2D substrate. This model would enable accurate estimation from imaging data of the mechanical properties of cells in configurations where direct mechanical measurement may not be possible. The specific aims are as follows:

2.1. AIM 1: DEVELOP THE FRAMEWORK FOR A SINGLE-CELL FINITE ELEMENT MODEL

The purposes of this aim are threefold. First, to develop a linear elastic finite element model (FEM) to show that the geometrical variations due to cell phenotypic differences in nanoindentation experiments can significantly alter the estimated elastic modulus obtained from the standard Hertz analytical model for AFM nanoindentation. Secondly, to incorporate viscoelastic properties observed in AFM studies into the finite element model. Lastly, to further develop the model by expanding it to 3D and incorporating simple structural elements such as beams and trusses to represent greatly simplified cytoskeletal networks. This model will be capable of reproducing AFM nanoindentation simulations more accurately than the linear elastic model; however, it will still be dependent upon geometric over-simplifications.

2.2. AIM 2: DEVELOP A TECHNIQUE TO CONVERT MICROSCOPE IMAGES OF STRUCTURAL SUBCELLULAR FEATURES INTO REPRESENTATIVE FEM ASSEMBLIES

In order to incorporate cellular geometries based on microscope images of actual cells, we will develop a novel process to generate FEM structures representative of entire phenotypes. This will be accomplished by combining an average of AFM cell height data with averages of cell boundaries from confocal microscopy images of contractile and synthetic VSMCs to generate a representative plasma membrane. Cytoskeletal elements will then be analyzed using 2D FFTs to construct representative vector fields and statistical analysis tools such as Hough transforms and random walks will be used to convert those vector fields into generic representative model structures.

2.3. AIM 3: INTEGRATE THE COMPUTER-GENERATED ASSEMBLIES INTO THE MODEL

The ultimate objective of the research in this proposed work is to develop a novel finite element model composed of multiple networks of microscopy-based structural elements that is capable of reproducing data from AFM nanoindentation experiments based solely on representative images of the cytoskeletal organization of the synthetic and contractile phenotypes of VSMCs. Because the mechanical response of the model will be based on the material properties of each component, which are well characterized, we believe that such an automated model will function equally well for any phenotype of any cell. The results of this model will then be compared to AFM indentation tests performed on living VSMCs in media for validation. This type of single cell mechanics

model, comprised of a three-dimensional compound structure based on microscopy images of the nanoscale structural components of the cell is unprecedented in the literature and will be a good starting point for multiscale models of tissue that include not only cells but their nanoscale structures as well. Such models would have the potential to significantly increase the speed and decrease the cost of development of new pharmaceutical drugs and engineered tissue therapies, possibly paving the way for better and less expensive health care.

CHAPTER 3

LITERATURE REVIEW

3.1. INTRODUCTION

"The current focus of medicine on molecular genetics ignores the physical basis of disease even though many of the problems that lead to pain and morbidity [which] bring patients to the doctor's office result from changes in tissue structure or mechanics." – Donald Ingber [1]

In order to fully and properly understand the physiological mechanisms of diseases at the cellular level, it is necessary to have a thorough understanding of how changes in cellular structure affect their mechanical properties. For the better part of the last half-century, medical researchers and practitioners were under the belief that the cell had no internal structural features, but rather that it acted simply as a viscous 'balloon full of molasses' [1]. Advances in that time have led to the discovery of a complex cytoskeletal network that serves to balance and transmit forces throughout the cell thereby providing it with the stability required to maintain the complex phenotypes found in tissues throughout the body. Research has also recently shown that the shapes generated by the cytoskeleton can influence cell fate, likely via energetic principles as shown in Figure 3.1[2].
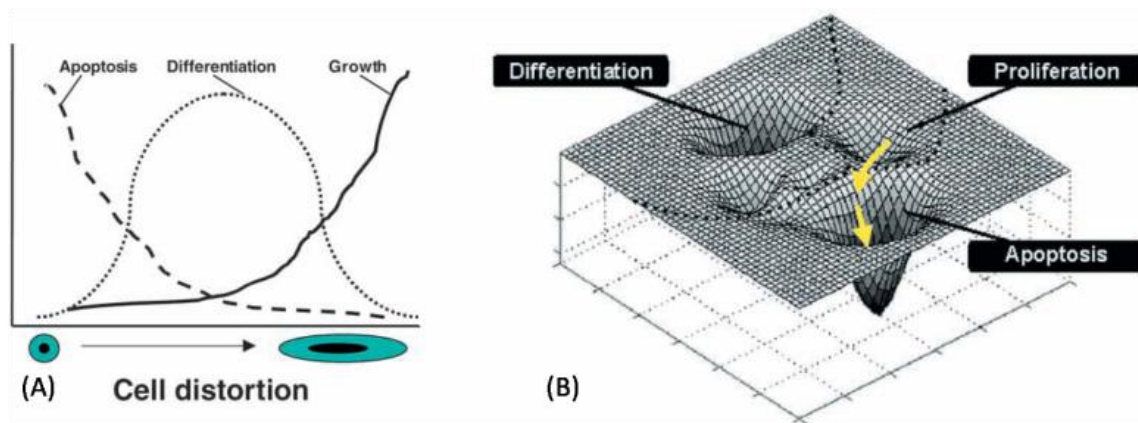
Figure 3.1. (A) Regulation of cell fate by cell distortion and (B) theoretical energetic landscape representation of cell fate determination where the xy plane corresponds to some configuration of the cytoskeleton and the z axis corresponds to the energy required to maintain each configuration; the lowest points in the valleys represent specific cell fates and the yellow arrows show a potential path from cell growth to apoptosis [2]

Deviations in the behavior of cellular mechanics and mechanotransduction (the process by which cells sense and respond to mechanical signals) have been connected to or are suspected to be linked with a wide variety of diseases [1] (a short list is shown in Table 3.1), likely through the pathways depicted in Figure 3.2 [3]. By developing accurate rheological models cell mechanics, it may be possible to broaden our understanding of cellular pathomechanics, leading to more sophisticated treatment protocols for diseases such as those listed in Table 3.1. Furthermore, these models would likely be cheaper and faster than current experimentation methods, thereby allowing for high throughput of simulated testing which would speed development of new therapies (i.e. biomaterials, medical devices, or even engineered tissues) [1, 4]. These models could also potentially aid in predicting clinical effects of drugs before they go to market, leading to a reduction in harmful side effects.
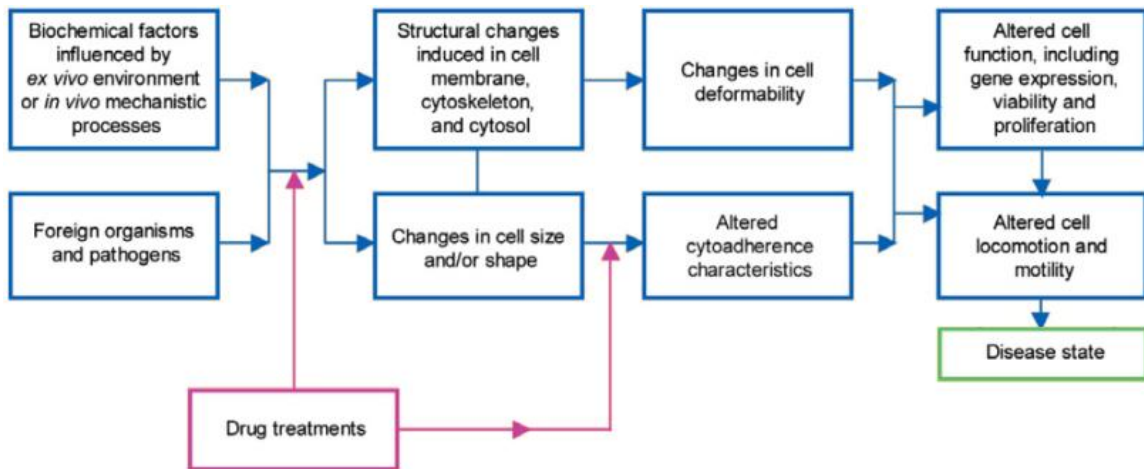
Figure 3.2. Flow chart depicting possible pathways connecting cellular pathomechanics to disease states; adapted from [3]

3.2. THE CYTOSKELETON

The cytoskeleton was discovered by Kitching in 1954 [5], relatively recently given the nearly 350 years [6] of cellular observations. As such, the precise roles it play in the life of the cell has remained a source of much debate to this day. The cytoskeleton is a biopolymer network comprised of several components, including actin stress fibers, microtubules, and a variety of structures known as intermediate filaments, and it is the primary mechanism responsible for maintenance of cell shape. The schematic in Figure 3.3 shows how these structures are typically arranged within cells.

17

Cardiology	Angina (vasospasm)	C T
	Atherosclerosis	T M
	Atrial fibrillation	M
	Heart failure	C T M?
	Intimal hyperplasia	C T M?
Gastroenterology	Irritable bowel syndrome	C M?
Nephrology	Diabetic nephropathy	C T M?
Neurology	Facial tics	C
	Hydrocephalus	T C?
	Migraine	C M?
	Stroke	C T
Oncology	Cancer	C T M?
	Metastasis	C
Opthalmology	Glaucoma	C T M?
Orthopaedics	Carpal tunnel syndrome	C T
	Chronic back pain	C T
	Osteoporosis	T M
Pediatrics	Congenital deafness	C T M
	Musculodystrophies	C T M
Pulmonary medicine	Asthma	C T M?
	Pulmonary hypertension	C T M?
Reproductive medicine	Pre-eclampsia	C T M?
	Sexual dysfunction (male & female)	C M?
Urology	Urinary frequency/incontinence	C M?

Partial list of diseases whose ætiology or clinical presentation likely results from abnormal cell mechanics (C), alterations in tissue structure (T), or deregulation of mechanochemical conversion (i.e. mechanotransduction, M); '?' indicates that M has yet to be demonstrated experimentally

Table 3.1. Partial List of Diseases related to cellular mechanics [1]
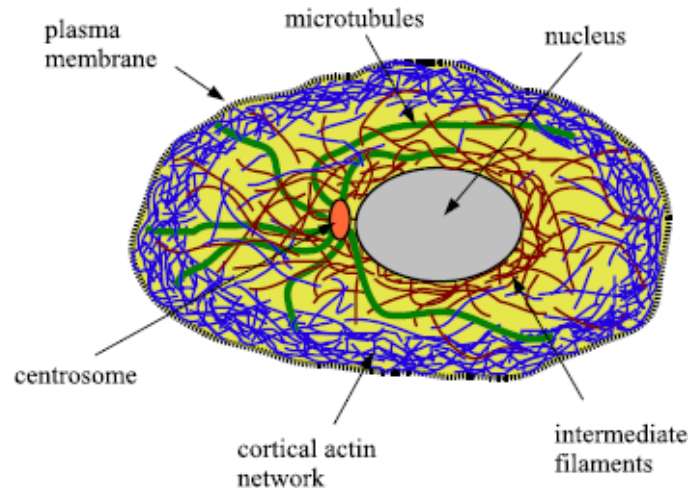
Figure 3.3. Schematic of typical cytoskeletal arrangement within an eukaryotic cell [7]

3.2.1. Actin

Actin microfilaments (f-actin) are $7 - 9$ nm diameter polarized polymers comprised of globular actin (g-actin) monomers as shown in Figure 3.4. These microfilaments exhibit a highly dynamic behavior regulated by the proteins profiling (+) and cofilin (-). The microfilaments are relatively stiff and have a persistence length of 15 μm in dilute solution and an elastic modulus of $1.3 - 2.5$ GPa [3]. The cortical actin network shown in Figure 3.3 is a thin network of microfilaments that surrounds the cell along the plasma membrane and is the primary structural component of non-adherent cells such as erythrocytes and leukocytes. In adherent cells, actin microfilaments are also found bound together by actin binding proteins to form closely packed arrays known as actin stress fibers. These stress fibers orient themselves largely along the direction of the stress field applied to the cell by its surroundings. A key feature of actin stress fibers is the prestress

that is actively exhibited upon them by the actomyosin complexes which are formed by the association of myosin motor proteins with the actin filaments [7].
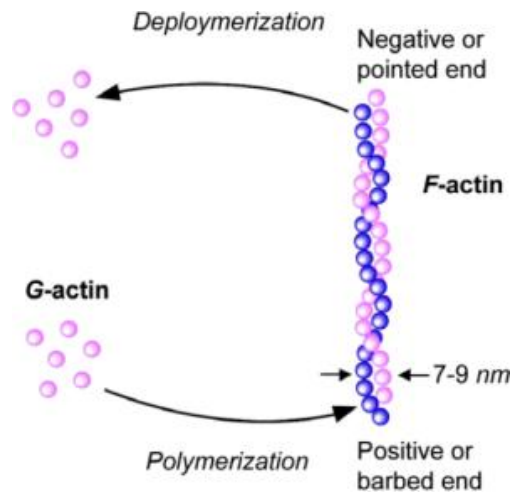
Figure 3.4. Actin microfilament structure [3]

3.2.2. Microtubules

Microtubules are highly dynamic polarized hollow tube polymers formed by the spontaneous assembly [7] of alternating α and β tubulin subunits as shown in Figure 3.5. They often originate from the centrosome near the center of the cell. These microfilaments have a 25 nm outer diameter/14 nm inner diameter, a persistence length of 6 mm in dilute solution and an elastic modulus of 1.9 GPa [3]. However, the persistence length of microtubules observed inside cells is several orders of magnitude smaller than the value measured in solution due to buckling under the stresses exerted upon them, [3].
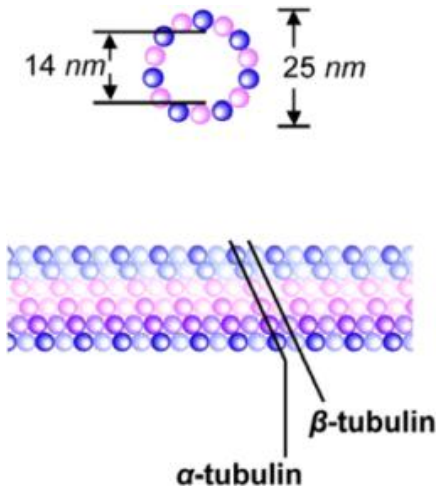
Figure 3.5. Microtubule structure [3]

3.2.3. Intermediate Filaments

Intermediate filaments are so named due to the fact that their diameter (10 nm) is less than that of microtubules but greater than that of actin microfilaments. Unlike f-actin and microtubules, intermediate filaments are not highly dynamic structures and form very highly stable structures in the cell. This stability allows them to play an important role in cell structure by providing lateral stabilization to buckling microtubules and connecting the cell nucleus to the plasma membrane. There are seven types of intermediate filaments (Type I – VII), each expressed in different types of cells. The filaments are typically composed of a central α-helical domain of over 300 amino acid dimers that self-assemble in a staggered anti-parallel array to form apolar tetramers. These connect end-to-end to form protofilaments, that come together roughly 8 at a time to form a rope-like structure (Figure 3.6). Intermediate filaments have a persistence length of approximately 1 – 3 μm in dilute solution and an elastic modulus of 1 – 5 GPa [3].
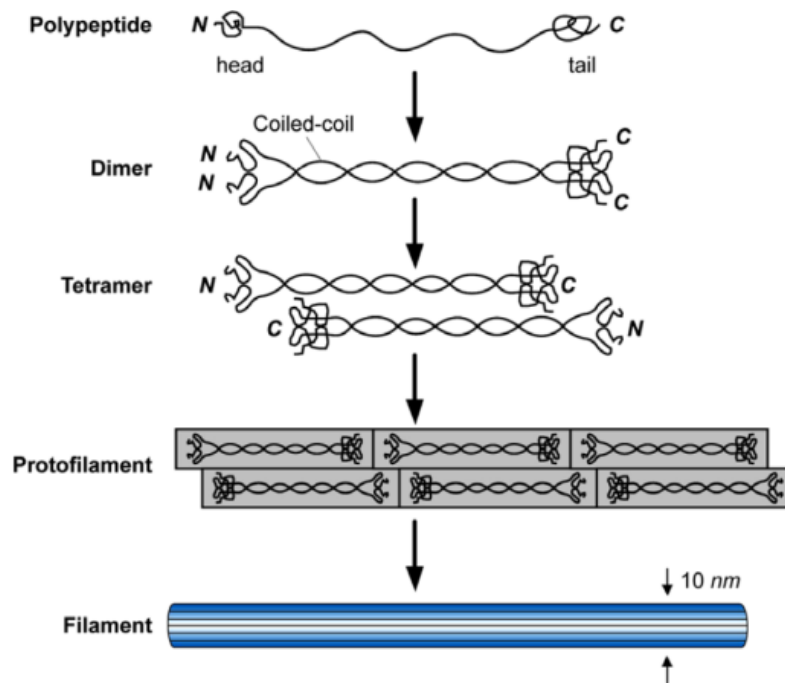
Figure 3.6. Intermediate filament structure [3]

3.2.4. Mechanotransduction

The process by which cells sense and respond to mechanical signals is known as Mechanotransduction. This process is regulated by the extracellular matrix (ECM), transmembrane integrin receptors, the cytoskeletal structures described above, and their associated signaling molecules [1]. A schematic of this process is shown in Figure 3.7 where forces applied either to the ECM cell substrate (A) or directly to the cell (B) travel along the ECM ↔ integrin ↔ cytoskeleton pathway.
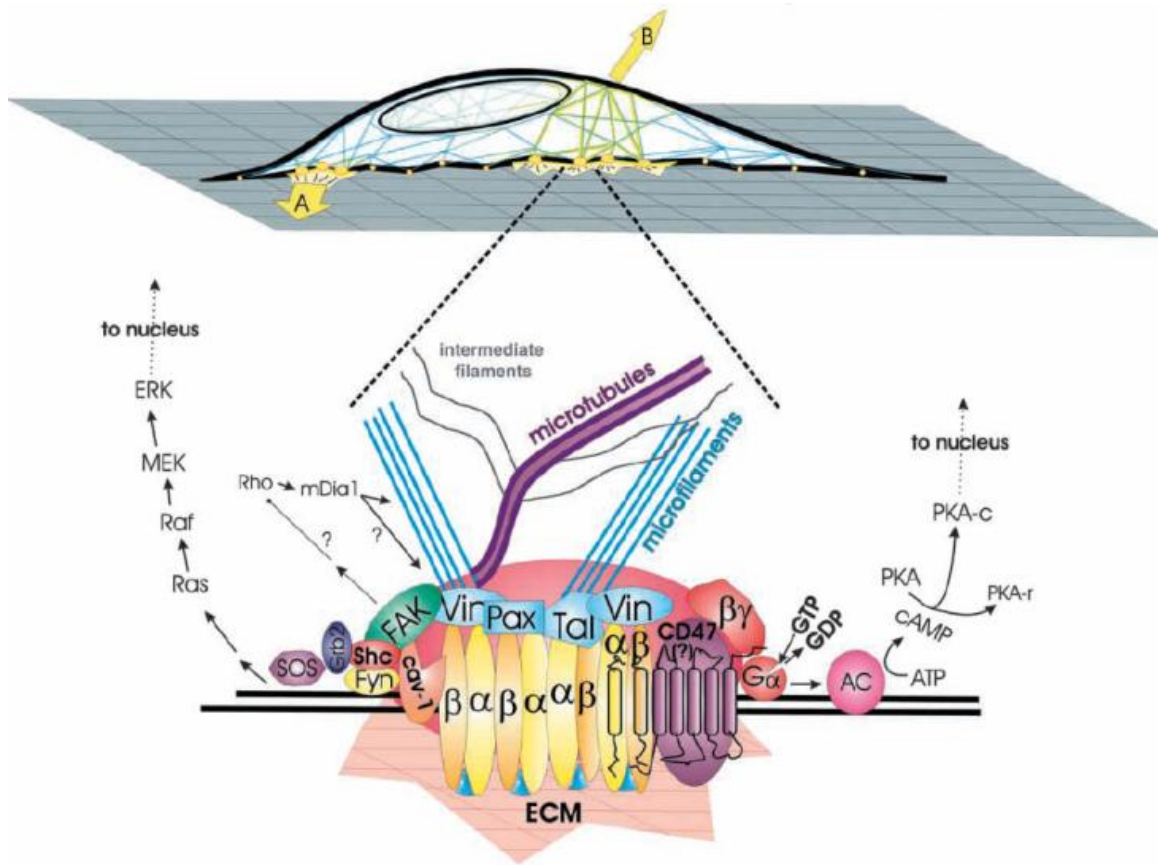
Figure 3.7. Mechanotransduction pathway [2]

3.3. IMAGING TECHNIQUES

3.3.1. Overview

The mechanical properties of any structure are commonly known to be primarily dependent upon two factors: its shape and the material it's made of. Therefore, in order to model the mechanical properties of cells, it is essential to have knowledge of the shapes of the structures that form them. The first images of cells were illustrated by Robert Hooke in 1665 and imaging technology has been developing ever since [6].

There are now many ways to image intracellular structures, with each making specific

compromises between resolution and preservation of the live (i.e. in vivo, in vitro, etc.)

structure of the cells (Figure 3.8).
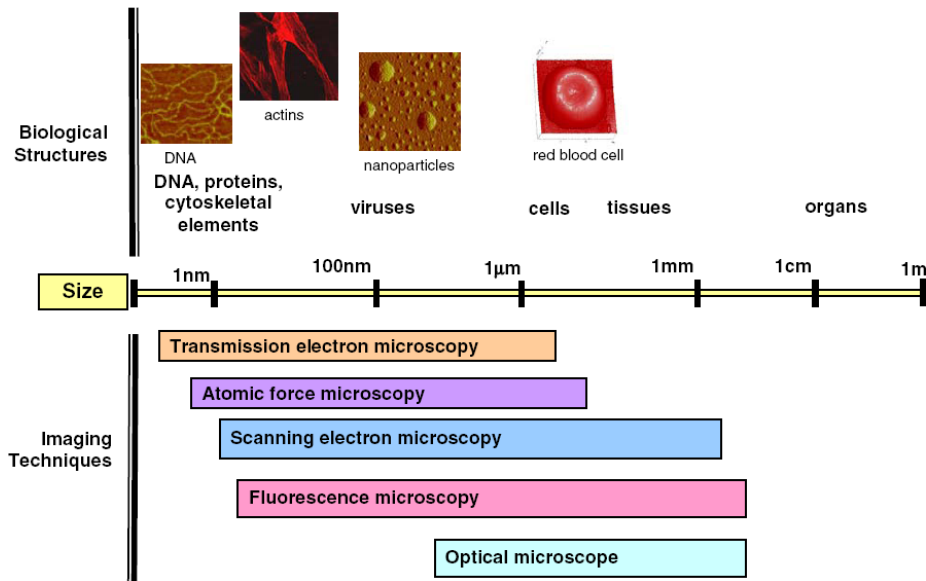
Figure 3.8. Common cellular imaging techniques and the types of structures and
length-scales for which they are primarily used; adapted from [8]

3.3.2. Widefield Fluorescence Microscopy

TECHNIQUES

Visualization of intracellular structures is accomplished in fluorescence microscopy

by utilizing the interaction of light with fluorescent molecules, known as fluorophores,

which are capable of binding to the proteins those structures are composed of. When

fluorophores are irradiated by light of a proper wavelength, they emit light at a longer

wavelength, as seen in Figure 3.9 [9].
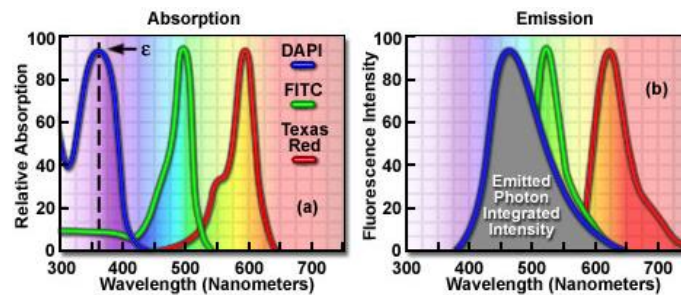
Figure 3.9. Spectral profiles of traditionally popular fluorophores [10]

Though fluorophores are capable of binding to some proteins directly, this is difficult

to accomplish without some sort of mechanism directing specific fluorophores to specific

proteins within the cell. One widely acclaimed technique that has been used to achieve

exquisite selectivity in biological fluorescence imaging since 1941 is

Immunocytochemistry, or ICC [11, 12]. This is accomplished by tagging antibodies,

usually IgG [13], with fluorophores and taking advantage of natural antigen-antibody

interactions to label specific proteins [14]. Early attempts at ICC focused on tagging the

specific antibody directly with a fluorophore, however this proved to be a largely

ineffective method due to insufficient emission by the fluorophores [11]. The more

sensitive indirect method of immunostaining was later developed in which two

fluorescently labeled antibodies bind to each specific antibody, as seen in Figure 3.10

[15]. This technique allows for the emission of twice as many photons as the direct

method and is therefore the current standard method of immunolabeling specific proteins within cells [16].
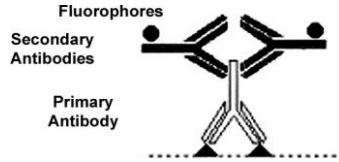
Figure 3.10. Illustration of indirect method of immunostaining [17]

3.3.2.1. LIMITATIONS AND SAMPLE PREPARATION

The predominant limitations of fluorescence microscopy are resolution, the number of stains that can be used on any given sample, photobleaching, and background fluorescence. Because fluorescence relies on the interaction of light waves with the sample, lateral resolution is limited to approximately 230 nm (based on Equation 3.1) and axial resolution to approximately 840 nm (based on Equation 3.2), though they can vary based on the wavelength of light used, the numerical aperture of the lens, and the refractive index of the medium [18].

Equation 3.1. Lateral resolution (R_L) of widefield microscopy, where λ is wavelength of light and NA is the numerical aperture of the lens [19]

$$R_L = \frac{0.61\lambda}{NA}$$

Equation 3.2. Axial resolution (R_A) of widefield microscopy, where n is the refractive index of the medium [19]

$$R_A = \frac{2n\lambda}{NA^2}$$

Additionally, as seen in Figure 3.11, the absorption spectra of different fluorophores can easily overlap to some degree. Because of this and the relatively long length of absorption spectra in relation to the length of the visible spectrum, it is traditionally held that only three fluorophores may be used before excitation overlap causes interference between signals. Even with careful selection, it is extremely difficult to find more than four fluorophores that can be used synchronously without interference.

Photobleaching, the photochemical destruction of a fluorophore, can also be an issue when using fluorescence microscopy since the entire sample area is typically illuminated for extended periods of time. While photobleaching is a phenomenon common to all fluorophores, careful dye selection can aid in mitigating this problem.
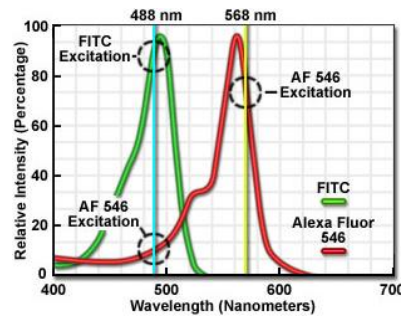
Figure 3.11. Illustration of fluorophore excitation overlap [10]

Background fluorescence can also often cause problems when using fluorescence microscopy. Some biological proteins, e.g. collagen and elastin, are autofluorescent and are therefore naturally capable of fluorescent excitation [20]. Consequently, it would be imprudent if examining a specimen containing an autofluorescent substance to select a fluorescent dye with an excitation spectrum similar to that of said substance. Since, as seen in Figure 3.9 and Figure 3.11, excitation spectra tend not to be narrow bands, an autofluorescent specimen would be limited to even fewer dyes than normal. Another typical cause of background fluorescence is nonspecific binding of the secondary antibody in ICC, though this can be minimized by blocking the nonspecific antibodies within the sample using serum or albumin, typically from the same type of animal that the secondary was grown in [21].

Sample preparation for fluorescence microscopy is somewhat conducive to viewing cells in their living state. Some stains, such as those in the CellMask line, are capable of being absorbed by living cells, though many stains and most antibodies are too large to pass through the cell membrane without first fixing and permeabolizing the cells [14, 22]. Therefore, some proteins can be viewed in live cells via fluorescence but many cannot without the more complicated technique of gene transfection to produce a fluorescent version of the protein inside the cell. However, even though cells may need to be fixed and permeabolized before the proteins of interest can be visualized, this process can be easily achieved with minimal change to the structure of the cells [23].

3.3.3. Confocal Microscopy

3.3.3.1. TECHNIQUES

Confocal microscopes make use of fluorescence staining as well; however they provide both enhanced resolution over wide field microscopy and the ability to generate three-dimensional images by using a pinhole to block out-of-focus light from the detector, as seen in Figure 3.12(a) [1, 24-27]. There are two types of confocal microscopes: laser scanning and spinning disk.

Laser scanning confocal microscopes use a laser to illuminate one very small section (of full thickness) of the specimen at a time. Out of focus like is blocked using a pin-hole that is conjugated to the focal plane (hence "con-focal" imaging). The emitted light from the sample is then collected on a photomultiplier tube (PMT), resulting in one pixel of the specimen image. The complete image of the specimen is obtained by raster scanning the laser and PMT together very quickly across the entire sample area. Because each point is scanned individually, laser scanning microscopy is capable of producing very high resolution images.

A spinning disk confocal microscope, seen in Figure 3.12(b), uses a Nipkow disk (Figure 3.13) spinning at a high speed to create a series of virtual pinholes. This system allows for visualization of roughly 1000 points on the specimen at any given time, thereby allowing the entire sample area to be imaged instantaneously. Consequently, spinning disk confocal microscopy allows for real-time confocal imaging of dynamic

systems which can be invaluable in observing biological phenomena [25]. Laser scanning confocal often takes more than 10 seconds per frame to obtain a high quality image stack, which is longer than most cells remain motion-free [28]. Since spinning disk confocal is capable of capturing an entire frame instantaneously, it is a powerful technique for high quality video and image capture of live cells.
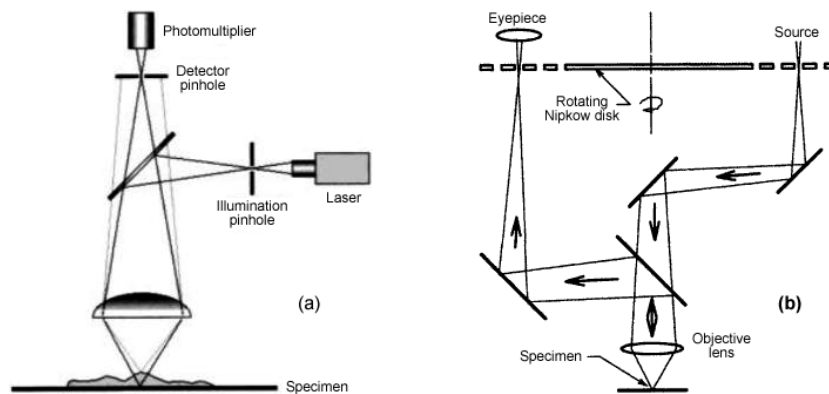
Figure 3.12. Diagram of the two types of confocal microscopes (a) laser scanning [26] and (b) spinning disk [27]

Another important function of confocal microscopy is the ability to obtain three-dimensional images. This is possible because samples of sufficient thickness contain multiple focal planes; due to out-of-focus light getting blocked by the pinhole, each of these focal planes can be imaged individually (Figure 3.14). When these images are subsequently combined through the use of deconvolution algorithms and tomographic techniques, the result is a 3D image (Figure 3.15). However, in order to faithfully recreate a 3D image the sample must be imaged at least the Nyquist sampling rate; that is,

30

each image in the stack must be offset from its neighbors in the Z-direction by no more than half the thickness of the images [29]. For example, if each image is sampling a section of a tissue 10 μm thick, then sequential images must be offset by no more than 5 μm.

3.3.3.2. LIMITATIONS AND SAMPLE PREPARATION

While confocal microscopy represents a significant advance from widefield microscopy, it too is not without pitfalls. Being an optical technique as well, its resolution limits are still subject to the wavelength of light used. The maximum lateral resolution (based on Equation 3.3) is approximately 180 nm and the maximum axial resolution (based on Equation 3.4) is roughly 500 nm, which is an improvement overwidefield microscopy but still leaves much to be desired when trying to visualize fine details within the microstructure of cells [18].
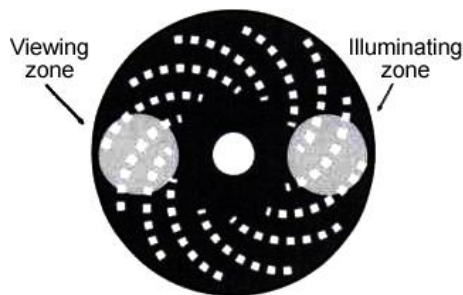
Figure 3.13. Diagram of a Nipkow disk [25]
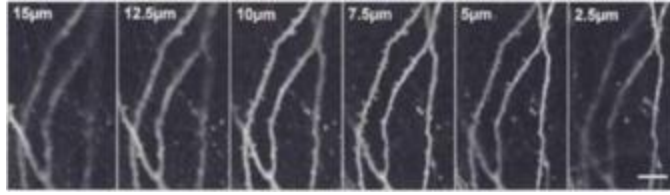
Figure 3.14. Confocal stack of images of dendrites in a rat brain [30]
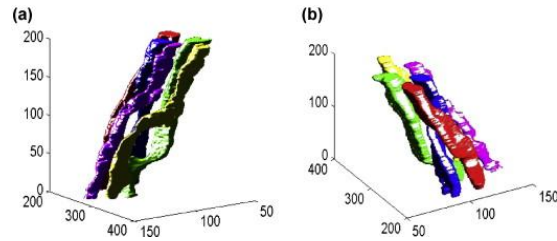
Figure 3.15. 3D Reconstruction of two confocal images of mouse axons [7]

Equation 3.3. Lateral resolution of confocal microscopy [19]

$$R_L = \frac{0.61\lambda}{\sqrt{2}NA}$$

Equation 3.4. Axial resolution of confocal microscopy [19]

$$R_A = \frac{2n\lambda}{\sqrt{2}NA^2}$$

Photobleaching is also still an issue in confocal microscopy. While less of the sample is illuminated at any given time than in widefield (Figure 3.16) the laser light in the illuminated area is much more focused and therefore much more intense. It is also worth noting that although only a thin section of the sample area is imaged at any given time,

the entire thickness is still illuminated and thus subject to photobleaching.

Photobleaching can be limited in laser scanning confocal by scanning the sample at a

faster rate than normal, though this leads to a great sacrifice in image quality. Fast

scanning may not be possible in samples that have a weak fluorescent signal and is

therefore reserved for image setup. Multi-photon (or two-photon) microscopy techniques

can achieve confocal resolution with less photobleaching since they only stimulate

fluorescence of the fluorophores in the focal plane. Sample preparation for confocal

microscopy is identical to that of widefield fluorescence microscopy.
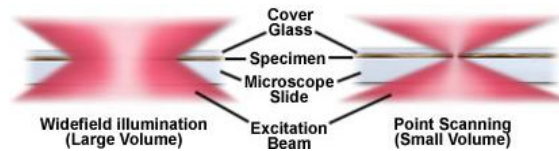
Figure 3.16. Illustration of widefield vs. confocal illumination patterns [25]

3.3.4. Scanning Electron Microscopy

3.3.4.1. TECHNIQUES

Typically, if one wants to view the structure of a cell down to the molecular level one

must resort to electron microscopy [18]. Rather than rely on the interaction of photons

with a sample, electron microscopy instead utilizes the interaction of electrons. There are

two types of electron microscopes: the Transmission Electron Microscope (TEM) and

Scanning Electron Microscope (SEM).

In Transmission electron microscopy, an electron beam passes through the sample in a vacuum (i.e. a particle-free environment) onto a fluorescent screen to produce a transmitted image (Figure 3.17(a)). The setup is very similar to standard transmission optical microscopy. Because the electrons must pass through the specimen, TEM requires a very thin section (40 – 90 nm thick) which is difficult to accomplish with biological and other elastomeric materials using the traditional ultramicrotomy methods of sample preparation [9, 31]. The major disadvantage of TEM with regards to mechanics modeling, however, is its limitation for creating a three-dimensional view [32]. While it is possible to create a 3D image using TEM, images must be captured at several angles; however, angular tilt is severely limited by a loss of resolution [33].

Scanning electron microscopy by contrast utilizes the interaction of the electron beam with the surface of a sample in a vacuum to generate an image. As shown in Figure 3.18, the incident beam (primary electrons) displaces orbital electrons from the atoms in the specimen thus causing the emission of secondary electrons. When secondary electrons contact a positively charged detector, a point of illumination is generated on a connected CRT screen. Before the primary electrons encounter the specimen, they are bent by deflector coils in order to raster scan the electron beam across the sample area. In addition to being connected to the detector, the CRT screen is also connected to the deflector coils to allow synchronization of the screen with the scanning electron beam as it moves across the sample.

Some electrons do not collide with orbital electrons, but instead pass near enough to the nucleus of the atom that their path is significantly altered (Figure 3.18). The energy

of these backscattered electrons depends directly on the size of the nucleus with which they interact; therefore, backscatter detection can be used to distinguish between the elemental components of a sample.

2.3.4.2. LIMITATIONS AND SAMPLE PREPARATION

The primary limitation of SEM with regards to imaging biological samples is the harsh environment and sample preparation that is required to stabilize them. This environment consists of the arid (i.e. non-aqueous), high vacuum chamber mentioned previously and radiation from the incident beam and scattered electrons [34]. In order to process the samples to make them electrically conductive, it is necessary to coat them in harsh chemicals such as heavy metal salts and silver or osmium [34]. While it is possible to image biological samples using these techniques, the sample preparation and imaging environment (in particular the non-aqueous nature of it) are capable of altering the structure of biological materials (i.e. producing artifacts) [34].
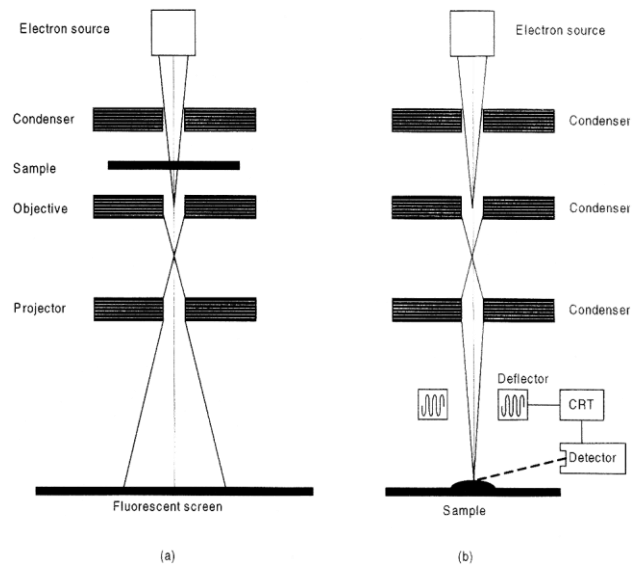
Figure 3.17. Diagram of the two types of electron microscope (a) TEM and (b) SEM [31]
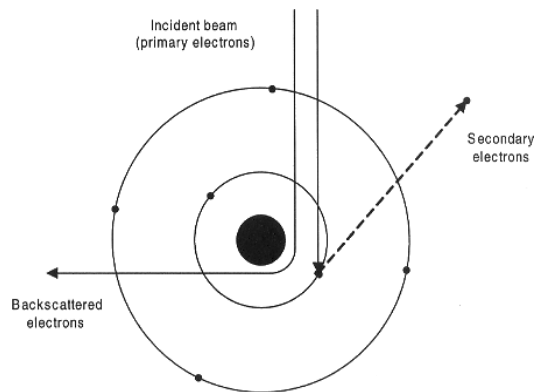
Figure 3.18. Illustration of electron interactions in SEM [31]

3.3.5. Scanning Probe Microscopy

3.3.5.1. TECHNIQUES

Scanning probe microscopy techniques such as Atomic Force Microscopy (AFM) allow for the imaging of cellular topography with the potential for atomic-scale resolution. This is accomplished by scanning a cantilever with a microfabricated tip across the sample using piezoelectric scanners as shown in Figure 3.19. Measurement of cantilever deflection is achieved via reflection of a laser off the cantilever onto a 4-quadrant detector. Figure 3.20 shows an example of cells imaged by AFM. There are multiple modes of AFM use, the most common of which are contact, intermittent (aka tapping), and non-contact. In contact mode the tip remains in contact with the sample and scans the sample at near constant force. This mode is generally used for topographic imaging and force measurements of hard samples and is typically done with a sharp, pyramidal tip. In intermittent mode (a.k.a. tapping mode on Veeco brand AFMs) the tip oscillates above the sample, coming into contact with it only briefly and intermittently. The tapping amplitude is kept constant as the tip is rastered over this surface. This mode is generally used for topographic imaging and force measurements of softer samples, including cells and is typically performed with a pyramidal tip. Data in tapping mode is derived from the height data obtained from the change in piezo distance that is required to keep the amplitude of the cantilever vibration constant. In non-contact mode, the tip is brought very near to but not touching the sample. Deflection of the cantilever is caused by van der Waals forces or electrostatic repulsion. This method is

applicable only to topographical imaging and can be particularly useful for imaging very

soft samples.
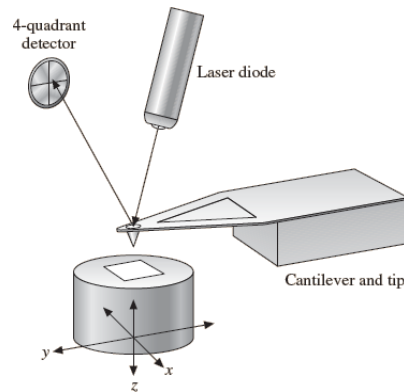
Figure 3.19. Schematic of Atomic Force Microscopy (AFM) [35]
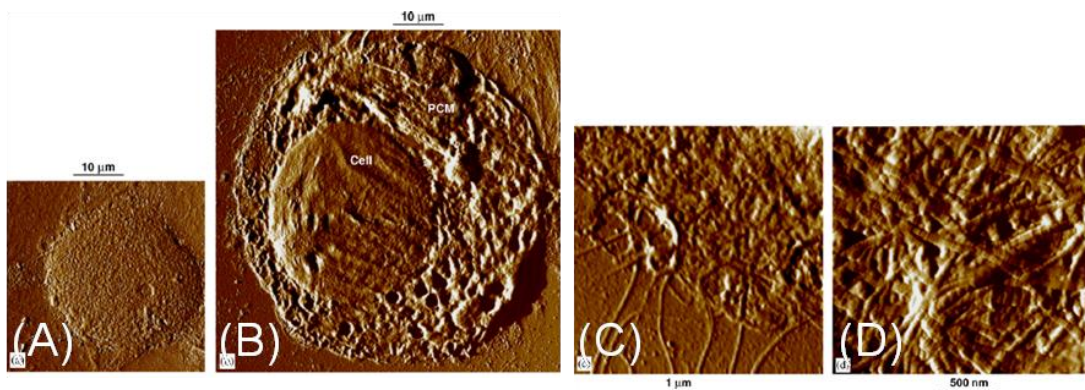
Figure 3.20. AFM images of calf chondrocytes adsorbed on mica substrates. (a) Freshly isolated chondrocyte (day 0), (b) chondrocyte released from alginate culture at day 11 where the pericellular matrix (PCM) is clearly distinguishable from the cell body, (c) chondrocyte released from alginate culture at day 18 shows single collagen fibrils emanating out of the dense fibrillar network of the PCM, (d) a higher resolution image of the dense network which exhibit fibril diameter characteristic of type II collagen fibrils [36]

3.3.5.2. LIMITATIONS AND SAMPLE PREPARATION

As opposed to all previously discussed imaging techniques, sample preparation is actually a strength of AFM imaging since the only requirement for AFM sample preparation is that the sample (e.g., cell(s)) be be attached to a substrate [30]. Cells may be imaged in air or in fluid and can be imaged while alive. Despite these advantages, AFM imaging does have some practical limitations. First of all, the depth of field in an AFM image is restricted by the travel distance of the *z*-directional piezoelectric scanner. Secondly, the depth of field is also limited by the relationship between the tip geometry and the surface topography of the sample. If a large spherical tip is used and small grooves are present in the sample, the tip will be unable to fit within the grooves and produce a true image of the sample.

3.4. MECHANICAL TESTING INSTRUMENTATION

3.4.1. Overview

There are several methods of probing the mechanical responses of cells to applied stimuli, but most fit within two categories: those which probe the entire cell at once and those which are more focused and probe only a small portion of the cell at any given time. A brief summary of the length scales and types of structures each of these techniques is useful for testing is presented in Figure 3.21.

3.4.2. Subcellular Region Probing Techniques

3.4.2.1. CYTOINDENTATION

3.4.2.1.1. GENERAL CYTOINDENTATION

As its name implies, cytoindentation involves indenting a region of a cell with a small probe, as seen in Figure 3.22 and Figure 3.23. There are two variations of this technique, general cytoindentation using a cylindrical probe and AFM indentation techniques. In general cytoindentation experiments, a probe (typically made of glass [20]) is indented into the cell using a piezoelectric transducer. Deflection is equal to the displacement of the piezo and force is calculated based on linear beam theory, given in Equation 3.5 [10, 20]. Probe diameters can range from smaller to larger than the diameter of the cell [10, 16, 17]. Cytoindentation can be used to perform indentation force measurement and creep experiments [16, 17].

Equation 3.5. Linear beam theory equation, where F is indentation force, E, I, and L are the elastic modulus, moment of inertia, and length of the probe, respectively, and U is its deflection

$$F = 3\frac{EI}{L^3}U$$
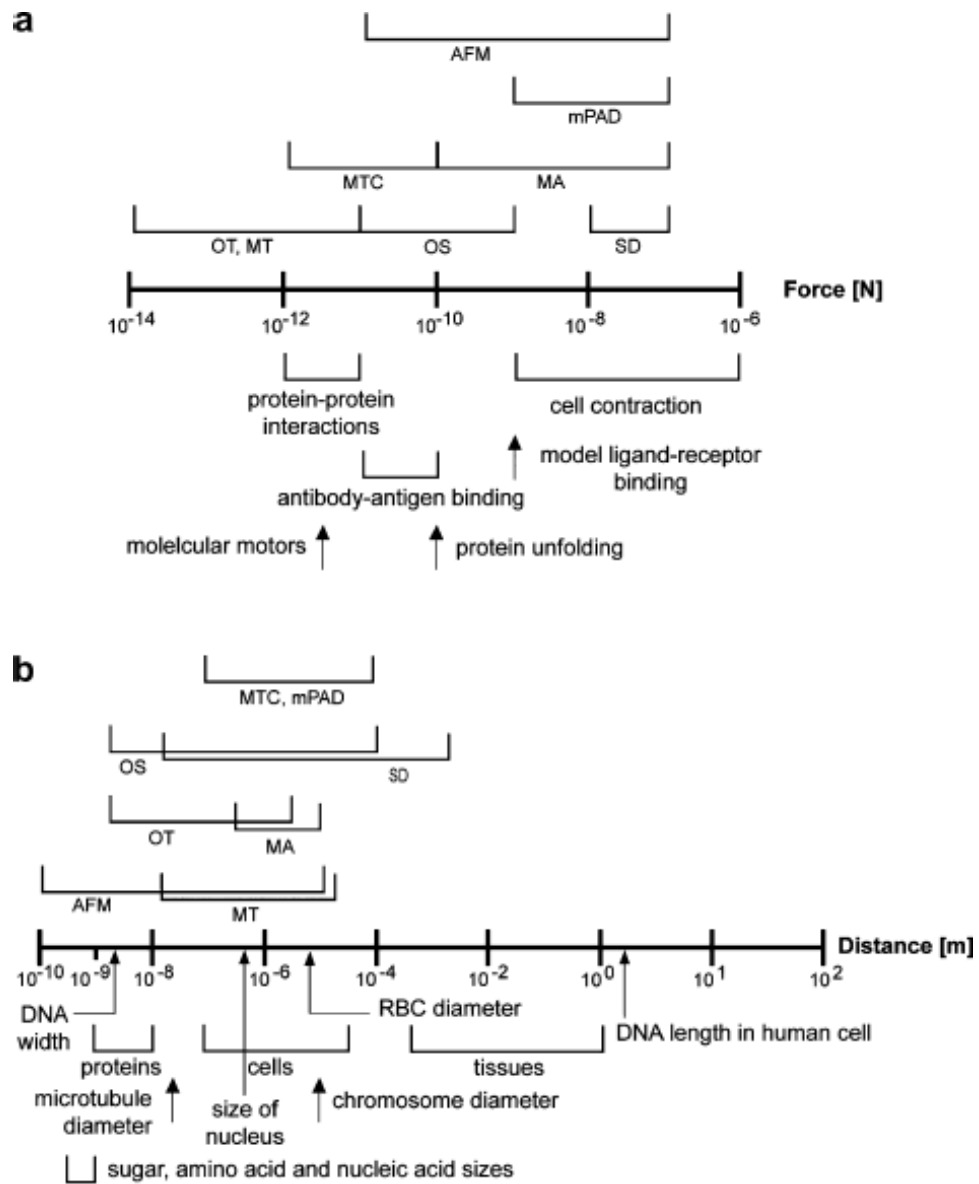
Figure 3.21. Common rheological testing techniques and the (a) force scales and (b) length scales for which they are primarily used within the field of cellular mechanics; AFM: atomic force microscopy, MTC: magnetic twisting cytometry, OT: optical tweezers, MS: microplate stretcher, mPAD: micro-post array deformation, MA: micropipette aspiration, SD: substrate deformation, [3]

3.4.2.1.2. AFM MECHANICS

In addition to its imaging capabilities, AFM is also capable of mechanical measurements. Rather than dragging the tip across the sample, AFM mechanics measurements utilize the spring characteristics of the cantilever to measure the force of resistance when the tip is indented in the cell. Atomic force microscopes can be used to perform stress relaxation tests that measure deflection of the cantilever over time at a constant displacement of the *z*-directional piezoelectric scanner and nanoindentation tests that measure the force of resistance as the tip is indented into the cell (Figure 3.24).

3.4.2.2. MAGNETIC TWISTING CYTOMETRY

In magnetic rheological experiments, one or more magnetic particles are either bound to the surface of a cell or internalized by it and the resulting displacement of the particle(s) in the presence of a magnetic field is measured to quantify their rheological response. Magnetocytometry experiments have been conducted for more than 85 years, dating back to Freundlich and Seifriz in 1922 (Figure 3.25) [37]. Early experiments based on the work Crick and Hughes in 1950 [38] which build upon that of Freundlich and Seifriz used superparamagnetic, ferromagnetic, or ferrimagnetic particles in a magnetic field gradient to generate a translational force on cells [6, 29, 32, 33, 39].
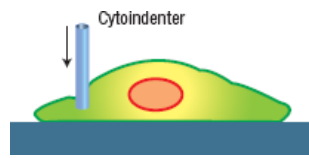
Figure 3.22. Cytoindentation [40]
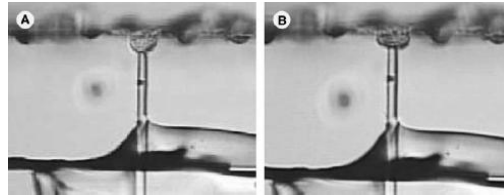
Figure 3.23. Cytoindentation of a single chondrocyte (A) before and (B) after indentation with a 5µm-diameter probe [10]
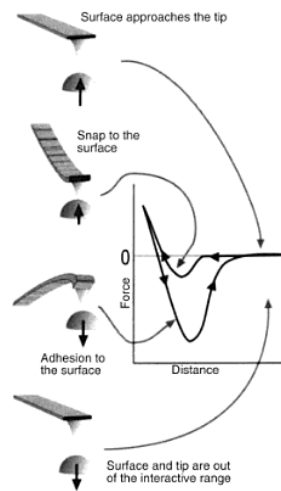
Figure 3.24. Schematic of AFM nanoindentation force measurement [18]
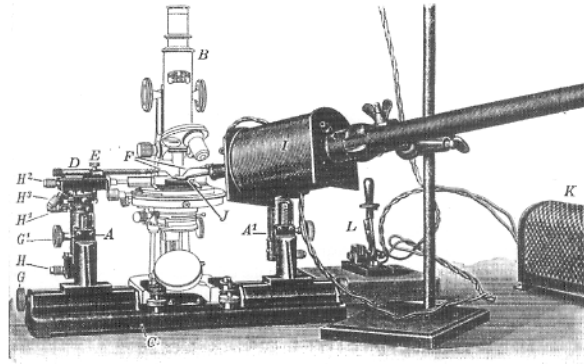
Figure 3.25. The magnetic manipulation system used in the first magnetocytometry experiments by Freundlich and Seifriz in 1922 [37]

Due to the inherent difficulty in producing well-controlled field gradients, more recent experiments primarily focus on magnetic twisting cytometry (MTC) [20]. In MTC, ferromagnetic particles are subjected to a homogeneous magnetic field, which can be easily produced. The method most widely used was developed by Wang et al. in 1993 (Figure 3.26) and consists of using a strong magnetic pulse to magnetize a large number of ferromagnetic particles already bound to a culture of cells and then inducing rotation by subjecting the particles to a weaker magnetic field oriented 90° to the earlier pulse [41]. The rotation is then measured either with video microscopy or with laser particle tracking, which is the more precise of the two [22].
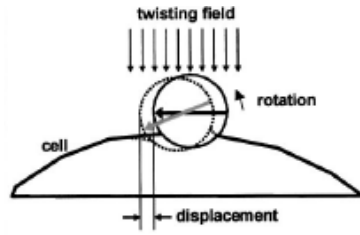
Figure 3.26. Magnetic twisting cytometry [23]

Magnetic twisting cytometry is generally performed using particles of up to 5 μm in diameter that are coated with ligands to specific receptors within or on the periphery of the cells of interest. A sinusoidal magnetic field is produced by Helmholtz coils (Figure 3.27) which can generate a magnetic torque of $450 - 1200$ pN $\times$ μm. The torque is limited on the low end by the amount of signal required to overcome the magnetic noise of the measurement system and on the high end by the amount of current required to avoid excessive heating in the Helmholtz coils. The resulting cell deformation is estimated based on the mean bead rotation angle, which is calculated using a theoretical formula (Equation 3.6) based on the change in the magnetic moment of the beads that assumes homogeneous bead rotation. MTC experiments are most often used to perform creep experiments [7, 42-45]. [44]

Although most MTC experiments rely on Equation 3.6 and its assumption of homogeneous bead rotation, this assumption does not truly reflect reality. However if small enough beads are used, multiple beads can be targeted to cytoskeletal structures within each cell. When video microscopy is used to measure bead rotation, it is possible to create a map of bead rotation throughout the cell [7].
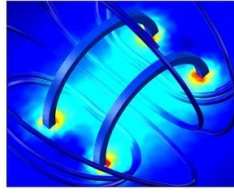
Figure 3.27. Finite element plot of magnetic field density produced by Helmholtz coils; image generated in COMSOL Multiphysics [46]

Equation 3.6. Magnetic bead rotation angle formula used in MTC, where θ is bead rotation and B is magnetic moment of the beads [44]

$$\theta(t) = \arccos\left(\frac{B(t)}{B_0}\right)$$

One advantage of MTC over AFM is that measurements of an entire population of cells can be taken at once providing instant homogenization of cell behavior rather than probing each cell individually. Another advantage is that MTC has the potential to be adapted for future in vivo applications in humans by using helium-3 magnetic resonance imaging (MRI) technology or a superconducting quantum interference device (SQUID) to generate a map of the magnetic field [44].

There are, however, several weaknesses of MTC. The chief weakness is the difficulty in quantifying how the location of particle binding affects the results of each experiment. For example, a particle bound to receptors inside the cell will react less strongly to a magnetic field than will a particle in the same field that is bound to receptors on the outside of the cell membrane. [44]

3.4.3. Whole Cell Deformation Techniques

3.4.3.1. MICROPIPETTE ASPIRATION

Micropipette aspiration is a simple technique for measuring the mechanical properties of cells. In this technique a constant negative hydrostatic pressure of $10^{-1} - 10^{5}$ Pa [7] is applied to a cell, either in suspension or attached to a substrate, using a micropipette of < $1 - 10$ μm diameter [8] as shown in Figure 3.28. The resulting deformation of the cell into the micropipette is then measured using video microscopy to calculate the mechanical response of the cell. Micropipette aspiration is primarily used for performing creep experiments on cells with relatively little more mechanical support than a thin spectral cytoskeleton adhering tightly to the cell membrane (generally non-adherent cells such as red blood cells (RBCs) and leukocytes) [7]. It can be used to calculate the elastic modulus, cytoplasmic viscosity, and Poisson's ratio of cells, usually without considering the effects of friction between the cell and the walls of the micropipette [3, 20, 21, 47].
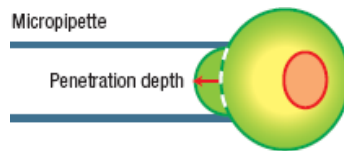
Figure 3.28. Micropipette aspiration [40]

3.4.3.2. OPTICAL TRAP

When a laser is focused through a high numerical aperture microscope objective and shined on a refractive particle whose refractive index is higher than that of the medium it is in, optical forces are generated. A 'gradient force,' which scales linearly with volume (i.e. has a d^3 dependence) that pulls the particle toward the focal point of the laser and a 'scattering force,' which scales squarely with volume (i.e. has a d^6 dependence) [20] that pushes the particle away from the focal point of the laser. These forces can be broken down into forces which act radially and axially to the direction of laser propagation. With careful selection of particle refractive index and size, the gradient force is capable of overcoming the scattering force resulting in the particle becoming trapped at the laser focal point. When two micron-sized trapped particles are coated in ligands which bind to receptors on a cell are attached to diametrically opposing ends of the cell they can be used to mechanically deform the cell (Figure 3.29). This technique is known as an optical trap. It can also be performed with a single bead bound to the cytoskeleton of a cell that is attached to a substrate [3].
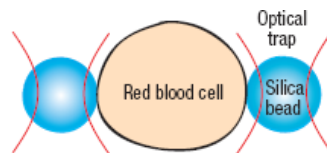
Figure 3.29. Laser/optical tweezers [48]

Like micropipette aspiration, the optical trap method of cell rheology is generally used on very soft cells (e.g. RBCs) for analysis at the whole cell level; however it can

also provide valuable information about local mechanics of a cell if the beads are bound to the cytoskeleton rather than the cell membrane. Through analysis of geometry changes resulting from oscillatory forces, optical traps can provide the viscoelastic responses of cells. However, optical traps are only capable of generating forces of up to several hundred pN [3]; orders of magnitude smaller than AFM and micropipette aspiration are capable of [8]. Because of this, it only provides information about the viscoelastic response of cells in the low force linear regime [7, 20].

3.4.3.3. MICROPLATE STRETCHING

Microplate testing involves growing a cell on a rigid plate and attaching a flexible plate functionalized with adhesion promoting proteins to the top of it as shown in Figure 3.30. The flexible plate can then be used to apply a known deformation or force to the cell using a piezoelectric translator. The bending of the flexible plate can then be measured using an optic fiber technique. Microplate stretching can be used to perform stress relaxation, creep, oscillatory, and shear experiments on cells with forces ranging from 10 nN to 10 μN [7, 20].
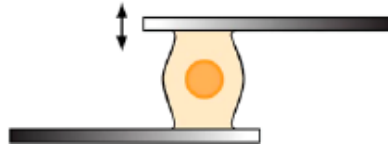
Figure 3.30. Microplate stretcher [3]

3.4.3.4. MICROPOST ARRAYS

All of the mechanical testing techniques discussed so far have focused on how cells react to externally imposed forces. In order to fully understand the cytoskeletal mechanics of cells however, it is also vital to understand the forces built into the cytoskeletal network by the cell itself. This can be achieved by measuring the traction forces (i.e. using traction cytometry) of a cell against a patterned substrate of polydimethyl siloxane (PDMS) posts attached to a rigid plate as shown in Figure 3.31. Because the properties of the PDMS posts are well-known, a force-deflection curve can be easily generated in finite element software as shown in Figure 3.32. This curve can then be used to correlate the deformation of the posts with the forces acting on them [49].

3.5. SINGLE CELL MECHANICS MODELS

3.5.1. Overview

Figure 3.31. Cell contraction on microarray substrate [3]
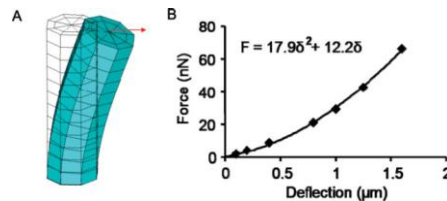
Figure 3.32. Schematic of (A) FEM model for a micropost with a lateral force exerted on its top and (B) lateral force determined by FEM [49]

For as long as there have been observations of the mechanical properties of cells, there have been models put forth to attempt to describe those observations. At the most basic level, there are two categories of these models: continuum and structure-based. The first models of cellular mechanics as a 'balloon full of molasses' [50] were continuum models which by definition lack internal structure [4]. Despite the overwhelming evidence in support of structural elements within cells, these types of models remain popular with bioengineers due to their relative simplicity and similarity with the earliest mechanical principles taught to young engineers. Structure-based models, on the other hand, are comprised of a network(s) of discrete structural elements which work in

harmony to explain the mechanical responses of cells. These models have many benefits, as will be discussed shortly, but can quickly become computationally expensive. In order to become widely accepted by the scientific community, any complete model of cellular mechanics must likely take into account aspects of both models, namely the viscoelastic, nonlinear and heterogenic mechanical responses of cells as well as their numerous structural components and their ability to actively remodel those components in response to applied stresses.

3.5.2. Continuum-Based Approaches

3.5.2.1. THE HERTZ MODEL

One of the earliest models relevant to cellular mechanics was described by Heinrich Hertz in 1882 [13]. Hertz was primarily concerned with describing the mechanics of contact between two elastic spheres and as such, built several assumptions into his model. These assumptions [51, 52] can be summarized as follows:

1. Each body is a half space loaded over a small elliptical area

2. The material properties of each body are homogeneous, isotropic, and linear elastic

3. Deformations are infinitesimal (i.e. small strains)

4. No plastic deformation occurs over the contact area

5. The contact surfaces are frictionless

6. The stress resulting from contact vanishes at a distance far from the contact

   area

7. The thickness (in the case of cylinders) and dimensions of each body are

   infinite

The equation governing the relation of force of indentation to the elastic modulus of an

indented sample according to the Hertz model is given below in Equation 3.7 [20, 31,

53]:

Equation 3.7. Equation governing the force, F, of a spherical indenter on a sample
according to the Hertz model

$$F = \frac{4}{3}\frac{E}{(1-v^2)}R^{\frac{1}{2}}\delta^{\frac{3}{2}}$$

where E and v are the elastic modulus and Poisson's ratio of the sample, respectively, δ is

the depth of indentation, and R is the radius of the spherical indenter. Contact area, a, is

given by the Hertz model as shown in Equation 3.8 below [54]:

Equation 3.8. Area of contact between a sample and a spherical indenter as defined by the
Hertz model

$$a = \sqrt[3]{\frac{3F}{4}\frac{\frac{(1-v_{indenter}^2)}{E_{indenter}} + \frac{(1-v_{sample}^2)}{E_{sample}}}{\frac{1}{R_{indenter}} + \frac{1}{R_{sample}}}}$$

The Hertz model is frequently used to analyze AFM measurements due to its simplicity, however this is often not a meaningful method of analysis based on the inability of any of the assumptions listed earlier to accurately describe the behavior of cells when indented [20, 51]. Despite its inaccuracy, the Hertz model is commonly used for comparison purposes since it is the most rudimentary form of analysis and more complex analytical methods may not correlate well with one another. It should also be noted that the Hertz model is close to accurate at small strains (up to approximately 10%) [31].

3.5.2.2. VISCOELASTIC MODELS

3.5.2.2.1. BASICS OF VISCOELASTICITY

Cells often exhibit viscoelastic behaviors upon deformation. Although there are many types, or models, of viscoelastic behavior, the same underlying mechanism of compound structure is responsible for each of them. This behavior is most commonly described in polymers which derive their viscoelastic behavior from being able to deform based on both bond stretching and/or bond rotating (conformational shifts). In cells, this compound mechanical structure consists of the cytoskeletal features discussed in Section 3.2, which, as discussed earlier, all have different mechanical properties on their own. As these structures work synchronously to resist forces acting equally upon them, each will contribute to the behavior of the cell to a different degree. This accounts for two important characteristics of the stress-strain curves of cells.

Due to the viscoelastic nature of cells, they do not exhibit a linear region of elastic deformation as seen in Figure 3.33 (A), but rather a parametric one as seen in Figure 3.33 (B). Furthermore, the dissipation of energy upon loading leads to a different stress-strain curve upon unloading. This effect is known as hysteresis and is characterized by the area between the loading and unloading curves.
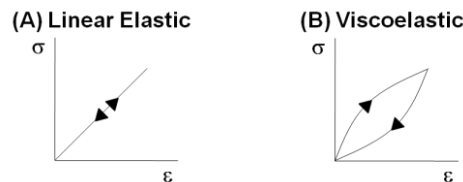
Figure 3.33. Examples of linear elastic and viscoelastic stress-strain curves

In order to experimentally characterize viscoelastic materials, cells included, two types of tests are commonly employed: creep and stress-relaxation tests. Creep tests are performed by application of a steady uniaxial stress and measurement of strain over time (Figure 3.34 [a]), while stress relaxation tests are performed by the application of a steady strain and measuring the resulting stress in the material over time (Figure 3.34 [b]) [55, 56].

3.5.2.2.2. MODELS OF VISCOELASTICITY

BASICS OF VISCOELASTIC MODELS

Viscoelastic materials can frequently be thought to act as represented by a number of Hookean springs described by

Equation 3.9 [56] and Newtonian dashpots (viscous dampers) described by Equation

3.10 [56] working together in some prescribed arrangement analogous to an electrical

circuit. There are an infinite number of possible configurations, however only a select

few are commonly used to model the mechanical properties of cells.
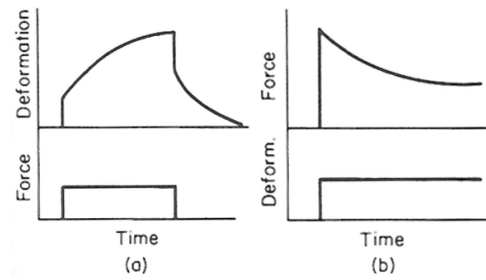
Figure 3.34. Characteristic (a) creep and (b) stress relaxation curves [55]

Equation 3.9. Viscoelastic spring equation, where σ is analogous to force, ϵ to
displacement, and k to the Young's modulus of the spring

$$\sigma = k\epsilon$$

Equation 3.10. Viscoelastic dashpot equation, where η is viscosity and $\dot{\epsilon}$ is the strain rate

$$\sigma = \eta\dot{\epsilon}$$

Being analogous to the elastic modulus, the units of k are N/m^2, while the units of η

are N·s/m^2. It is often helpful to consider the ratio of viscosity to stiffness shown in

Equation 3.11, which is a constant value referred to as the relaxation time and has units of seconds, in the analysis of experimental data since time is a parameter that can be easily measured.

Equation 3.11. Viscoelastic relaxation time constant, τ

$$\tau = \frac{\eta}{k}$$

Comprising the various models are two basic building blocks: Maxwell and Kelvin elements. The first and most simple is the Maxwell element, represented by a spring and a dashpot in series as shown in Figure 3.35 (A). In a "Maxwell solid," the total strain is equal to the sum of the strain in each element, while the stress on each component is the same and equal to the applied stress as shown in the equations below, where the subscripts s and d represent the spring and dashpot respectively.

Equation 3.12. Maxwell component stress

$$\sigma = \sigma_s = \sigma_d$$

Equation 3.13. Maxwell component strain

$$\epsilon = \epsilon_s + \epsilon_d$$

In order to develop a constitutive equation representing the complete behavior of a Maxwell element, it is useful to differentiate Equation 3.12 and then express the spring and dashpot strain rates in terms of the stress as shown in Equation 3.14.

Equation 3.14. Constitutive equation for a Maxwell element [56]

$$\dot{\epsilon} = \dot{\epsilon}_s + \dot{\epsilon}_d = \frac{\dot{\sigma}}{k} + \frac{\sigma}{\eta}$$

Equation 3.14 can be simplified by multiplying by k and employing the use of the time constant τ as shown in Equation 3.15.

Equation 3.15. Simplified constitutive equation for a Maxwell element [56]

$$k\dot{\epsilon} = \dot{\sigma} + \frac{1}{\tau}\sigma$$

When a sudden constant force σ is applied to a Maxwell solid (as in the case of a creep test), the elastic spring deforms instantaneously while the dashpot then deforms proportionally with respect to time ($\epsilon(0) = 0$) as shown in Figure 3.35 (B). The equation governing the deformation, or creep function, can be determined by solving for ϵ in the constitutive equation assuming $\dot{\sigma}$ is equal to zero (Equation 3.16).
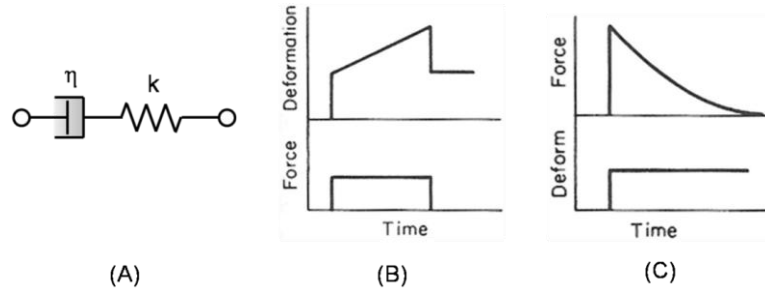
Figure 3.35. Maxwell model of viscoelasticity (a) representation of Maxwell model, (b) creep function of Maxwell model, (c) Relaxation function of Maxwell model; adapted from [55]

Equation 3.16. Maxwell element creep function [55]

$$\epsilon(t) = \sigma\left(\frac{1}{k} + \frac{t}{\eta}\right) = \sigma\left(1 + \frac{t}{\tau}\right)$$

The ratio of strain to stress in creep tests is known as the "creep compliance" [56] and is defined by Equation 3.17. Remembering that $\sigma = \sigma_0$, this leads to a compliance function as given by Equation 3.18.

Equation 3.17. Creep compliance

$$C_{crp}(t) = \frac{\epsilon(t)}{\sigma_0}$$

Equation 3.18. Maxwell element compliance function

$$C_{crp}(t) = 1 + \frac{t}{\tau}$$

When a sudden constant deformation ϵ is applied to a Maxwell solid (as in the case of a stress relaxation test), the spring again responds instantaneously while the dashpot responds over time ($\sigma(0) = 0$) as shown in Figure 3.35 (C). The equation governing the relaxation can be determined by solving for σ in the constitutive equation assuming $\dot{\epsilon}$ is equal to zero (Equation 3.19). Since σ_0 is known and $\sigma(t)$ is measured in stress relaxation tests, τ can be easily calculated.

Equation 3.19. Maxwell element relaxation function

$$\sigma(t) = \sigma_0 e^{-\frac{t}{\tau}}$$

The ratio of strain to stress in stress relaxation tests is known as the "relaxation modulus" [56] and is defined by Equation 3.20. Remembering that $\sigma_0 = k\epsilon_0$, this leads to a compliance function as given by Equation 3.21. Since ϵ_0 is known and $\sigma(t)$ is measured during the stress relaxation experiment, Equation 3.21 allows for the calculation of k which after solving for τ leads to the calculation of η and therefore the complete characterization of the Maxwell solid.

Equation 3.20. Relaxation modulus

$$E_{rel}(t) = \frac{\sigma(t)}{\epsilon_0}$$

Equation 3.21. Maxwell element relaxation modulus function

$$E_{rel}(t) = ke^{-\frac{t}{\tau}}$$

<u>VISCOELASTIC MODELS USED IN CELLULAR MECHANICS</u>

The Kelvin element (also frequently referred to as the Standard Linear Solid (SLS) model of viscoelasticity) can be represented by a spring in parallel with a Maxwell element as shown in Figure 3.36 (A). The addition of the parallel spring to the Maxwell element provides a limitation of deformation to the Kelvin element which more closely represents the nature of biological materials [56]. This spring has a stiffness of k_e, so named because it provides an equilibrium stiffness that remains after the extension of the dashpot in the Maxwell arm has relaxed away the stresses that element.

In a Kelvin solid, the total stress is equal to the sum of the stress in each arm, while the strain on each arm is the same and equal to the applied stress as shown in the equations below, where the subscripts e and m represent the equilibrium and Maxwell arms respectively.
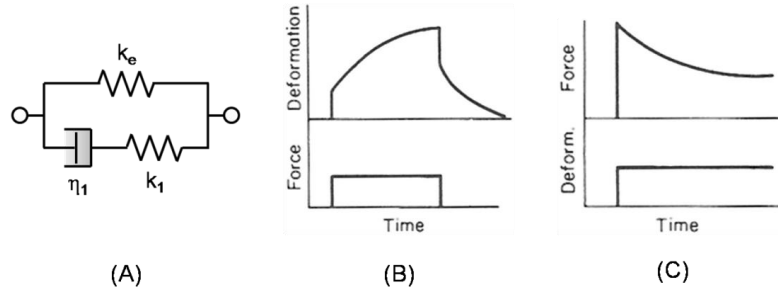
Figure 3.36. Kelvin model of viscoelasticity (a) representation of Kelvin model, (b) creep function of Kelvin model, (c) Relaxation function of Kelvin model; adapted from [55]

Equation 3.22. Kelvin arm stress

$$\sigma = \sigma_e + \sigma_m$$

Equation 3.23. Kelvin arm strain

$$\epsilon = \epsilon_e = \epsilon_m$$

In order to develop a constitutive equation representing the complete behavior of a Kelvin body Equation 3.15 can be substituted into Equation 3.22 for σ_m. After rearranging terms, the constitutive equation for a Kelvin body is shown in Equation 3.24, where τ_ϵ and τ_σ are the relaxation times for constant strain and stress, respectively.

Equation 3.24. Kelvin body constitutive equation [55]

$$\sigma + \left\{\frac{\eta_1}{k_1}\right\}\dot{\sigma} = k_e\left(\epsilon + \left\{\frac{\eta_1}{k_e}\left[1 + \frac{k_e}{k_1}\right]\right\}\dot{\epsilon}\right) \quad \Longleftrightarrow \quad \sigma + \tau_\epsilon\dot{\sigma} = k_e(\epsilon + \tau_\sigma\dot{\epsilon})$$

62

Solving this equation is awkward, however, due to the presence of both stress and strain

and their time derivatives in the same equation. It is useful then to use a Laplace

transformation to change Equation 3.24 from a differential equation to an algebraic one in

order to make it easier to solve [56]. Denoting the transformed functions with an overline

and multiplying the time derivatives by the Laplace variable s gives $\mathcal{L}(\dot{\epsilon}) = s\bar{\epsilon}$ and

$\mathcal{L}(\dot{\sigma}) = s\bar{\sigma}$ which leads to the transformed form of Equation 3.24 shown in Equation

3.25.

Equation 3.25. Laplacian Kelvin body constitutive equation [56]

$$\bar{\sigma} = \left(k_e + \frac{k_1 s}{s + \frac{1}{\tau_\epsilon}} \right) \bar{\epsilon}$$

Equation 3.25 can be rewritten to resemble Hooke's Law ($\sigma = E\epsilon$) by introducing a

parameter $\mathcal{E}$ as shown in the equations below. This Laplacian version of Hooke's Law is

known as the associated viscoelastic constitutive equation and holds true for any model

of viscoelasticity using the appropriate value of $\mathcal{E}$ for each model [56].

Equation 3.26. Kelvin body parameter, $\mathcal{E}$

$$\mathcal{E} = k_e + \frac{k_1 s}{s + \frac{1}{\tau}}$$

Equation 3.27. Associated viscoelastic constitutive equation

$$\bar{\sigma} = \mathcal{E}\bar{\epsilon}$$

When a sudden constant deformation ϵ is applied to a Kelvin body (as in the case of a stress relaxation test), the springs again respond instantaneously while the dashpot responds over time ($\sigma(0) = 0$) as shown in Figure 3.36 (C). The equation governing the relaxation can be determined by solving for σ using the associated viscoelastic constitutive equation assuming $\dot{\epsilon}$ is equal to zero (Equation 3.28 through Equation 3.30).

Equation 3.28. Laplace transform of $\epsilon(t) = \epsilon$

$$\bar{\epsilon} = \frac{\epsilon}{s}$$

Equation 3.29. Laplacian Kelvin body constitutive equation based on Equation 3.28

$$\frac{\bar{\sigma}}{\epsilon} = \frac{k_e}{s} + \frac{k_1}{s + \frac{1}{\tau_\epsilon}}$$

The Kelvin body relaxation modulus can then be easily solved for by inverting Equation 3.29 using the inverse Laplace transform $\mathcal{L}^{-1}\{1/(s + a)\} = e^{-at}$.

Equation 3.30. Kelvin body relaxation modulus function [56]

$$E_{rel}(t) = \frac{\sigma(t)}{\epsilon} = k_e + k_1 e^{-\frac{t}{\tau}}$$

It is of interest to note that the Kelvin body relaxation modulus function is simply equal to the Maxwell element relaxation modulus shifted upward by the value of k_e as apparent between Figure 3.35(C) and Figure 3.36(C).

When a sudden constant force σ is applied to a Kelvin body (as in the case of a creep test), the springs deform instantaneously while the dashpot then deforms proportionally with respect to time ($\epsilon(0) = 0$) as shown in Figure 3.36(B). Since using the associated viscoelastic constitutive equation to solve for strain generated by a given stress is awkward due to the parameter $\mathcal{E}$ appearing in the denominator, it is easier to determine the equation governing the deformation, or creep function, by solving for ϵ in the Kelvin body constitutive equation assuming $\dot{\sigma}$ is equal to zero (Equation 3.31).

Equation 3.31. Kelvin body creep function [55]

$$\epsilon(t) = \frac{1}{k_e}\left(1 - \left[1 - \frac{\tau_\epsilon}{\tau_\sigma}\right]e^{-\frac{t}{\tau_\sigma}}\right)\sigma$$

The Kelvin, or SLS, model is the most frequently used model in the literature due to its relative simplicity, however it has been shown to be among the least accurate models of viscoelasticity for the representation of cellular mechanics [14, 21, 53, 57-59]. Other commonly used models of viscoelasticity include the Quasilinear Viscoelastic (QLV) model, the Generalized Maxwell or Weichert model, and the Power Law relaxation model [14, 21, 55, 56, 60]. The QLV model is represented by an infinite series of Kelvin bodies as shown in Figure 3.37. The reduced relaxation function for the QLV model is shown in Equation 3.32, where c is a dimensionless constant.

65
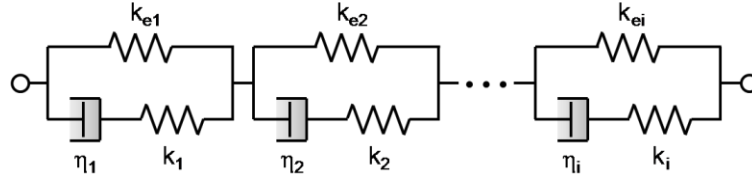
Figure 3.37. Quasilinear Viscoelastic (QLV) model

Equation 3.32. QLV reduced relaxation function, $G(t)$ [55]

$$G(t) = \frac{1 + c \int_{\tau_1}^{\tau_2} \frac{e^{-\frac{t}{\tau}}}{\tau} d\tau}{1 + c \int_{\tau_1}^{\tau_2} \frac{1}{\tau} d\tau}$$

The Generalized Maxwell model behaves similarly to the QLV model [60] and is represented by a spring in parallel with an infinite series of Maxwell elements as shown in Figure 3.38. The associated viscoelastic constitutive equation and relaxation modulus function are given in Equation 3.33 and Equation 3.34, respectively. For both the QLV and Generalized Maxwell models, it is important to note that by employing the use of a large number of elements any relaxation curve can be fit with great accuracy; however this situation is rarely representative of the underlying mechanisms governing the actual relaxation behavior. In choosing the appropriate number of elements to incorporate into a model, it is necessary to interpret the number of rates of decay in the relaxation curve. If the number of rates of decay is unknown, the constitutive equations can be simplified to integral relationships with a small number of fitting parameters by using an infinite number of elements. However, cells often exhibit a fast and slow rate of relaxation [14];

therefore it is often acceptable to incorporate however many elements are required to

obtain two time constants.
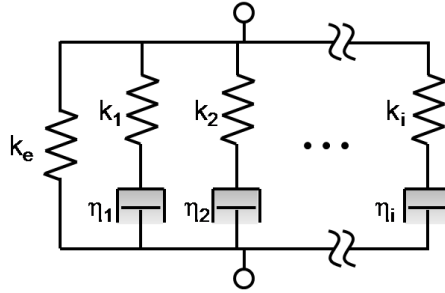
Figure 3.38. Generalized Maxwell model

Equation 3.33. Associated viscoelastic constitutive equation for the Generalized Maxwell model [56]

$$\bar{\sigma} = \bar{\sigma}_e + \sum_i \bar{\sigma}_i = \left\{ k_e + \sum_i \frac{k_i s}{s + \frac{1}{\tau_i}} \right\} \bar{\epsilon} = \mathcal{E}\bar{\epsilon}$$

The final viscoelastic model of note is the Power-law structural damping model. The

Power-law has no time constants, springs, or dashpots. It is a purely mathematical tool

for fitting a relaxation curve. The relaxation function for the Power-law is given in

Equation 3.35, where A corresponds to the relaxation curve and α governs the rate of

decay.

Equation 3.34. Relaxation modulus function for the Generalized Maxwell model [56]

$$E_{rel}(t) = k_e + \sum_i k_i e^{-\frac{t}{\tau_i}}$$

Equation 3.35. Power-law relaxation function

$$At^{-\alpha}$$

These viscoelastic models are commonly used to analyze data from each type of experiment described in Section 3.4 [21]. Each of these models is capable of describing experimental data from cell mechanics experiments with a reasonable degree of accuracy. Which model is selected appears in the literature to be based on the structural complexity of the cell being analyzed and the extent to which each researcher is willing to perform complex analytical techniques.

3.5.3. Structure-Based Approaches

3.5.3.1. MOLECULAR NETWORKS

The most simplistic model of cellular mechanics which accounts for the internal structures of cells is the molecular network model. These models consist of networks of an infinite number of filaments that distort in an affine manner [61, 62] as the network is deformed as shown in Figure 3.39. Molecular networks are useful for analyzing cellular cytoskeletal components, namely actin stress fibers [63] and microtubules [64] as Euler-Bernoulli beams to determine the contribution of each of these structures to the

rheological behavior of cells. However, since these models have the aforementioned strict assumptions that do not match experimental observations of cells, do not account for the contribution of more than one cytoskeletal filament type, and are modeled as networks floating free in solution rather than anchored to a substrate, they are useful primarily for gaining inputs for parameters in more realistic models.

3.5.3.2. TENSEGRITY

Tensegrity is a theory of cell mechanics that appears to be followed by a small but dedicated few researchers. It is based on the idea that structures can stabilize their shape by continuous
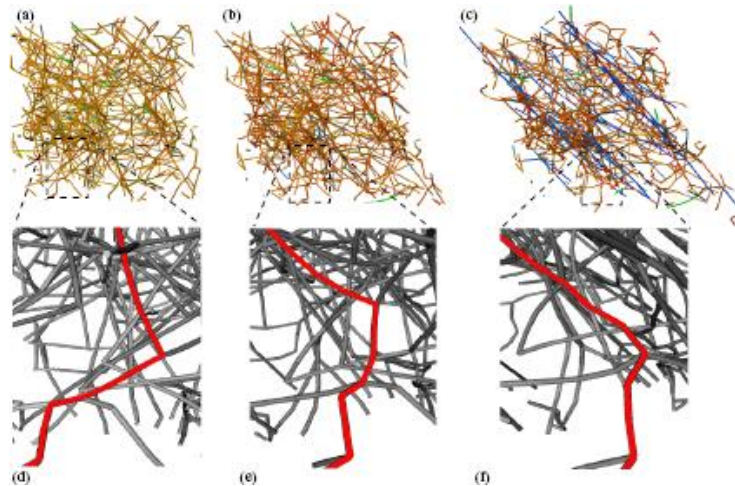
Figure 3.39. Deformation of a 3D molecular network model of cross-linked actin stress fibers [63]

tension, or 'tensional integrity,' (like a tent) rather than by continuous compression (like a stone arch) – a building principle which has been utilized to varying degrees since the

69

day man first used rope to hold flint axe heads and spear tips in place on a stick but was not described as a single cohesive theory of mechanics until R. Buckminster Fuller coined the term 'tensegrity' in 1961 [65]. Fuller initially described two broad classes of structures as falling within the definition of tensegrity: geodesic and prestressed networks. Geodesic structures are composed of triangular structural members oriented along geodesics (minimal paths) to constrain movement, while prestressed structures constrain movement through the use of pre-existing tensile stress of isometric tension ('prestress'). The definition of tensegrity has since been broadened and is now considered to include tensed networks that resist shape distortion and self-stabilize by incorporating other support elements that resist compression. All of these structures would fail to maintain their shape when mechanically stressed without continuous transmission of tensional forces [65-67].

There are two *a priori* predictions of tensegrity structures based on the principle of virtual work [68] that must be satisfied in cellular behavior to be able to even consider the possibility that cellular mechanics is governed by tensegrity. The first and most critical is that their level of prestress should be a major determinant of their stiffness [69]. This prestress is generated both passively by the extracellular matrix and actively by the contractile actomyosin apparatus [4]. Through the use of traction cytometry to quantify the prestress of various cell types, several experiments [43, 70-73] have been conducted by the Wang and Ingber groups showing that this is indeed a phenomenon observed in cells. Wang et al. have demonstrated that cell shear stiffness, G, increases in direct proportion to the prestress in the cytoskeleton, P ($G \approx 1.04P$) [74, 75]. It is important to

note that, as with much of the evidence in support of cellular tensegrity, this relationship may have other explanations but is a necessary characteristic of any tensegrity structure.

The second *a priori* prediction of tensegrity structures is that cells must behave like discrete mechanical networks rather than as a mechanical continuum. One characteristic difference between the two is the ability of local stresses to produce global strains. This property of discrete networks is due to the ability of the structural elements to change their orientation and relative spacing due to an applied load until a new equilibrium position is achieved and is in direct contradiction with continuum models of cell mechanics, in which the strains generated by a local stress have no structural elements to travel along and therefore dissipate rapidly away from the point of contact [4]. A number of research groups have shown experimentally [41, 76-83] using magnetic twisting cytometry, optical and magnetic tweezers, traction cytometry, and cytoindentation techniques that this is the case. In one example of this, Kumar and Ingber showed this by surgically severing a single actin stress fiber with a femtosecond laser nanoscissor and using traction force microscopy and embedded fluorescence microscopy to observe changes is stress within an adherent cell as shown in Figure 3.40 [83].
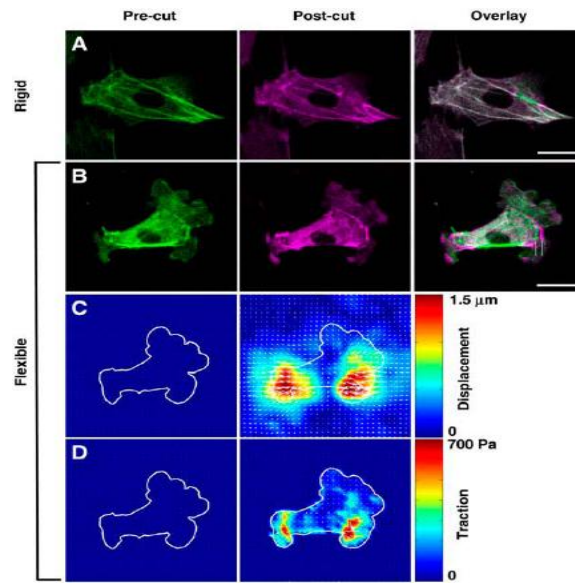
Figure 3.40. Results of severing a single actin stress fiber on displacement and traction forces within an adherent bovine capillary endothelial cell on both flexible and rigid ECM substrates [83]

CORTICAL MEMBRANE MODEL OF CELLULAR TENSEGRITY

Donald Ingber introduced the concept of a tensegrity model for cellular mechanics in the early 1980's [84, 85]. There are three different tensegrity models which have been proposed by Ingber and others in efforts to accurately model cellular rheology. The first of these is the Cortical Membrane model. This is a geodesic tensegrity model (Figure 3.41) that assumes the main load-bearing elements of the cytoskeleton are confined to the thin spectral cytoskeleton that adheres tightly to the cell membrane. Under the conditions of this model, the cortical membrane is considered to be under sustained tension which is balanced by the compressive forces of cytoplasmic pressure and traction forces provided by extracellular adhesions in the case of adherent cells [20]. This model has been able to

72

successfully describe the mechanics of non-adherent cells [86, 87], but has had only

limited success in modeling the behavior of adherent cells [88].
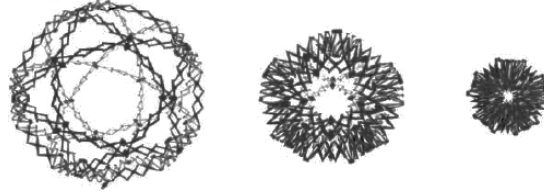
Figure 3.41. Visualization of expansion and contraction behavior of a geodesically structured Hoberman Sphere (Hoberman Toys, Inc.) representing the cortical membrane model of cellular tensegrity [4]

The constitutive equation for adherent cells in this model has been developed using

magnetic twisting cytometry [89], as shown in Figure 3.42. In this study, 4.5 μm

ferromagnetic beads were bound to integrin receptors on the apical surface of adherent

human airway smooth muscle cells and twisted by a magnetic field. It was found that the

shear stiffness, G, of the cells (Equation 3.36) is directly proportional to the prestress of

the membrane as observed experimentally.

Equation 3.36. Constitutive equation of adherent cells as governed by the cortical membrane model of cellular tensegrity [89]

$$G = \frac{1}{\pi} P_m \frac{h}{D} \frac{\sin \theta}{\theta}$$

When experimentally based values for h (100 nm), D (4.5 μm), and P_m ($10^4 - 10^5$ Pa) are

substituted into Equation 3.36, values of G on the order of $10^2 - 10^3$ Pa are obtained.

These values are consistent with experimentally obtained values [75], however there are several aspects of this model that are not consistent with experimental observations.
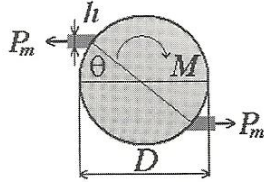
Figure 3.42. Free body diagram of a magnetic twisting cytometry experiment, where M is the applied moment, P_m is the prestress in the membrane, h is the membrane thickness, D is the bead diameter, and θ is the measured angle of rotation of the bead (equivalent to angular strain of the membrane) [20]

Firstly, Equation 3.36 predicts that G is inversely proportional to the angular strain θ which is equivalent to strain softening behavior whereas Wang [41] and Fabry [43] have shown that cells exhibit either stress hardening behavior or constant stiffness in MTC experiments. Secondly, this equation predicts that G in also inversely proportional to bead diameter, D, however Wang and Ingber [70] have shown the opposite behavior in cultured endothelial cells. It is thought that these discrepancies arise from the faulty assumption of the cortical membrane model that the cortical layer carries only tensile force and cannot support bending, as is routinely exhibited by erythrocytes, and that the cytoskeleton is limited to the cortical membrane which as has been shown extensively is not the case for adherent cells.

TENSED CABLE NETWORK MODEL OF CELLULAR TENSEGRITY

The second of the cellular tensegrity models is the Tensed Cable Network model. This model postulates that the cytoskeleton behaves as a reticulated network composed entirely of tensile cable elements [69]. In this model, the prestress of the cables is either balanced externally by adhesions to the extracellular matrix or internally by osmotic forces in the cytoplasm. Using the assumptions that local strains follow the global strain field and all cable orientations in the network are equally probable, Stamenović [90] has shown that the shear modulus behaves in accordance with Equation 3.37

Equation 3.37. Constitutive equation for the tensed cable net model of cellular tensegrity [90]

$$G = (0.8 + 0.2B)P$$

where P is the prestress and B is a nondimensional cable stiffness parameter ($B \equiv (dF/dL)/(F/L)$). This constitutive equation has been shown to be moderately accurate based on measurements of isolated stress fibers, overestimating G by approximately 20 % [20]. Like the cortical membrane model, the tensed network model has been shown to describe the behavior of suspended cells very well [87] but incapable of accurately describing the properties of adherent cells [88].

CABLE-AND-STRUT MODEL OF CELLULAR TENSEGRITY

The final cellular tensegrity model, favored by most tensegrity enthusiasts, is the Cable-and-Strut model. In this model, a prestressed cable net is balanced by

compression-supporting struts as shown in Figure 3.43(A) rather than by inflating pressure. As with the previous models, the compression can be balanced by adhesions to the extracellular matrix as well. Unlike the previous two models microtubules are modeled as semi-flexible struts which act as compressive elements within the cell by and, the tensile elements in this model are represented by actin stress fibers (rather than the cortical actin network) as shown in Figure 3.43(B). Intermediate filaments may also be incorporated as additional tensile elements utilized for lateral stabilization of the compressive microtubules and connection of the nucleus with the cortical and internal cytoskeletal networks for a more complete model. A useful analogy for this type of system is a camp tent. In this analogy, the microtubules are analogous to the tent poles, the prestressed actin stress fibers are analogous to the taut tent fabric, the extracellular matrix is analogous to the ground on which the tent is planted and any overhead branches to which it may be tethered, integrins are analogous to the tent pegs, and the intermediate filaments represent the guy wires used for stabilization of the tent poles. If a lantern were hung in the tent representing (note: not analogous to) the nucleus, the intermediate filaments would also be analogous to the guy wires used to secure it in place.
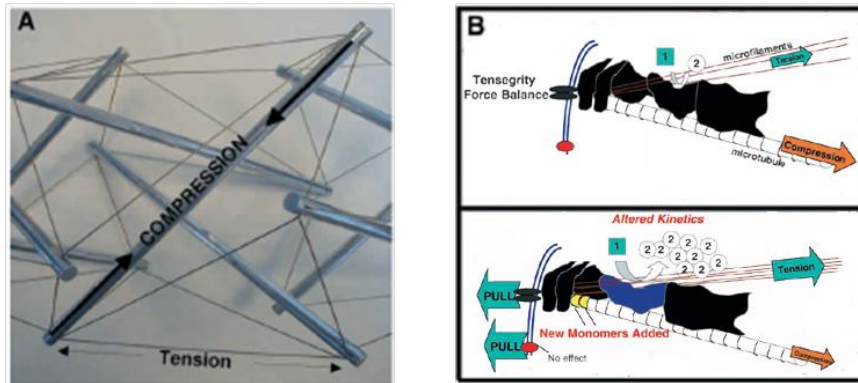
Figure 3.43. (A) Cable-and-strut model of cellular tensegrity, (B) Schematic showing the force balance between actin stress fibers (or microfilaments), microtubules, and the ECM [2, 4]

One readily identifiable advantage of this model is that it can predict the global deformation of a cell due to a local force (as required by the second *a priori* prediction discussed earlier; Figure 3.44[A]) and further that attachment of a round cell to a substrate at just a few points of contact results in cell spreading as is commonly observed in cell cultures (Figure 3.44[B]). This model can also be made multi-modular to incorporate structures such as the nucleus (shown in Figure 3.44[B]) and the cortical actin network (modeled as either a geodesic cortical membrane or a tensed cable net). One of the most prized abilities of the cellular tensegrity model over other mechanics models is the ability for stresses applied at the cell periphery to be transmitted to and deform the nucleus as shown in Figure 3.44(B) [41].

Another advantage is that this model supports the experimental observations that stresses induced anywhere along the cell membrane other than at a point of integrin attachment to the extracellular matrix forces are not transferred globally throughout the structure but rather dissipate locally [29, 41, 70, 91]. Furthermore, this model supports

the counterintuitive phenomenon of a tensed member of one size scale to be able to resist

compression on a smaller size scale [4]. To illustrate this concept, imagine a mouse

running along the tensile guy wires in our tent analogy. This is accomplished by

compression of the guy wire between the front and rear feet of the mouse, but is only

possible if the guy wire is tensionally stiffened (pre-stressed). This phenomenon is

enhanced by crosslinking of tensile filaments into larger bundles which stabilizes the

lateral connections between filaments to prevent buckling, as is the case for actin stress

fibers in the filipodia that create the leading edge of migratory cells [92]. Similar

stabilization of crosslinked microtubules is thought to stabilize cilia and long neurite cell

processes [93].
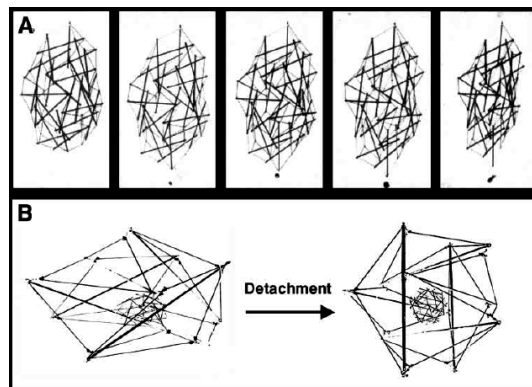
Figure 3.44. Cable-and-strut tensegrity models illustrating (A) global
displacement due to a local force and (B) cell spreading when attached to a rigid
substrate and becoming spherical when detached from a substrate [41]

The theory of cellular tensegrity was initially a purely intuitive model [85], however Stamenović determined [90] that the constitutive equation governing the behavior of the cable-and-strut model of cellular tensegrity can be expressed as

Equation 3.38. Constitutive equation of the cable-and-strut model of cellular tensegrity [90]

$$G = 0.8(P - P_Q) + 0.2(BP - B_Q P_Q)$$

where P is the prestress of the cables, P_Q is the portion of P that is counteracted by the struts, B is the dimensionless cable stiffness parameter introduced in Equation 3.37, and B_Q is a similar dimensionless strut stiffness ($B_Q \equiv (dQ/dL)/(Q/L)$) determined based on the buckling behavior of microtubules [94]. The portion of P that is balanced by the substrate is given as

Equation 3.39. Portion of cable prestress that is balanced by the substrate, P_S [90]

$$P_S = P - P_Q$$

and is the parameter that is measured in traction microscopy [75]. It was shown in [20] that this constitutive equation is reasonably accurate, overestimating G by only ~ 14 %. Interestingly, if $P_Q = 0$, as is the case when microtubules are disrupted, Equation 3.39 reduces to Equation 3.38. This may help explain yet another experimental observation: the decreased role of microtubules and increased role of the extracellular matrix at resisting compressive stresses in highly spread cells [93, 95]. As P_Q decreases P_S must

compensate, assuming a constant value of *P*. This situation is analogous to using a using tent poles that are an order of magnitude shorter in length than the length of the tent; the tent poles will not bear as much of the compressive force as they would if they were on the same length scale as the tent but the tent pegs will compensate by bearing more of the force. This lack of softening, and even occasional stiffening, of highly spread cells such as smooth muscle cells adhered to a rigid substrate has been used to contradict the theory of cellular tensegrity [96], however, as just shown this is not the case when a mathematical analysis of the system is considered.

Detractors of cellular tensegrity primarily focus on three issues. The first and most troubling to detractors is the presence of compression struts inside the cell [4]. This is due to the long-held dogma of biologists that the cell is like a balloon full of molasses. If this were true, however, cell shape would be independent of substrate stiffness [50], yet this is not what is observed experimentally [97]. Furthermore, the cell would have no mechanism with which to explain the observed "compression wrinkles" that adherent cells create on a soft substrate between adhesion points [4, 98]. The second main concern that has been raised focuses on the ability of long microtubules that extend throughout the cytoplasm to bear compression. Their ability to do so has, however, been demonstrated by Wang et al [74] who showed that a straight, elongated microtubule buckles when it impinges head-on with the stiff actin cortex surrounding the cell (Figure 3.45).
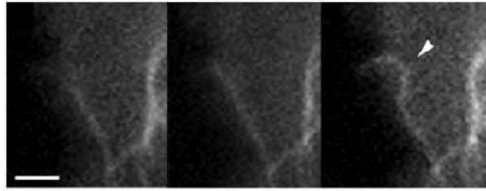
Figure 3.45. Sequential images of a microtubule, indicated by the arrowhead, approaching the actin cortex and buckling upon head-on impingement with it [74]

The third reason given by detractors for ruling out the relevance of cellular tensegrity is that disruption of one element within a single tensegrity module causes the collapse of the entire structure, which is not what is observed in cells [83, 91, 99, 100]. This can be explained, however, by the multimodular tensegrity structure of cells proposed earlier that allows for modeling of the internal cytoskeleton together with the nucleus and the cortical actin network. In multimodular tensegrity structures, destruction of one element results only in a local response [4]. This is analogous to the severing of the Achilles tendon in which foot stability is lost but the stability of the rest of the body remains unaltered. It is also important to note that although there are alternatives which can account many of the controversial aspects of cellular tensegrity, only tensegrity is able to provide an explanation for all of the behaviors discussed above (e.g. strain hardening, nuclear deformation, prestress, etc.) together [4].

Despite all the controversy over the issue however, even the most strident critics of the cellular tensegrity theory are willing to admit that certain aspects of tensegrity behavior may be applicable to cellular mechanics along with the more traditional continuum behaviors [99].

3.6. EPILOGUE: MULTISCALE MODELING

Tensegrity architecture can be used to explain the behavior of structures all the way from the macro-scale [65, 66, 101] to the molecular scale [2, 4, 102]. The variety of tensegrity structures combined with the ability to combine different structures into a single multimodular tensegrity structure at each of and between these scales is reflected in the structure of living organisms as systems within systems within systems. For example, bones and muscles comprise a cable-and-strut tensegrity system [103, 104], the heart and lungs are also comprised of prestressed tissues balanced by blood and air pressure, respectively, and even the extracellular matrix throughout the body is comprised of prestressed fibers (e.g. crosslinked collagen and elastin bundles) balanced by the incompressible hydrophilic glycosaminoglycans (GAGs). It is this balance that is responsible for the spontaneous retraction of wound edges when a tissue is incised by a scalpel [105, 106]. It has even been shown that tensegrity may be responsible for the behavior of biological polymers such as actin microfilaments, individual proteins, and even RNA and DNA molecules [67, 107, 108]. This ability of tensegrity principles to describe such fundamental elements of life has led some to postulate that these same principles, known since the dawn of civilization yet still not completely understood [99], may be able to finally explain the origin of life on Earth [107]. It is evident, therefore, that any single model (tensegrity or otherwise) which is capable of fully describing cell behavior (e.g. viscoelasticity, nonlinearity, heterogeneity, active remodeling, and numerous structural components) will likely also be able to elucidate the mechanisms

responsible for mechanics at every length scale and point in the life cycle (e.g. from prenatal morphogenesis to geriatric pathology) relevant to life [109, 110].

Although the tensegrity model shows great promise for modeling the mechanics of life, it would simply be much too computationally intensive to create a single model which incorporates tensegrity structures at every level from the nano to the macro scale. Rather, if these mechanics are to be fully characterized and modeled in a realistic manner, multiscale models must be utilized which are each capable of building upon the principles of the more fundamental models below them. Any future model which would be capable of taking into account accurate representative cytoskeletal geometries in order to elucidate the complex mechanical behaviors (i.e. viscoelasticity and tensegrity) which cells routinely exhibit, would be a good starting point for these multiscale models of tissue that include not only cells but their nanoscale structures as well. This type of model would finally provide a means to bridge the gap, testified to in the quote that opens this review, which spans between the current focus of medical research and the molecular basis of disease.

3.7. REFERENCES

1.   Ingber, D.E., *Mechanobiology and diseases of mechanotransduction.* Annals of Medicine, 2003. 35(8): p. 564-577.

2.   Ingber, D.E., *Tensegrity II. How structural networks influence cellular information processing networks.* Journal of Cell Science, 2003. 116(8): p. 1397-1408.

3.   Suresh, S., *Biomechanics and biophysics of cancer cells.* Acta Materialia, 2007. 55(12): p. 3989-4014.

4.   Ingber, D.E., *Tensegrity I. Cell structure and hierarchical systems biology.* Journal of Cell Science, 2003. 116(7): p. 1157-1173.

5.   Jeon, K.W., *International review of cytology: a survey of cell biology.* Vol. 201. 2000: Academic Press. 284.

6.   Trepat, X., et al., *Oscillatory magnetic tweezers based on ferromagnetic beads and simple coaxial coils.* Review of Scientific Instruments, 2003. 74(9): p. 4012-4020.

7.   Pullarkat, P.A., P.A. Fernández, and A. Ott, *Rheological properties of the Eukaryotic cell cytoskeleton.* Physics Reports, 2007. 449(1-3): p. 29-53.

8.   Lim, C.T., et al., *Experimental techniques for single cell and single molecule biomechanics.* Materials Science and Engineering: C, 2006. 26(8): p. 1278-1288.

9.   Dintwa, E., E. Tijskens, and H. Ramon, *On the accuracy of the Hertz model to describe the normal contact of soft elastic spheres.* Granular Matter, 2008. 10: p. 209-221.

10.   Park, S.-G., et al., *The variation of biomechanical property of chondrocyte under the various biological conditions.* Current Applied Physics, 2005. 5(5): p. 493-496.

11.   Coons, A.H., H.L. Creech, and R.N. Jones, *Immunological properties of an antibody containing a fluorescent group.* Proceedings of the Society for Experimental Biology and Medicine, 1941. 47: p. 200-202.

12.   Markov, D.A., et al., *Noninvasive fluid flow measurements in microfluidic channels with backscatter interferometry.* Electrophoresis, 2004. 25(21-22): p. 3805-3809.

13.   Hertz, H., *Über die Berührung Fester Elastischer Körper (On the Contact of Elastic Solids).* J. Reine Angew. Math., 1882. 92: p. 156-171.

14.   Hemmer, J.D., et al., *Role of Cytoskeletal Components in Stress-Relaxation Behavior of Adherent Vascular Smooth Muscle Cells.* Journal of Biomechanical Engineering-Transactions of the Asme, 2009. 131(4): p. 9.

15.   Smith, B.A., et al., *Probing the Viscoelastic Behavior of Cultured Airway Smooth Muscle Cells with Atomic Force Microscopy: Stiffening Induced by Contractile Agonist.* Biophysical Journal, 2005. 88(4): p. 2994-3007.

16.   Peeters, E.A.G., et al., *Mechanical and failure properties of single attached cells under compression.* Journal of Biomechanics, 2005. 38(8): p. 1685-1693.

17.   Shieh, A.C. and K.A. Athanasiou, *Biomechanics of single zonal chondrocytes.* Journal of Biomechanics, 2006. 39(9): p. 1595-1602.

18.   Ratner, B.D., *Biomaterials science: an introduction to materials in medicine*. Second Illustrated ed2004: Academic Press. 851.

19.   Spring, K.R., T.J. Fellers, and M.W. Davidson. *Resolution and Contrast in Confocal Microscopy*. 2004 2009 November 2, 2009]; Available from: http://www.olympusconfocal.com/theory/resolutionintro.html.

20.   Mofrad, M.R.K. and R.D. Kamm, eds. *Cytoskeletal Mechanics*. 2006, Cambridge University Press: New York, NY. 244.

21.   Lim, C.T., E.H. Zhou, and S.T. Quek, *Mechanical models for living cells--a review.* Journal of Biomechanics, 2006. 39(2): p. 195-216.

22.   Hoffman, B.D., et al., *The consensus mechanics of cultured mammalian cells.* Proceedings of the National Academy of Sciences of the United States of America, 2006. 103(27): p. 10259-10264.

23.   Fabry, B., et al., *Time scale and other invariants of integrative mechanical behavior in living cells.* Physical Review E, 2003. 68(4).

24.   Li, C. and Q. Xu, *Mechanical stress-initiated signal transduction in vascular smooth muscle cells in vitro and in vivo.* Cellular Signalling, 2007. 19(5): p. 881-891.

25.   Fellers, T.J. and M.W. Davidson. *Olympus FluoView Resource Center: Introduction to Confocal Microscopy*. 2009 [cited 2009 October 21]; Available from: http://www.olympusfluoview.com/THEORY/CONFOCALINTRO.HTML.

26.   Hawes, C. and B. Satiat-Jeunemaitre, *Plant Cell Biology: A Practical Approach*. Second ed2001: Oxford University Press. 338.

27.   Lammi, M.J. *Current perspectives on cartilage and chondrocyte mechanobiology*. 2004. Ios Press.

28.   Kasza, K.E., et al., *The cell as a material.* Current Opinion in Cell Biology, 2007. 19(1): p. 101-107.

29.   Bausch, A.R., et al., *Local Measurements of Viscoelastic Parameters of Adherent Cell Surfaces by Magnetic Bead Microrheometry.* Biophysical Journal, 1998. 75(4): p. 2038-2049.

30. Stroscio, M.A. and M. Dutta, *Biological nanostructures and applications of nanostructures in biology: electrical, mechanical, and optical properties.* Illustrated ed. Vol. 2 of Bioelectric engineering. 2004: Springer. 178.

31. Hemmer J.D., D.D., Vertegel A., Langan E. III, LaBerge M., *Effects of serum deprivation on the mechanical properties of adherent vascular smooth muscle cells.* Proc Inst Mech Eng [H], 2008. 222(5): p. 761-72.

32. Keller, M., J. Schilling, and E. Sackmann, *Oscillatory magnetic bead rheometer for complex fluid microrheometry.* Review of Scientific Instruments, 2001. 72(9): p. 3626-3634.

33. Bausch, A.R., W. Möller, and E. Sackmann, *Measurement of Local Viscoelasticity and Forces in Living Cells by Magnetic Tweezers.* Biophysical Journal, 1999. 76(1): p. 573-579.

34. Echlin, P., *Handbook of Sample Preparation for Scanning Electron Microscopy and X-Ray Microanalysis.* Illustrated ed2009: Springer. 330.

35. Bhushan, B., *Nanomechanical properties of solid surfaces and thin films*, in *Springer Handbook of Nanotechnology*2004, Springer-Verlag: Berlin Heidelberg New York. p. 1221.

36. Ng, L., et al., *Nanomechanical properties of individual chondrocytes and their developing growth factor-stimulated pericellular matrix.* Journal of Biomechanics, 2007. 40(5): p. 1011-1023.

37. Freundlich, H. and W. Seifriz, *Über die Elastizität von Sollen und Gelen.* Z. Phys. Chem., 1922. 104: p. 233-61.

38. Crick, F.H.C. and A.F.W. Hughes, *The physical properties of cytoplasm : A study by means of the magnetic particle method Part I. Experimental.* Experimental Cell Research, 1950. 1(1): p. 37-80.

39. Valberg, P.A. and H.A. Feldman, *Magnetic particle motions within living cells - measurement of cytoplasmic viscosity and motile activity.* Biophysical Journal, 1987. 52(4): p. 551-561.

40. Vaziri, A. and A. Gopinath, *Cell and biomolecular mechanics in silico.* Nature Materials, 2008. 7(1): p. 15-23.

41. Wang, N., J.P. Butler, and D.E. Ingber, *Mechanotransduction across the cell-surface and through the cytoskeleton.* Science, 1993. 260(5111): p. 1124-1127.

42.   Massiera, G., et al., *Mechanics of Single Cells: Rheology, Time Dependence, and Fluctuations.* Biophysical Journal, 2007. 93(10): p. 3703-3713.

43.   Fabry, B., et al., *Scaling the microrheology of living cells.* Physical Review Letters, 2001. 87(14).

44.   Féréol, S., et al., *Cell mechanics of alveolar epithelial cells (AECs) and macrophages (AMs).* Respiratory Physiology & Neurobiology, 2008. 163(1-3): p. 3-16.

45.   Deng, L.H., et al., *Fast and slow dynamics of the cytoskeleton.* Nature Materials, 2006. 5(8): p. 636-640.

46.   COMSOL. *COMSOL : Model Gallery : Helmholtz Coil - 15*. 2009 [cited 2009 October 22]; Available from: http://www.comsol.com/showroom/gallery/15/.

47.   Trickey, W.R., et al., *Determination of the Poisson's ratio of the cell: recovery properties of chondrocytes after release from complete micropipette aspiration.* Journal of Biomechanics, 2006. 39(1): p. 78-87.

48.   Bao, G. and S. Suresh, *Cell and molecular mechanics of biological materials.* Nature Materials, 2003. 2(11): p. 715-725.

49.   Li, B., et al., *Development of micropost force sensor array with culture experiments for determination of cell traction forces.* Cell Motility and the Cytoskeleton, 2007. 64(7): p. 509-518.

50.   Brookes, M., *Hard cell, soft cell.* New Scientist, 1999. 164(2206): p. 42-46.

51.   Costa, K.D., A.J. Sim, and F.C.P. Yin, *Non-Hertzian approach to analyzing mechanical properties of endothelial cells probed by atomic force microscopy.* Journal of Biomechanical Engineering-Transactions of the Asme, 2006. 128(2): p. 176-184.

52.   Shabana, A.A., K.E. Zaazaa, and H. Sugiyama, *Railroad vehicle dynamics: a computational approach*. Illustrated ed2007: CRC Press.

53.   Darling, E.M., S. Zauscher, and F. Guilak, *Viscoelastic properties of zonal articular chondrocytes measured by atomic force microscopy.* Osteoarthritis and Cartilage, 2006. 14(6): p. 571-579.

54.   Bushby, A.J. and N.M. Jennett, *Determining the area function of spherical indentors for nanoindentation.* Matr. Res. Soc. Symp., 2001. 649: p. Q7.17.1-Q7.17.6.

55. Fung, Y.C., *Biomechanics: Mechanical Properties of Living Tissues*. Second ed1993, New York, NY: Springer-Verlag New York, Inc. 568.

56. Roylance, D., *Engineering Viscoelasticity*, 2001, Department of Materials Science and Engineering at Massachusetts Institute of Technology. p. 37.

57. Leipzig, N.D. and K.A. Athanasiou, *Unconfined creep compression of chondrocytes.* Journal of Biomechanics, 2005. 38(1): p. 77-85.

58. Merryman, W.D., et al., *Viscoelastic Properties of the Aortic Valve Interstitial Cell.* Journal of Biomechanical Engineering-Transactions of the Asme, 2009. 131(4).

59. Liao, D., et al., *Viscoelastic properties of isolated rat colon smooth muscle cells.* Cell Biology International, 2006. 30(10): p. 854-858.

60. Nekouzadeh, A., et al., *A simplified approach to quasi-linear viscoelastic modeling.* Journal of Biomechanics, 2007. 40(14): p. 3070-3078.

61. Mackintosh, F.C., J. Kas, and P.A. Janmey, *Elasticity of semiflexible biopolymer networks.* Physical Review Letters, 1995. 75(24): p. 4425-4428.

62. Storm, C., et al., *Nonlinear elasticity in biological gels.* Nature, 2005. 435(7039): p. 191-194.

63. Huisman, E.M., et al., *Three-dimensional cross-linked F-actin networks: Relation between network architecture and mechanical behavior.* Physical Review Letters, 2007. 99(20): p. 4.

64. Nishimura, S., et al., *Microtubules modulate the stiffness of cardiomyocytes against shear stress.* Circulation Research, 2006. 98(1): p. 81-87.

65. Fuller, R.B., *Tensegrity.* Portfolio Artnews Annual, 1961. 4: p. 112-127.

66. Fuller, R.B. and L.C. Keat, *Synergetics.* Portfolio1979, Philadelphia & Singapore.

67. Ingber, D.E., *The architecture of life.* Scientific American, 1998. 278(1): p. 48-57.

68. Stamenović, D., et al., *Experimental tests of the cellular tensegrity hypothesis.* Biorheology, 2003. 40: p. 221-225.

69. Volokh, K.Y. and O. Vilnay, *New cases of reticulated underconstrained structures.* Int. J. Solids Structures, 1997. 34: p. 1093-1104.

70. Wang, N. and D.E. Ingber, *Control of the cytoskeletal mechanics by extracellular matris, cell shape, and mechanical tension.* Biophys. J., 1994. 66: p. 2181-2189.

71.   Pourati, J., et al., *Is cytoskeletal tension a major determinant of cell deformability in adherent endothelial cells?* Am. J. Physiol. Cell Physiol., 1998. 274: p. C1283-C1289.

72.   Cai, S., et al., *Regulation of cytoskeletal mechanics and cell growth by myosin light chain phosphorylation.* Am. J. Physiol. Cell Physiol., 1998. 275: p. C1349-C1356.

73.   Hubmayr, R.D., et al., *Pharmacological activation changes stiffness of cultured human airway smooth muscle cells.* Am. J. Physiol. Cell Physiol., 1996. 271: p. C1660-C1668.

74.   Wang, N., et al., *Mechanical behavior in living cells consistent with the tensegrity model.* Proc. Natl. Acad. Sci., 2001. 98: p. 7765-7770.

75.   Wang, N., et al., *Cell prestress. I. Stiffness and prestress are closely associated in adherent contractile cells.* American Journal of Physiology-Cell Physiology, 2002. 282(3): p. C606-C616.

76.   Yoshida, M., et al., *Leukocyte adhesion to vascular endothelium induces e-selectin association with the actin cytoskeleton.* J. Cell Biol., 1996. 133: p. 445-455.

77.   Brown, M.J., et al., *Rigidity of circulating lymphocytes is primarily conferred by vimentin intermediate filaments.* J. Immunol., 2001. 166: p. 6640-6646.

78.   Ezzell, R.M., et al., *Vinculin promotes cell spreading by mechanically coupling integrins to the cytoskeleton.* Exp. Cell Res., 1997. 231: p. 14-26.

79.   Alenghat, F.J., et al., *Analysis of Cell Mechanics in Single Vinculin-Deficient Cells Using a Magnetic Tweezer.* Biochemical and Biophysical Research Communications, 2000. 277(1): p. 93-99.

80.   Choquet, D., D.P. Felsenfeld, and M.P. Sheetz, *Extracellular matrix rigidity causes strengthening of integrin-cytoskeleton linkages.* Cell, 1997. 88: p. 39-48.

81.   Rivline, D., et al., *Focal contacts as mechanosensors: externally applied local mechanical force induces growth of focal contacts by an mDia1-dependent and ROCK-independent mechanism.* J. Cell Biol., 2001. 153: p. 1175-1186.

82.   Maniotis, A., C. Chen, and D.E. Ingber, *Demonstration of mechanical connections between integrins, cytoskeletal filaments and nucleoplasm that stabilize nuclear structure.* Proc. Nat. Acad. Sci. USA, 1997. 94: p. 849-854.

83. Kumar, S., et al., *Viscoelastic retraction of single living stress fibers and its impact on cell shape, cytoskeletal organization, and extracellular matrix mechanics.* Biophys. J., 2006. 90: p. 3762-3773.

84. Ingber, D.E., J.A. Madri, and J.D. Jameison, *Role of basal lamina in the neoplastic disorganization of tissue architecture.* Proc. Nat. Acad. Sci. USA, 1981. 78: p. 3901-3905.

85. Ingber, D.E. and J.D. Jameison, *Cells as tensegrity structures: Architectural regulation of histodifferentiation by physical forces transduced over basement membrane.* Gene Expression during Normal and Malignant Differentiation, ed. L.C. Anderson, G.C. Gahmberg, and P. Ekblom1985, Orlando, FL: Academic Press.

86. Zhelev, D.V., D. Needham, and R.M. Hochmuth, *Role of the membrane cortex in neutrophil deformation in small pipettes.* Biophys. J., 1994. 67: p. 696-705.

87. Discher, D.E., D.H. Boal, and S.K. Boey, *Stimulations of the erythrocyte cytoskeleton at large deformation. II. Micropipette aspiration.* Biophys. J., 1998. 75: p. 1584-1597.

88. Coughlin, M.F. and D. Stamenovic, *A prestressed cable network model of adherent cell cytoskeleton.* Biophys. J., 2003. 84: p. 1328-1336.

89. Stamenović, D. and D.E. Ingber, *Models of cytoskeletal mechanics of adherent cells.* Biomech. Model Mechanobiol., 2002. 1: p. 95-108.

90. Stamenović, D., *Microtubules may harden or soften cells, depending on the extent of cell distension.* J. Biomech., 2005. 38: p. 1728-1732.

91. Heidemann, S.R., et al., *Direct observations of the mechanical behaviors of the cytoskeleton in living fibroblasts.* J. Cell Biol., 1999. 145: p. 109-122.

92. Sheetz, M.P., D.B. Wayne, and A.L. Pearlman, *Extension of filopodia by motor-dependent actin assembly.* Cell Motil. Cytoskeleton, 1992. 22: p. 160-169.

93. Joshi, H.C., et al., *Tension and compression in the cytoskeleton of PC 12 neurites.* J. Cell Biol., 1985. 101: p. 697-705.

94. Stamenović, D., et al., *Cell prestress. II. Contribution of microtubules.* J. Appl. Physiol., 2002. 96: p. 1600-1605.

95. Putnam, A.J., et al., *Microtubule assembly is regulated by externally applied strain in cultured smooth muscle cells.* J. Cell Sci., 1998. 111: p. 3379-87.

96. Obara, K., et al., *Effects of microtubules and microfilaments on [Ca(2+)](i) and contractility in a reconstituted fibroblast fiber.* Am. J. Physiol. Cell Physiol., 2000. 279: p. C785-C796.

97. Banerjee, S.D., R.H. Cohn, and M.R. Bernfield, *Basal lamina of embryonic salivary epithelia. Production by the epithelium and role in maintaining lobular morphology.* J. Cell Biol., 1977. 2: p. 445-463.

98. Harris, A.K., P. Wild, and D. Stopak, *Silicone rubber substrata: a new wrinkle in the study of cell locomotion.* . Science 1980. 208: p. 177-180.

99. Heidemann, S.R., et al., *Opposing views on tensegrity as a structural framework for understanding cell mechanics.* Journal of Applied Physiology, 2000. 89(4): p. 1670-1678.

100. Forgacs, G., *On the possible role of cytoskeletal filamentous networks in intracellular signaling: an approach based on percolation.* J. Cell Sci., 1995. 108: p. 2131-2143.

101. Snelson, K., *Snelson on the tensegrity invention.* Int. J. Space Struct., 1996. 11: p. 43-48.

102. Luo, Y., et al., *A multi-modular tensegrity model of an actin stress fiber.* Journal of Biomechanics, 2008. In Press, Corrected Proof.

103. Levin, S.M., *A different approach to the mechanics of the human pelvis: tensegrity*, in *Movement, Stability and Low Back Pain*, A. Vleeming, et al., Editors. 1997, Churchill Livingston: London. p. 157-167.

104. Chen, C.S. and D.E. Ingber, *Tensegrity and mechanoregulation: from skeleton to cytoskeleton.* Osteoarthritis Cartilage, 1999. 7: p. 81-94.

105. Liu, S.Q. and Y.C. Fung, *Relationship between hypertension, hypertrophy, and opening angle of zero-stress state of arteries following aortic constriction.* J. Biomech. Eng., 1989. 111: p. 325-335.

106. Omens, J.H. and Y.C. Fung, *Residual strain in rat left ventricle.* Circ. Res., 1990. 66: p. 37-45.

107. Ingber, D.E., *The origin of cellular life.* Bioessays, 2000. 22(12): p. 1160-1170.

108. Farrell, H.M., Jr, et al., *Molten globule structures in milk proteins: implications for potential new structure-function relationships.* J. Dairy Sci., 2002. 85: p. 459-471.

109. Hunter, P.J. and T.K. Borg, *Integration from proteins to organs: the Physiome Project.* Nature Reviews Molecular Cell Biology, 2003. 4(3): p. 237-243.

110. Davidson, L., M. von Dassow, and J. Zhou, *Multi-scale mechanics from molecules to morphogenesis.* Int. J. Biochem. & Cell Biol., 2009. 41: p. 2147-2162.

CHAPTER 4

EFFECTS OF GEOMETRIC VARIANCE
IN MODELING OF CELL INDENTATION
(AIM 1)

4.1. INTRODUCTION

Because physical distortion can affect cell growth, differentiation, contractility, motility, and apoptotic tendency [1], the ability to predict the mechanical behavior of cells may be critical to prevention and treatment of many diseases [1-5]. The most frequently used model of single-cell mechanics for analysis of atomic force microscopy (AFM) nanoindentation [6], the Hertzian linear elastic solid analytical model [7], is widely recognized as oversimplified because it cannot account for the viscoelastic, nonlinear, and nonheterogeneous properties of the cell, as well as its compound structure and ability to actively remodel itself [6, 8, 9]. In addition, for standard AFM pyramidal tips, the model does not accurately represent the tip geometry [10]. However, the Hertzian model's frequency and ease of use make it an important tool for the purpose of comparison [10-12].

In our previous studies, the mechanical properties of adherent vascular smooth muscle cells (VSMCs) were characterized using AFM indentation with a spherical probe indenter. The spread-out VSMCs exhibiting a synthetic (or proliferative) phenotype were found to be significantly softer than elongated contractile VSMCs [13]. To estimate elastic modulus and to facilitate comparison with other groups, Hertzian linear elastic theory was applied to the data. Equation 4.1 shows the relationship between force and

elastic modulus as described by the Hertz model for indentation of a semi-infinite

substrate with a spherical indenter:

Equation 4.1. The Hertz contact model

$$F = \frac{4}{3}\frac{E}{(1 - v^2)}R^{\frac{1}{2}}\delta^{\frac{3}{2}}$$

Where F is measured force, E is elastic modulus, v is Poisson's ratio, R is spherical

indenter radius, and d is indentation depth. In this model the contact radius, a, is

calculated as shown in Equation 4.2.

Equation 4.2. The Hertz contact radius

$$a = \left(\frac{3FR}{4E_R}\right)^{\frac{1}{3}}$$

Where E_R is the reduced elastic modulus, given by Equation 4.3.

Equation 4.3. The Hertz reduced elastic modulus

$$\frac{1}{E_R} = \frac{\left(1 - v_{indenter}^2\right)}{E_{indenter}} + \frac{\left(1 - v_{sample}^2\right)}{E_{sample}}$$

While there have previously been studies investigating the effect of probe tip geometry on the validity of the standard Hertzian models for AFM measurements [14, 15], the diversity of cell shapes and sizes suggests that approximating the cell as either a semi-infinite plane [16] or a sphere [17] may also need to be inspected. In this study, we used a linear, elastic, solid finite element model (FEM) of VSMC geometries capable of reproducing AFM nanoindentation data to determine how variation in cell size and shape can affect elastic modulus estimates obtained using the standard linear Hertzian analytical formulation.

4.2. METHODS

4.2.1. Finite Element Model Formulation

Contractile and synthetic VSMCs were modeled as axisymmetric structures (COMSOL 3.5a) (Figure 4.1). Geometries were based on averages of reported AFM [13] and confocal images of the vascular cells with cell heights of 2.0 μm, a contractile cell width of 10 μm, and a synthetic cell width of 50 μm indented by a spherical indenter of 5 μm diameter (Figure 4.1). Cell widths were taken from confocal images as the cross-sectional width of each cell type at the area of nanoindentation (Figure 4.2). The model was given isometric material properties matching the assumptions of the Hertzian analytical model. Previously reported results from the same study were used for the input elastic moduli: 15.3 kPa for contractile and 11.1 kPa for synthetic cells. A Poisson's ratio of 0.49 was chosen because it was within literature values [18]. The indenter was

assigned the elastic modulus and Poisson's ratio of borosilicate, 62 MPa and 0.22 respectively.

To replicate experiments, the probe was prescribed a displacement of 350 nm (15% of cell height) towards the cell at 5 nm increments for the first 60 nm (3% of cell height) and at 50 nm increments from 100 to 350 nm. Using Equation 4.1, elastic modulus calculations were then performed based on the output force of the model at an indentation depth of 200 nm (10 % of cell height), as reported previously [13].

4.2.2. Geometric Dependence Testing

Three sets of simulations were run to determine the susceptibility of the model to the geometric inputs (Figure 4.3). In the first set, the diameter of the spherical indenter was held constant at 5 μm, while the estimated modulus was determined for cells with widths varying from 5 – 100 μm. The second set of simulations varied the indenter diameter from 1 – 20 μm while the cell width was held constant at 20 μm. The third set of simulations matched the Hertzian condition of a sphere in contact with a semi-infinite substrate (i.e. the cell) and the indenter diameter was varied between 1 – 20 μm.

For all three sets of geometric dependence simulations, an input elastic modulus of 13.2 kPa was used. This value was the average of the moduli of contractile and synthetic cells [13]. Cell heights and all other properties of the model were held constant throughout the different simulations at the same values discussed in Section 4.2.1.
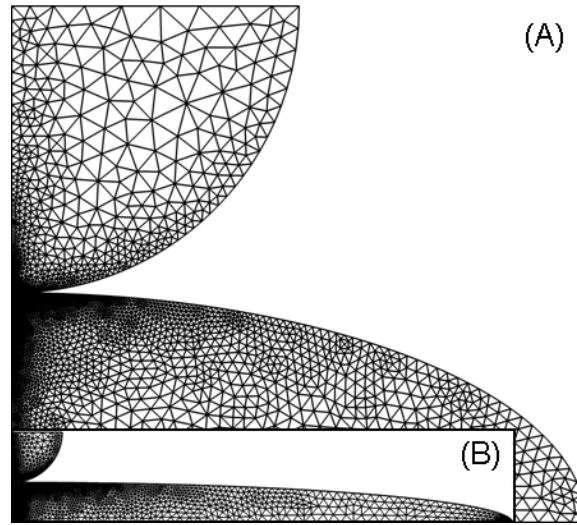
Figure 4.1. Axisymmetric finite element mesh of a representative contractile VSMC (bottom) and AFM probe (top); Inset: representative synthetic VSMC (bottom) and AFM probe (top). The contractile AFM probe geometry was given a radius of 2.5 µm, the contractile VSMC geometry a half-width of 5 µm, and the synthetic VSMC geometry a half-width of 25 µm. Both contractile and synthetic VSMC geometries were given a height of 2 µm. The model is meshed using an element growth rate of 1.05 from the initial point of contact with a maximum element size of 5 nm along boundaries intersecting with the point of initial contact.
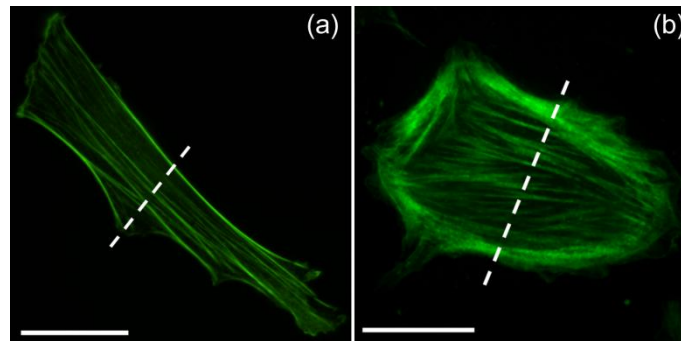
Figure 4.2. Confocal microscopy images of a single representative (a) contractile VSMC and (b) synthetic VSMC. Cells were stained with Alexa Fluor[®] 488 phalloidin to stain filamentous actin. Dashed line denotes the cross section used to assign the radius used in the finite element mesh geometries based on average AFM and confocal images of each phenotype. Scale bars correspond to a length of 20 µm.

| (A) Changing Cell Radius | (B) Changing Tip Radius | (C) Changing Tip Radius |

$R_{indenter}$ = 2.5 µm $\qquad$ $R_{indenter}$ = 0.5 – 10 µm $\qquad$ $R_{indenter}$ = 0.5 – 10 µm

2 µm $\qquad\qquad$ 2 µm $\qquad\qquad$ 2 µm

R_{cell} = 2.5 – 50 µm $\qquad$ R_{cell} = 10 µm $\qquad$ $R_{cell} \gg R_{indenter}$
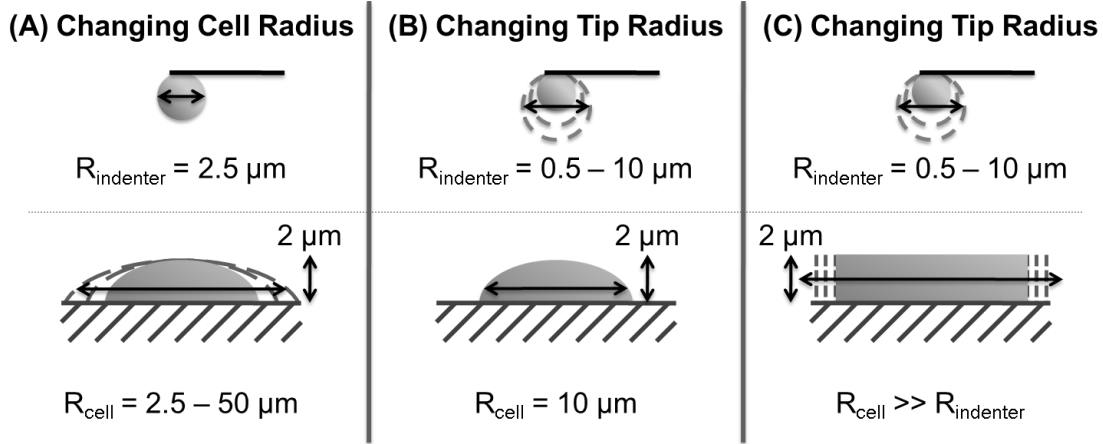
Figure 4.3. Diagram showing the three simulations that were used to determine the susceptibility of the model to geometric inputs: (a) constant AFM probe diameter of 5 µm with cell widths ranging from 5 – 100 µm, (b) variable AFM probe diameter ranging from 1 – 20 µm with a constant cell width of 20 µm, and (c) variable AFM probe diameter ranging from 1 – 20 µm with a cell width much larger than the probe diameter representing the Hertzian condition of contact with an infinitely large sphere.

4.3. RESULTS

4.3.1. AFM Replication

The overall agreement between the model and the AFM nanoindentation data was good (Figure 4.4). Over the entire range of depths simulated by the model (350 nm), the model agreed more closely with data for contractile cells (R^2 = 0.993) than for synthetic cells (R^2 = 0.988). Agreement between the model and AFM data for both phenotypes was closer over the first 60 nm of indentation, with R^2 values of 0.999 for both contractile and synthetic cells.

Force-Depth Indentation Curves
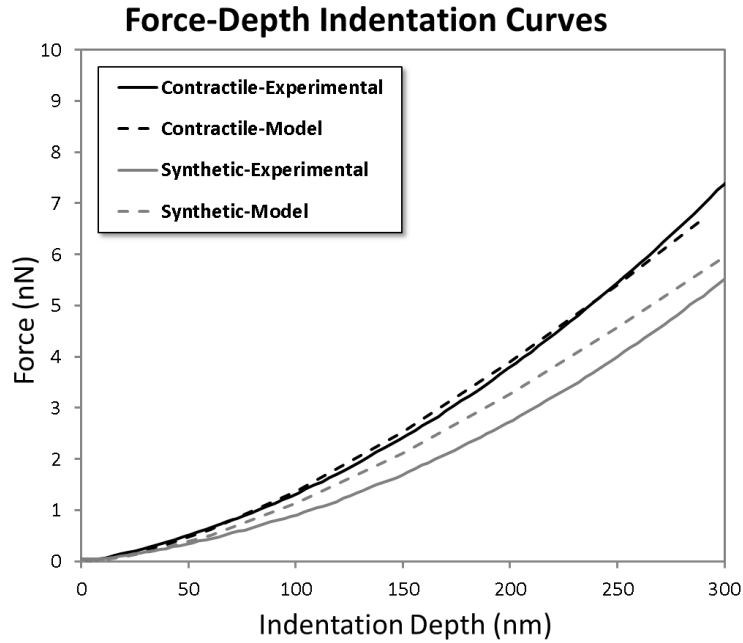
Figure 4.4. Force-indentation curves comparing experimental AFM nanoindentation data and finite element model results for contractile and synthetic VSMC phenotypes.

4.3.2. Geometric Dependence

By modifying only the relationship between the size of the cell and the indenter, it was found that as the contact radius (Equation 4.2), increased, so did the estimated modulus predicted by the analytical Hertz equation (Figure 4.5), as expected. This effect shows that the estimated Hertzian modulus was highly dependent upon cell width up to a width of ~40 μm, at which point the estimated Hertzian modulus plateaued and became nearly independent of cell size (Figure 4.6). Notably, while the synthetic phenotype lies at the edge of the geometrically insensitive range, the contractile phenotype is in the highly geometrically sensitive range (Figure 4.6).

Contact Area Vs. Stiffness
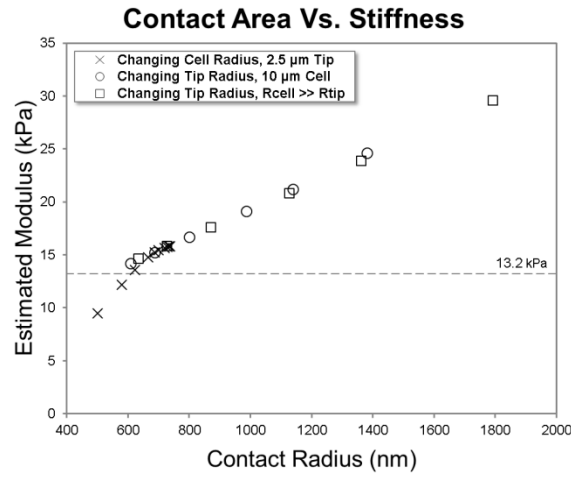
Figure 4.5. Plot showing the relationship between the contact radius and the estimated modulus predicted by the Hertzian analytical model. In each simulation, cells were given an input elastic modulus of 13.2 kPa. If the Hertzian analytical model were geometrically insensitive, it would predict the same value (13.2 kPa if it were fully accurate) under every condition in each simulation.

Shape Dependence of Estimated Modulus
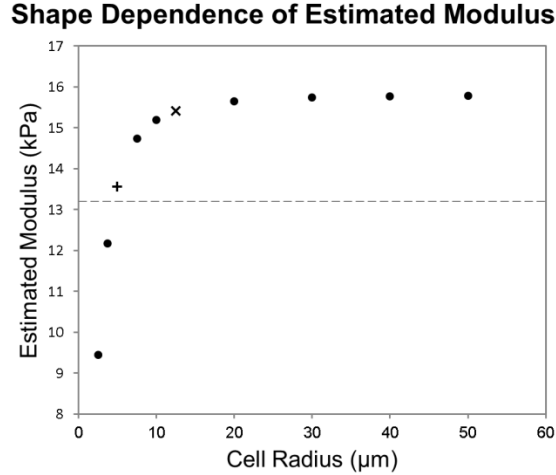
Figure 4.6. Plot showing the relationship between the cell radius and the estimated modulus predicted by the Hertzian analytical model. Cells of each width were given an input elastic modulus of 13.2 kPa. If the Hertzian analytical model were geometrically insensitive, it would predict the same value (13.2 kPa if it were fully accurate) for cells of any width. The + symbol denotes a width of 10 μm which corresponds to the contractile VSMC geometry. The × symbol denotes a width of 50 μm which corresponds to the synthetic VSMC geometry.

100

4.4. DISCUSSION

The FEM model more closely matched the data for contractile VSMCs than for synthetic VSMCs (Figure 4.4). Synthetic VSMCs show an increased amount of hysteresis in indentation experiments compared to contractile VSMCs [13]. Therefore, the purely elastic model does not match the more viscous cell data as well.

Our FEM model shows that the Hertzian linear elastic solid analytical model for a spherical indenter over a semi-infinite plane (Equation 4.1) overestimates the elastic modulus for cells with different geometries by different amounts. When the Hertz analytical model was used for modulus calculation, the moduli for the contractile and synthetic VSMC phenotypes were overestimated by 2.62 % and 18.93 %, respectively. This suggests that the difference in elastic modulus between contractile and synthetic phenotypes was underestimated in [13]. Based on these error margins, the elastic moduli for contractile and synthetic VSMCs are in fact closer to 14.9 kPa and 9.0 kPa, respectively, rather than the previously reported values of 15.3 kPa and 11.1 kPa. This nearly 19% over-estimation in the modulus of the synthetic cells is greater than the variation due to the experimental measure.

Obviously, different cell types can have large difference in geometry [19] and, as with the VSMCs, even cells of one type can vary significantly in shape and size depending on their phenotype. The analytical Hertzian model was insensitive to the size of the cell when the cell width was 5 – 10 times larger than the indenter diameter. However, it should be noted that this condition does not always hold true in experiments

[5, 12, 13]. Therefore, special care should be taken when using the standard formulation of the Hertzian model to those data sets.

The Hertz analytical model is often maligned in the field of cell mechanics due to its incorrect assumptions about biological material properties (i.e. linear elasticity). In addition, previous groups have commented on the effect of indenter geometry changes on the accuracy of the Hertzian modulus estimates for cell indentation data [14, 15]. Here, we have noted that the model also yields incorrect estimates due to its inability to compensate for the geometry of the cell; the assumption that adherent cells are planar compared to the AFM probe tip during indentation is not correct in every instance. More importantly, the semi-infinite plane assumption can sometimes lead to errors in estimation of apparent cell elastic moduli that are on the order of the variability found between cell types [20]. Cellular geometry differences must therefore be taken into account when comparing indentation data from different cell types. Consequently, it is essential to properly model geometry to obtain accurate estimates of mechanical properties, particularly when making comparisons across groups of cells with varying sizes and shapes.

4.5. REFERENCES

1.   Ingber, D.E., Mechanobiology and diseases of mechanotransduction. Annals of Medicine, 2003. 35(8): p. 564-577.

2.   Li, C. and Q. Xu, Mechanical stress-initiated signal transduction in vascular smooth muscle cells in vitro and in vivo. Cellular Signalling, 2007. 19(5): p. 881-891.

3.   Suresh, S., Biomechanics and biophysics of cancer cells. Acta Materialia, 2007. 55(12): p. 3989-4014.

4.   Lammi, M.J. Current perspectives on cartilage and chondrocyte mechanobiology. 2004. Ios Press.

5.   Li, Q.S., et al., AFM Indentation Study of Breast Cancer Cells. Biochemical and Biophysical Research Communications, 2008. 374(4): p. 609-613.

6.   Costa, K.D., A.J. Sim, and F.C.P. Yin, Non-Hertzian approach to analyzing mechanical properties of endothelial cells probed by atomic force microscopy. Journal of Biomechanical Engineering-Transactions of the Asme, 2006. 128(2): p. 176-184.

7.   Hertz, H., Über die Berührung Fester Elastischer Körper (On the Contact of Elastic Solids). J. Reine Angew. Math., 1882. 92: p. 156-171.

8.   Ingber, D.E., Tensegrity I. Cell structure and hierarchical systems biology. Journal of Cell Science, 2003. 116(7): p. 1157-1173.

9.   Dintwa, E., E. Tijskens, and H. Ramon, On the accuracy of the Hertz model to describe the normal contact of soft elastic spheres. Granular Matter, 2008. 10: p. 209-221.

10.   Costa, K.D. and F.C.P. Yin, Analysis of Indentation: Implications for Measuring Mechanical Properties With Atomic Force Microscopy. Journal of Biomechanical Engineering, 1999. 121(5): p. 462-471.

11.   Kuznetsova, T.G., et al., Atomic force microscopy probing of cell elasticity. Micron, 2007. 38(8): p. 824-833.

12.   Pillarisetti, A., et al. Mechanical Characterization of Mouse Embryonic Stem Cells. in IEEE Engineering in Medicine and Biology Society. 2009. Minneapolis, MN.

13.   Hemmer, J.D., et al., Effects of serum deprivation on the mechanical properties of adherent vascular smooth muscle cells. Proc IMechE H: Journal of Engineering in Medicine, 2008. 222(5): p. 761-72.

14.   Bao, G. and S. Suresh, Cell and molecular mechanics of biological materials. Nature Materials, 2003. 2(11): p. 715-725.

15.   Pullarkat, P.A., P.A. Fernández, and A. Ott, Rheological properties of the Eukaryotic cell cytoskeleton. Physics Reports, 2007. 449(1-3): p. 29-53.

16.   Darling, E.M., S. Zauscher, and F. Guilak, Viscoelastic properties of zonal articular chondrocytes measured by atomic force microscopy. Osteoarthritis and Cartilage, 2006. 14(6): p. 571-579.

17.   Ng, L., et al., Nanomechanical properties of individual chondrocytes and their developing growth factor-stimulated pericellular matrix. Journal of Biomechanics, 2007. 40(5): p. 1011-1023.

18.   Smith, B.A., et al., Probing the Viscoelastic Behavior of Cultured Airway Smooth Muscle Cells with Atomic Force Microscopy: Stiffening Induced by Contractile Agonist. Biophysical Journal, 2005. 88(4): p. 2994-3007.

19.   Stroscio, M.A. and M. Dutta, Biological nanostructures and applications of nanostructures in biology: electrical, mechanical, and optical properties. Illustrated ed. Vol. 2 of Bioelectric engineering. 2004: Springer. 178.

20.   Mathur, A.B., et al., Endothelial, cardiac muscle and skeletal muscle exhibit different viscous and elastic properties as determined by atomic force microscopy. Journal of Biomechanics, 2001. 34(12): p. 1545-1553.

CHAPTER 5

AUTOMATED SEGEMENTATION OF SUBCELLULAR STRUCTURES FROM CONFOCAL IMAGES FOR GENERATION OF STRUCTURALLY REPRESENTATIVE 3D GEOMETRIC MODELS OF SINGLE CELLS
(AIM 2)

5.1. INTRODUCTION

The goal of this study is to create a fully automated algorithm capable of reconstructing the cell membrane, nucleus, and actin stress fiber network of single cells in 3D based on fluorescent confocal microscopy images of each of those cellular components in such a way that they are optimized for structural analysis using finite element methods. If generated, such geometries could be utilized in various types of multiscale models to bridge the gap between the nano- and macro-scale models currently in use. The use of 3D computational models to simulate experimental techniques could significantly increase the efficiency of experimentation, leading to reduced times for discovery of mechanobiology principles as well as translation of those principles from bench top to bed side in clinically relevant devices and medications.

The traditional primary focus of modern medical research is the investigation of molecular biology and genetic factors in disease, which sometimes leads to a tendency to ignore changes in tissue structure and mechanics that can also lead to pain and morbidity [1]. However, that lack of focus on the physical basis of disease has been changing in recent years with the growing emphasis on evidence-based medicine in U.S. hospitals [2,

3] together with the substantial growth and maturation of the field of mechanobiology over the past decade [4]. Indeed, there has been a great deal of effort to develop and utilize geometrically accurate 3D structural models at both the tissue and molecular levels [5, 6]. However, there has been much less effort focused at the single-cell level and therefore comparatively little progress has been made toward generation of equally accurate 3D representations of the structural components of single cells.

The ability to predict the behavior of cells from their sub-micron and nanoscale structures could elucidate the mechanisms behind many tissue mechanical properties [7]. For as long as there have been observations of the mechanical properties of cells, there have been models put forth to attempt to describe those observations. At the most basic level, there are two categories of these models: continuum and structure-based. Continuum models, which lack internal structure, were the first type of model utilized to describe the mechanical behavior of cells and generally consider the cell to be equivalent to a simple "balloon full of molasses" [7, 8]. These types of models therefore make predictions with minimal use of geometric variables [9, 10]. Despite the growing amount of overwhelming evidence in support of the existence of structural elements within cells that has been published throughout the past several decades [1, 7, 11-29], these types of models remained popular with bioengineers due to their relative simplicity and ease of implementation.

Structure-based models, on the other hand, are comprised of one or more networks of discrete structural elements that work in harmony to determine the mechanical responses of cells. These models tend to utilize Finite Element Analysis (FEA) to allow for analysis

of complicated cellular and sub-cellular geometries. Many single-cell Finite Element Models (FEMs) rely on idealized geometries [10, 30, 31], however recent efforts have incorporated geometries obtained from image segmentation. The first efforts to generate accurate 3D representations of subcellular structural components using image segmentation techniques focused primarily on nuclei [32, 33], and the most advanced structure-based cellular mechanics models to date utilize stacks of confocal photomicrographs of a cell to generate 3D model structures. There have been a small number of these types of models proposed in the last several years [34, 35], each of which has taken important steps towards the development of a fully representative 3D model of single cell mechanics. However, none of those models has been constructed with entirely non-idealized geometries for all mechanically relevant components of a cell.

Few 3D single cell models have included any form of cytoskeletal elements inside the cells [35]; yet even though these models represent a significant step towards reality, they still rely on the manual addition of a limited number of cytoskeletal components. There has not yet been a system put forth in the literature that is either fully automated or capable of reconstructing any elements of the cytoskeletal networks of cells in a representative manner. The goal of this study is to present such a fully automated cellular geometric reconstruction system based on 3D confocal microscopy images of single subconfluent cells.

5.2. METHODS

5.2.1. Data acquisition: Cell culture, staining, and imaging

Primary rat aortic vascular smooth muscle cells (VSMCs) obtained from female Sprague Dawley rats are used in this study. The cells are cultured in high glucose Dulbecco's Modified Eagle's Medium (DMEM) (HyClone Laboratories, Logan, UT USA) with an antibiotic solution of penicillin and streptomycin (HyClone Laboratories) added to a concentration 0.5 percent, and an antimycotic solution of amphotericin B (HyClone Laboratories) added to a concentration 0.5 percent. Cells are cultured in T75 cell culture polystyrene flasks and maintained in an incubator at 37 °C and five percent CO_2 with fresh media being exchanged every other day. VSMCs are utilized between passages five and eight. Once the cells reach about 90 % confluency, they are trypsinized with a solution of 0.25 % trypsin and 0.02 % ethyldiaminetetraacetic acid (EDTA) in 1X HBSS without sodium bicarbonate, calcium, or magnesium (Mediatech, Manassas, VA, USA) and seeded at 7,000 cells/cm^2 on 25 mm diameter glass coverslips (VWR, Radnor, PA, USA) that has been coated with 50 µg/mL type I rat tail collagen (BD Biosciences, Bedford, MA, USA) 24 hours prior to seeding. The cells are then cultured for three to five days to reach about 25 % confluency.

Upon reaching 25% confluency, cells are fixed with four percent paraformaldehyde (Sigma-Aldrich, St. Louis, MO, USA) at 37 °C for ten minutes. After fixation, cells are treated with 130 nM AlexaFluor 488 phalloidin (Invitrogen, Eugene, OR, USA) at room temperature for 15 minutes to visualize filamentous actin (F-actin), rinsed three times

with phosphate buffered saline (PBS) (MP Biomedicals, Solon, OH, USA), and then mounted onto glass slides using SlowFade® Gold antifade reagent with DAPI (Invitrogen) to visualize the nucleus. The cells are then imaged using an Olympus PLAPON60XO 60x oil objective (NA = 1.42) on an Olympus IX81 inverted microscope equipped with a DSU spinning disc confocal unit and a Hamamatsu ImagEM CCD camera (Hamamatsu Photonics K.K., Hamamatsu City, Japan). Image stacks are taken using a Nyquist step size of 200 nm between image planes for maximum resolution in the Z-direction as calculated by the microscope controller software (MetaMorph® for Olympus Basic, Version 7.7.1.0, Molecular Devices, Sunnyvale, CA, USA).

It should be noted that several types of microscopy were originally considered for this study. Atomic Force Microscopy (AFM) is capable of atomic-level resolution, but was eliminated from consideration due to its topographical nature and therefore inherent inability to image intracellular structures more than a few nanometers below the apical surface of a cell. Scanning Electron Microscopy (SEM) and Transmission Electron Microscopy (TEM) also provide more-than-sufficient levels of resolution for imaging sub-cellular structures; however, each was ultimately eliminated from consideration due to limitations of the imaging environment and sample preparation. Electron microscopy usually requires samples to be imaged in an arid (i.e. non-aqueous) vacuum chamber and bombarded by an incident electron beam. Because electrons must pass through the specimen, TEM requires a very thin (40 – 90 nm thick) section which is difficult to accomplish with biological materials using traditional ultramicrotomy methods of sample preparation. In order to process the samples to make them electrically conductive for

109

SEM, it is often necessary to coat them in harsh chemicals such as heavy metal salts and silver or osmium. While it is possible to image biological samples using electron microscopy techniques, the sample preparation and imaging environment (in particular the non-aqueous nature) are capable of producing artifacts (i.e. altering their structure) [36] that could cause 3D reconstruction of those images to be inaccurate using the image processing techniques utilized in this study. Confocal microscopy does not provide the same level of resolution as any of the aforementioned techniques; however, with a maximum lateral resolution of approximately 180 nm and maximum axial resolution of roughly 500 nm [37] it is still sufficiently capable of imaging the structurally relevant sub-cellular components at the whole-cell level. Ultimately, confocal microscopy was chosen for this study due to its ability to image cells in their native aqueous environment, its non-destructive nature, its relative low-cost compared to electron microscopy, and the fact that it is generally considered to be the standard modality for cytoskeletal imaging. An additional benefit of this imaging technique is that it may be utilized to image live cells. This allows for imaging a cell for which mechanical characterization is also obtained, thus enabling direct validation of eventual models.

5.2.2. Image Pre-Processing

All images are saved and analyzed as 8-bit grayscale images in TIF format, at a size of 256 x 256 pixels. For each image, the f-actin data and the data for the nucleus of the cell are stored in separate image stacks. Each image stack is then deconvolved using MetaMorph® for Olympus Premier Offline (Version 7.7.0.0) using a 3D deconvolution

algorithm based on measured point spread functions using a single iteration. For all further image processing, pixel intensities for each image stack are loaded into MATLAB (Release 2010b, MathWorks®, Natick, MA, USA) as a 3D matrix, creating a voxel map of each image channel. The matrix is then scaled in each dimension to match the dimensions of the sampled volume in cubic micrometers, so that each voxel is 1 µm x 1 µm x 0.2 µm.

5.2.3. Construction of Nucleus and Cell Boundary Meshes

Segmentation of the cell nucleus is achieved similarly to previously reported techniques for nucleus segmentation [38-40]. We begin by first thresholding the nucleus voxel map using 5 % of maximum voxel intensity as an empirically chosen cutoff value. The matrix is then dilated to remove boundary gaps and interior gaps in the matrix were filled. All objects lying along the xy border of the voxel map are then removed and the image matrix is smoothed with a diamond shaped erosion element. The final step of nucleus segmentation is to identify all connected components of the image matrix and retain only the largest one. This is accomplished by first creating a label matrix of the same size as the image voxel map with each voxel assigned an integer value corresponding to its component label and then retaining only the component with the largest number of voxels.

Segmentation of the cell boundary from the data is conducted in almost the exact same manner, with the following exceptions. First, rather than constructing the image voxel map from only one image, the cell boundary is constructed using the data from

both the actin and nucleus images from each plane. This ensures that any slight errors in the data set due to chromatic or spherical aberration that may be present in the microscope do not cause any subcellular component to end up being located slightly outside the segmented periphery of the cell in the final product. After combining both images from each of the planes into a single image voxel map, a 3D Gaussian filter is applied to the resulting matrix to smooth out any extraneous small geometric details (those two or more orders of magnitude less than the scale of the entire data set). Secondly, due to the nature of the 2D cell culture techniques employed in this study it is assumed that there is no empty space underneath any part of the cell that is not part of the cell. To account for this assumption, the image matrix is filled downward with equal intensity.

In order to create isosurfaces of the cell boundary and nucleus, each image matrix is down-sampled using an empirically chosen percentage of matrix size and smoothed using a 3D Gaussian filter. Down-sampling is necessary at this stage as an additional method of smoothing in order to reduce the size of elements in the mesh to a range that allows for accurate geometric representation of the data without unnecessarily increasing computational intensity or generating elements of poor quality to make the mesh fit unnecessarily minute geometric details. Three-dimensional isosurfaces composed of three-node triangular faces are then generated for the cell boundary and nucleus. On average, the time required for generation of the cell boundary and nucleus isosurfaces is approximately one minute on an Intel® Xeon® 5160 dual core CPU at 3.00 GHz with 4.00 GB RAM.

The simplistic segmentation approach above is amply sufficient for the segmentation of the images used in this study, since the generation of representative actin fibers is our primary objective. Of course, more sophisticated techniques from the literature could be used to make the segmentation more robust (e.g. to handle multiple cells per image) if necessary.

5.2.4. Generation of Representative Actin Fibers

In this section, we describe a novel method for generating a representative network of actin fibers, based on an algorithmic framework. Due to the limited resolution of fluorescence confocal microscopy preventing high resolution visualization of individual f-actin fibers together with the inherent complexity of the actin stress fiber network, the strategy presented is not to reconstruct the exact fibers in the original image, but rather to generate a statistically *representative* reconstruction of entire fiber network.

We begin by generating a set of candidate fibers. We assume all fibers are straight line segments, although our methods can in principle all be generalized to handle more complicated geometric fiber shapes at the expense of additional computational cost. We say a fiber is *geometrically feasible* if it lies entirely within the cytosolic space of the cell (which we define as inside the cell boundary mesh but outside the nucleus boundary mesh). If the nucleus and cell boundary meshes are stored in appropriate spatial data structures (e.g. binary space partition trees), then feasibility of any fiber can be tested efficiently. Let E denote the set of all possible fiber endpoints – we currently take E to be the set of all nodes on the cell boundary mesh, although more elaborate options are also

possible; for example, we could identify through immunocytochemical staining and further image analysis a more specific set of "integrin" sites at which fibers are likely to attach. The set of candidate fibers for our actin network now consists of all geometrically feasible fibers with endpoints in E. We denote these fibers $f_1 \ldots f_n$. It will be prohibitive to generate all such fibers, since n can easily range into the millions; in these cases, we take $f_1 \ldots f_n$ to be a randomly-sampled subset of 10,000 geometrically feasible fibers. Our goal is to select a small number of these fibers to represent the actin stress fiber network.

All of our methods discretize the interior of the cell into a 3D volumetric grid of regularly-spaced voxels (currently separated by five pixels from their neighbors). Each voxel is further subdivided into 8 *directional voxels* (dvoxels), each representing a "bow tie" shaped angular range of 45° of directionality in the xy plane of the voxel (Figure 5.1). Directionality is measured only in the *xy* plane due to the limited *z* resolution inherent in confocal microscopy. We denote the set of all dvoxels $d_1 \ldots d_m$. For each dvoxel d_j, let a_j denote its intensity in the confocal image; that is, a_j reflects the amount of 2D textural directionality in the angular range of the *xy* plane and 3D location corresponding to the dvoxel d_j. We measure a_j as follows: we first isolate the *z* image plane of the dvoxel and apply a 2D Gaussian filter of size 33 x 33 centered at its *(x, y)* location, thereby extracting a 33 x 33 image of the local 2D neighborhood surrounding d_j (Figure 5.5[a-b]). We then perform a 2D FFT on this image (Figure 5.5[c]), and sum the magnitudes of all the points in the FFT image corresponding to d_j's angular range (Figure 5.5[d]). It is important to note that due to the way the 2D FFT produces its output, the dvoxel represents textures internally at a 90 degree rotation to their original orientation.

Additionally, the middle point of the image, being shared between all 8 angular ranges, contributes 1/8 to each of them. Figure 5.5(e-m) shows the angular contribution of all dvoxels co-located at a single voxel.
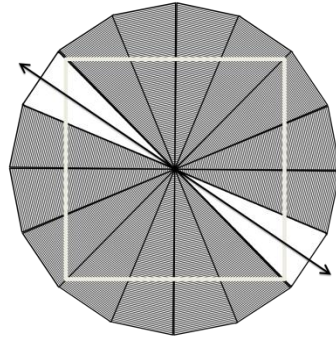
Figure 5.1. Illustration of a dvoxel. Note that the directions associated with a dvoxel form a symmetric pair of sectors each representing 22.5° of the circle.

Now that we have defined our candidate fibers $f_1...f_n$ and discretized the cell into dvoxels $d_1...d_m$, we build a sparse n x m matrix A for which A_{ij} reflects the "influence" of candidate fiber f_i on dvoxel d_j. A_{ij} is small if f_i either lies far from d_j or does not run in a direction compatible to those represented by d_j. We compute A_{ij} just as we computed a_j above, only starting with a "synthetic" confocal image consisting of a black background on which only fiber f_i is drawn, modeled as a cylinder of diameter 1 pixel, with the intensity of each voxel along its path set to the volume of the cylinder passing through the cubical volume represented by the voxel. Since we measure A_{ij} and a_j the same way, these two values are directly comparable.

5.2.4.1. GENERATING REPRESENTATIVE ACTIN FIBERS: A LINEAR

PROGRAMMING APPROACH

We can regard the problem of computing a representative actin fiber network as an inverse problem, where we seek to find a linear superposition of candidate fibers $\sum_i x_i f_i$ (with $0 \leq x_i \leq 1$ for each $i = 1...n$) that best matches the confocal image. The decision variable x_i allocated to each fiber f_i represents the extent to which fiber f_i is present in the solution. This can be regarded as a "fuzzy" measurement of fiber presence or equivalently as the probability of f_i being present. For a particular linear combination of fibers, the total contribution to each dvoxel d_j is given by $s_j = \sum_i A_{ij} x_i$, and the error between this and the actual intensity of d_j in the confocal image is $e_j = |a_j - s_j|$. Our goal is to minimize the total error $\sum_j e_j$, yielding the following optimization problem:

$$
\begin{aligned}
&\text{Minimize:} \quad && \sum_j e_j && \\
&\text{Subject to:} \quad && e_j \geq a_j - s_j && \text{for all } j = 1...m \\
& && e_j \geq s_j - a_j && \text{for all } j = 1...m \\
& && s_j = \sum_i A_{ij} x_i && \text{for all } j = 1...m \\
& && 0 \leq x_i \leq 1 && \text{for all } i = 1...m.
\end{aligned}
$$

As the objective and all constraints above are linear, this is a *linear program*, which can be solved relatively efficiently in practice, even for large instances. Another natural objective might be to minimize the quadratic error function $\sum_j e_j^2$, but this is much more

computationally prohibitive given the extremely large instances we are dealing with. After solving the linear program above for $x_1...x_n$, we must choose which fibers to include in our actin network. The ideal method for this task is to flip a biased coin for each fiber f_i, including f_i in the final network with probability x_i. This approach gives a set of fibers that matches, in expectation, the distribution output by the linear program. In several applications, however, we may wish to limit the number of fibers present in the final network; for example, if the network is to be used in a finite element model, then it may prove computationally intractable to include too many fibers. In this case, two different approaches can be used: we can either select all fibers f_i for which x_i is at least some specified threshold T, or we can regard $x_1...x_n$ as a probability distribution and randomly sample some specified number K of fibers (where fiber f_i is sampled with probability $x_i / \sum x_i$. The difficulty with the former approach is picking an appropriate threshold T, and with the latter approach the difficulty lies in choosing an appropriate value for K. We set the threshold in order to limit the generated actin network to only the most representative fibers and limit the computational complexity of the finite element models ultimately generated from our geometry. The threshold value we used typically resulted in the acceptance of approximately $135 - 450$ fibers per cell.

An advantage of the linear programming framework above is that we can place length constraints on the fibers in our solution. Ideally, we would like the actin network to consist of relatively long fibers, say of average length at least some threshold L (we set L to the length of the minor axis of the cell). Letting L_i denote the length of fiber f_i. We can

write this constraint as $(\sum_i x_i L_i)/(\sum_i x_i) \geq L$, which can be re-written as the linear constraint $\sum_i (L_i - L) x_i \geq 0$.

5.3. RESULTS

5.3.1. Cell Imaging

The deconvoluted images of the cell used in the analysis are shown in Figure 5.2 with the actin shown on the left in each pane, the nucleus shown on the right in each pane, and a distance between image planes of 200 nm. Note that a portion the nucleus still clearly appears in the upper-most image planes whereas the actin network, though present, is much more difficult to distinguish. This is a result of "bleed-through" in the z direction due to the intense brightness of the DAPI stain coupled with the limited axial resolution of the spinning disk confocal microscope. Figure 5.3 shows a 3D reconstruction of the cell generated in MetaMorph® displaying orthogonal views of the cell with the actin network shown in green and the nucleus shown in blue for use as a comparison to the image processing results.
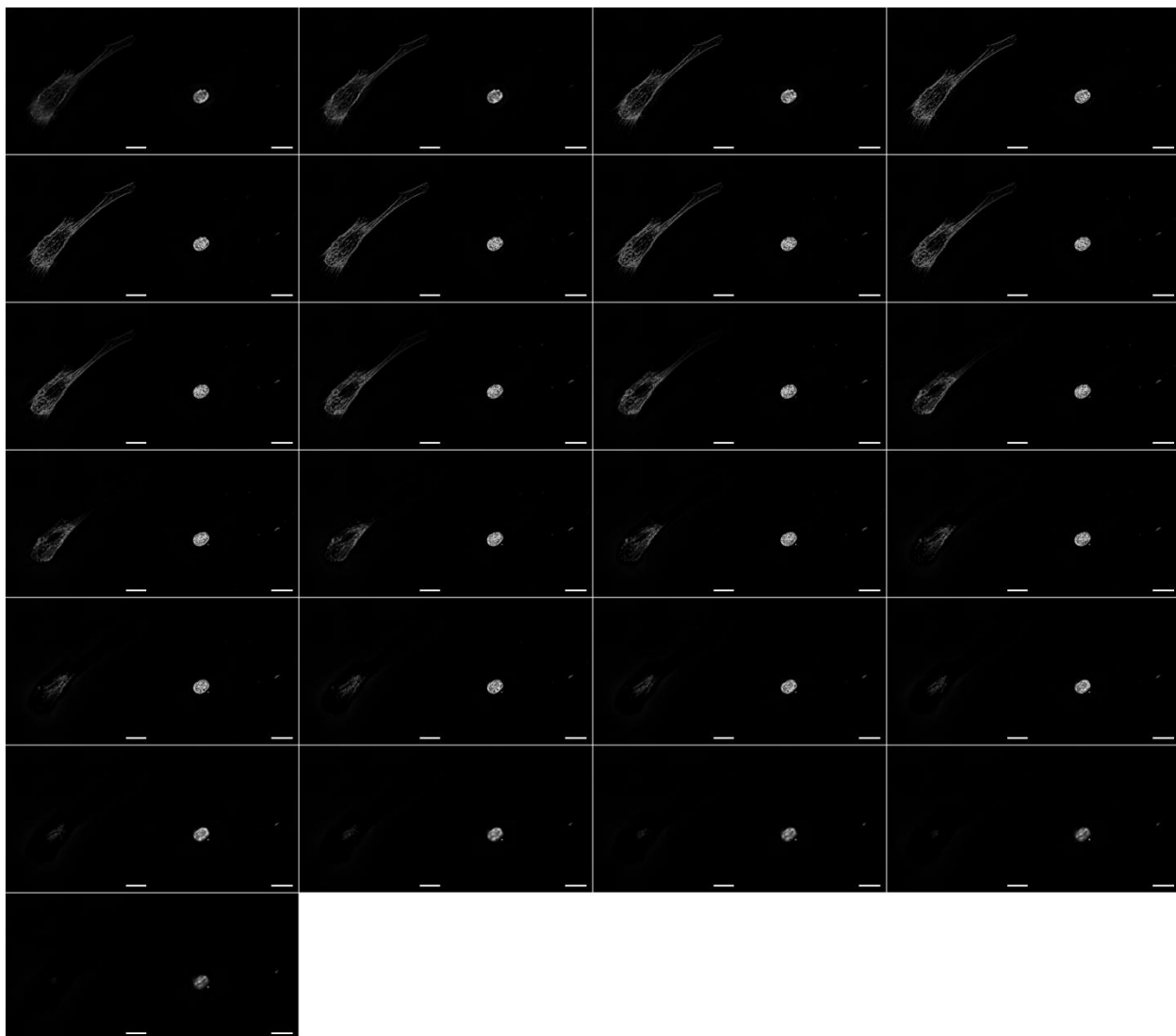
Figure 5.2. Image stack of deconvoluted confocal images. Actin shown on left in each pane, nucleus shown on right in each pane. The distance between image planes is 200 nm. Scale bar = 20 μm.
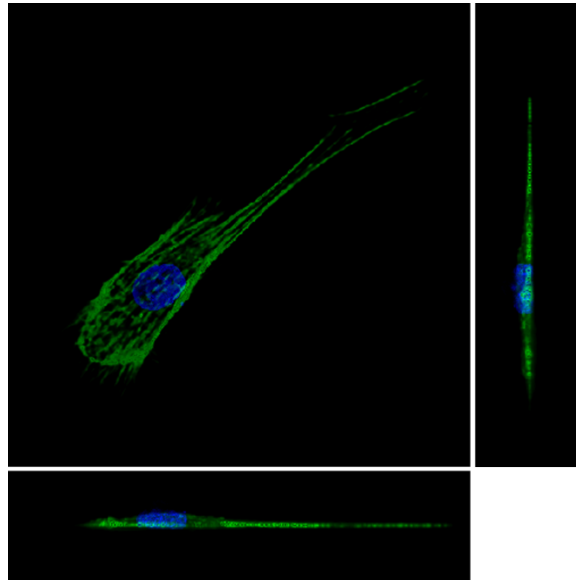
Figure 5.3. Orthogonal views of 3D reconstruction of the actin stress fiber network (green) and nucleus (blue) of the cell generated in MetaMorph®

5.3.2. Nucleus and Cell Boundary Meshes

The results of nucleus and cell boundary segmentation are shown in Figure 5.4. Note in the front and side views, that the synthetic cell is taller in the z direction than the original data shown in Figure 5.3. This phenomenon is a result of an extra dilation of the actin image data in the z direction to ensure sufficient cytosolic space above the nucleus for the elements above the nucleus to be of sufficient quality for eventual use in finite element models.
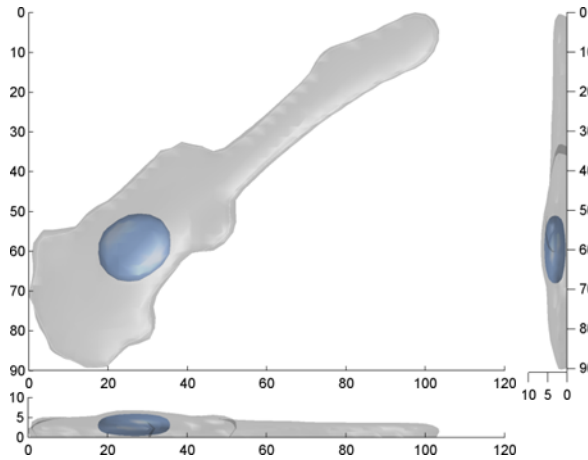
Figure 5.4. Results of image analysis showing cell periphery and nucleus (shown in blue).

5.3.3. Generation of Representative Actin Fibers

The results of dvoxel processing are shown in Figure 5.5. Figure 5.5(a) shows the location of the 33 x 33 pixel sampling unit on the original image. Figure 5.5(b) shows the result of negating the influence of neighboring sampling units using a Gaussian filter, and Figure 5.5(c) shown the result of the 2D FFT applied to Figure 5.5(b). The mask of a single dvoxel is shown in Figure 5.5(d), and Figure 5.5(e-l) show the result of the application of the mask for each dvoxel to Figure 5.5(c) with the sum of all intensity magnitudes for each dvoxel shown in brackets. The angular contributions of all dvoxels co-located at a single voxel are shown in Figure 5.5(m).
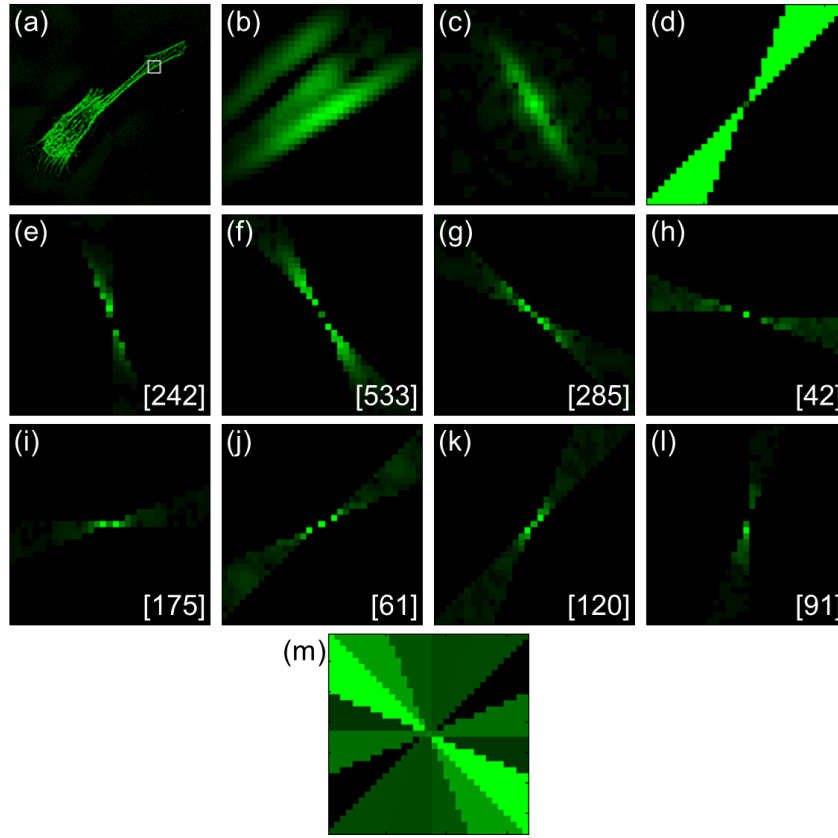
Figure 5.5. Dvoxel processing. (a) Original image with 33 x 33 pixel sampling unit shown. (b) Gaussian filter applied in sampling unit. (c) 2D FFT of Gaussian filter. (d) Mask applied at one dvoxel. (e – l) Results of 2D FFT multiplied by the mask of each dvoxel with the sum of all intensity magnitudes shown in brackets. m) Angular contribution of all dvoxels co-located at a single voxel; note that the dvoxel represents textures internally at a 90 degree rotation to their original orientation, due to the way the 2D FFT produces its output.

The final results of our image processing are shown in

Figure 5.6, showing the cell periphery (gray), the nucleus (blue), and a representative actin stress fiber network (green). The intensity of the color of each fiber correlates to the decision variable x_i, with brighter fibers having higher scores. Results of our image processing algorithm are shown for VSMCs of a variety of shapes and sizes in Figure 5.7. The generation of actin fibers takes on average 11.75 ± 7.5 hours to complete on an Intel®

122

Core® i7 CPU 860 at 2.80GHz with 8 cores and 16 GB RAM. The maximum time required for generation of actin fibers for the cells in Figures 5.6 and 5.7 was 15.0 hours.
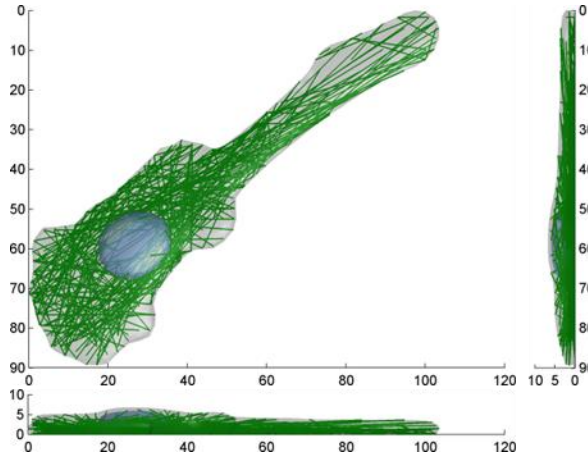
Figure 5.6. Results of image analysis showing cell periphery, nucleus (shown in blue), and representative actin stress fiber network (shown in green). Intensity of fiber color correlates to decision variable x_i, with brighter fibers having higher scores.
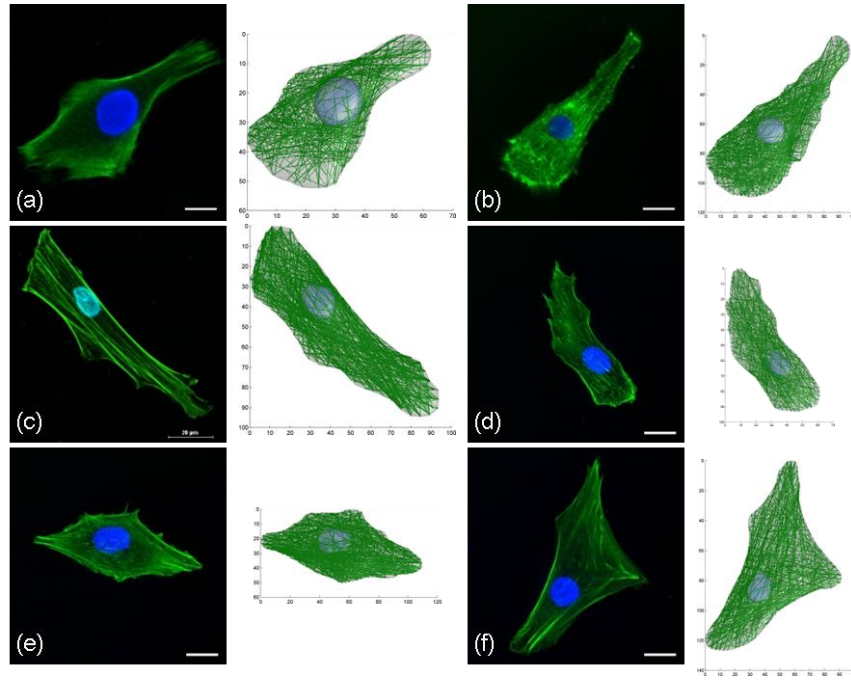
Figure 5.7. Results of image processing on multiple VSMCs with original confocal images shown on right of each subset; all scale bars are 20 µm.

5.4. DISCUSSION

5.4.1. Potential Applications

As mentioned above, the synthetic actin stress fiber networks generated in this study do not exactly match those of the original images they were generated from. This is intentional due to the fact that the geometries generated in this study are produced with the primary goal of utilization in finite element models for structural analysis. Therefore, it is imperative that the geometries be both an accurate representation of the original geometry yet sufficiently simple that the models can be solved in a reasonable timeframe on the average high-end consumer PC workstation. It is with this criterion in mind that

124

we choose to generate a *representative* reconstruction of the actin stress fiber network rather than an exact replica. This strategy also lends itself toward the potential for the generation of "average" synthetic cells that may be able to represent an entire phenotype in structural finite element models.

The principles used in the fiber generation algorithm may also be applicable for the generation of representative tissue-level structures as well, especially in non-invasive imaging techniques. One such example is the potential reconstruction of representative muscle fibers from ultrasound images, where resolution limitations can make exact reconstructions difficult, for structural or dynamic finite element analysis, where exact reconstructions are not a necessity.

5.4.2. Limitations

The linear programming method for actin fiber generation used in this study is currently somewhat slow. The computation time is dependent on the size of the cell being solved. Therefore, smaller cells will tend to take less time than larger ones to process. Increasing the level of downsampling will speed up the computation. In addition, this algorithm could be made faster through the utilization of more efficient spatial data structures.

The final, and most significant limitation identified by the authors lies in the imaging modality. Because the resolution of confocal microscopy being approximately 840 nm in the z-direction [41], it is much easier to distinguish the directionality of subcellular components laterally than axially. For instance, if an actin stress fiber were oriented in

exactly the *z*-direction, it would appear in the data only as a series of disjointed dots rather than a solid line and would be ignored by the 2D FFT that sets the basis for directionality within the present algorithm. Therefore, this technique is best suited for analysis and representation of adherent cells in 2D culture which tend to be much wider than they are tall. In order to modify the present algorithm to best analyze and reconstruct the components of cells in 3D culture, a 3D FFT would likely need to be utilized, which would be both more computational expensive and require greater axial resolution in the original image data set than the current 2D FFT approach.

5.5. SUMMARY AND CONCLUSIONS

An automated method for generation of structural components of single cells based on 3D stacks of confocal microscope images for use in structural finite element analysis is presented. The major contribution of this study is the novel technique presented for generation of a representative actin stress fiber network.

Cell and nucleus boundaries are segmented using simple thresholding techniques. Generation of a representative actin stress fiber network is achieved by analyzing a random distribution of all geometrically feasible fibers within the segmented geometries and using a linear optimization problem to select appropriate fibers based on the directionality of the image stack at each point as measured by a 2D FFT. For qualitative validation, analysis of 13 3D confocal image stacks of adherent vascular smooth muscle cells grown in 2D culture is performed. The method used in this study is currently slow, taking on average 11.75 ± 7.5 hours to complete on an Intel® Xeon® 5160 dual core CPU

126

at 3.00 GHz with 4.00 GB RAM; however it could be made faster through the utilization of more efficient spatial data structures or further down-sampling of the confocal images.

Recent models have been proposed that allow for near-realistic representation of single cell geometries for finite element analysis. The method presented here is the first of its kind, however, that is able to both segment 3D geometries of the cell boundary and nucleus, as well as generate a representative F-actin network of a cell that are fit for direct importation and implementation in structural finite element models for analysis of the mechanics of a single cell in a fully automated fashion. Models of this type are currently uncommon in biomedical research due to several factors, but could potentially be used to speed discoveries in the fields of regenerative medicine, mechanobiology, and drug discovery. This method promises to lower a substantial hurdle toward the use of such models – the ability to reconstruct cytoskeletal networks in an automated and representative manner.

Future directions of research include investigation of the use of a random sampling approach using the *Metropolis* algorithm to sample fibers using a random walk and the use of a mixture modeling approach for fiber generation based on the *Expectation Maximization* algorithm. Either of these methods, as well as the presented method, could also potentially be used for generation of representative networks of more geometrically complex cytoskeletal components such as microtubules or intermediate filaments.

5.6. REFERENCES

1.   Ingber, D.E., *Mechanobiology and diseases of mechanotransduction.* Annals of Medicine, 2003. 35(8): p. 564-577.

2.   Kaufman, S.R., *Making longevity in an aging society: linking Medicare policy and the new ethical field.* Perspectives in Biology and Medicine, 2010. 53(3): p. 407-424.

3.   Jonathan E. Fielding, M., MPH and M. Steven M. Teutsch, MPH, *An opportunity map for societal investment in health.* JAMA, 2011. 305(20): p. 2110-2111.

4.   Butler, P. and Y. Wang, *Editorial Note: Molecular Imaging and Mechanobiology.* Cellular and Molecular Bioengineering, 2011. 4(2): p. 123-124.

5.   Biswas, P.K., et al., *Simultaneous Use Of Class-i And Class-ii Force Fields In CHARMM For Solid-liquid Multiphase Simulation Of Protein-surface Interaction.* Biophysical Journal, 2009. 96(3, Supplement 1): p. 405a-406a.

6.   Wu, T., et al., *Design of a custom angled abutment for dental implants using computer-aided design and nonlinear finite element analysis.* Journal of Biomechanics, 2010. 43(10): p. 1941-1946.

7.   Ingber, D.E., *Tensegrity I. Cell structure and hierarchical systems biology.* Journal of Cell Science, 2003. 116(7): p. 1157-1173.

8.   Li, B., et al., *Development of micropost force sensor array with culture experiments for determination of cell traction forces.* Cell Motility and the Cytoskeleton, 2007. 64(7): p. 509-518.

9.   Cao, G.X. and N. Chandra, *Evaluation of biological cell properties using dynamic indentation measurement.* Physical Review E, 2010. 81(2).

10.   Unnikrishnan, G.U., V.U. Unnikirishnan, and J.N. Reddy, *Constitutive material modeling of cell: a micromechanics approach.* Journal of Biomechanical Engineering-Transactions of the Asme, 2007. 129(3): p. 315-323.

11.   Pullarkat, P.A., P.A. Fernández, and A. Ott, *Rheological properties of the Eukaryotic cell cytoskeleton.* Physics Reports, 2007. 449(1-3): p. 29-53.

12.   Suresh, S., *Biomechanics and biophysics of cancer cells.* Acta Materialia, 2007. 55(12): p. 3989-4014.

13. Ingber, D.E., *Tensegrity II. How structural networks influence cellular information processing networks.* Journal of Cell Science, 2003. 116(8): p. 1397-1408.

14. Kasza, K.E., et al., *The cell as a material.* Current Opinion in Cell Biology, 2007. 19(1): p. 101-107.

15. Bathe, M., et al., *Cytoskeletal bundle mechanics.* Biophysical Journal, 2008. 94(8): p. 2955-2964.

16. Tseng, Y., et al., *How actin crosslinking and bundling proteins cooperate to generate an enhanced cell mechanical response.* Biochemical and Biophysical Research Communications, 2005. 334(1): p. 183-192.

17. Deng, L.H., et al., *Fast and slow dynamics of the cytoskeleton.* Nature Materials, 2006. 5(8): p. 636-640.

18. Deshpande, V.S., et al., *A bio-mechanical model for coupling cell contractility with focal adhesion formation.* Journal of the Mechanics and Physics of Solids, 2008. 56(4): p. 1484-1510.

19. Mizuno, D., et al., *Nonequilibrium mechanics of active cytoskeletal networks.* Science, 2007. 315(5810): p. 370-373.

20. Pollard, T.D., *The cytoskeleton, cellular motility and the reductionist agenda.* Nature, 2003. 422(6933): p. 741-745.

21. Chaudhuri, O., S.H. Parekh, and D.A. Fletcher, *Reversible stress softening of actin networks.* Nature, 2007. 445(7125): p. 295-298.

22. Li, T., *A mechanics model of microtubule buckling in living cells.* Journal of Biomechanics, 2008. 41(8): p. 1722-1729.

23. Hawkins, T., et al., *Mechanics of microtubules.* Journal of Biomechanics. 43(1): p. 23-30.

24. Bursac, P., et al., *Cytoskeletal remodelling and slow dynamics in the living cell.* Nature Materials, 2005. 4(7): p. 557-561.

25. Hardin, J. and T. Walston, *Models of morphogenesis: the mechanisms and mechanics of cell rearrangement.* Current Opinion in Genetics & Development, 2004. 14(4): p. 399-406.

26. Stamenović, D., *Cytoskeletal mechanics in airway smooth muscle cells.* Respiratory Physiology & Neurobiology, 2008. 163(1-3): p. 25-32.

27.   Stamenović, D., *Microtubules may harden or soften cells, depending on the extent of cell distension.* J. Biomech., 2005. 38: p. 1728-1732.

28.   Stamenović, D., et al., *Mechanical Stability Determines Stress Fiber and Focal Adhesion Orientation.* Cellular and Molecular Bioengineering, 2009. 2(4): p. 475-485.

29.   Hemmer, J.D., et al., *Role of Cytoskeletal Components in Stress-Relaxation Behavior of Adherent Vascular Smooth Muscle Cells.* Journal of Biomechanical Engineering-Transactions of the Asme, 2009. 131(4): p. 9.

30.   Karcher, H., et al., *A Three-Dimensional Viscoelastic Model for Cell Deformation with Experimental Verification.* Biophysical Journal, 2003. 85(5): p. 3336-3349.

31.   Peeters, E.A.G., et al., *Mechanical and failure properties of single attached cells under compression.* Journal of Biomechanics, 2005. 38(8): p. 1685-1693.

32.   Funnell, W. and D. Maysinger, *Three-dimensional reconstruction of cell nuclei, internalized quantum dots and sites of lipid peroxidation.* J Nanobiotechnology, 2006. 4(10).

33.   Gladilin, E., et al., *Shape normalization of 3D cell nuclei using elastic spherical mapping.* Journal of Microscopy-Oxford, 2008. 231(1): p. 105-114.

34.   Dailey, H.L., et al., *Image-based finite element modeling of alveolar epithelial cell injury during airway reopening.* Journal of Applied Physiology, 2009. 106(1): p. 221-232.

35.   Slomka, N. and A. Gefen, *Confocal microscopy-based three-dimensional cell-specific modeling for large deformation analyses in cellular mechanics.* Journal of Biomechanics, 2010. 43(9): p. 1806-1816.

36.   Echlin, P., *Handbook of Sample Preparation for Scanning Electron Microscopy and X-Ray Microanalysis.* Illustrated ed2009: Springer. 330.

37.   Spring, K.R., T.J. Fellers, and M.W. Davidson. *Resolution and Contrast in Confocal Microscopy.* 2004 2009 November 2, 2009]; Available from: http://www.olympusconfocal.com/theory/resolutionintro.html.

38.   Lin, G., et al., *A hybrid 3D watershed algorithm incorporating gradient cues and object models for automatic segmentation of nuclei in confocal image stacks.* Cytometry A, 2003. 56(1): p. 23-36.

39. Lin, G., et al., *Hierarchical, model-based merging of multiple fragments for improved three-dimensional segmentation of nuclei.* Cytometry A, 2005. 63(1): p. 20-33.

40. Russell, R.A., et al., *Segmentation of fluorescence microscopy images for quantitative analysis of cell nuclear architecture.* Biophys J, 2009. 96(8): p. 3379-89.

41. David E, W., *The Optics of Microscope Image Formation*, in *Methods in Cell Biology*, S. Greenfield and E.W. David, Editors. 2007, Academic Press. p. 11-42.

CHAPTER 6

STRUCTURAL MODELING OF VASCULAR SMOOTH MUSCLE CELL MECHANICS USING MSC MARC (AIM 3)

6.1. INTRODUCTION

The goal of this study is to construct a representative 3D inverse[1] finite element model (FEM) of a biological cell based on the sub-cellular structures that provide the cell with its mechanical properties. The geometries for the model are constructed in MATLAB from photomicrographs of cells using the proprietary analytical algorithms presented in Chapter 5, imported into MSC Patran for pre-processing, and submitted to MSC Marc for analysis.

The ability to model the mechanical responses of cells to physical stimuli presents many opportunities to the world of medical research. Chief among these is the ability to further our understanding of the ætiology of many diseases [1, 2]. There are a wide variety of diseases whose ætiology or clinical presentation are either known or suspected to be related to abnormal cellular mechanics, alteration of cellular mechanotransduction processes, or changes in tissue structure [1]. Because physical distortion can affect cell

---

[1] An inverse finite element model is a model that is based on something that already exists for the purpose of reproducing existing results. In contrast, a standard FEM generally refers to a model based on computer-aided design (CAD) drawings of something that doesn't exist yet for the purpose of predicting results. The distinction between the two is typically used when defining a model, but not when referring to a model.

growth, differentiation, contractility, motility, and apoptotic tendency [1], the ability to predict the mechanical behavior of cells in response to pathological conditions and medical treatments may be critical to prevention and treatment of many of these diseases [1, 3-6].

There has been much effort put into characterizing the behavior of cells throughout the years, however there has not been quite as much effort put into utilizing those models in one of the most powerful analytical tools available to the engineer: the finite element model. This is largely due to the highly complex geometries and material nonlinearity exhibited by cells which until recently was more computationally expensive than was feasible on the average personal computer (PC) [7]. There have been attempts to create 2D finite element models of cells since PC computing power began increasing in the 1990s [2, 7-9]; however, despite the ever-growing availability of sufficient computing power for more complex models, only two 3D confocal-based models have been published [2, 10]. Furthermore, of those models that have been published, only one employs large strain mechanics [2], only one utilizes a compound structure [2], neither is based on accurate geometries capable of representing an entire cellular phenotype, and neither model is validated by comparing predictions against experimental data. The model presented in this study provides the next step toward allowing finite element analysis to become a widely used tool within the field of cellular mechanics. The work proposed in this study could also eventually be incorporated into multiscale models, providing a key link between the prediction of mechanical responses to pathological conditions and medical treatments from the tissue level down to the molecular level.

6.2. MATERIALS AND METHODS

6.2.1. System Considered

Blood vessels are composed of three different layers of cells. The most predominant cell type in the thickest layer is the vascular smooth muscle cell (VSMC). These cells are constantly under dynamic load due to arterial pressure in normal healthy conditions. In response to injurious mechanical loading, VSMCs can undergo significant cytoskeletal remodeling, leading to changes in mechanical properties that may eventually contribute to atherosclerosis [11]. The cytoskeleton is the primary mechanism responsible for maintenance of cell shape and determination of the mechanical properties of cells [1]. It is a biopolymer network comprised of several components, including actin stress fibers, microtubules, and a variety of structures known as intermediate filaments. Actin microfilaments (f-actin) are $7-9$ nm diameter polarized polymers comprised of globular actin (g-actin) monomers. These microfilaments exhibit a highly dynamic behavior regulated by the proteins profilin and cofilin. The microfilaments are relatively stiff and have a persistence length of 15 µm and an elastic modulus of $1.3-2.5$ GPa in dilute solution [12]. In adherent cells, actin microfilaments are found bound together by actin binding proteins to form closely packed arrays known as actin stress fibers. These stress fibers orient themselves largely along the direction of the stress field applied to the cell by its surroundings. A key feature of actin stress fibers is the prestress that is actively exhibited upon them by the actomyosin complexes which are formed by the association of myosin motor proteins with the actin filaments [13].

VSMCs in this study are cultured on glass coverslips following previously reported methods (Chapter 5.3.1). Three cells are highlighted in this study: the cell from Figure 5.6. (heretofore referred to as Cell A), the cell from Figure 5.7(a) (heretofore referred to as Cell B), and the cell from Figure 5.7(b) (heretofore referred to as Cell C). The image in Figure 6.1 shows how the actin stress fiber network (left) and nucleus (right) are arranged within Cell B.

6.2.2. Mechanical Characterization of Live Cells

Atomic force microscopy (AFM) is utilized in this study to characterize the mechanics of the VSMCs. AFM indentation utilizes the spring characteristics of a cantilever to measure the force of resistance when a conical, pyramidal, or spherical tip is indented into a sample. Atomic force microscopes can therefore be used to perform nanoindentation tests that measure the force of resistance as the tip is indented into the cell. Figure 6.2 shows an average force-indentation curve for the type of VSMC used in this study [14]. As has been noted by prior studies [14], however, there is a great deal of heterogeneity in the mechanical properties of individual cells even within a single sample; therefore, the curve shown in Figure 6.2 should be taken simply as a representative case. Cells are indented here to a depth of approximately 1 µm (Figure 6.3) at 0.5 µm/sec using a 5 µm diameter spherical tip on a cantilever with a spring constant of 0.18 nN/nm. For indentation, the AFM probe is placed above the estimated center of the nucleus (Figure 6.4[b]); however due to the difficult nature of observation of the cells and their nuclei before fluorescent labeling (Figure 6.4[a]), this placement is not exact.

136
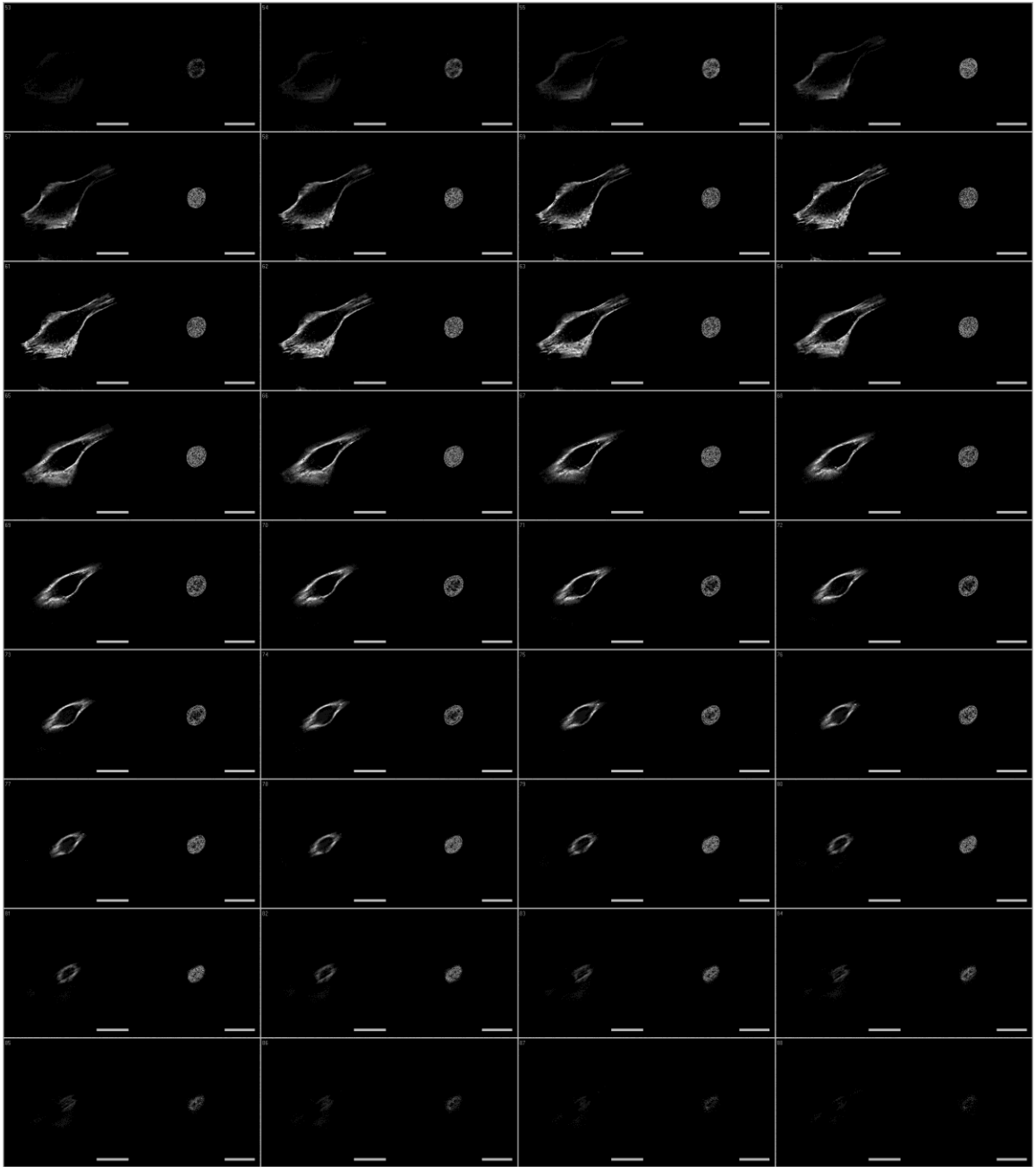
Figure 6.1. Montage of image planes used to create the geometry of the model for Cell B: each frame represents one plane of the cell of 200 nm thickness that has been processed using a 3D deconvolution algorithm. The left half of each frame shows the f-actin distribution within the cell and the right half shows the nucleus of the cell (Scale bar = 20 µm).

137

Indentation Curves
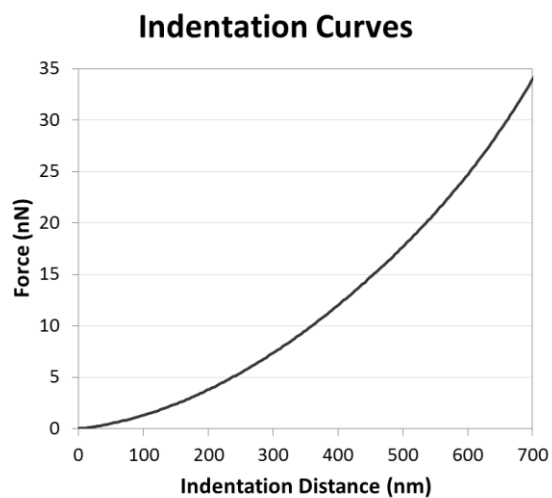
Figure 6.2. Typical force-indentation curve for a VSMC of the type used in this study indented with a 5 µm spherical probe at 0.5 µm/s in standard cell culture media [14]
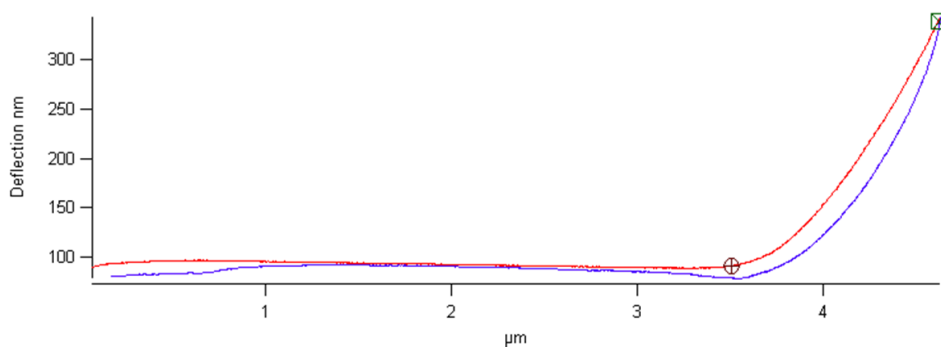
Figure 6.3. Raw AFM Indentation data; the red line shows deflection of the cantilever upon indentation, the blue line shows deflection of the cantilever upon retraction, and the distance between the circle and square along the abscissa represents the approximate indentation depth
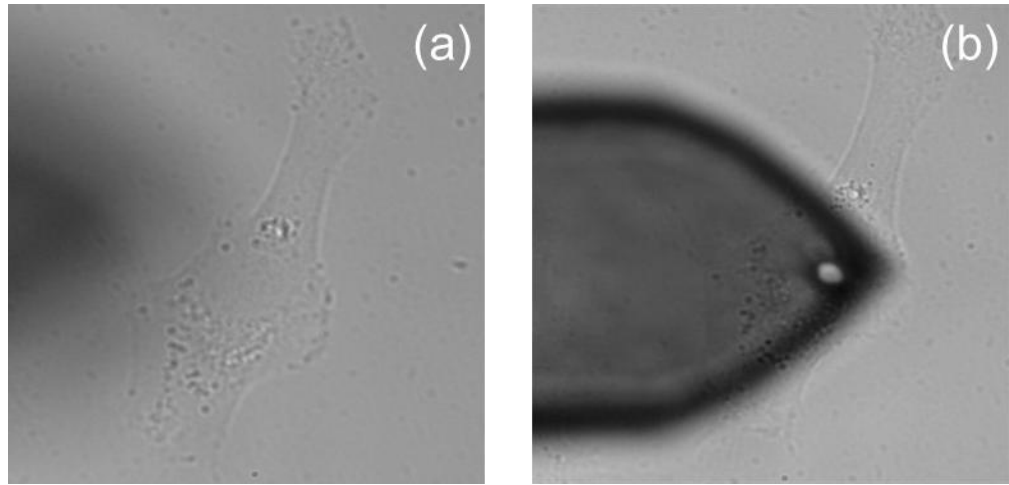
Figure 6.4. Cell B as viewed through AFM camera with 60X oil objective (a) prior to indentation and (b) during indentation

6.2.3. Confocal Imaging of Cells

Following mechanical characterization of cells, the cells are fixed in place on the microscope using 4% paraformaldehyde and permeabolized using a solution of 0.1% Triton-X and 0.01 M Glycine (to quench the excess aldehyde). They are then treated with solutions of 130 nM AlexaFluor 488 phalloidin and 350 nM DAPI to fluorescently label the actin stress fiber network and nucleus, respectively (Figure 6.1). The cells are then imaged in accordance with the methods described in Chapter 5.3.1.

6.2.4. Analysis of Mechanical Characterization

The Hertz contact model is used to estimate the apparent elastic modulus of the cell. The equation governing the relation of force of indentation to the elastic modulus of an

indented sample using a spherical indenter according to the Hertz model is given in

Equation 6.1.

Equation 6.1. The Hertz contact model

$$F = \frac{4}{3}\frac{E}{(1-v^2)}R^{\frac{1}{2}}\delta^{\frac{3}{2}}$$

where E and v are the elastic modulus and Poisson's ratio of the sample, respectively, δ is

the depth of indentation, and R is the radius of the spherical indenter. The Hertz model is

applied at a depth of 200 nm indentation, or approximately 10 % of cell height, as this is

within the range that the Hertz model remains accurate [14].

6.2.5. Finite-Element Model of System

6.2.5.1. MODELING ASSUMPTIONS

The microtubule network of VSMCs is highly complex, with no common, easily

discernible patterns typically present. Therefore, in order to reduce the complexity of this

model the microtubule network is assumed to be distributed homogeneously throughout

the cell and can therefore be modeled as a continuum. Additionally, it is highly difficult

to discern from confocal microscopy images the number of actin microfilaments

comprising a single actin stress fiber. It is therefore assumed that each stress fiber has a

radius of 100 nm based on previously reported values [15]. As described in Chapter 5, all

fibers that are determined to have a fiber score of $T > 0.001$ in the solution of image

analysis are accepted for finite element analysis, resulting in the incorporation of 361 out of a possibly 945 fibers into the model presented here. See Appendix C.2 and Appendix C.3 for data showing dependence of results on fiber parameters.

6.2.5.2. GEOMETRIC MODEL

Three-dimensional confocal microscopy image stacks are analyzed using an algorithm capable of generating representative model geometries consisting of the cell body, nucleus, and actin stress fiber network as described in Chapter 5. The algorithm uses simple thresholding techniques to generate the cell body and nucleus, and 2D frequency analysis combined with linear programming approaches to generate the actin stress fiber network. The resulting geometries are shown in Figure 6.5, with the grey surface representing the cell periphery, the blue surface representing the nucleus periphery, and the green lines representing the actin stress fibers for each cell. Using the fiber score threshold value ascribed in Chapter 5, Cell A was generated with 361 fibers, Cell B was generated with 615 fibers, and Cell C was generated with 291 fibers. It should be noted that in order to replicate physical conditions and ensure the ability of the model to solve successfully, the actin stress fibers are not allowed to intersect with either the cell or nucleus periphery and are therefore contained completely within the cytoplasmic volume of the model cell.
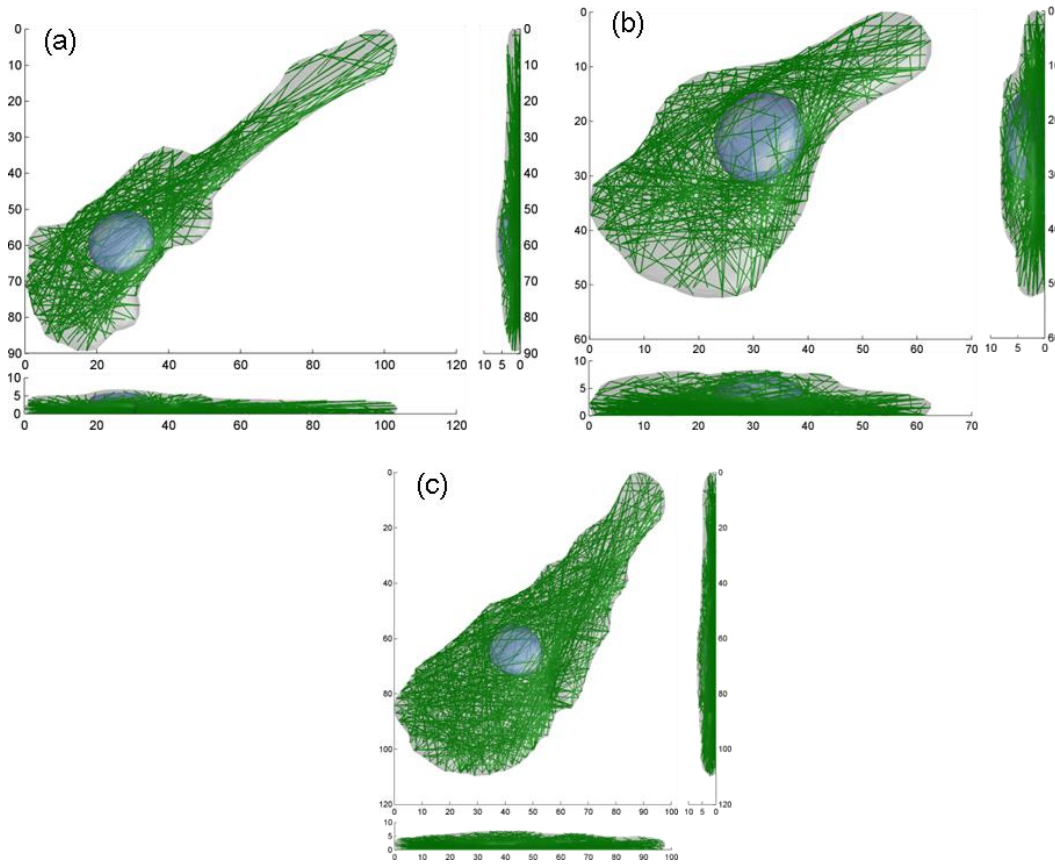
Figure 6.5. Geometry of (a) Cell A (361 fibers), (b) Cell B (615 fibers), and (c) Cell C (291 fibers) as generated by MATLAB image processing: grey represents the cytoplasm, blue represents the nucleus, and green represents the actin fibers

The geometry created in MATLAB is composed of two-dimensional 3-noded triangle (Tria3) and one-dimensional 2-noded bar (Bar2) elements in 3D space and is imported into Patran via a session file written in MATLAB. The session file builds the mesh into Patran from the ground up by generating each individual node and element. It automatically creates meshes constructed of 10-noded tetrahedral (Tet10) elements for the nucleus and cytoplasm, meshes the actin stress fibers with Bar2 elements of average length approximately consistent with the persistence length of actin filaments (15 µm

[12]), and constructs the spherical cap representative of the AFM probe directly above the highest node of the cell (Figure 4). Positioning the AFM probe in such a manner typically ensures proper probe placement to match the experimental condition of indenting the cell at the approximate center of the nucleus.
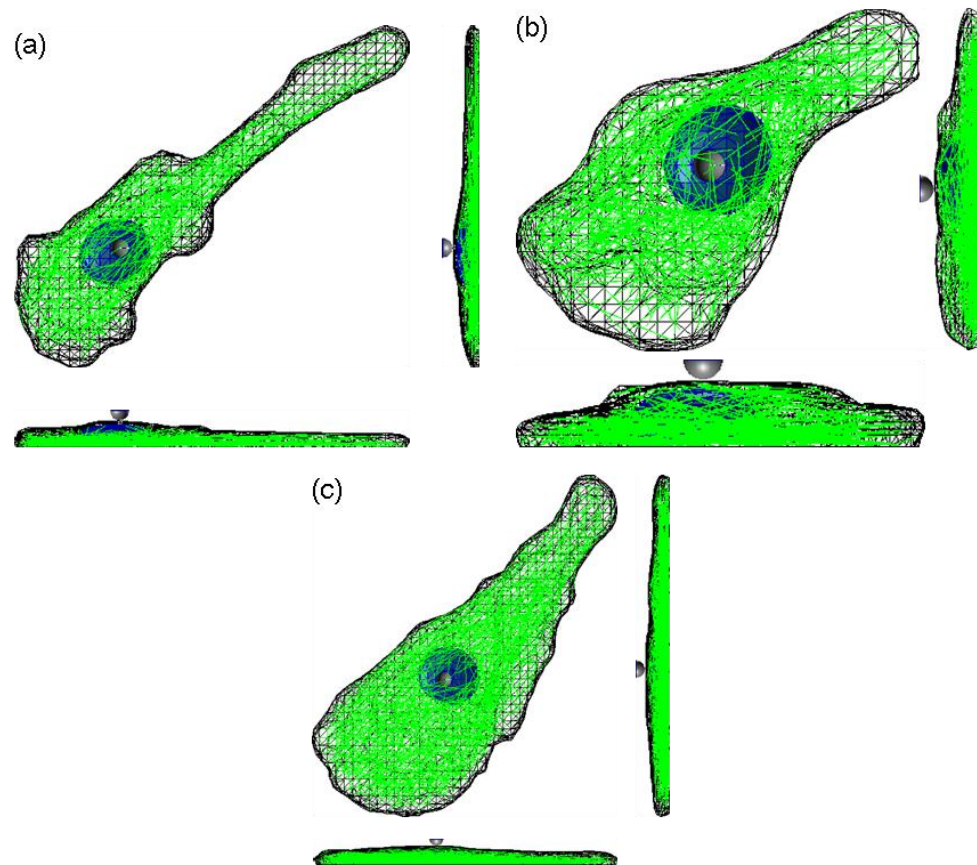
Figure 6.6. Mesh of (a) Cell A, (b) Cell B, and (c) Cell C with Geometry of AFM Probe in Patran After Importing From Matlab

6.2.5.3. MATERIAL MODELS

The VSMCs modeled herein are composed of three separate linear isotropic materials, each with a Poisson's ratio of 0.49 [14]. Two types of simulations are performed in this study – models with actin, and models without actin. The nucleus and actin filaments (where appropriate) are modeled using Young's moduli of 3.3 kPa and 1.9 GPa, respectively, based on literature values [12, 16]. For the models with actin, the cytoplasm is given a Young's modulus of 2.25 kPa based on experimental data of VSMCs treated with cytochalasin D to depolymerize actin filaments. For the models without actin, the cytoplasm is given a Young's modulus based on the apparent elastic modulus estimate obtained via Equation 6.1 from the AFM indentation data of that particular data set.

The actin filaments are represented in the model as truss elements, and the cell body and nucleus are both constructed of Tet10 elements. It should be noted that truss elements do have two primary limitations relative to general beam elements for this type of model. First, they only transmit forces axially and therefore do not exhibit any bending characteristics. Secondly, trusses elements in Marc are incapable of supporting prestress; however, prestress values in actin stress fibers vary throughout the cell [17] and therefore would be highly difficult to incorporate accurately even if supported. Despite their limitations, truss elements are chosen for this study because they are the most stable 1D embeddable element type in Marc and are therefore highly recommended for this type of analysis by the developers of the software.

6.2.5.3.1. EMBEDDING FIBERS IN MARC

All pre- and post-processing of the model is performed in Patran 2010. However, Patran 2010 is not capable of embedding 1D elements into 3D solids as needed for a model of this nature. Therefore, the model was submitted to the Analysis Deck in Patran, and an INSERT card is manually written into the resulting .dat file in order to define the host and embedded elements before submission to Marc (Appendix D.1.1.).

6.2.5.4. LOADS AND BOUNDARY CONDITIONS

Two sets of boundary conditions are applied to the model to match experimental conditions. First, the bottom-most layer of nodes is fixed in position to represent the physical attachment of the cell to its substrate. Second, a rigid spherical cap is plunged into the deformable cell body using contact parameters to represent the indentation of the AFM probe into the cell, as described in the Analysis section below.

6.2.6. Analytical Parameters

Analysis is performed using MSC Marc 2010.2. In order to simulate contact between the AFM probe and the cell, each component is defined as a separate contact body with the former being rigid and the latter being deformable. Global remeshing is utilized for the analysis, with a strain of 0.25 used as the threshold to trigger remeshing, however it should be noted that the 0.25 strain threshold is not reached in any of the simulations performed in this study. To match experimental conditions, the probe is prescribed a

displacement of 1 μm into the cell in 25 nm increments at 0.5 μm/sec. For all models, the Large Displacement/Large Strains solution parameter is utilized.

6.3. RESULTS AND DISCUSSION

6.3.1. Indentation

The distribution of von Mises stresses throughout the model cell with actin at a probe indentation depth of 1 μm is shown in Figure 6.7. The maximum value of stress experienced by the cytoplasm and nucleus of the cell is 0.95 kPa and the maximum value of stress experienced by the actin stress fiber network is 78 kPa. While these values are meaningless on their own since there are no experimental methods to measure intracellular stresses with which to compare them against, they do provide a promising demonstration of two different principles. First, the fact that the stresses experienced in the actin stress fiber network are approximately two orders of magnitude higher than those in the rest of the cell body suggests that the load exerted upon the cell is primarily distributed through the actin, which matches physical expectations. Secondly, the stresses are carried throughout the entirety of the cell through the actin stress fiber network, matching observations of cell behavior obtained experimentally [18]. Of note, Figure 6.7 shows an anisotropic distribution of stresses throughout the cell, emphasizing the importance of the geometric arrangement of the actin stress fibers within the cell on the mechanical characteristics of the cell.
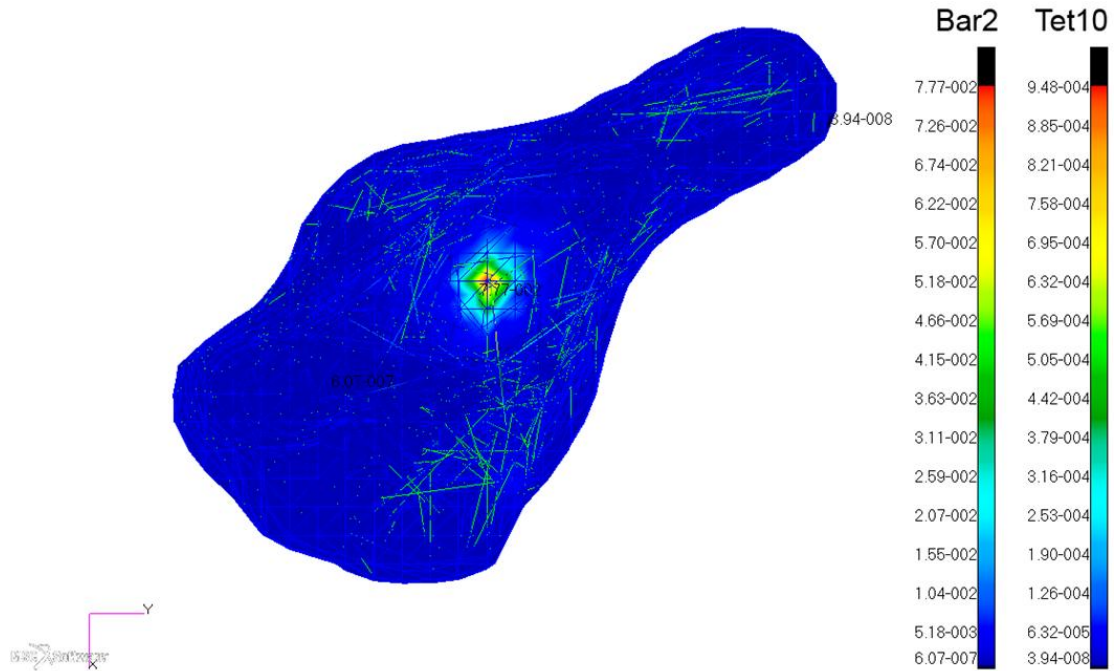
Figure 6.7. Representative von Mises stress distribution (shown in Cell B)

The force-indentation curves of AFM nanoindentation and both FEM cases (models with and without actin) for all 3 cells are shown in Figure 6.8. The AFM curve is presented with error bars displaying the 99 % confidence interval (n = 5). As shown in Figure 6.9, both FEM cases match the experimental data very well (average $R^2 > 0.99$) up to an indentation depth of 250 nm and still match the experimental data reasonably well (average $R^2 > 0.9$) at an indentation depth of 500 nm, however there is a precipitous drop-off in the correlation between the experimental data and the model at or beyond 750 nm of indentation (with average R^2 values ranging between -0.15 and 0.45). As such, it is not recommended that the current model be used to predict AFM nanoindentation data beyond 500 nm of indentation. Multiple analyses were performed on the sensitivity of the model to the number of fibers and fiber diameter and neither was found to be a primary

147

determinant of the results of the model (see below in Chapter 6.3.2.1 and Chapter 6.3.2.2.), thus reinforcing the importance of geometry determined in Chapter 4. In addition, Chapter 6.3.2.3. shows how the difference between indentation curves in live VSMCs with and without actin corresponds to the difference between indentation curves of model VSMCs with and without actin.

On average, the model with actin incorporated into it matches the experimental data more closely than the model without actin for all depth ranges. This demonstrates that the cytoskeletal geometries generated by the novel image processing techniques presented in Chapter 5 are successful at replicating AFM nanoindentation experiments more accurately than traditional finite element model techniques. The apparent elastic modulus estimates of the cells based on the AFM and FEM indentation curves are shown in Figure 6.10 with error bars displaying the 99 % confidence interval.
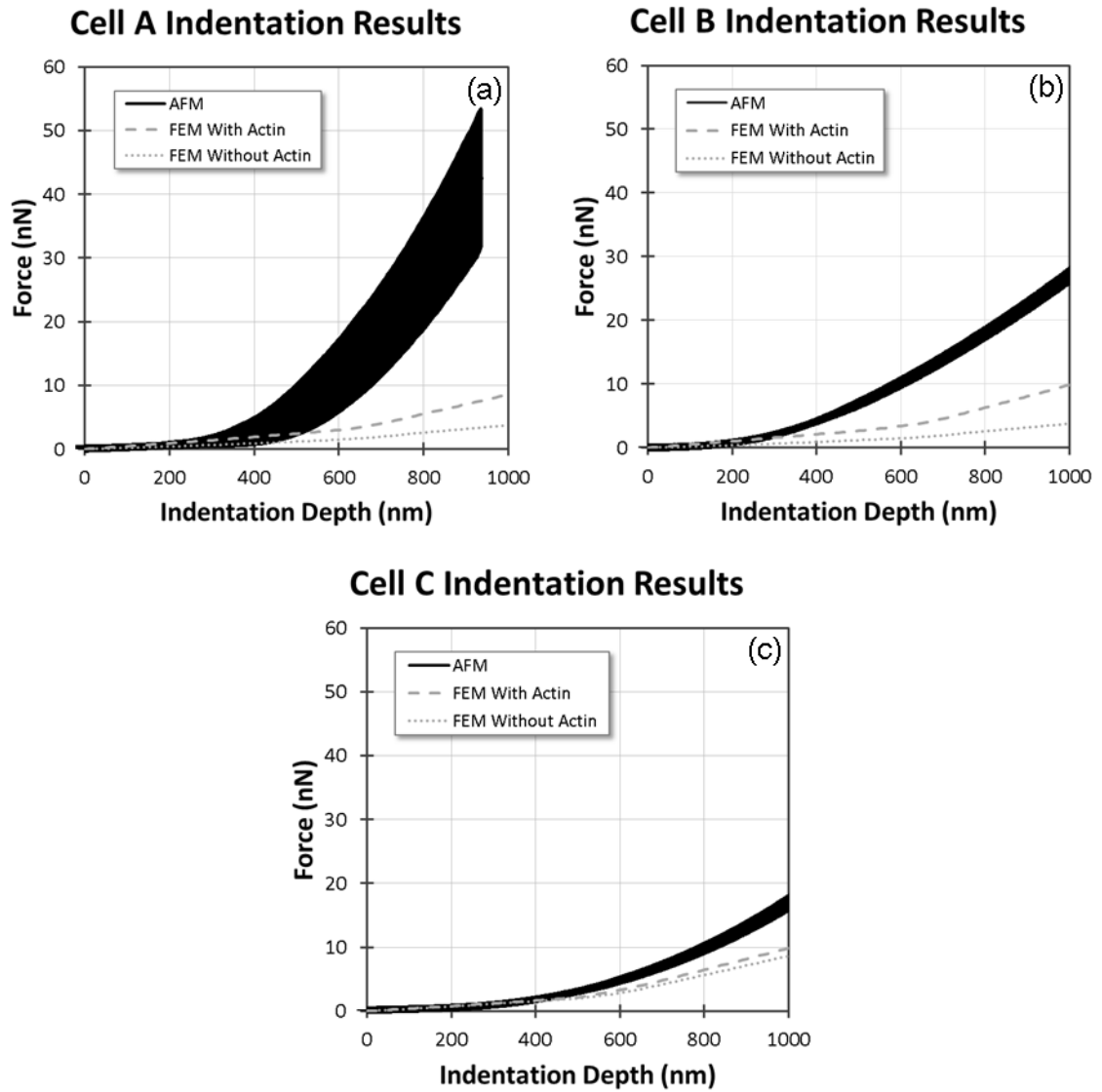
Figure 6.8. AFM and FEM force-indentation curves for (a) Cell A, (b) Cell B, and (c) Cell C; error bars display 99 % Confidence Interval (n = 5)
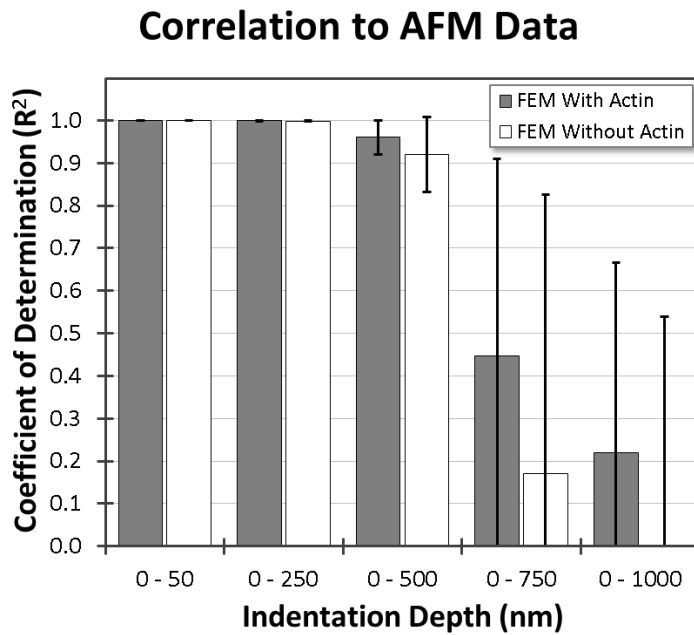
Figure 6.9. R^2 Values of FEM indentation curves at various indentation depths relative to AFM data; error bars show 99 % Confidence Interval (n = 3)
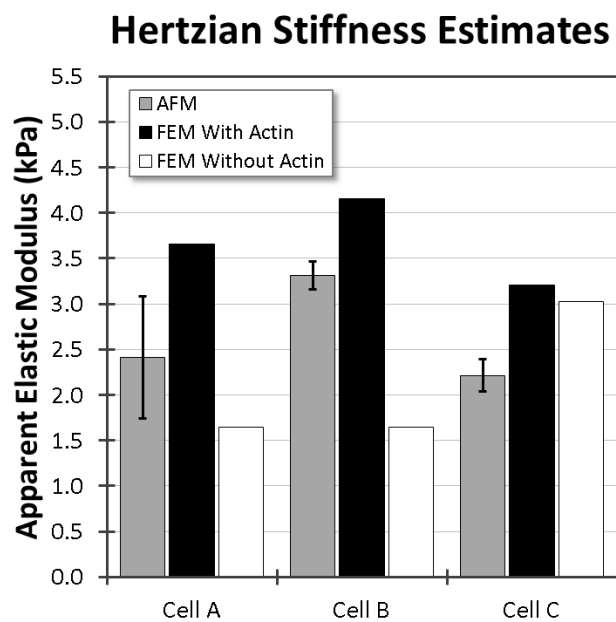
Figure 6.10. Hertzian stiffness estimates of the cell as measured via AFM and FEM indentation curves; error bars show 99 % Confidence Interval (n = 5)

6.3.2. Sensitivity Analyses

6.3.2.1. FIBER NUMBER SENSITIVITY ANALYSIS

Fiber density sensitivity analysis was performed on a 3D axisymmetric model in Patran/Marc, with results of the model compared when varying numbers of synthetic actin stress fibers are utilized (Figure 6.11). The "% Change" line in Figure 6.11 denotes the percentage change relative to the model with the previous number of fibers. Error bars show 99% confidence intervals (n = 3). A diameter of 200 μm was used for all models in this analysis. The Apparent Elastic Modulus was calculated using the Hertz Analytical Model (Chapter 1.3.1.) at an indentation depth of 200 nm, and values were normalized to the stiffness of the model with zero fibers. As expected, the number of fibers is roughly proportional to the stiffness of the cell, however the amount of variation in these results suggests that the number of fibers used in the model is not the primary determinant of the stiffness of the model.
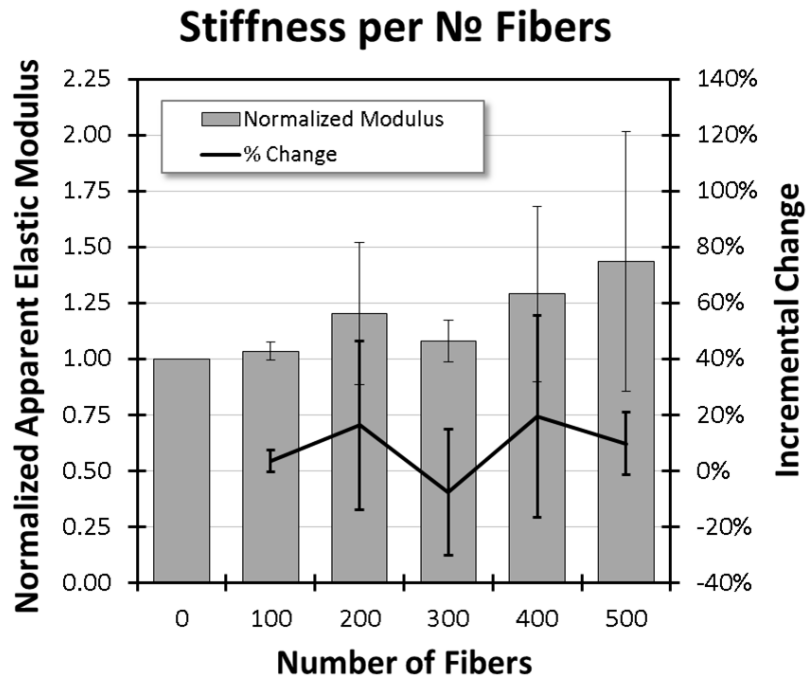
Figure 6.11. Fiber diameter sensitivity analysis; error bars show 99 % Confidence Intervals (n = 3).

6.3.2.2. FIBER DIAMETER SENSITIVITY ANALYSIS

Fiber diameter sensitivity analysis was performed on a 3D axisymmetric model in Patran/Marc, with results of the model compared when varying diameters of synthetic actin stress fibers are utilized (Figure 6.12). The "% Change" line in Figure 6.12 denotes the percentage change relative to the model with the previous diameter of fibers. Error bars show 99% confidence intervals (n = 3). The number of fibers utilized was 500 for all models in this analysis. The Apparent Elastic Modulus was calculated using the Hertz Analytical Model (Chapter 1.3.1.) at an indentation depth of 200 nm, and values were normalized to the stiffness of the model incorporating 7 nm diameter fibers (the diameter of a single f-actin filament [12]). As expected, the diameter of fibers does impact the

stiffness of the cell, however the amount of variation in these results suggests that the diameter of the fibers used in the model is not the primary determinant of the stiffness of the model.
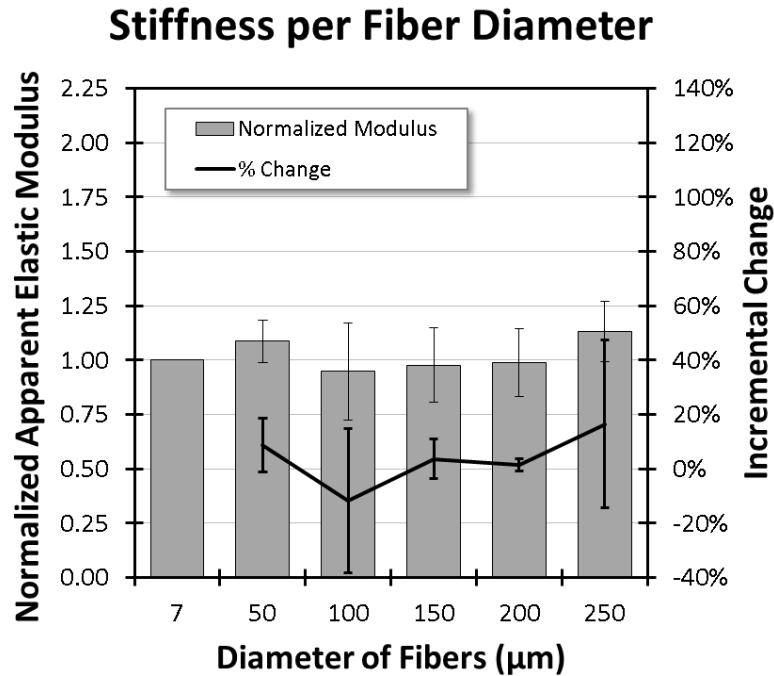
Figure 6.12. Fiber diameter sensitivity analysis; error bars show 99 % Confidence Intervals (n = 3).

6.3.2.3. EFFECT OF ACTIN FIBERS

In order to determine if the addition of actin fibers to the model has a similar effect on the mechanical properties as the addition of actin stress fibers does to a live cell, the force-indentation curve of a control VSMC was normalized against the force-indentation curve of a VSMC treated with Cytochalasin D to depolymerize f-actin. A similar curve was generated for a FEM indentation curve of cells with and without actin (Figure 6.13).

Although the two lines are nearly isometric, it is interesting to note that the curves

intersect very near an indentation depth of 200 nm, suggesting that apparent elastic

modulus estimates obtained using the Hertz contact model as done in Chapter 6 would

indicate a similar relationship between the stiffness of the FEM models with and without

actin as exists between the live treated and untreated cells.

Effect of Actin Fibers
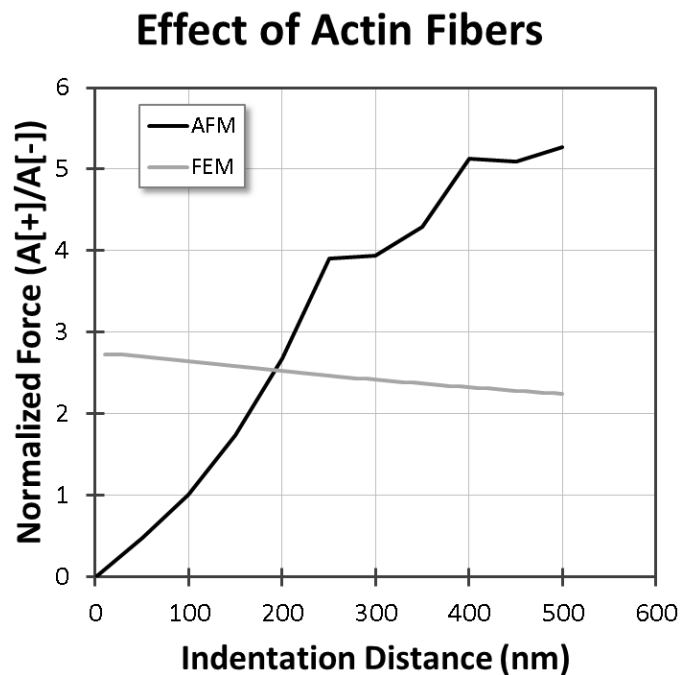
Figure 6.13. Effect of actin fibers on force-indentation curves; A(+)/A(-) denotes
that the normalized force is equal to the force for the curve with actin normalized
against the curve without actin.

6.3.3. Advantages and Limitations

The approach taken here represents a new paradigm for the construction of a cellular

mechanics model. All previous attempts to model the mechanical behavior of cells have

focused on altering the material parameters of the model to match experimental data. This model, however, utilizes only material parameters taken from experimental data (either directly from the cell modeled or from literature values) and relies on the geometric arrangement of the structural components of the cell to provide the model with realistic results. It is important to note that the results above could easily be made to match the experimental data better by altering our material parameters. However the major advantage of this new paradigm of model construction is that because the material parameters are based on physical reality and not simply altered to try to match the data as closely as possible the results are therefore more meaningful and are more likely to be predictive across samples and potentially even across cell types.

However, although this novel approach is more ideal than the previous paradigm, it does still have some limitations. Primarily, it is reliant on two factors relating to how the material parameters from the literature were obtained.

The first of these factors is that the material parameters for actin taken from the literature were obtained from single filaments of f-actin in dilute solution. This therefore relies on two assumptions for the presented model about actin stress fibers. The first is that actin stress fibers (which are composed of many actin filaments) have the same tensile modulus as a single filament, which is highly unlikely. Secondly, because the fibers in the model are all independent of one another, the model relies on the assumption that the cross-linking of actin stress fibers observed in VSMCs does not alter the mechanical properties observed from actin filaments in dilute solution.

155

The second limiting factor is the assumption that the Poisson's ratio taken from the literature was obtained using micropipette aspiration on non-adherent cells. This therefore relies on the assumption that the Poisson's ratio of cells is independent of their geometry – specifically, that it is independent of the arrangement of the points of attachment of the cell to its substrate. Because the Poisson's ratio is a definition of how a material deforms in multiple directions this assumption of geometric insensitivity is unlikely to be fully realistic. Nevertheless, the value used here is used extensively throughout the literature and therefore remains the most appropriate value to use until a method to measure the Poisson's ratio of an adherent cell is proposed.

It is also noteworthy that the model proposed herein is similar in nature to the multiphasic models commonly utilized to characterize the mechanical responses of biological tissues. However, these are not appropriate for this model because, in the case of mixture models they assume that the material is a superimposed continua of two materials where each point within the material is occupied simultaneously by a material point of each phase and in the case of biphasic models such as poroelasticity, they assume that the mechanical properties are dominated by factors such as fluid flux and permeability. Mixture models could potentially be incorporated into a model of the type proposed here to describe the mechanics of the cytoplasm but to use them to describe the mechanics of the entire system would be to neglect the geometric arrangements that we have shown to play a crucial role the mechanics of cells. Poroelastic models, however, are not appropriate for use in a model of single vascular smooth muscle cell mechanics because although there is fluid flow within the cell during deformation, previous

unpublished studies in our lab have shown that deformation of VSMCs does not result in fluid flux between the cell and its extracellular environment. This phenomenon may not be the case for all cell types, however, and therefore should be further investigated to determine the applicability of poroelastic models across all cell types.

Finally, the most important limitation of a finite element model of this type is that cells are living systems capable of active responses which this type of model cannot replicate. This limitation, however, does have benefits. Primarily, the lack of active responses in the model can provide crucial data to aid in better understanding the field of mechanotransduction. If we are one day able to eliminate the assumptions listed above to improve the accuracy of the model to the point that we are entirely confident in its ability to model the inactive mechanical responses of cells, we may then be able to use the model to better distinguish the difference between the active and inactive responses of cells. Such an understanding would potentially have many far-reaching effects on the field of drug discovery where researchers would be better able to target the appropriate mechanisms to elicit the desired responses for new pharmaceutical therapeutics. It would also potentially have consequences for the fields of tissue engineering and regenerative medicine, where mechanical stimuli at the cellular level are critical toward directing tissue development and remodeling.

6.4. CONCLUSIONS AND FUTURE WORK

The inverse finite element model presented in this study represents an important step toward the ability to use finite element analysis for accurately modeling biological cells

and provides a solid foundation from which to build an even more representative model. It is capable of both construction of entirely representative geometries produced in a completely automated manner and validation of its results using experimental data taken from the same cell that was modeled on the same day that the images of the cell were obtained. In future studies, we plan to incorporate viscoelastic material properties based on AFM stress relaxation data.

Future studies will also incorporate multiphysics modeling approaches. MSC.Software offers a wide variety of computer aided engineering (CAE) modeling software packages that can work in conjunction with Marc. XFlow is a particle-based computational fluid dynamics (CFD) software package that could conceivably be used to model protein movement inside a cell during deformation. Adams is claimed by MSC to be the most widely used multibody dynamics and motion analysis software in the world and could conceivably be used to model motion of cytoskeletal networks due to applied strains. SimXpert is an umbrella software that ties the various MSC software packages together as a multiphysics platform. Pairing of Marc, Adams, and XFlow could one day potentially lead to the development of models capable of reproducing complex passive cellular behavior such as the tensegrity dynamics observed during cytoskeletal fiber severing experiments [18] or even active cell responses such as cell migration.

The work presented in the current study represents an important step toward the ability to use finite element models to accurately predict the mechanical behavior of biological cells and provides a solid foundation from which to build even more representative models. Such models could potentially be utilized to elucidate the

mechanisms of mechanotransduction or even increase the speed and decrease the cost of

drug development, tissue engineering, and regenerative medicine therapies, thereby

possibly increasing the quality and longevity of millions of lives across the current and

future eras of modern medicine.

6.5. REFERENCES

1. Ingber, D.E., *Mechanobiology and diseases of mechanotransduction.* Annals of Medicine, 2003. 35(8): p. 564-577.

2. Slomka, N. and A. Gefen, *Confocal microscopy-based three-dimensional cell-specific modeling for large deformation analyses in cellular mechanics.* Journal of Biomechanics, 2010. 43(9): p. 1806-1816.

3. Lammi, M.J. *Current perspectives on cartilage and chondrocyte mechanobiology*. 2004. Ios Press.

4. Li, C. and Q. Xu, *Mechanical stress-initiated signal transduction in vascular smooth muscle cells in vitro and in vivo.* Cellular Signalling, 2007. 19(5): p. 881-891.

5. Li, T., *A mechanics model of microtubule buckling in living cells.* Journal of Biomechanics, 2008. 41(8): p. 1722-1729.

6. Suresh, S., *Biomechanics and biophysics of cancer cells.* Acta Materialia, 2007. 55(12): p. 3989-4014.

7. *When f =/= Ku*, MSC.Software, Editor 2009. p. 2-11.

8. Peeters, E.A.G., et al., *Mechanical and failure properties of single attached cells under compression.* Journal of Biomechanics, 2005. 38(8): p. 1685-1693.

9. Unnikrishnan, G.U., V.U. Unnikirishnan, and J.N. Reddy, *Constitutive material modeling of cell: a micromechanics approach.* Journal of Biomechanical Engineering-Transactions of the Asme, 2007. 129(3): p. 315-323.

10. Dailey, H.L., et al., *Image-based finite element modeling of alveolar epithelial cell injury during airway reopening.* Journal of Applied Physiology, 2009. 106(1): p. 221-232.

11.   Buerke, M., et al., *Intramural delivery of Sirolimus prevents vascular remodeling following balloon injury.* Biochimica et Biophysica Acta (BBA) - Proteins & Proteomics, 2007. 1774(1): p. 5-15.

12.   Mofrad, M.R.K. and R.D. Kamm, eds. *Cytoskeletal Mechanics*. 2006, Cambridge University Press: New York, NY. 244.

13.   Pullarkat, P.A., P.A. Fernández, and A. Ott, *Rheological properties of the Eukaryotic cell cytoskeleton.* Physics Reports, 2007. 449(1-3): p. 29-53.

14.   Hemmer J.D., D.D., Vertegel A., Langan E. III, LaBerge M., *Effects of serum deprivation on the mechanical properties of adherent vascular smooth muscle cells.* Proc Inst Mech Eng [H], 2008. 222(5): p. 761-72.

15.   Deguchi, S., T. Ohashi, and M. Sato, *Tensile properties of single stress fibers isolated from cultured vascular smooth muscle cells.* Journal of Biomechanics, 2006. 39(14): p. 2603-2610.

16.   Athanasiou, K.A., et al., *Development of the cytodetachment technique to quantify mechanical adhesiveness of the single cell.* Biomaterials, 1999. 20(23-24): p. 2405-2415.

17.   Park, C.Y., et al., *Mapping the cytoskeletal prestress.* American Journal of Physiology-Cell Physiology, 2010. 298(5): p. C1245-C1252.

18.   Luo, Y., et al., *A multi-modular tensegrity model of an actin stress fiber.* Journal of Biomechanics, 2008. In Press, Corrected Proof.

CHAPTER 7

CONCLUSIONS AND RECOMMENDATIONS FOR FUTURE WORK

7.1. CONCLUSIONS

The present research is motivated by the desire to further our understanding of the ætiology of many diseases through the ability to model the mechanical responses of cells of physical stimuli. The wide variety of diseases whose ætiology or clinical presentation are either known or suspected to be related to abnormal cellular mechanics, alteration of cellular mechanotransduction processes, or changes in tissue structure are primary motivators, and the ability to predict the mechanical behavior of cells in response to pathological conditions and medical treatments may be critical to prevention and treatment of many of these diseases.

It was shown in Chapter 4 that the ability to model the mechanical behavior of cells using finite element analysis is dependent upon incorporating appropriate geometries, as results were shown to change when the only parameters that were varied were geometrical. Chapter 5 presented a novel, fully automated image analysis algorithm which utilizes image segmentation techniques for the reconstruction of 3D geometries for the periphery and nucleus of a cell together with a linear programming approach to optimize the superposition of cytoskeletal fibers, for the generation of a representative actin stress fiber network of the cell that can all be incorporated into finite element models for structural analysis. A 3D inverse finite element model is presented in Chapter

6 which is the first model of its kind that utilizes representative cytoskeletal structural components in addition to accurate cell boundary and nucleus all constructed automatically from confocal images of actual cells. This model is also the first of its kind to be validated directly against experimental data taken from the exact cells used in the model within minutes of their imaging. The model shows good agreement with the experimental data up to 500 nm of indentation by a 5 μm diameter spherical AFM probe.

The work presented here represents an important step toward the ability to use finite element models to accurately predict the mechanical behavior of biological cells and provides a solid foundation from which to build even more representative models. Such models could potentially be incorporated into multiscale models for use in elucidating the mechanisms of mechanotransduction as well as increasing the speed and decreasing the cost of both drug development and tissue engineering/regenerative medicine therapies, thereby possibly increasing the quality and longevity of millions of lives throughout the current and future eras of modern medicine.

7.2. RECOMMENDATIONS FOR FUTURE WORK

1. **Expand the model to different cell types.** The techniques presented in the current work show great promise for the establishment of a useful finite element model to predict the mechanical responses of vascular smooth muscle cells, however VSMCs are the only cell type studied here. We predict that the techniques presented here will be applicable across a wide variety of cell types, so it is recommended that future studies focus on many other types of cells.

2. **<u>Expand the model to different physical experiments.</u>** As shown in Chapter 3, there are many techniques that can be used for mechanical characterization of cells, however only one (AFM) was used for these studies. We predict that the techniques presented here will translate across many other types of physical experiments It is recommended, therefore, that future studies utilize additional mechanical characterization techniques. Suggested techniques include Shear Flow, Micropost Arrays, Whole-Cell Compression, Cell-Stretching, and Magnetocytometry.

3. **<u>Live Cell Actin Imaging.</u>** G-actin monomers are able to polymerize into 100 nm of f-actin in 1.5 ms [1], yet the static and dynamic mechanical tests performed in this work ranged from 1 to 120 seconds and fixing of those cells was performed up to 5 minutes after mechanical characterization. Therefore, it is unknown the degree of cytoskeletal rearrangement which takes place during mechanical characterization. Because of this, it is recommended that studies be performed in which mechanical characterization takes place on live cells which have had their cytoskeletal networks and nuclei fluorescently labeled. This will provide a better ability to reconstruct the actin stress fiber network of the cell as it is at the exact moment of testing and a better understanding of how the cells respond to mechanical stimuli. Live cell staining could be achieved using gene transfection, which is expensive and time-consuming or alternatively, studies have shown promise in using established inkjet printing techniques to permeabolize cell membranes enough to allow for fluorescently-labeled antibodies to enter the cytosol.

4. **Integrate Viscoelasticity.** The mechanical behavior of VSMCs is well characterized by the Generalized Maxwell model of viscoelasticity. Finite element models which can successfully incorporate this model of viscoelasticity are expected to be more accurate than the model presented in Chapter 6.

5. **Generate Average Phenotype Geometries.** The image analysis techniques presented in Chapter 5 could conceivably be expanded to the analysis of multiple confocal image stacks of multiple cells at a time. If those images could be merged into an "average" geometry, it would then be possible to generate cell geometries that were capable of statistically representing an entire phenotype. Such geometries would be more meaningful for predictive finite element modeling techniques than the inverse finite element modeling technique presented in Chapter 6. One long-term result of this work could be the generation of a cell database, not unlike the Protein Database, from which users around the world could download any of the cell types relevant to their work.

6. **Incorporation of Additional Structural Components.** The actin stress fiber network is just one of many structural networks inside and outside the cell that affect its mechanical behavior. Future models would potentially benefit from the incorporation of other cytoskeletal features such as microtubules, integrins, and intermediate filaments.

7. **Expand the Model to a Multiphysics Platform.** MSC.Software is one of the 10 oldest software companies on the planet. As such, they offer a wide variety of computer aided engineering (CAE) modeling software. XFlow is a visually exciting

particle-based computational fluid dynamics (CFD) software package that could

conceivably be used to model protein movement inside a cell during deformation.

Adams is claimed by MSC to be the most widely used multibody dynamics and

motion analysis software in the world. Adams could conceivably be used to model

motion of cytoskeletal networks. SimXpert is an umbrella software that ties the

various MSC software packages together as a multiphysics platform. Pairing of Marc,

Adams, and XFlow could one day potentially lead to the development of models

capable of reproducing complex passive cellular behavior such as the tensegrity

dynamics observed during cytoskeletal fiber severing experiments [2] or even active

cell responses such as cell migration.

8. **<u>Integrate the Model into a Multiscale Model.</u>** The ultimate fulfillment of the work

presented in this dissertation would be its incorporation into a multiscale model,

leading to the ability to more easily tie macro-scale behaviors to nano-scale

phenomena. Such a multiscale model could potentially be used to increase the speed

and decrease the cost of drug development and tissue engineering/regenerative

medicine therapies, thereby possibly increasing the quality and longevity of millions

of lives over future eras of medicine.

7.3. REFERENCES

1.   Lee, K.-C. and A.J. Liu, New Proposed Mechanism of Actin-Polymerization-Driven Motility. Biophysical Journal, 2008. 95(10): p. 4529-4539.

2.   Luo, Y., et al., A multi-modular tensegrity model of an actin stress fiber. Journal of Biomechanics, 2008. In Press, Corrected Proof.

APPENDICES

APPENDIX A

IMAGE ANALYSIS MATLAB CODE

The MATLAB .m files used for image analysis are presented below in the order in which they are utilized. Notes for use are presented at the beginning of each section where appropriate.

A.1. reconstruct_whole_cell.m

NOTES

This function is the top-level function used for image analysis. All other functions presented in this appendix are called through this function. The function is called by typing "`reconstruct_whole_cell(id)`" in the MATLAB command window, where "`id`" is the identification number of the cell desired for reconstruction. All parameters required for analysis are given at the beginning of the file in the "`% INPUT PARAMETERS`" section.

MATLAB CODE

```
function reconstruct_whole_cell(id)

timecount = tic;

% Cell to visualize
%id = 1; %%[no need for this?] -- only useful if you run it by clicking
     ">"
%above, rather than from the matlab command prompt

% INPUT PARAMETERS
```

```matlab
patran_dir = 'c:\MSC.Work\Research\111024';  % don't add a \ to the
     end...
downsample = [0.1 0.1 .25]; % x y z downsampling -- reduce to coarsen
     mesh
inflation_factor = [1 1 1];  % just to make cell look a bit bigger than
     it is, ideally set to [1 1 1]

frad = 100e-3; % radius of actin fibers, in um
fcross = pi * frad^2; % cross-sectional area of actin fibers, in um^2
avg_fiber_len = 20; % for the fiber generation, in microns, generally
     set to ~minor axis width
generate_actin = 0; % set to 0 if we just want to generate meshes, but
     no actin
voxel_density = 5;  % skip by this many pixels to form lattice of
     voxels
num_potential_fibers = 10000; % delete fiber_cache_"id".txt if this
     changes
probe_speed = 0.5; % indenter speed, in um/s
probe_indent = 1; % depth of indentation into cell, in microns
fiber_sample_cutoff = 0.001; % score above which we keep fibers (range
     0..1)
%Nfibers = 0; % number of actin fibers to generate (used before
     implementation of cutoff)

% READ IN CELL IMAGE DATA AND SEGMENT NUCLEUS AND MAIN CELL BOUNDARY
[nucleus, actin, membrane, dims] = acquire_image_data(id);
disp(sprintf('Image stack has dimensions %d x %d x %d voxels',
     size(nucleus,1), size(nucleus,2), size(nucleus,3)));
[nfaces, nverts, nvoxels] = extract_nucleus(nucleus, downsample);
if size(nverts,1)==0
    disp('Error -- no nucleus segmented.  Maybe it got downsampled out
     of existence?');
    return;
end
disp(sprintf('Nucleus mesh has %d vertices and %d triangles',
     size(nverts,1), size(nfaces,1)));

[cfaces, cverts, cvoxels] = extract_cell_boundary(actin, membrane,
     nvoxels, downsample);
disp(sprintf('Cell boundary mesh has %d vertices and %d triangles',
     size(cverts,1), size(cfaces,1)));
disp(sprintf('Cell volume made up of %d total voxels',
     sum(sum(sum(cvoxels)))));

% TRANSLATE AND RESIZE COORDINATES TO APPROPRIATE DIMENSIONS AND MERGE
% NUCLEUS + CELL MESHES INTO COMBINED LIST
```

```matlab
rescale_factor = ones ./ (size(nucleus) .* downsample) .* dims .*
    inflation_factor;
cverts = cverts * diag(rescale_factor);
nverts = nverts * diag(rescale_factor);
translate_amt = min(cverts);
nverts = nverts - ones(size(nverts,1),3) * diag(translate_amt);
cverts = cverts - ones(size(cverts,1),3) * diag(translate_amt);
for i=1:size(cverts,1)
    if cverts(i,3) < 1.1 * rescale_factor(3);
        cverts(i,3) = 0;
    end
end
rescale_factor = rescale_factor .* downsample;

if generate_actin > 0

    % COMPUTE INTEGRINS AND ACTIN FIBERS
    [fibers, fverts] = compute_actin_fibers(id, cfaces, cverts, nfaces,
      nverts, num_potential_fibers);

    write_lp(id, cvoxels, nvoxels, actin, fibers, fverts,
      avg_fiber_len, rescale_factor, translate_amt, voxel_density);
    solve_lp(id);

    filename = sprintf('actin%d.sol', id);
    sol = load(filename);
else
    filename = sprintf('actin%d.sol', id);
    f = fopen(filename, 'r');
    if f < 0
        disp(sprintf('No fibers yet; cannot open %s', filename));
        sol = [];
        fverts = [];
    else
        disp(sprintf('Cached fiber solution was read from %s',
      filename));
        fclose (f);
        sol = load(filename);
        filename = sprintf('fiber_coordinates_%d.txt', id);
        fverts = load(filename);
    end
end

write_stl('nucleus.stl', nfaces, nverts);
write_stl('cell.stl', cfaces, cverts);

%sampled_fibers = sample_actin_fibers(sol, Nfibers);
```

```matlab
sampled_fibers = sample_actin_fibers_bycutoff(sol, ...
    fiber_sample_cutoff);

volmesh_size = dims(1) / 256; % Volume mesh edge length roughly 2
    pixels wide
write_patran_session(patran_dir, nfaces, nverts, cfaces, cverts, ...
    fverts, volmesh_size, sampled_fibers, probe_speed, probe_indent, ...
    id, fcross, frad);

% DRAW EVERYTHING
cell_3d_vis(nfaces, nverts, fverts, cfaces, cverts, sampled_fibers, 1);
h = get(1, 'CurrentAxes'); t = get(h, 'CameraTarget');
set(h, 'CameraPosition', t + [0 0 1000]);
set(h, 'CameraUpVector', [-1 0 0]);
set(h, 'View', [89.999999 90]);
set(h, 'View', [90 90]);
set(1,'Position',[50 50 600 900]);
p = get(1,'Position');
p2 = get(h, 'Position');
aspect = get(h, 'PlotBoxAspectRatio');
ysize = p(3) * p2(3) * aspect(1) / aspect(2);

cell_3d_vis(nfaces, nverts, fverts, cfaces, cverts, sampled_fibers, 4);
h = get(4, 'CurrentAxes'); t = get(h, 'CameraTarget');
set(h, 'CameraPosition', t + [1000 0 0]);
set(h, 'CameraUpVector', [0 0 1]);
p = get(4, 'Position');
p(3) = 600;
set(4,'Position',p);

cell_3d_vis(nfaces, nverts, fverts, cfaces, cverts, sampled_fibers, 5);
h = get(5, 'CurrentAxes'); t = get(h, 'CameraTarget');
set(h, 'CameraPosition', t + [0 1000 0]);
set(h, 'CameraUpVector', [-1 0 0]);
p = get(5, 'Position');
p(4) = 900;
set(5,'Position',p);
p = get(5,'Position');
p2 = get(h, 'Position');
p2(4) = ysize / p(4);
set(h, 'Position', p2);
set(h, 'YTickLabel', []);
set(h, 'YTick', []);

print_cell(sprintf('figure_%da.png', id), 6, 8, 1);
print_cell(sprintf('figure_%db.png', id), 6, 8, 4);
print_cell(sprintf('figure_%dc.png', id), 6, 7, 5);
```

```
disp(sprintf('Finished generating Cell%d', id));
toc(timecount);
end
```

A.2. acquire_image_data.m

NOTES

This file accomplishes two purposes: 1) assign an identification number (`id`) to each cell, and 2) assign the stack of images that define that cell (through use of the term, `level`). For ease of use, each image stack is given its own subfolder inside the base folder, `base_dir`. The file is constructed in such a way that the nucleus is assigned based on one set of images and the actin and membrane are assigned based another set of images, however it could be easily modified to accommodate different cellular components (e.g. incorporation of microtubules, integrins, or a separate image channel for the plasma membrane) if desired.

MATLAB CODE

```
function [nucleus, actin, membrane, dims] = acquire_image_data(id)

disp(sprintf('Reading image stack'));

base_dir = 'C:\Users\finou\Documents\Scott\Research\Image
    Conversion\Images for Conversion';

if id==1
    image_downsample = 1;
    for level = 25:70
```

173

```matlab
        filename = sprintf('%s\\cell_001\\contractile vsmc
    40x_1x2.68x_107xtot_focused separatedz%03dc1.tif', base_dir,
    level);
        I = imresize(imread(filename),image_downsample);
        nucleus(:,:,71-level) = double(I(:,:,1) + I(:,:,2) + I(:,:,3))
    / 256 / 3;
        filename = sprintf('%s\\cell_001\\contractile vsmc
    40x_1x2.68x_107xtot_focused separatedz%03dc2.tif', base_dir,
    level);
        I = imresize(imread(filename),image_downsample);
        actin(:,:,71-level) = double(I(:,:,1) + I(:,:,2) + I(:,:,3)) /
    256 / 3;
        membrane(:,:,71-level) = double(I(:,:,1) + I(:,:,2) + I(:,:,3))
    / 256 / 3;
        dims = [118 118 0.15*size(nucleus,3)];
    end
end

if id==2
    image_downsample = 1;
    for level = 1:28
        filename = sprintf('%s\\cell_002\\STW01-02 100414 Synthetic
    VSMC 100x 001%02d.jpg', base_dir, level * 3);
        I = imresize(imread(filename),image_downsample);
        nucleus(:,:,level) = double(I) / 256;
        filename = sprintf('%s\\cell_002\\STW01-02 100414 Synthetic
    VSMC 100x 001%02d.jpg', base_dir, level * 3 - 2);
        I = imresize(imread(filename),image_downsample);
        actin(:,:,level) = double(I) / 256;
        membrane(:,:,level) = double(I) / 256;
        dims = [82 82 0.20*size(nucleus,3)];
    end
end

if id==3
    for level = 1:36
        filename = sprintf('%s\\cell_003\\STW01-03 Synthetic &
    Contractile VSMCs 60x 001 Deconvolved%03d.jpg', base_dir, level *
    3);
        I = imresize(imread(filename),image_downsample);
        nucleus(:,:,level) = double(I) / 256;
        filename = sprintf('%s\\cell_003\\STW01-03 Synthetic &
    Contractile VSMCs 60x 001 Deconvolved%03d.jpg', base_dir, level *
    3 - 2);
        I = imresize(imread(filename),image_downsample);
        actin(:,:,level) = double(I) / 256;
```

```matlab
        filename = sprintf('%s\\cell_003\\STW01-03 Synthetic &
      Contractile VSMCs 60x 001 Deconvolved%03d.jpg', base_dir, level *
        3 - 1);
          I = imresize(imread(filename),image_downsample);
          membrane(:,:,level) = double(I) / 256;
          dims = [137 137 0.20*size(nucleus,3)];
      end
  end

  if id==4
      image_downsample = 1;
      for level = 1:36
          filename =
        sprintf('%s\\cell_004\\Deconvolved\\Cell4_DAPI_Deconvolved_%03d.T
        IF', base_dir, (level+54) + 100);
          I = imresize(imread(filename),image_downsample);
          nucleus(:,:,level) = double(I) / 256;
          filename =
        sprintf('%s\\cell_004\\Deconvolved\\Cell4_FITC_Deconvolved_%03d.T
        IF', base_dir, (level+54) + 100);
          I = imresize(imread(filename),image_downsample);
          actin(:,:,level) = double(I) / 256;
          membrane(:,:,level) = double(I) / 256;
      end
      dims = [80 80 0.20*size(nucleus,3)];
  end

  if id==5
      image_downsample = 1;
      for level = 1:25
          filename = sprintf('%s\\cell_005\\20110911_Cell1_60X_w2Camera -
        FW- DAPI_Deconvolved%03d.TIF', base_dir, (level+108));
          I = imresize(imread(filename),image_downsample);
          nucleus(:,:,level) = double(I) / 256;
          filename = sprintf('%s\\cell_005\\20110911_Cell1_60X_w1Camera -
        FW- FITC_Deconvolved%03d.TIF', base_dir, (level+108));
          I = imresize(imread(filename),image_downsample);
          actin(:,:,level) = double(I) / 256;
          membrane(:,:,level) = double(I) / 256;
      end
      dims = [137 137 0.20*size(nucleus,3)];
  end

  if id==6
      image_downsample = 1;
      for level = 1:25
```

175

```matlab
        filename = sprintf('%s\\cell_006\\20110911_Cell2_60X_w2Camera -
    FW- DAPI_Deconvolved%03d.TIF', base_dir, (level+121));
        I = imresize(imread(filename),image_downsample);
        nucleus(:,:,level) = double(I) / 256;
        filename = sprintf('%s\\cell_006\\20110911_Cell2_60X_w1Camera -
    FW- FITC_Deconvolved%03d.TIF', base_dir, (level+121));
        I = imresize(imread(filename),image_downsample);
        actin(:,:,level) = double(I) / 256;
        membrane(:,:,level) = double(I) / 256;
    end
    dims = [137 137 0.20*size(nucleus,3)];
end

if id==7
    image_downsample = 1;
    for level = 1:23
        filename = sprintf('%s\\cell_007\\20111010_VSMC_S-
    _Cell1_60x_DAPI_Deconvolved%02d.TIF', base_dir, (level+17));
        I = imresize(imread(filename),image_downsample);
        nucleus(:,:,level) = double(I) / 256;
        filename = sprintf('%s\\cell_007\\20111010_VSMC_S-
    _Cell1_60x_FITC_Deconvolved%02d.TIF', base_dir, (level+17));
        I = imresize(imread(filename),image_downsample);
        actin(:,:,level) = double(I) / 256;
        membrane(:,:,level) = double(I) / 256;
    end
    dims = [137 137 0.20*size(nucleus,3)];
end

if id==8
    image_downsample = 1;
    for level = 1:19
        filename = sprintf('%s\\cell_008\\20111010_VSMC_S-
    _Cell2_60x_DAPI_Deconvolved%02d.TIF', base_dir, (level+30));
        I = imresize(imread(filename),image_downsample);
        nucleus(:,:,level) = double(I) / 256;
        filename = sprintf('%s\\cell_008\\20111010_VSMC_S-
    _Cell2_60x_FITC_Deconvolved%02d.TIF', base_dir, (level+30));
        I = imresize(imread(filename),image_downsample);
        actin(:,:,level) = double(I) / 256;
        membrane(:,:,level) = double(I) / 256;
    end
    dims = [137 137 0.20*size(nucleus,3)];
end

if id==9
    image_downsample = 1;
```

```matlab
    for level = 1:18
        filename = sprintf('%s\\cell_009\\20111010_VSMC_S-
    _Cell3_60x_DAPI_Deconvolved%02d.TIF', base_dir, (level+19));
        I = imresize(imread(filename),image_downsample);
        nucleus(:,:,level) = double(I) / 256;
        filename = sprintf('%s\\cell_009\\20111010_VSMC_S-
    _Cell3_60x_FITC_Deconvolved%02d.TIF', base_dir, (level+19));
        I = imresize(imread(filename),image_downsample);
        actin(:,:,level) = double(I) / 256;
        membrane(:,:,level) = double(I) / 256;
    end
    dims = [137 137 0.20*size(nucleus,3)];
end

if id==10
    image_downsample = 1;
    for level = 1:23
        filename = sprintf('%s\\cell_010\\20111010_VSMC_S-
    _Cell4_60x_DAPI_Deconvolved%02d.TIF', base_dir, (level+16));
        I = imresize(imread(filename),image_downsample);
        nucleus(:,:,level) = double(I) / 256;
        filename = sprintf('%s\\cell_010\\20111010_VSMC_S-
    _Cell4_60x_FITC_Deconvolved%02d.TIF', base_dir, (level+16));
        I = imresize(imread(filename),image_downsample);
        actin(:,:,level) = double(I) / 256;
        membrane(:,:,level) = double(I) / 256;
    end
    dims = [137 137 0.20*size(nucleus,3)];
end

if id==11
    image_downsample = 1;
    for level = 1:21
        filename = sprintf('%s\\cell_011\\20111010_VSMC_S-
    _Cell5_60x_DAPI_Deconvolved%02d.TIF', base_dir, (level+16));
        I = imresize(imread(filename),image_downsample);
        nucleus(:,:,level) = double(I) / 256;
        filename = sprintf('%s\\cell_011\\20111010_VSMC_S-
    _Cell5_60x_FITC_Deconvolved%02d.TIF', base_dir, (level+16));
        I = imresize(imread(filename),image_downsample);
        actin(:,:,level) = double(I) / 256;
        membrane(:,:,level) = double(I) / 256;
    end
    dims = [137 137 0.20*size(nucleus,3)];
end

if id==12
```

```matlab
    image_downsample = 1;
    for level = 1:23
        filename = sprintf('%s\\cell_012\\20111010_VSMC_S-
    _Cell6_60x_DAPI_Deconvolved%02d.TIF', base_dir, (level+16));
        I = imresize(imread(filename),image_downsample);
        nucleus(:,:,level) = double(I) / 256;
        filename = sprintf('%s\\cell_012\\20111010_VSMC_S-
    _Cell6_60x_FITC_Deconvolved%02d.TIF', base_dir, (level+16));
        I = imresize(imread(filename),image_downsample);
        actin(:,:,level) = double(I) / 256;
        membrane(:,:,level) = double(I) / 256;
    end
    dims = [137 137 0.20*size(nucleus,3)];
end

if id==13
    image_downsample = 1;
    for level = 1:21
        filename = sprintf('%s\\cell_013\\20111010_VSMC_S-
    _Cell7_60x_DAPI_Deconvolved%02d.TIF', base_dir, (level+20));
        I = imresize(imread(filename),image_downsample);
        nucleus(:,:,level) = double(I) / 256;
        filename = sprintf('%s\\cell_013\\20111010_VSMC_S-
    _Cell7_60x_FITC_Deconvolved%02d.TIF', base_dir, (level+20));
        I = imresize(imread(filename),image_downsample);
        actin(:,:,level) = double(I) / 256;
        membrane(:,:,level) = double(I) / 256;
    end
    dims = [137 137 0.20*size(nucleus,3)];
end

if id==14
    image_downsample = 1;
    for level = 1:22
        filename = sprintf('%s\\cell_014\\20111010_VSMC_S-
    _Cell8_60x_DAPI_Deconvolved%02d.TIF', base_dir, (level+20));
        I = imresize(imread(filename),image_downsample);
        nucleus(:,:,level) = double(I) / 256;
        filename = sprintf('%s\\cell_014\\20111010_VSMC_S-
    _Cell8_60x_FITC_Deconvolved%02d.TIF', base_dir, (level+20));
        I = imresize(imread(filename),image_downsample);
        actin(:,:,level) = double(I) / 256;
        membrane(:,:,level) = double(I) / 256;
    end
    dims = [137 137 0.20*size(nucleus,3)];
end
```

```matlab
% Add 5 blank z levels to the top
z_levels = size(nucleus,3);
for i = 1:5
    nucleus(:,:,z_levels+i) = zeros;
    actin(:,:,z_levels+i) = zeros;
    membrane(:,:,z_levels+i) = zeros;
end
dims(3) = dims(3) * (z_levels + 5) / z_levels;

for level=1:size(nucleus,3)
    nucleus(:,:,level) = nucleus(:,:,level)';
end
for level=1:size(actin,3)
    actin(:,:,level) = actin(:,:,level)';
end
for level=1:size(membrane,3)
    membrane(:,:,level) = membrane(:,:,level)';
end

end
```

A.3. extract_nucleus.m

NOTES

This file generates the mesh for the nucleus.

MATLAB CODE

```matlab
function [Faces, Vertices, Voxelmap] = extract_nucleus(nucleus,
      downsample)

disp(sprintf('Segmenting nucleus'));
[R, C, L] = size(nucleus); %R: Rows, C: Columns, L: Levels - 3D matrix


% EXTRACT IMAGE

% Segment based on simple thresholding
max_intensity = max(max(max(nucleus)));
min_intensity = min(min(min(nucleus)));
```

179

```matlab
threshold = min_intensity + 0.25 * (max_intensity - min_intensity);
      %cutoff pixel intensities at 25% (empirically chosen) of max
Voxelmap = nucleus > threshold;

% Dilate the image twice (hopefully closing boundary gaps)
Voxelmap = imdilate(Voxelmap, ones(3,3,3));
Voxelmap = imdilate(Voxelmap, ones(3,3,3));

% Fill interior gaps
Voxelmap = imfill(Voxelmap, 'holes');

% Remove connected components touching borders in x and y
mask = zeros(3,3,3); mask(:,:,2) = ones;
Voxelmap = imclearborder(Voxelmap, mask);

% Erode image to smooth out its boundary
Voxelmap([1 R],:,:) = zeros; %zero out top and bottom rows
Voxelmap(:,[1 C],:) = zeros; %zero out right and left columns
Voxelmap(:,:,[1 L]) = zeros; %zero out top and bottom levels - allows
      smoothing to work along borders
mask = ones(3,3,3); mask(1:2:3, 1:2:3, 1:2:3) = zeros; %diamond-shaped
      erosion element (all corners = 0)
Voxelmap = imerode(Voxelmap, mask);
Voxelmap = imerode(Voxelmap, mask);
Voxelmap = imerode(Voxelmap, mask);
Voxelmap = imerode(Voxelmap, mask);
Voxelmap = imerode(Voxelmap, mask);

% Find connected components and retain only the largest one
Voxelmap = retain_largest_component(Voxelmap);


% COMPUTE MESH OUTLINE

% smooth3 applies gaussian filter, takes everything > 0.5 to apply
      isosurface
new_dims = round(downsample .* size(Voxelmap));
temp = zeros(new_dims(1)+2, new_dims(2)+2, new_dims(3)+2);
temp(2:new_dims(1)+1,2:new_dims(2)+1,2:new_dims(3)+1) =
      smooth3(downsample_matrix(Voxelmap, new_dims));
fv = isosurface(temp, 0.1);
%fv = reducepatch(fv, 0.05, 'fast');
Faces = fv.faces; %list of image faces, n by 3, each row has indices
      (into fv.vertices) of points around a triangular face
Vertices = fv.vertices; %list of all points in mesh, one per row (n by
      3), each row x,y,z of one point
Vertices = Vertices - 1;
```

```
end
```

A.4. extract_cell_boundary.m

NOTES

This file generates the mesh for the cell boundary.

MATLAB CODE

```matlab
function [Faces, Vertices, Voxelmap] = extract_cell_boundary(actin,
      membrane, nvoxels, downsample)

disp(sprintf('Segmenting cell boundary'));
[R, C, L] = size(actin);

% FILL DOWNWARD
Voxelmap = actin + membrane;
Voxelmap = smooth3(Voxelmap); %gaussian smoothing
%fill in vertical holes by taking brightest point and filling with
      equal
%intensity downward (no overhangs)
for r=1:R
    for c=1:C
        for l=1:L
            Voxelmap(r,c,l) = max(max(max(Voxelmap(r,c,l:L))));
        end
    end
end

% EXTRACT IMAGE
% segment based on simple thresholding
max_intensity = max(max(max(Voxelmap)));
min_intensity = min(min(min(Voxelmap)));
threshold = min_intensity + 0.05 * (max_intensity - min_intensity);
Voxelmap = double(Voxelmap > threshold) + nvoxels - double(Voxelmap >
      threshold) .* nvoxels; %make sure nucleus is inside cell

% Dilate the image (hopefully closing boundary gaps)
Voxelmap = imdilate(Voxelmap, ones(3,3,3));
```

```matlab
add_room_at_top = zeros(3,3,3); add_room_at_top(2,2,2) = 1;
      add_room_at_top(2,2,3) = 1;
Voxelmap = imdilate(Voxelmap, add_room_at_top); Voxelmap = ...
      imdilate(Voxelmap, add_room_at_top);
Voxelmap = imdilate(Voxelmap, add_room_at_top); Voxelmap = ...
      imdilate(Voxelmap, add_room_at_top);


% Fill interior gaps
Voxelmap = imfill(Voxelmap, 'holes');
for i=1:L
    Voxelmap(:,:,i) = imfill(Voxelmap(:,:,i), 'holes');
end

% Remove connected components touching borders in x and y
mask = zeros(3,3,3); mask(:,:,2) = ones;
Voxelmap = imclearborder(Voxelmap, mask);

% Erode image to smooth out its boundary
Voxelmap([1 R],:,:) = zeros;
Voxelmap(:,[1 C],:) = zeros;
Voxelmap(:,:,[1 L]) = zeros;
mask = ones(3,3,3); mask(1:2:3, 1:2:3, 1) = zeros;
Voxelmap = imerode(Voxelmap, mask);
Voxelmap = imerode(Voxelmap, mask);

% Find connected components and retain only the largest one
Voxelmap = retain_largest_component(Voxelmap > 0);

% COMPUTE MESH OUTLINE
new_dims = round(downsample .* size(Voxelmap));
temp = zeros(new_dims(1)+2, new_dims(2)+2, new_dims(3)+2);
temp(2:new_dims(1)+1,2:new_dims(2)+1,2:new_dims(3)+1) = ...
      smooth3(downsample_matrix(Voxelmap, new_dims));
[Faces Vertices] = isosurface(temp, 0.1);
Vertices = Vertices - 1;


end
```

A.5. compute_actin_fibers.m

This file generates the mesh for the actin fibers.

MATLAB CODE

```matlab
function [fibers, fverts] = compute_actin_fibers(id, cfaces, cverts,
      nfaces, nverts, num_potential_fibers)

filename = sprintf('fiber_cache_%d.txt', id);
fid = fopen (filename, 'r');
if fid ~= -1
    fclose (fid);
    disp(sprintf('Reading cached actin fiber matrix from %s',
      filename));
    fibers = load(filename);
    filename = sprintf('fiber_coordinates_%d.txt', id);
    fverts = load(filename);
    disp(sprintf('Matrix contains %d geometrically feasible fibers',
      sum(sum(fibers))));
    return;
end

averts = [cverts; nverts];
afaces = [cfaces; nfaces+size(cverts,1)];

fprintf('Computing all potential actin fibers (this takes a
      while...)\n');
tic;
N = size(cverts,1);
fibers = zeros(N,N);

nucleus_centroid = mean(nverts);

fprintf ('        ');
for v1=1:N
    fprintf ('\b\b\b\b\b\b%5.1f%%', v1*100 / N);
    for v2=v1+1:N
        if rand < num_potential_fibers / (N*(N-1)/2),
```

```
            fibers(v1,v2) = actin_fiber_score(v1, v2, afaces, averts,
    nucleus_centroid);
        end
    end
end
fprintf ('\b\b\b\b\b\b%.1f%%\n', 100);

disp(sprintf('Saving cache of actin fiber matrix in %s', filename));
save(filename,'fibers','-ascii');

filename = sprintf('fiber_coordinates_%d.txt', id);
disp(sprintf('Saving cache of actin fiber endpoint coordinates in %s',
      filename));
save(filename,'cverts','-ascii');
fverts = cverts;

toc

end
```

A.6. write_lp.m

NOTES

This file generates the linear program that is used to compute the actin fiber scores.

MATLAB CODE

```
function write_lp(id, cvoxels, nvoxels, actin, fibers, fverts,
      avg_fiber_len, rescale_factor, translate_amt, voxel_density)

% Parameters
Ndirs = 8;              % number of (2d) directions at each voxel

disp('Writing humongous linear program');

% Compute sampled voxel grid
num_voxels = 0;
vox_i = [];
vox_j = [];
vox_k = [];
```

```matlab
vox_d = [];
vox_m = [];
tic

% set up the colormap for a figure
function set_colormap(fig_number, reds, greens, blues)
    cmap = zeros(256,3);
    cmap(:,1) = reds;
    cmap(:,2) = greens;
    cmap(:,3) = blues;
    set(fig_number, 'Colormap', cmap);
end


for k=1:voxel_density:size(cvoxels,3)
    for i=1:voxel_density:size(cvoxels,1)
        for j=1:voxel_density:size(cvoxels,2)
            if cvoxels(i,j,k) - nvoxels(i,j,k) > 0,
                I = 0;
                for d=0:Ndirs-1,
                    num_voxels = num_voxels + 1;
                    vox_i(num_voxels) = i;
                    vox_j(num_voxels) = j;
                    vox_k(num_voxels) = k;
                    vox_d(num_voxels) = d;
                    %First two lines are the "eye candy" version:
                    %[vox_m(num_voxels), I2] =
    measure_directional_voxel_withgraphics(actin(:,:,k), i, j, d,
    Ndirs);
                    %I = I + I2;
                    %Following one line is for no "eye candy"
                    vox_m(num_voxels) =
    measure_directional_voxel(actin(:,:,k), i, j, d, Ndirs);
                end
                %Following 4 lines are for "eye candy" version
                %figure(3);
                %bw_color_curve = linspace(0,1,256) .^ 0.5;  % add
    small amount of gain
                %set_colormap(3, 0*bw_color_curve, bw_color_curve,
    0*bw_color_curve);
                %imagesc(I);
            end
        end
    end
end
toc
```

```matlab
disp(sprintf('Subsampled voxel grid for LP has %d voxels * %d
        directions = %d total dvoxels', num_voxels / Ndirs, Ndirs,
        num_voxels));

filename = sprintf('actin%d.lp', id);
fid = fopen(filename, 'w');
if fid < 0,
    disp(sprintf('Error opening file %s for writing', filename));
    return;
end

fprintf (fid, 'Minimize ');
for i=1:num_voxels
    if i>1, fprintf (fid,'+'); end
    fprintf (fid, 'z%d', i);
end
fprintf (fid, '\n');

fprintf (fid, 'Such that\n');
for i=1:num_voxels
    fprintf (fid, '-y%d - z%d <= -%.4f\n', i, i, vox_m(i));
    fprintf (fid, 'y%d - z%d <= %.4f\n', i, i, vox_m(i));
end

tic;
fimage = 0*actin;
num_fibers = sum(sum(fibers));
coeffs = sparse(num_fibers, num_voxels);
f = 1;
fprintf ('        ');
for i=1:size(fibers,1)
    for j=1:size(fibers,2)
        if fibers(i,j)>0
            fprintf ('\b\b\b\b\b\b%5.1f%%', 100 * f / num_fibers);
            p1 = (fverts(i,:)+translate_amt)./rescale_factor;
            p2 = (fverts(j,:)+translate_amt)./rescale_factor;
            tmp = p1(2); p1(2) = p1(1); p1(1) = tmp;
            tmp = p2(2); p2(2) = p2(1); p2(1) = tmp;
            [I,J,K,vals] = draw_one_actin(p1, p2);
            for r=1:length(I)
                if I(r)>=1 && I(r)<=size(fimage,1) && J(r)>=1 &&
    J(r)<=size(fimage,2) && K(r)>=1 && K(r)<=size(fimage,3),
                    fimage(I(r),J(r),K(r)) = vals(r);
                end
            end
            for v=1:num_voxels
```

```matlab
                    if dist_pt_to_segment([vox_i(v) vox_j(v) vox_k(v)], p1,
        p2) < 8
                        coeff =
        measure_directional_voxel(fimage(:,:,vox_k(v)), vox_i(v),
        vox_j(v), vox_d(v), Ndirs);
                        if coeff > 0.001, coeffs(f, v) = coeff * 1000; end
                    end
                end
                for r=1:length(I)
                    if I(r)>=1 && I(r)<=size(fimage,1) && J(r)>=1 &&
        J(r)<=size(fimage,2) && K(r)>=1 && K(r)<=size(fimage,3),
                        fimage(I(r),J(r),K(r)) = 0;
                    end
                end
                f = f + 1;
            end
        end
end
fprintf ('\b\b\b\b\b\b%5.1f%%\n', 100);
toc

[fibers_i, fibers_j] = find(fibers);
for v=1:num_voxels
    fprintf (fid, '-y%d', v);
    f = 1;
    [I, J, vals] = find(coeffs(:,v));
    k = 1;
    for r=1:length(fibers_i)
        i = fibers_i(r);
        j = fibers_j(r);
        if k<=length(I)
            if I(k)==f
                fprintf (fid, '+%.3fx%dx%d', vals(k), i, j);
                k=k+1;
            end
        end
        f = f + 1;
    end
    fprintf (fid, ' = 0\n');
end

first = 1;
for i=1:size(fibers,1)
    for j=1:size(fibers,2)
        if fibers(i,j)>0
            L = norm(fverts(i,:) - fverts(j,:));
            if first==0 && L-avg_fiber_len>=0, fprintf(fid,'+'); end
```

187

```matlab
            first = 0;
            fprintf (fid,'%.3fx%dx%d',L-avg_fiber_len, i, j);
        end
    end
end
fprintf (fid, ' >= 0\n');

fprintf (fid, 'Bounds\n');
for i=1:size(fibers,1)
    for j=1:size(fibers,2)
        if fibers(i,j)>0
            fprintf (fid, ' 0 <= x%dx%d <= 1\n', i, j);
        end
    end
end

fprintf (fid, 'End\n');

fclose (fid);

end
```

A.7. solve_lp.m

NOTES

This file solves the linear program and computes the actin fiber scores.

MATLAB CODE

```matlab
function solve_lp(id)

f = fopen ('run_cplex.txt', 'w');
fprintf (f, 'read actin%d.lp\n', id);
fprintf (f, 'opt\n', id);
fprintf (f, 'disp sol var x*\n', id);
fprintf (f, 'quit\n', id);
fclose (f);

disp('Running CPLEX now...');
```

```
cmd = sprintf ('cplex < run_cplex.txt | grep "^x" | tr "x" " " >
      actin%d.sol', id);
system(cmd);
disp('Finished running CPLEX');

end
```

A.8. write_stl.m

NOTES

This file generates a .stl mesh for the nucleus and cell boundary. STL files are simple

mesh files of 3 node triangles and are a universal type of mesh file and are therefore

useful for testing a mesh in a new computer aided engineering (CAE) software or for

printing on a 3D rapid prototyping printer.

MATLAB CODE

```
function write_stl(filename, faces, verts)

f = fopen(filename, 'w');

fprintf (f, 'solid %s\n', filename);

for i=1:size(faces,1)
    fprintf (f, ' facet normal 0.0 0.0 0.0\n');
    fprintf (f, '  outer loop\n');
    v1 = faces(i,1);
    v2 = faces(i,2);
    v3 = faces(i,3);
    fprintf (f, '   vertex %.1f %.1f %.1f\n', verts(v1,1), verts(v1,2),
      verts(v1,3));
    fprintf (f, '   vertex %.1f %.1f %.1f\n', verts(v2,1), verts(v2,2),
      verts(v2,3));
    fprintf (f, '   vertex %.1f %.1f %.1f\n', verts(v3,1), verts(v3,2),
      verts(v3,3));
    fprintf (f, '  endloop\n');
    fprintf (f, ' endfacet\n');
```

```
end

fprintf (f, 'endsolid\n');

fclose (f);
```

A.9. sample_actin_fibers_bycutoff.m

NOTES

This file samples all generated actin fibers and assigns only those fibers that are

greater than the cutoff value, `cutoff` (assigned in reconstruct_whole_cell.m), to the

model.

MATLAB CODE

```
function s = sample_actin_fibers_bycutoff(all_fibers, cutoff)

s = [];
if size(all_fibers,1) > 0
    s = all_fibers(find(all_fibers(:,3)>=cutoff),:);
    disp(sprintf('Selected %d actin fibers (with scores at least %.4f)
      from %d in total distribution', size(s,1), cutoff,
      size(all_fibers,1)));
end

end
```

A.10. sample_actin_fibers.m

NOTES

This file samples all generated actin fibers and randomly assigns a specific number of

fibers, `Nfibers` (assigned in reconstruct_whole_cell.m), to the model from the

probabilistic distribution of their fiber scores. By selecting fibers in this manner, the

fibers are weighted so that those with higher scores are more likely to be chosen. This

code was not used for the final analysis, but rather for studies where a specific number of

fibers were desired for model validation purposes.

MATLAB CODE

```matlab
function s = sample_actin_fibers(all_fibers, Nfibers)

N = size(all_fibers,1);

if Nfibers > N,
    disp(sprintf('Warning: %d fibers requested, when only %d exist to
      sample from!', Nfibers, N));
    s = all_fibers;
    return;
end

x = zeros(N,1);

for i=1:Nfibers
    while 0<1
        r = rand * sum(all_fibers(:,3));
        j = 1;
        while 0<1
            r = r - all_fibers(j, 3);
            if r < 0, break; end
            j = j + 1;
        end
        if x(j) == 0, break; end
    end
    x(j) = 1;
end

s = all_fibers(find(x),:);

disp(sprintf('Sampled %d actin fibers from %d in total distribution',
      Nfibers, N));

end
```

A.11. write_patran_session.m

This file generates a session file (.ses) that is read by Patran to import the meshes generated in MATLAB into the finite element software. This file organizes meshes into groups that can be used to easily select individual components of the cell. It also defines linear elastic material properties for the actin, cytoplasm, and nucleus and assigns those properties to the actin fibers. Material properties are not automatically assigned to the cytoplasm and nucleus due to the unpredictable nature of the way Patran converts their 2D mesh outlines into 3D mesh solids. This file also automatically generates the geometry for the AFM probe and places it 0.25 μm above the highest node of the cell boundary as well as defining the parameters for movement of the AFM probe. Finally, this file sets up the analysis parameters (solver type, number of increments, analytical time, adaptive meshing, etc.) used in the model. Each of these parameters may be changed to fit various analysis types either in Patran or in this file, should such changes be desired.

MATLAB CODE

```matlab
function write_patran_session(patran_dir, nfaces, nverts, cfaces,
    cverts, fverts, volmesh_size, fibers, probe_speed, probe_indent,
    id, fcross, frad)

filename = sprintf('%s\\build_cell%d.ses', patran_dir, id);
f = fopen(filename, 'w');

%% Initial Setup
% Header stuff
```

```matlab
fprintf (f, 'uil_file_new.go(
      "C:\\MSC.Software\\Patran_x64\\20102\\md_template.db",
      "%s\\Cell%d.db" )\n', patran_dir, id);
fprintf (f, 'set_current_dir( "%s" )\n', patran_dir);
fprintf (f, 'uil_pref_analysis.set_analysis_preference( "MSC.Marc",
      "Structural", ".dat",  ".t16", "No Mapping" )\n');
fprintf (f, 'ui_exec_function( "mesh_seed_display_mgr", "init" )\n');

% Isometric View
fprintf (f, 'ga_view_aa_set( -67., 0., -34. )\n');

% Increase Node Size
fprintf (f, 'node_size( 9 )\n');

% Create all groups
fprintf (f, 'ga_group_create( "nimport" )\n');
fprintf (f, 'ga_group_create( "cimport" )\n');
fprintf (f, 'ga_group_create( "cimport_base" )\n');
fprintf (f, 'ga_group_create( "AFMprobe" )\n');
fprintf (f, 'ga_group_create( "ntet" )\n');
fprintf (f, 'ga_group_create( "ctet" )\n');
fprintf (f, 'ga_group_create( "actin" )\n');

%% Properties (Part 1/3)
%%% Isotropic
%%%%% Actin
fprintf (f, 'material.create( "Analysis code ID", 20, "Analysis type
      ID", 1, "actin_mat", @\n');
fprintf (f, '0, "Date: 23-Aug-11         Time: 13:39:16",
      "Isotropic", 1, @\n');
fprintf (f, '"Directionality", 1, "Linearity", 1, "Homogeneous", 0,
      "Elastic", 1, @\n');
fprintf (f, '"ModelOptions & IDs", ["Entered Values", "", "", "", ""],
      [139, 0, 0, 0, 0], @\n');
fprintf (f, '"Active Flag", 1, "Create", 10, "External Flag", FALSE,
      "Property IDs", @\n');
fprintf (f, '["Elastic Modulus", "Poisson Ratio"], [2, 5, 0], "Property
      Values", @\n');
fprintf (f, '["1.9e3", "0.49", ""] )\n');
%%%%% Nucleus
fprintf (f, 'material.create( "Analysis code ID", 20, "Analysis type
      ID", 1, "nucleus_mat", @\n');
fprintf (f, '0, "Date: 23-Aug-11         Time: 13:39:16",
      "Isotropic", 1, @\n');
fprintf (f, '"Directionality", 1, "Linearity", 1, "Homogeneous", 0,
      "Elastic", 1, "Model @\n');
```

```
fprintf (f, 'Options & IDs", ["Entered Values", "", "", "", ""], [139,
        0, 0, 0, 0], "Active @\n');
fprintf (f, 'Flag", 1, "Create", 10, "External Flag", FALSE, "Property
        IDs", ["Elastic @\n');
fprintf (f, 'Modulus", "Poisson Ratio"], [2, 5, 0], "Property Values",
        ["3.3e-3", "0.49", ""] )\n');
%%%%% Cytoplasm
fprintf (f, 'material.create( "Analysis code ID", 20, "Analysis type
        ID", 1, "cytoplasm_mat"@\n');
fprintf (f, ', 0, "Date: 23-Aug-11          Time: 13:39:16",
        "Isotropic", 1, @\n');
fprintf (f, '"Directionality", 1, "Linearity", 1, "Homogeneous", 0,
        "Elastic", 1, "Model @\n');
fprintf (f, 'Options & IDs", ["Entered Values", "", "", "", ""], [139,
        0, 0, 0, 0], "Active @\n');
fprintf (f, 'Flag", 1, "Create", 10, "External Flag", FALSE, "Property
        IDs", ["Elastic @\n');
fprintf (f, 'Modulus", "Poisson Ratio"], [2, 5, 0], "Property Values",
        ["2.25e-3", "0.49", ""] )\n');
%%% Create 1D Actin Beam Cross Section
fprintf (f, 'beam_section_create( "actin_xsection", "ROD", ["%d"] )\n',
        frad);

%% Geometry
% Add all nodes for nucleus
fprintf (f, 'ga_group_current_set( "nimport" )\n');
fprintf (f, 'STRING fem_create_nodes__nodes_created[VIRTUAL]\n');
for i=1:size(nverts,1)
    x = nverts(i,1);
    y = nverts(i,2);
    z = nverts(i,3);
    fprintf (f, 'fem_create_nodes_1( "Coord 0", "Coord 0", 3, "#",
      "[%.3f %.3f %.3f]", fem_create_nodes__nodes_created )\n', x, y,
     z);
end
nucleus_min_node = 1; nucleus_max_node = size(nverts,1);

% Add all nodes for cell and identify coordinates of the highest one
fprintf (f, 'ga_group_current_set( "cimport" )\n');
highest_z = 0;
for i=1:size(cverts,1)
    x = cverts(i,1);
    y = cverts(i,2);
    z = cverts(i,3);
    if z > highest_z
       highest_x = x;
       highest_y = y;
```

```matlab
        highest_z = z;
    end
    fprintf (f, 'fem_create_nodes_1( "Coord 0", "Coord 0", 3, "#",
      "[%.3f %.3f %.3f]", fem_create_nodes__nodes_created )\n', x, y,
      z);
end
cell_min_node = nucleus_max_node+1; cell_max_node =
      nucleus_max_node+size(cverts,1);

% Make a group out of the base vertices
base_cutoff = highest_z/10;
fprintf (f, 'ga_group_current_set( "cimport_base" )\n');
z_plane = min(cverts(:,3)); % min z plane of cell boundary mesh
base_verts = find(cverts(:,3) <= z_plane + base_cutoff);
for i=1:size(base_verts,1)
    fprintf (f, 'ga_group_entity_add( "cimport_base", "Node %d" )\n',
      size(nverts,1)+base_verts(i));
end

% Decrease Node Size
fprintf (f, 'node_size( 0 )\n');

% Add Elements for nucleus
fprintf (f, 'ga_group_current_set( "nimport" )\n');
fprintf (f, 'STRING fem_create_elemen_elems_created[VIRTUAL]\n');
count = 1;
count_node = 1;
nucleus_min_elt = 1;
nucleus_min_node = 1;
for i=1:size(nfaces,1)
    n1 = nfaces(i,1);
    n2 = nfaces(i,2);
    n3 = nfaces(i,3);
    fprintf (f, 'fem_create_elems_1( "Tri ", "Tria6", "%d", "Standard",
      3, "Node %d", "Node %d", "Node %d", "", "", "", "", "",
      fem_create_elemen_elems_created )\n', count, n1, n2, n3);
    count = count + 1;
    count_node = count_node + 6;
end
nucleus_max_elt = count-1;
nucleus_max_node = count_node - 1;

% Add Elements for base of cell
fprintf (f, 'ga_group_current_set( "cimport_base" )\n');
cell_min_elt = count;
cell_min_node = count_node;
for i=1:size(cfaces,1)
```

```matlab
        n1 = cfaces(i,1);
        n2 = cfaces(i,2);
        n3 = cfaces(i,3);
        face_max_z = max([cverts(n1,3) cverts(n2,3) cverts(n3,3)]);
        if face_max_z <= z_plane + base_cutoff
            fprintf (f, 'fem_create_elems_1( "Tri ", "Tria6", "%d",
         "Standard", 3, "Node %d", "Node %d", "Node %d", "", "", "", "",
         "", fem_create_elemen_elems_created )\n', count,
         n1+size(nverts,1), n2+size(nverts,1), n3+size(nverts,1));
            count = count + 1;
            count_node = count_node + 6;
        end
end
cell_max_base_elt = count - 1;
cell_max_base_node = count_node - 1;

% Add Elements for top of cell
fprintf (f, 'ga_group_current_set( "cimport" )\n');
fprintf (f, 'ga_group_entity_add( "cimport", "Element %d:%d" )\n',
     nucleus_max_elt+1, count);
for i=1:size(cfaces,1)
    n1 = cfaces(i,1);
    n2 = cfaces(i,2);
    n3 = cfaces(i,3);
    face_max_z = max([cverts(n1,3) cverts(n2,3) cverts(n3,3)]);
    if face_max_z > z_plane + base_cutoff
        fprintf (f, 'fem_create_elems_1( "Tri ", "Tria6", "%d",
     "Standard", 3, "Node %d", "Node %d", "Node %d", "", "", "", "",
     "", fem_create_elemen_elems_created )\n', count,
     n1+size(nverts,1), n2+size(nverts,1), n3+size(nverts,1));
        count = count+1;
    end
end
cell_max_elt = count-1;

%Add AFM probe
fprintf (f, 'ga_group_current_set( "AFMprobe" )\n');
fprintf (f, 'STRING asm_create_cord_3po_created_ids[VIRTUAL]\n');
probe_offset = 0.25; %um
fprintf (f, 'asm_const_coord_3point( "1", "Coord 0", 1, "[%d %d %d]",
     "[%d %d %d]", "[%d %d %d]", asm_create_cord_3po_created_ids )\n',
     highest_x,highest_y,highest_z+2.5+probe_offset,
     highest_x,highest_y,highest_z+4.5,
     highest_x+1,highest_y,highest_z+3.5);

fprintf (f, 'STRING sgm_create_curve_2d_created_ids[VIRTUAL]\n');
```

```matlab
    fprintf (f, 'sgm_const_curve_2d_arc2point_v2( "1", 1, 0., FALSE, FALSE,
        1, "Coord 1.1",  @\n');
    fprintf (f, '"[0 0 0]", "[0 2.5 0]", "[0 0 -2.5]", FALSE,
        sgm_create_curve_2d_created_ids )\n');
    fprintf (f, 'STRING sgm_sweep_surface_r_created_ids[VIRTUAL]\n');
    fprintf (f, 'sgm_const_surface_revolve( "1", "Coord 1.3", 360., 0.,
        "Coord 0", "Curve 1",  @\n');
    fprintf (f, 'sgm_sweep_surface_r_created_ids )\n');
    fprintf (f, 'STRING asm_delete_any_deleted_ids[VIRTUAL]\n');
    fprintf (f, 'asm_delete_coord( "Coord 1", asm_delete_any_deleted_ids
        )\n');

%%% Add fibers
fiber_min_elt = count;
num_divisions = 10;
fiber_max_elt = count-1+num_divisions;
fprintf (f, 'ga_group_current_set( "actin" )\n');
for i=1:size(fibers,1)
    node1_id = fibers(i,1);
    node2_id = fibers(i,2);
    node1_pos = fverts(node1_id, :); % node1_pos = [x y z]
    node2_pos = fverts(node2_id, :); % node2_pos = [x y z]
    node1_pos_shrunk = 0.1 * node2_pos + 0.9 * node1_pos;
    node2_pos_shrunk = 0.1 * node1_pos + 0.9 * node2_pos;
    fprintf (f, 'STRING asm_line_2point_created_ids[VIRTUAL]\n');
    fprintf (f, 'asm_const_line_2point( "#", "[%.3f %.3f %.3f]", "[%.3f
      %.3f %.3f]", 0, "", 50., 1, asm_line_2point_created_ids )\n',
      node1_pos_shrunk(1), node1_pos_shrunk(2), node1_pos_shrunk(3),
      node2_pos_shrunk(1), node2_pos_shrunk(2), node2_pos_shrunk(3));
    fprintf (f, 'ui_exec_function( "mesh_seed_display_mgr", "init"
      )\n');
    fprintf (f, 'mesh_seed_create( "Line %d", 1, %d, 0., 0., 0. )\n',
      i+1, num_divisions);
    fprintf (f, 'INTEGER fem_create_mesh_curve_num_nodes\n');
    fprintf (f, 'INTEGER fem_create_mesh_curve_num_elems\n');
    fprintf (f, 'STRING fem_create_mesh_c_nodes_created[VIRTUAL]\n');
    fprintf (f, 'STRING fem_create_mesh_c_elems_created[VIRTUAL]\n');
    len = norm(node1_pos_shrunk - node2_pos_shrunk) / num_divisions;
    fprintf (f, 'fem_create_mesh_curv_1( "Line %d", 16384, %.5f,
      "Bar2", "#", "#",  @\n', i+1, len);
    fprintf (f, '"Coord 0", "Coord 0", fem_create_mesh_curve_num_nodes,
      @\n');
    fprintf (f, 'fem_create_mesh_curve_num_elems,
      fem_create_mesh_c_nodes_created,  @\n');
    fprintf (f, 'fem_create_mesh_c_elems_created )\n');
%% Properties (Part 2/3)
    %Actin beam properties
```

```
%       %General Beam
%       fprintf (f, 'elementprops_create( "actin%d", 117, 35, 42, 11018,
        1, 20, [39, 13, 6, 1,  @\n', i);
%       fprintf (f, '30, 31, 11, 12, 10, 3019, 3026, 3028, 3006, 3008,
        3020, 3027, 3029, 3007,  @\n');
%       fprintf (f, '3009, 3021, 3003, 3061, 3056, 3999], [12, 5, 2, 1,
        1, 1, 1, 1, 1, 6, 1, 1, 6,  @\n');
%       fprintf (f, '6, 6, 6, 6, 6, 6, 6, 6, 1, 4, 4], ["actin_xsection",
        "m:actin_mat",  @\n');
%       fprintf (f, '"Construct 2PointVector(Evaluate Geometry([0 0
        0]))(Evaluate Geometry([%.3f %.3f %.3f]))",  @\n', node1_pos(1),
        node1_pos(2), node1_pos(3));
%       fprintf (f, '"3.8484512E-005", "3.8484512E-005", "3.8484512E-
        005", "1.1785882E-010",  @\n');
%       fprintf (f, '"1.1785882E-010", "2.3571764E-010", "", "", "", "",
        "", "", "", "", "",  @\n');
%       %fprintf (f, '"", "", "", "", "", ""], "Curve %d" )\n', i);
        %doesn't work in current form
%       fprintf (f, '"", "", "", "", "", ""], "Element %d:%d" )\n',
        fiber_min_elt, fiber_max_elt);

    %Truss
    fprintf (f, 'elementprops_create( "actin%d", 20, 25, 37, 1, 1, 15,
        [13, 1, 3061, 3056, 3999],  @\n', i);
    fprintf (f, '[5, 1, 1, 4, 4], ["m:actin_mat", "%d", "", "", ""],
        "Element %d:%d" )\n', fcross, fiber_min_elt, fiber_max_elt);

    fiber_min_elt = fiber_max_elt + 1;
    fiber_max_elt = fiber_max_elt + num_divisions;

end

%Count edges on base (since each one turns into a new tria6 node
%count = 0;
%for i=1:size(cfaces,1)
%    n1 = cfaces(i,1);
%    n2 = cfaces(i,2);
%    n3 = cfaces(i,3);
%    face_max_z = max([cverts(n1,3) cverts(n2,3) cverts(n3,3)]);
%    if face_max_z <= z_plane + 0.0001
%        count = count + 3;
%    end
%    n = 0;
%    if cverts(n1,3) <= z_plane + 0.0001, n = n + 1; end
%    if cverts(n2,3) <= z_plane + 0.0001, n = n + 1; end
%    if cverts(n3,3) <= z_plane + 0.0001, n = n + 1; end
%    if n == 2
```

198

```matlab
%        count = count + 1;
%    end
%end
%count = count / 2;
%tria6_base_min = size(nverts,1) + size(cverts,1) + 1;
%tria6_base_max = size(nverts,1) + size(cverts,1) + count;

%Convert to tri6's for cell
%fprintf (f, 'ga_group_current_set( "cimport_base" )\n');
%fprintf (f, 'STRING fem_modify_elem__elems_modified[VIRTUAL]\n');
%fprintf (f, 'fem_modify_elems( "", "Tri", "Tria6", "", "", "Elm
%       %d:%d", [0, 1, 0, 0, 0, 0, 0, 0, 0, 0],
%       fem_modify_elem__elems_modified )\n', cell_min_elt,
%       cell_max_base_elt);
%fprintf (f, 'ga_group_current_set( "cimport" )\n');
%fprintf (f, 'fem_modify_elems( "", "Tri", "Tria6", "", "", "Elm
%       %d:%d", [0, 1, 0, 0, 0, 0, 0, 0, 0, 0],
%       fem_modify_elem__elems_modified )\n', cell_max_base_elt+1,
%       cell_max_elt);
%fprintf (f, 'ga_group_entity_add( "cimport", "Node %d:%d" )\n',
%       tria6_base_min, tria6_base_max);

% Convert to tri6's for nucleus
%fprintf (f, 'ga_group_current_set( "nimport" )\n');
%fprintf (f, 'STRING fem_modify_elem__elems_modified[VIRTUAL]\n');
%fprintf (f, 'fem_modify_elems( "", "Tri", "Tria6", "", "", "Elm
%       %d:%d", [0, 1, 0, 0, 0, 0, 0, 0, 0, 0],
%       fem_modify_elem__elems_modified )\n', nucleus_min_elt,
%       nucleus_max_elt);

%% Meshing
% Mesh inside of nucleus
fprintf (f, 'ga_group_current_set( "ntet" )\n');
fprintf (f, 'INTEGER fem_create_mesh_solid_num_nodes\n');
fprintf (f, 'INTEGER fem_create_mesh_solid_num_elems\n');
fprintf (f, 'STRING fem_create_mesh_s_nodes_created[VIRTUAL]\n');
fprintf (f, 'STRING fem_create_mesh_s_elems_created[VIRTUAL]\n');
fprintf (f, 'fem_create_mesh_sol_5( "Elm %d:%d", "TetHybrid", "Tet10",
       4, ["%.2f", "0.1", "0.2", "0.0"], 49232, 0, 1, 0, 1, 0.005, "",
       "#", "#", @\n', nucleus_min_elt, nucleus_max_elt, volmesh_size);
fprintf (f, '"Coord 0", "Coord 0", fem_create_mesh_solid_num_nodes,
       fem_create_mesh_solid_num_elems, fem_create_mesh_s_nodes_created,
       fem_create_mesh_s_elems_created )\n');

% Mesh inside of cell
fprintf (f, 'ga_group_current_set( "ctet" )\n');
fprintf (f, 'STRING fem_modify_elem__elems_reversed[VIRTUAL]\n');
```

```
fprintf (f, 'fem_mod_elem_reverse( "Elm %d:%d",
      fem_modify_elem__elems_reversed )\n', nucleus_min_elt,
      nucleus_max_elt);
fprintf (f, 'INTEGER fem_create_mesh_solid_num_nodes\n');
fprintf (f, 'INTEGER fem_create_mesh_solid_num_elems\n');
fprintf (f, 'STRING fem_create_mesh_s_nodes_created[VIRTUAL]\n');
fprintf (f, 'STRING fem_create_mesh_s_elems_created[VIRTUAL]\n');
fprintf (f, 'fem_create_mesh_sol_5( "Elm %d:%d", "TetHybrid", "Tet10",
      4, ["%.2f", "0.1", "0.2", "0.0"], 49232, 0, 1, 0, 1, 0.005, "",
      "#", "#", @\n', nucleus_min_elt, cell_max_elt, volmesh_size);
fprintf (f, '"Coord 0", "Coord 0", fem_create_mesh_solid_num_nodes,
      fem_create_mesh_solid_num_elems, fem_create_mesh_s_nodes_created,
      fem_create_mesh_s_elems_created )\n');

%Delete Tri elements
fprintf (f, 'fem_delete_elem_and_node( "Elm %d:%d",
      fem_delete_element_deleted_ids )\n', nucleus_min_elt,
      cell_max_elt);

%% Properties (Part 3/3)
%%% 3D Solid
%%%%%% Nucleus
%fprintf (f, '?\n');
%%%%%% Cytoplasm
%fprintf (f, '?\n');

% Can't do these ones - don't know how many tet elements Patran will
      create!

%% Loads/BCs
%%% Fix position of bottom plane
% fprintf (f, 'loadsbcs_create2( "fixed", "Displacement", "Nodal", "",
      "Static", [ @\n');
% fprintf (f, '"Node %d:%d"], "FEM", "Coord 0", "1.", ["<0 0 0>",
      @\n', cell_min_node, cell_max_base_node);
% fprintf (f, '"<      >", "<      >", "<      >"], ["", "", "", ""]
      )\n');

% Doesn't select the correct nodes. Not sure why.

%%% Create Movement Field
fprintf (f, 'fields_create( "movement", "Non-Spatial", 1, "Scalar",
      "Real", "", "", "Table" @\n');
fprintf (f, ', 1, "t", "", "", "", "", "", FALSE, [0., %.2f, %.2f,
      %.2f, %.2f], [0.], [0.], [[[ @\n', probe_offset / probe_speed,
      (probe_offset + probe_indent) / probe_speed, (probe_offset + 2 *
```

```
        probe_indent) / probe_speed, (2 * probe_offset + 2 *
        probe_indent) / probe_speed);
fprintf (f, '0.]][[%.2f]][[%.2f]][[%.2f]][[0.]]] )\n', probe_offset,
        probe_offset + probe_indent, probe_offset);

%%% Rigid Contact Body (Probe)
fprintf (f, 'elementprops_create( "Lbc_probe_contact", 99, 25, 66, 28,
        2, 14, [38], [4], [ @\n');
fprintf (f, '"probe_contact"], "Surface 1" )\n');
fprintf (f, 'fields_create_general( "._Lbc_probe_contact2", 2, 5, 2,
        "Real", "Coord 0", "", @\n');
fprintf (f, ' 0, 0, 0, 0 )\n');
fprintf (f, 'fields_create_general_term( "._Lbc_probe_contact2", 0, 0,
        0, 17,  @\n');
fprintf (f, '"[1_contact_lbc()]" )\n');
fprintf (f, 'fields_create_general_term( "._Lbc_probe_contact2", 0, 1,
        1, 351,  @\n');
fprintf (f,
        '"contact_lbc(54|11|22|43|44|45|57|58|59|61|62|63|64|65|66|67|69|
        76|77|78|7" // @\n');
fprintf (f,
        '"9|92|93|94|95|96|97|98|99|100|101|103|104|102|105|109|606|607|6
        08|609|610" // @\n');
fprintf (f,
        '"|611|612|613|614|615|110|111|112|113|114|115|422|622|623|Lbc_pr
        obe_contac" // @\n');
fprintf (f, '"t|||0|1||||-1.|Position||<0., 0., -
        1.,>|||f:movement:f|0|-1.||||||||||-1.|" // @\n');
fprintf (f, '"<0., 0., 0.,>||-1.|60.0||||0|-
        1.||||||||||||||||||1/1/1/||)" )\n');
fprintf (f, 'loadsbcs_create2( "probe_contact", "Contact[Rigid Body]",
        "Element Uniform",  @\n');
fprintf (f, '"2D", "Static", ["Surface 1"], "Geometry", "Coord 0",
        "1.", ["-1.", "1.0", "", @\n');
fprintf (f, ' "", "<1.,1.,0.>", "<0.,0.,1.>", "<0., 0., -1.,>", "", "",
        @\n');
fprintf (f, '"f:._Lbc_probe_contact2"], ["", "", "", "", "", "", "",
        "", "", ""] )\n');

%%% Deformable Contact Body (Cell)
% Can't do this one - don't know how many tet elements Patran will
        create


%% Analysis
% Post only groups necessary for analysis
```

```
fprintf (f, 'uil_viewport_post_groups.posted_groups(
      "default_viewport", 3, ["AFMprobe", "ctet", "ntet", "actin"]
      )\n');

% Adaptive Meshing
% fprintf (f, 'analysis_create.job_char_param( "MSC.Marc", "test",
      "ADAPTIVITY TYPE",  @\n');
% fprintf (f, '"Global" )\n');
% fprintf (f, 'analysis_create.job_int_param( "MSC.Marc", "test",
      "NUMBER OF ZONES", 1 )\n');
% fprintf (f, 'analysis_create.job_char_param( "MSC.Marc", "test",
      "ZONE 1",  @\n');
% fprintf (f, '"amesh,Global,cell_contact,Tetrahedral,Previous Mesh
      Size, , , , ,TRUE,0.2" // @\n');
% fprintf (f, '"5, ,FALSE, , , ,FALSE, , , , , ,FALSE, , , ,100,60,1.5,
      , ,FALSE, " )\n');

% Can't do this one without being able to create deformable contact
      body
% for the cell: "cell_contact" in the example above

% Load Increment Parameters
fprintf(f, 'analysis_create.step( "MSC.Marc", "Default Static Step",
      @\n');
fprintf(f, '"This is a default static analysis step." )\n');
fprintf(f, '$# Question from application APP INTERFACES\n');
fprintf(f, '$#    The stepname (Default Static Step) is already
      defined in the database. \n');
fprintf(f, '$#  Do you wish to overwrite?\n');
fprintf(f, '$? YES 6016028 \n');
fprintf(f, 'analysis_create.step_char_param( "MSC.Marc", "Default
      Static Step",  @\n');
fprintf(f, '"LOAD CASE", "Default" )\n');
fprintf(f, 'analysis_create.step_int_param( "MSC.Marc", "Default Static
      Step",  @\n');
fprintf(f, '"LBCS WITH NO FIELDS", 0 )\n');
fprintf(f, 'analysis_create.step_char_param( "MSC.Marc", "Default
      Static Step",  @\n');
fprintf(f, '"SOLUTION TYPE", "NONLINEAR STATIC" )\n');
fprintf(f, 'analysis_create.step_char_param( "MSC.Marc", "Default
      Static Step",  @\n');
fprintf(f, '"GEOMETRIC", "Large Displacement/Large Strains" )\n');
fprintf(f, 'analysis_create.step_char_param( "MSC.Marc", "Default
      Static Step",  @\n');
fprintf(f, '"LOADS FOLLOW", "OFF" )\n');
fprintf(f, 'analysis_create.step_char_param( "MSC.Marc", "Default
      Static Step",  @\n');
```

```
fprintf(f, '"FORCES FOLLOW", "OFF" )\n');
fprintf(f, 'analysis_create.step_char_param( "MSC.Marc", "Default
    Static Step",  @\n');
fprintf(f, '"TYPE OF LOAD", "TOTAL" )\n');
fprintf(f, 'analysis_create.step_char_param( "MSC.Marc", "Default
    Static Step",  @\n');
fprintf(f, '"INCREMENT TYPE CODE", "FXDSTAT" )\n');
fprintf(f, 'analysis_create.step_char_param( "MSC.Marc", "Default
    Static Step",  @\n');
fprintf(f, '"INCREMENT TYPE", "Fixed" )\n');
fprintf(f, 'analysis_create.step_int_param( "MSC.Marc", "Default Static
    Step",  @\n');
fprintf(f, '"INCREMENTS", %d )\n', (probe_offset +
    probe_indent)/0.005);
fprintf(f, 'analysis_create.step_real_param( "MSC.Marc", "Default
    Static Step",  @\n');
fprintf(f, '"TOTAL TIME", %.2f )\n', (2 * probe_offset + 2 *
    probe_indent) / probe_speed);
fprintf(f, 'analysis_create.step_int_param( "MSC.Marc", "Default Static
    Step",  @\n');
fprintf(f, '"CONSTANT TIME STEP", 0 )\n');
fprintf(f, 'analysis_create.step_char_param( "MSC.Marc", "Default
    Static Step",  @\n');
fprintf(f, '"AUTO TIME STEP CUTBACK", "ON" )\n');
fprintf(f, 'analysis_create.step_int_param( "MSC.Marc", "Default Static
    Step",  @\n');
fprintf(f, '"MAX NUM CUTBACKS", 10 )\n');
fprintf(f, 'analysis_create.step_char_param( "MSC.Marc", "Default
    Static Step",  @\n');
fprintf(f, '"CONVERGED", "OFF" )\n');
fprintf(f, 'analysis_create.step_char_param( "MSC.Marc", "Default
    Static Step",  @\n');
fprintf(f, '"NON-POSITIVE DEFINITE", "OFF" )\n');
fprintf(f, 'analysis_create.step_char_param( "MSC.Marc", "Default
    Static Step",  @\n');
fprintf(f, '"INITIAL STRESS STIFFNESS", "Full" )\n');
fprintf(f, 'analysis_create.step_char_param( "MSC.Marc", "Default
    Static Step",  @\n');
fprintf(f, '"ITERATION METHOD", "Full Newton-Raphson" )\n');
fprintf(f, 'analysis_create.step_int_param( "MSC.Marc", "Default Static
    Step",  @\n');
fprintf(f, '"ITERATIONS", 20 )\n');
fprintf(f, 'analysis_create.step_int_param( "MSC.Marc", "Default Static
    Step",  @\n');
fprintf(f, '"MINIMUM ITERATIONS", 0 )\n');
fprintf(f, 'analysis_create.step_int_param( "MSC.Marc", "Default Static
    Step",  @\n');
```

```
fprintf(f, '"DESIRED ITERATIONS", 5 )\n');
fprintf(f, 'analysis_create.step_char_param( "MSC.Marc", "Default
     Static Step",  @\n');
fprintf(f, '"TOLERANCE METHOD", "Residual" )\n');
fprintf(f, 'analysis_create.step_char_param( "MSC.Marc", "Default
     Static Step",  @\n');
fprintf(f, '"ERROR TYPE", "Relative" )\n');
fprintf(f, 'analysis_create.step_char_param( "MSC.Marc", "Default
     Static Step",  @\n');
fprintf(f, '"MATRIX UPDATE METHOD", "Automatic" )\n');
fprintf(f, 'analysis_create.step_char_param( "MSC.Marc", "Default
     Static Step",  @\n');
fprintf(f, '"AUTOMATIC SWITCHING", "ON" )\n');
fprintf(f, 'analysis_create.step_real_param( "MSC.Marc", "Default
     Static Step",  @\n');
fprintf(f, '"TRANS TOLERANCE", 0.1 )\n');
fprintf(f, 'analysis_create.step_real_param( "MSC.Marc", "Default
     Static Step",  @\n');
fprintf(f, '"ROT TOLERANCE", 0. )\n');
fprintf(f, 'analysis_create.step_char_param( "MSC.Marc", "Default
     Static Step",  @\n');
fprintf(f, '"CONTACT DETECTION", "Default(by body #)" )\n');
fprintf(f, 'analysis_create.step_int_param( "MSC.Marc", "Default Static
     Step",  @\n');
fprintf(f, '"CONTACT-SETS-COUNT", 1 )\n');
fprintf(f, 'analysis_create.step_int_param( "MSC.Marc", "Default Static
     Step",  @\n');
fprintf(f, '"CONTACT-PAIR-NUM-PROPS-COUNT", 20 )\n');
fprintf(f, 'analysis_create.step_int_param( "MSC.Marc", "Default Static
     Step",  @\n');
fprintf(f, '"CONTACT-PAIR-NUM-SETTINGS-COUNT", 6 )\n');
fprintf(f, 'analysis_create.step_int_list_param( "MSC.Marc", "Default
     Static Step",  @\n');
fprintf(f, '"CONTACT-TABLE-SETS-COUNT", "0 " )\n');
fprintf(f, 'analysis_create.step_int_list_param( "MSC.Marc", "Default
     Static Step",  @\n');
fprintf(f, '"CONTACT-LBC-SETS", "1 " )\n');
fprintf(f, 'analysis_create.step_char_param( "MSC.Marc", "Default
     Static Step",  @\n');
fprintf(f, '"CONTACT-LBC-SET-NAMES", "probe_contact " )\n');
fprintf(f, 'analysis_create.step_int_list_param( "MSC.Marc", "Default
     Static Step",  @\n');
fprintf(f, '"CONTACT-TABLE-LBC-SETS", "" )\n');
fprintf(f, 'analysis_create.step_real_list_param( "MSC.Marc", "Default
     Static Step",  @\n');
fprintf(f, '"CONTACT-TABLE-DATA", "" )\n');
```

```
fprintf(f, 'analysis_create.step_char_param( "MSC.Marc", "Default
    Static Step",  @\n');
fprintf(f, '"CONTACT-TABLE-DATA2", "" )\n');
fprintf(f, 'analysis_create.step_int_list_param( "MSC.Marc", "Default
    Static Step",  @\n');
fprintf(f, '"CONTACT-TABLE-SETS-COUNT-GLUE", "0 " )\n');
fprintf(f, 'analysis_create.step_int_list_param( "MSC.Marc", "Default
    Static Step",  @\n');
fprintf(f, '"CONTACT-LBC-SETS-GLUE", "1 " )\n');
fprintf(f, 'analysis_create.step_int_list_param( "MSC.Marc", "Default
    Static Step",  @\n');
fprintf(f, '"CONTACT-TABLE-LBC-SETS-GLUE", "" )\n');
fprintf(f, 'analysis_create.step_real_list_param( "MSC.Marc", "Default
    Static Step",  @\n');
fprintf(f, '"CONTACT-TABLE-DATA-GLUE", "" )\n');
fprintf(f, 'analysis_create.step_char_param( "MSC.Marc", "Default
    Static Step",  @\n');
fprintf(f, '"CONTACT-TABLE-DATA2-GLUE", "" )\n');
fprintf(f, 'analysis_create.step_char_param( "MSC.Marc", "Default
    Static Step",  @\n');
fprintf(f, '"CONTACT-LBC-SETS-RELEASE", "N " )\n');
fprintf(f, 'analysis_create.step_char_param( "MSC.Marc", "Default
    Static Step",  @\n');
fprintf(f, '"CONTACT-LBC-SETS-RELEASE-VALUES", "0 " )\n');
fprintf(f, 'analysis_create.step_int_param( "MSC.Marc", "Default Static
    Step",  @\n');
fprintf(f, '"RESULTS INTERVALS", 1 )\n');
fprintf(f, 'analysis_create.step_int_param( "MSC.Marc", "Default Static
    Step",  @\n');
fprintf(f, '"PRINT INTERVALS", 1 )\n');
fprintf(f, 'analysis_create.step_char_param( "MSC.Marc", "Default
    Static Step",  @\n');
fprintf(f, '"WRITE ENERGY DATA", "OFF" )\n');
fprintf(f, 'analysis_create.step_char_param( "MSC.Marc", "Default
    Static Step",  @\n');
fprintf(f, '"SKIP INCREMENT ZERO", "OFF" )\n');
fprintf(f, 'analysis_create.step_int_param( "MSC.Marc", "Default Static
    Step",  @\n');
fprintf(f, '"NORMALIZATION ID", 0 )\n');
fprintf(f, 'analysis_create.step_int_param( "MSC.Marc", "Default Static
    Step",  @\n');
fprintf(f, '"NORMALIZATION COMPONENT", 1 )\n');
fprintf(f, 'analysis_create.step_int_param( "MSC.Marc", "Default Static
    Step",  @\n');
fprintf(f, '"NORMALIZATION FROM MODE", 0 )\n');
fprintf(f, 'analysis_create.step_int_param( "MSC.Marc", "Default Static
    Step",  @\n');
```

```
fprintf(f, '"NORMALIZATION THRU MODE", 0 )\n');
fprintf(f, 'analysis_create.step_int_param( "MSC.Marc", "Default Static
    Step",  @\n');
fprintf(f, '"INTEGRATION PTS", 5 )\n');
fprintf(f, 'analysis_create.step_char_param( "MSC.Marc", "Default
    Static Step",  @\n');
fprintf(f, '"WRITE MEMBRANE", "ON" )\n');
fprintf(f, 'analysis_create.step_int_list_param( "MSC.Marc", "Default
    Static Step",  @\n');
fprintf(f, '"WRITE INTEGRATION PTS", " 1 2 3 4 5" )\n');
fprintf(f, 'analysis_create.step_char_param( "MSC.Marc", "Default
    Static Step",  @\n');
fprintf(f, '"STRAIN, TOTAL COMPONENTS (301)", "ON,LayerOption ,Default"
    )\n');
fprintf(f, 'analysis_create.step_char_param( "MSC.Marc", "Default
    Static Step",  @\n');
fprintf(f, '"STRESS, COMPONENTS (global system) (411)", "ON,LayerOption
    ,Default" )\n');
fprintf(f, 'analysis_create.step_char_param( "MSC.Marc", "Default
    Static Step",  @\n');
fprintf(f, '"WRITE ITERATIVE DATA", "OFF" )\n');
fprintf(f, 'analysis_create.step_char_param( "MSC.Marc", "Default
    Static Step",  @\n');
fprintf(f, '"EXCLUDE GLUE FORCES", "OFF" )\n');
fprintf(f, 'analysis_create.step_char_param( "MSC.Marc", "Default
    Static Step",  @\n');
fprintf(f, '"MARC Nodal POST CODE Defaults", "ON" )\n');
fprintf(f, 'analysis_create.step_char_param( "MSC.Marc", "Default
    Static Step",  @\n');
fprintf(f, '"POST FILE NODE SELECTION FILTER", "Geometry" )\n');
fprintf(f, 'analysis_create.step_char_param( "MSC.Marc", "Default
    Static Step",  @\n');
fprintf(f, '"POST FILE NODE LIST", "" )\n');
fprintf(f, 'analysis_create.step_char_param( "MSC.Marc", "Default
    Static Step",  @\n');
fprintf(f, '"PRINT NODE", "NONE" )\n');
fprintf(f, 'analysis_create.step_char_param( "MSC.Marc", "Default
    Static Step",  @\n');
fprintf(f, '"PRINT ELEMENT", "NONE" )\n');
fprintf(f, 'analysis_create.step_char_param( "MSC.Marc", "Default
    Static Step", "SUMMARY", @\n');
fprintf(f, ' "OFF" )\n');
fprintf(f, 'analysis_create.step_char_param( "MSC.Marc", "Default
    Static Step",  @\n');
fprintf(f, '"INPUT FILE ECHO", "OFF" )\n');
fprintf(f, 'analysis_create.step_char_param( "MSC.Marc", "Default
    Static Step",  @\n');
```

```
fprintf(f, '"CONNECTIVITY ECHO", "OFF" )\n');
fprintf(f, 'analysis_create.step_char_param( "MSC.Marc", "Default
      Static Step",  @\n');
fprintf(f, '"COORDINATES ECHO", "OFF" )\n');
fprintf(f, 'analysis_create.step_char_param( "MSC.Marc", "Default
      Static Step",  @\n');
fprintf(f, '"PRINT CONVERGENCE", "ON" )\n');
fprintf(f, 'analysis_create.step_char_param( "MSC.Marc", "Default
      Static Step",  @\n');
fprintf(f, '"ERROR ESTIMATE", "None" )\n');
fprintf(f, 'analysis_create.step_char_param( "MSC.Marc", "Default
      Static Step",  @\n');
fprintf(f, '"WRITE HISTORY TEXT INPUT AT", "End" )\n');
fprintf(f, 'analysis_create.step_int_param( "MSC.Marc", "Default Static
      Step",  @\n');
fprintf(f, '"HISTORY INPUT 0", 0 )\n');
fprintf(f, 'analysis_create.step_int_param( "MSC.Marc", "Default Static
      Step",  @\n');
fprintf(f, '"NUMBER OF GLOBAL ADAPTIVE ZONES", 0 )\n');


fclose (f);

%% Mentat Insertion "Card"
filename = sprintf('%s\\cell%d_insert_card.dat', patran_dir, id);
f = fopen(filename, 'w');

fprintf(f, 'DEFINE    ELEMENT   SET       insert1_host_elements\n');
% Danger -- mesh on mesh will change the elt ranges in the next line!\
fprintf(f, '%6d    to%6d\n', -1, -1); % "-1"s Should be the range of
      IDs from the tet mesh
fprintf(f, 'DEFINE    ELEMENT   SET       insert1_embed_elements\n');
fprintf(f, '%6d    to%6d\n', fiber_min_elt, fiber_max_elt);
fprintf(f, 'INSERT\n');
fprintf(f, '\n');
fprintf(f, '         1         1          5.00000-2          0\n');
fprintf(f, 'insert1_host_elements\n');
fprintf(f, 'insert1_embed_elements\n');

fclose (f);

end
```

A.12. cell_3D_vis.m

This file generates three MATLAB figures showing the results of the image analysis in top, front, and side views.

MATLAB CODE

```matlab
function cell_3d_vis(nfaces, nverts, fverts, cfaces, cverts, sol,
      fignum)

figure(fignum);
clf;

%Draw nucleus
% vx = nverts(:,1);
% vy = nverts(:,2);
% vz = nverts(:,3);
%FVn.vertices = [vy vx vz]; FVn.faces = nfaces;
FVn.vertices = nverts; FVn.faces = nfaces;
pn = patch(FVn);
set(pn, 'facecolor', [0.5 0.7 1]); %[R G B]
set(pn, 'facealpha', 0.5); %translucency
set(pn, 'linestyle', 'none');

%Draw cell boundary
% vx = cverts(:,1);
% vy = cverts(:,2);
% vz = cverts(:,3);
%FVc.vertices = [vy vx vz]; FVc.faces = cfaces;
FVc.vertices = cverts; FVc.faces = cfaces;
pc = patch(FVc);
set(pc, 'facecolor', [0.4 0.4 0.4]);
set(pc, 'facealpha', 0.2); %translucency
set(pc, 'linestyle', 'none');  % uncomment to hide mesh

hold on

% View ALL actin that I've previously sampled
for i=1:size(sol,1)
```

```matlab
        v1 = sol(i, 1);
        v2 = sol(i, 2);
        p1 = fverts(v1, :);
        p2 = fverts(v2, :);
        %p1b = 0.1 * p2 + 0.9 * p1;
        %p2b = 0.1 * p1 + 0.9 * p2;
        p1b = p1;
        p2b = p2;
        %h = line([p1b(2) p2b(2)], [p1b(1) p2b(1)], [p1b(3) p2b(3)]);
        h = line([p1b(1) p2b(1)], [p1b(2) p2b(2)], [p1b(3) p2b(3)]);
        set(h, 'color', [0 0.5+sol(i,3)/2 0]);
        set(h, 'linewidth', 1);
end

daspect([1 1 1]);
axis xy;
camlight;
lighting phong;

end
```

A.13. print_cell.m

NOTES

This file generates three image files (in .png format) showing the results of the image

analysis in top, front, and side views.

MATLAB CODE

```matlab
function print_cell(filename, size_x, size_y, fignum)
% size_x and size_y are size in inches of image printout

p = get(fignum,'Position');
set(fignum, 'PaperUnits', 'inches');
set(fignum, 'PaperSize', [p(3)/100 p(4)/100]);
set(fignum, 'PaperPositionMode', 'manual');
set(fignum, 'PaperPosition', [0 0 p(3)/100 p(4)/100]);
set(fignum, 'renderer', 'OpenGL');
print(fignum, '-dpng', '-r300', filename);
```

209

end

APPENDIX B

ADDITIONAL AFM DATA

B.1. Concurrent Visualization and Characterization of Single Cell Mechanical Properties

B.1.1. BACKGROUND

The mechanical properties of cells and tissues are directly related to their shapes (Figure B.1). Fibroblasts are the most common cell type in the heart and are constantly under dynamic load in normal healthy conditions. In response to injurious mechanical loading, fibroblasts can undergo significant cytoskeletal remodeling through differentiation to a myofibroblast phenotype, leading to changes in mechanical properties that may eventually contribute to heart failure [1]. Prediction of cell behavior using structural properties of nanoscale components could elucidate mechanisms behind many tissue mechanical properties, which could lead to ability to development of more effective medical therapies [2]. Atomic Force Microscopy (AFM) and Confocal Microscopy are both useful individually for analysis of mechanical properties and nanoscale structures of cells but are much more powerful when used in conjunction with each other.
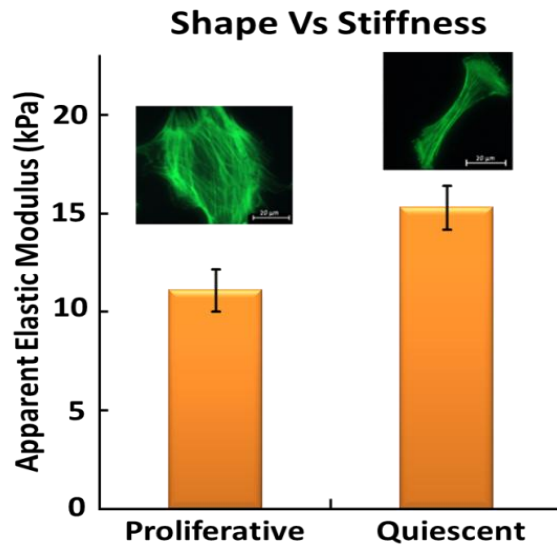
Figure B.1. Relationship between shape and stiffness of rat aortic vascular smooth muscle cells (VSMCs); f-actin labeled with AlexaFluor 488 phalloidin [3]

B.1.2. METHODS

An Olympus IX81 Inverted Microscope with Spinning Disc Confocal Microscope and Asylum Research MFP-3D Extended Head Atomic Force Microscope were used as shown in Figure B.2. NIH 3T3 Fibroblasts are seeded at 7×10^3 cells/cm^2 on glass-bottom Petri dishes coated with 50 µL of 1 mg/mL Type I Collagen (Rat Tail) 1 hr prior to cell seeding and allowed to grow for $2 - 3$ days in DMEM with 10% FBS. The live cells were then stained with DAPI (25 µg/mL in DMEM with 10% FBS) to visualize the nucleus and CellMask™ Deep Red (7.5 µg/mL in DMEM with 10% FBS) to visualize the plasma membrane. Cells are then incubated at 37 °C, 5 % CO_2 in DAPI/CellMask solution for 1 hour immediately prior to concurrent experimentation and visualization.

The DAPI/CellMask solution is then removed and replaced with standard media at the start of the experiment.
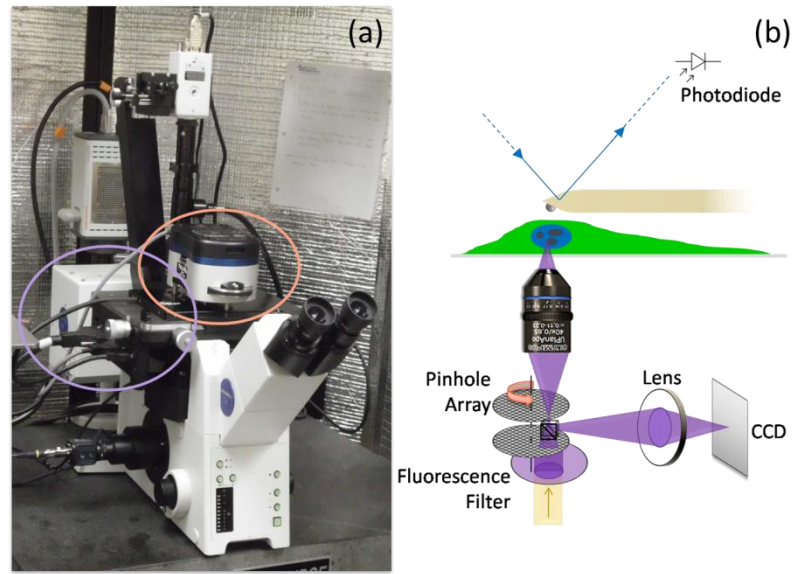
Figure B.2. (a) Olympus IX81 Inverted Microscope with: Spinning Disc Confocal Microscope: Disc Spinning Unit (DSU, purple circle) and Atomic Force Microscope: Asylum Research MFP-3D Extended Head (orange circle) (b) block diagram of experimental setup

During mechanical characterization with the AFM, the cells are maintained at 37 °C. A 2.5 µm radius borosilicate spherical-tipped probe with a spring constant of 0.2 N/m is utilized for all mechanical measurements. First, a stress relaxation test is performed using an indentation depth of 5 µm, indentation velocity of 100 µm/sec, and an indentation dwell time of 5 minutes. After obtaining stress relaxation data for the cell, a force map is obtained using indenting to 150 nm of cantilever deflection (representing approximately 1 − 5 µm of cell depth), and an indentation velocity of 5 µm/sec. Measurements are taken

every 2.5 µm to satisfy the Nyquist criterion. Scan times for force maps are

approximately 1 hour.

B.1.3. RESULTS

Results are shown in Figures B.3 through B.9.
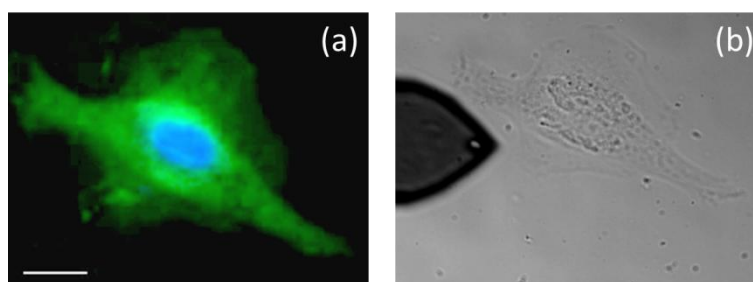
Figure B.3. (a) Fluorescent Image of 3T3 fibroblast, scale bar: 20 µm (b) View of same cell from (a) and AFM tip as seen in AFM software; both images taken prior to conducting AFM experiments
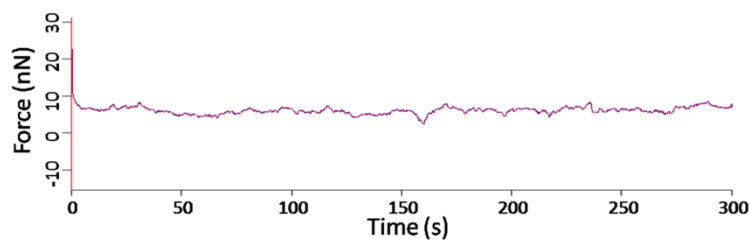
Figure B.4. Deflection of AFM probe during stress relaxation experiment
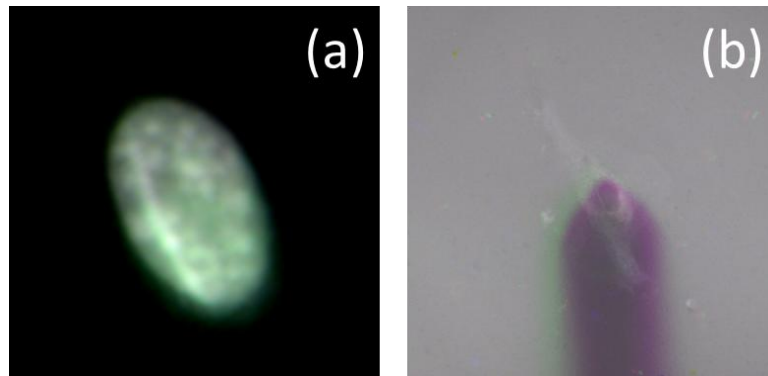
(**R**) t_0 : Just Before Indentation
(**G**) t_1 : Just After Indentation
(**B**) t_2 : 6 min After Indentation

Figure B.5. (a) Overlay of confocal images of nucleus ~ 500 ms before, ~ 300 ms after, and 6 min after indentation. Notice that the green channel is dominant indicating a bulging of the nucleus immediately following indentation. (b) Overlay of confocal images of cell membrane ~ 500 ms before, ~ 300 ms after, and 6 min after indentation. Notice that the cell appears white indicating a lack of movement, however the shadow of the AFM probe is visible as being in the same location before and after indentation (purple) but is in a different location immediately following indentation.
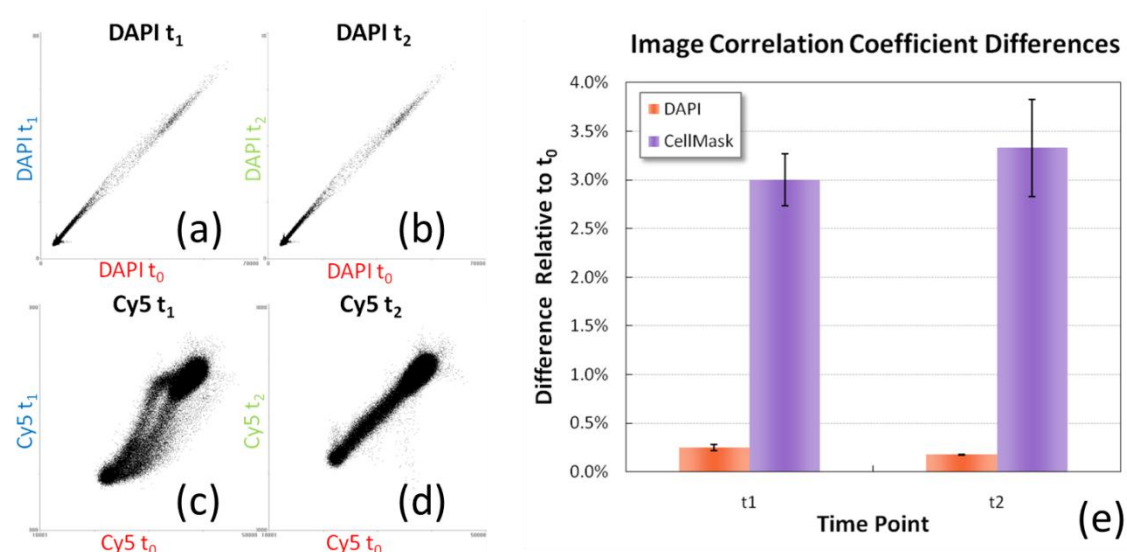
Figure B.6. Correlation Plots comparing pixel intensities in G and B channels relative to R channels of images in Fig 5. Plots for images of: (a) nucleus just after indentation (b) nucleus 6 min after indentation (c) cell membrane just after indentation (d) cell membrane 6 min after indentation (e) Graph of percentage difference between each correlation coefficient from the plots in Fig. 6 relative to the correlation coefficient for t0. The values for the cell membrane images are most likely higher due to the movement of the shadow of the AFM probe as seen in Fig 5. This problem can be solved by utilizing a stain with a higher signal-to-noise ratio than CellMask™ Deep Red. Error bars show 90% confidence interval.
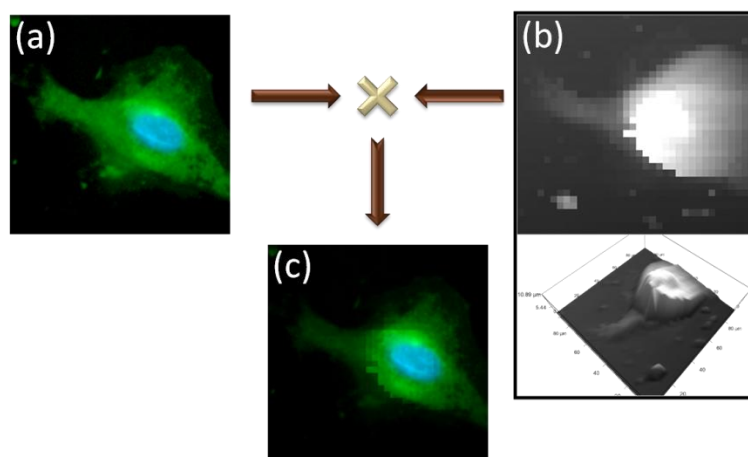
Figure B.7. (a) Fluorescent image of 3T3 fibroblast; (b) top: 2D AFM height profile of same cell, bottom: 3D version of same plot; (c) overlay of (a) onto (b)

216

and multiplication of pixel intensities resulting in the higher areas of the cell being brighter and the lower areas being darker
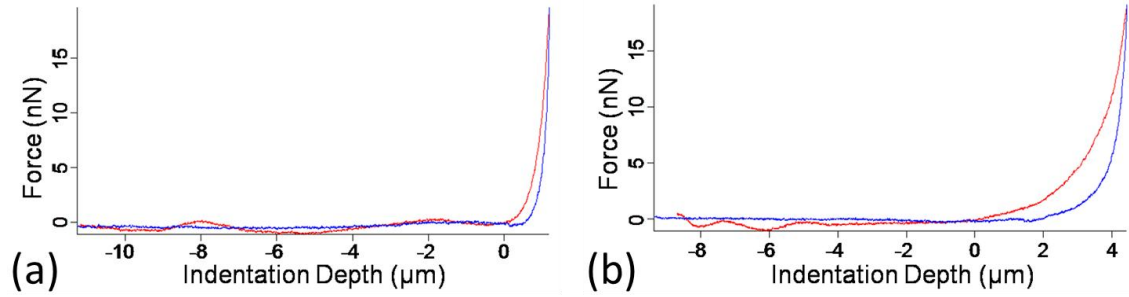
Figure B.8. (a) Force-Indentation curve taken along cell periphery (b) Force-Indentation curve taken in the middle of the cell
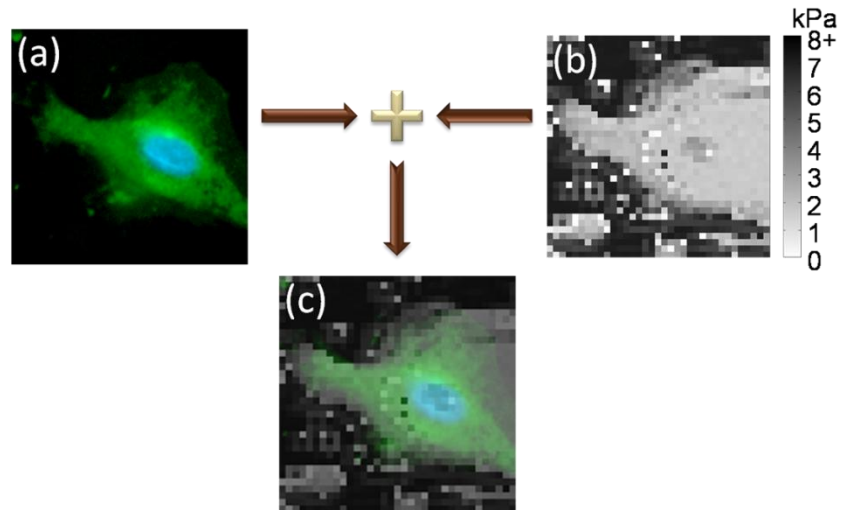
Figure B.9. (a) Fluorescent image of 3T3 fibroblast, (b) Hertzian modulus map of same cell, (c) overlay of (a) onto (b) showing the stiffer areas of the cell as darker and the softer areas as lighter

B.1.4. DISCUSSION

The concurrent use of AFM nanoindentation with confocal microscopy provides a useful novel method for the visualization of the effects of AFM nanoindentation on cell shape and structure. This technique is particularly interesting due to its ability to observe these effects in live cells that actively respond to AFM nanoindentation as images could be taken in real time if so desired. Cells did not try to move away from the AFM probe during stress relaxation measurements as expected. AFM Height measurements can compensate for low z-axis resolution of 3D confocal data to more accurately determine cell height. Cells were found to be stiffer when indenting over the nucleus than the area surrounding the nucleus, and the cells were stiffest at the periphery due to substrate effects. In future studies, the force maps and confocal images generated in these experiments will be incorporated into a 3D structure-based finite element model in order to provide a unique and compelling method of validation for our model.

B.1.5. REFERENCES

1.   Porter, K.E. and N.A. Turner, *Cardiac fibroblasts: At the heart of myocardial remodeling.* Pharmacology & Therapeutics, 2009. 123(2): p. 255-278.

2.   Ingber, D.E., *Tensegrity I. Cell structure and hierarchical systems biology.* Journal of Cell Science, 2003. 116(7): p. 1157-1173.

3.   Hemmer J.D., D.D., Vertegel A., Langan E. III, LaBerge M., *Effects of serum deprivation on the mechanical properties of adherent vascular smooth muscle cells.* Proc Inst Mech Eng [H], 2008. 222(5): p. 761-72.

APPENDIX C

ADDITIONAL FEM DATA

C.1. Mesh Sensitivity Analysis

Mesh sensitivity analysis was performed on the 2D axisymmetric version of the model from Chapter 4 in Patran/Marc, with results of the model compared at varying element densities.

C.1.1. MESH 1

- Created Quad8 Paver Mesh with no mesh seed
    - Global Edge Length = 0.25
    - 122 Elements
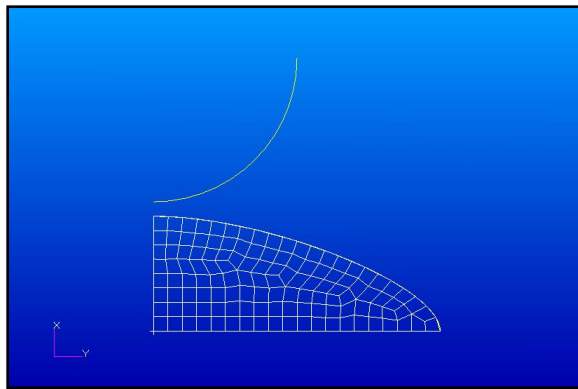
Figure C.1. Mesh 1 Prior to Indentation
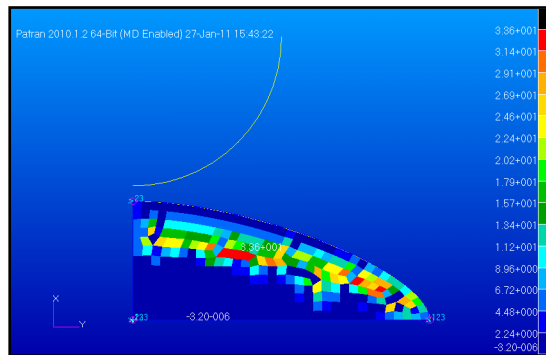
    - 4 Elements Failed

- Skew: 2
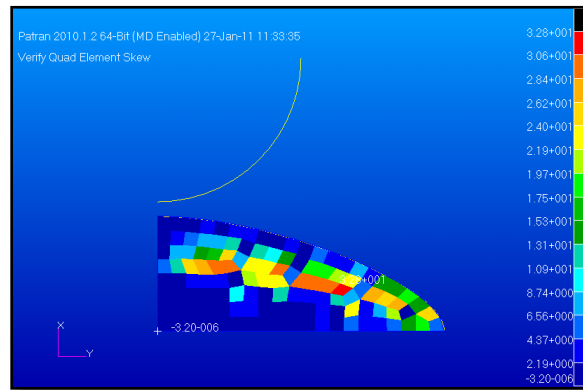
Figure C.2. Mesh 1 Skew Element Quality Prior to Indentation
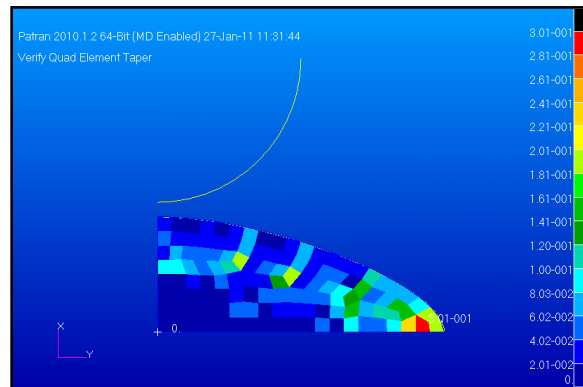
- Taper: 2

Figure C.3. Mesh 1 Taper Element Quality Prior to Indentation

- Mesh not smoothed in hopes that intial mesh will match final mesh

- Results

  o Solution Time: 13 sec

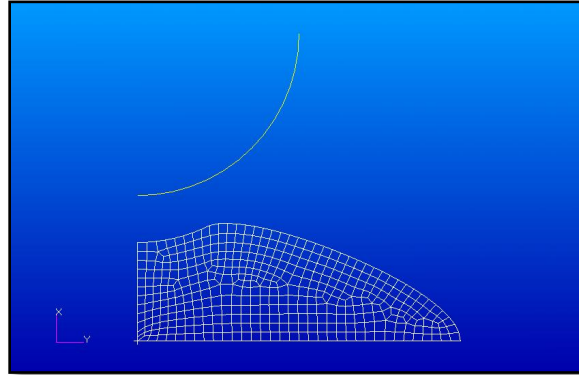 o Mesh at 500 nm indentation
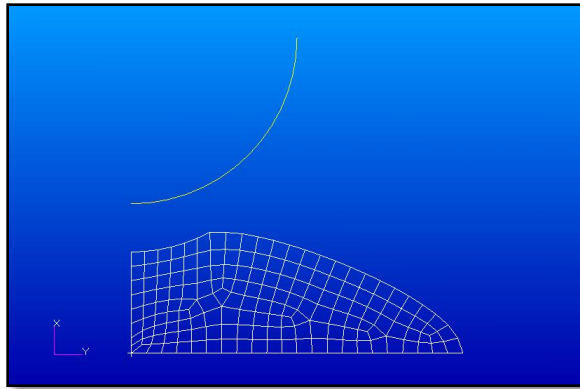
Figure C.4. Mesh 1 at 500 nm Indentation

- 157 Elements
    - o Mesh after retraction
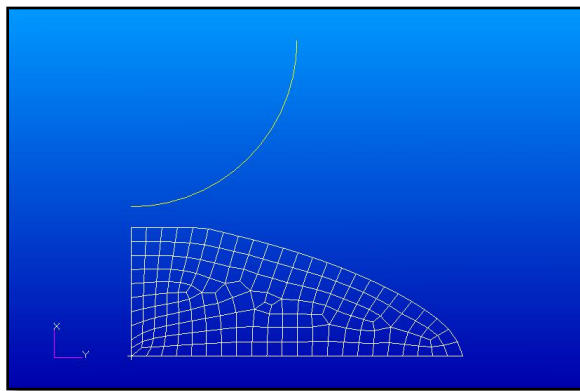
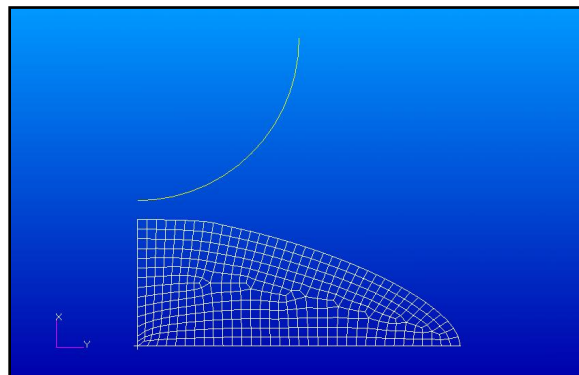Figure C.5. Mesh 1 After Retraction

- 169 Elements
- Not identical to initial mesh
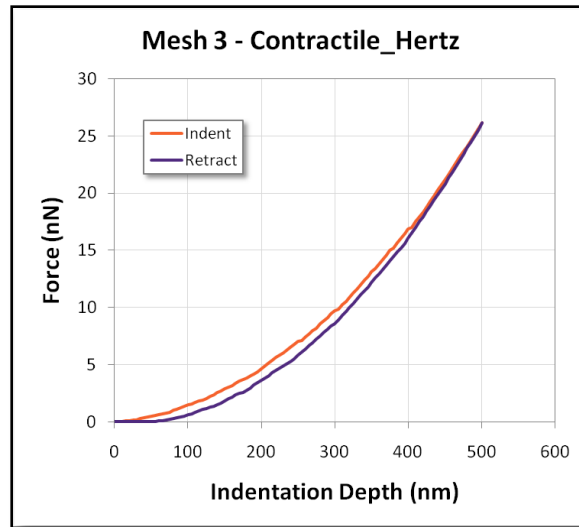   - o Indentation Curve
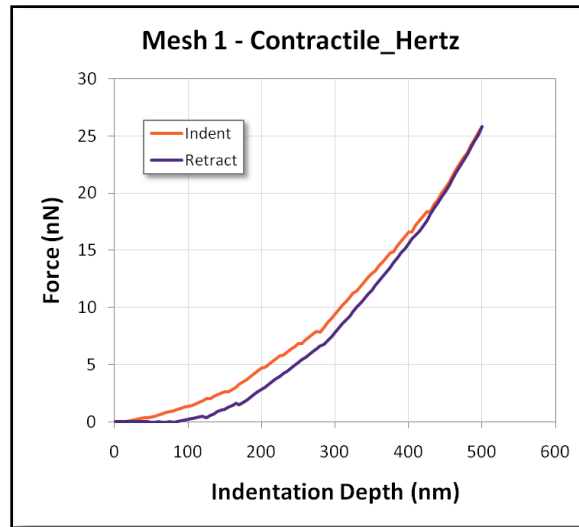
Figure C.6. Mesh 1 Indentation Curve

- 12.2% Hysteresis

  o Will try refining mesh next to see if that gets rid of hysteresis

C.1.2. MESH 2

- Created Quad8 Paver Mesh with no mesh seed

 o Global Edge Length = 0.20

  o 201 Elements
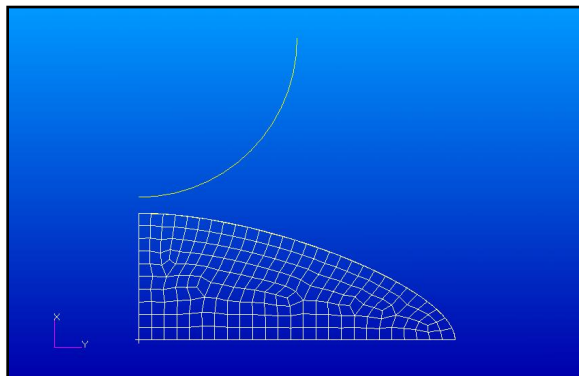
Figure C.7. Mesh 2 Prior to Indentation

- o 5 Elements Failed
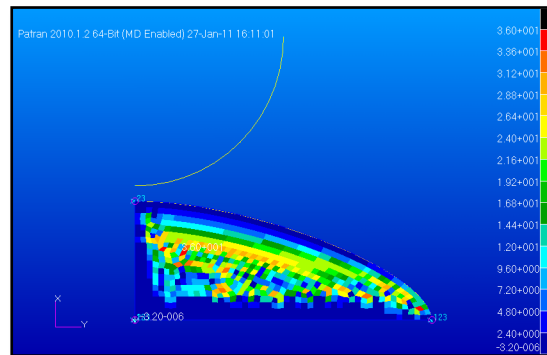
  - Skew: 3 Failed

    - Max = 38.4
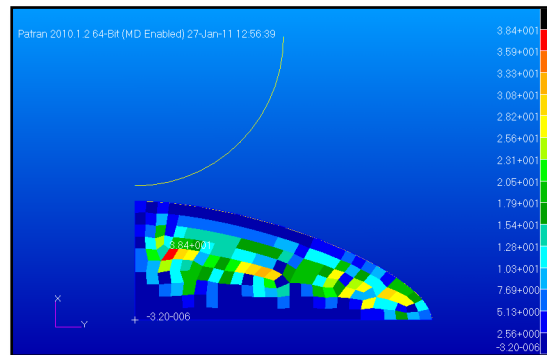
Figure C.8. Mesh 2 Skew Element Quality Prior to Indentation

  - Taper: 2 Failed

    - Min = 0.785
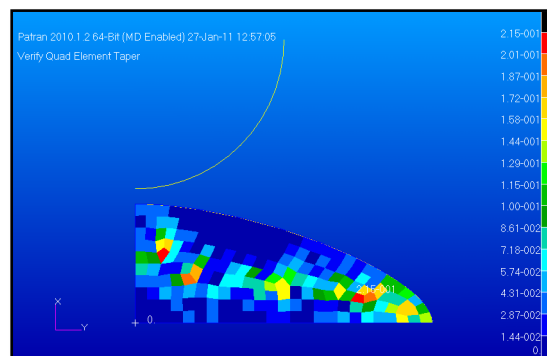
Figure C.8. Mesh 2 Taper Element Quality Prior to Indentation

  - Mesh not smoothed in hopes that intial mesh will match final mesh

- Results

  o Solution Time: 34 sec

  o Mesh at 500 nm indentation
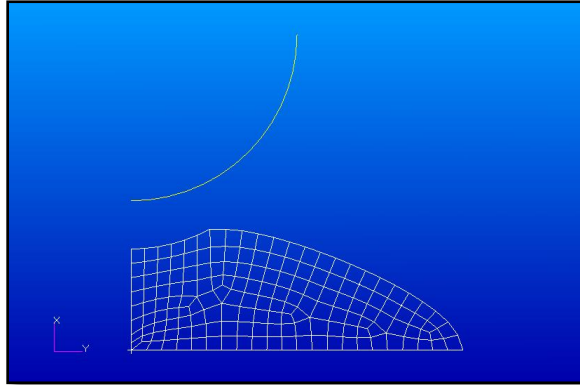
Figure C.9. Mesh 2 at 500 nm Indentation

  ▪ 257 Elements

  o Mesh after retraction
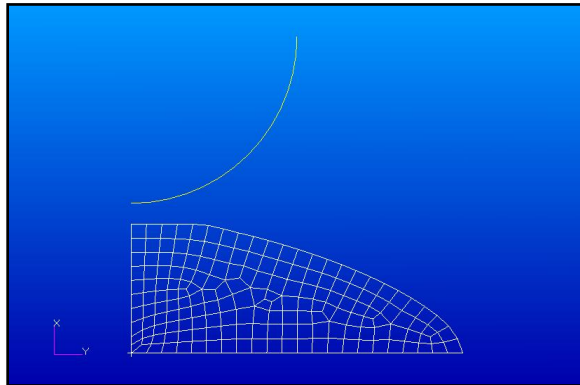
Figure C.10. Mesh 2 After Retraction

  ▪ 263 Elements

  ▪ Not identical to initial mesh

o Indentation Curve
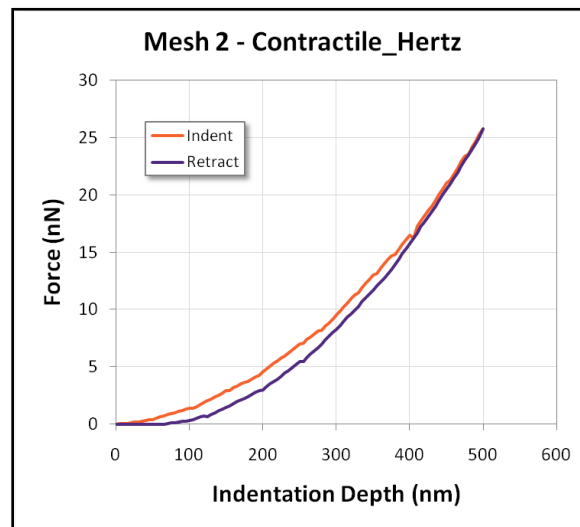
Figure C.11. Mesh 2 Indentation Curve

▪ 10.7% Hysteresis

C.1.3. MESH 3

- Created Quad8 Paver Mesh with no mesh seed

  o Global Edge Length = 0.15

  o 337 Elements
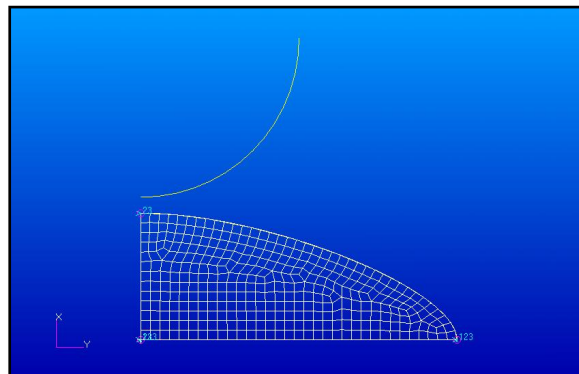
Figure C.12. Mesh 3 Prior to Indentation

- o 12 Elements Failed

  - ▪ Skew: 8 Failed

    - • Max = 33.6

Figure C.13. Mesh 3 Skew Element Quality Prior to Indentation
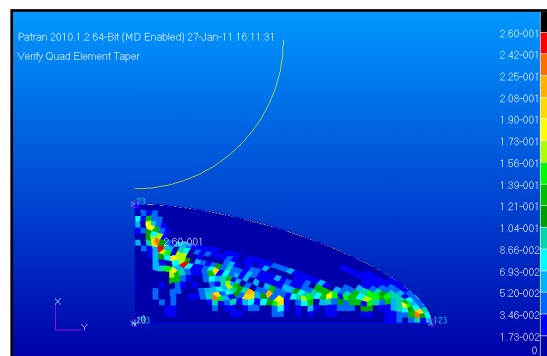
  - ▪ Taper: 4 Failed

    - • Min = 0.726
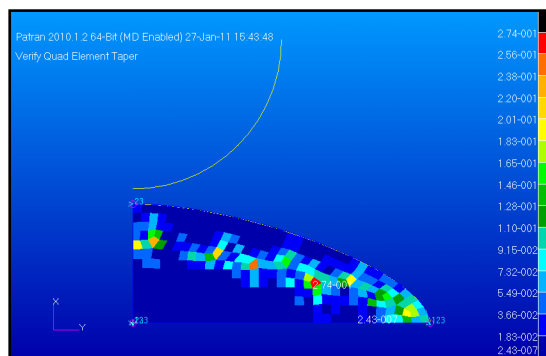
Figure C.14. Mesh 3 Taper Element Quality Prior to Indentation

- • Results

- o Solution Time: 44 sec
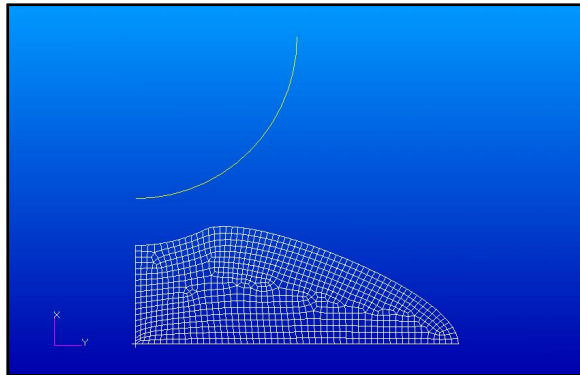
- o Mesh at 500 nm indentation

Figure C.15. Mesh 3 at 500 nm Indentation

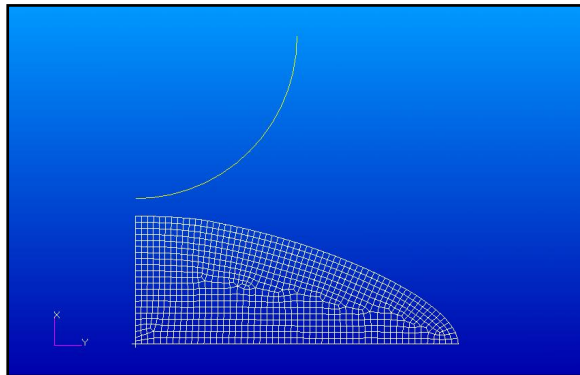- ▪ 398 Elements

- o Mesh after retraction

Figure C.16. Mesh 3 After Retraction

- ▪ 384 Elements

- ▪ Not identical to initial mesh

- o Indentation Curve

Figure C.17. Mesh 3 Indentation Curve

- 8.1% Hysteresis

C.1.4. MESH 4

- Created Quad8 Paver Mesh with no mesh seed

  o Global Edge Length = 0.10

  o 787 Elements
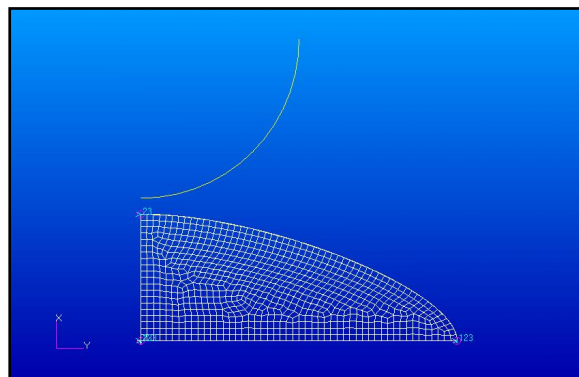
Figure C.18. Mesh 4 Prior to Indentation

- o 25 Elements Failed

  - Skew: 17 Failed

    - Max = 36.0

Figure C.19. Mesh 4 Skew Element Quality Prior to Indentation

  - Taper: 8 Failed

    - Min = 0.740

Figure C.20. Mesh 4 Taper Element Quality Prior to Indentation

- Results

  o Solution Time: 78 sec

  o Mesh at 500 nm indentation

Figure C.21. Mesh 4 at 500 nm Indentation

  ▪ 868 Elements

  o Mesh after retraction

Figure C.22. Mesh 4 After Retraction

  ▪ 868 Elements

  o Indentation Curve
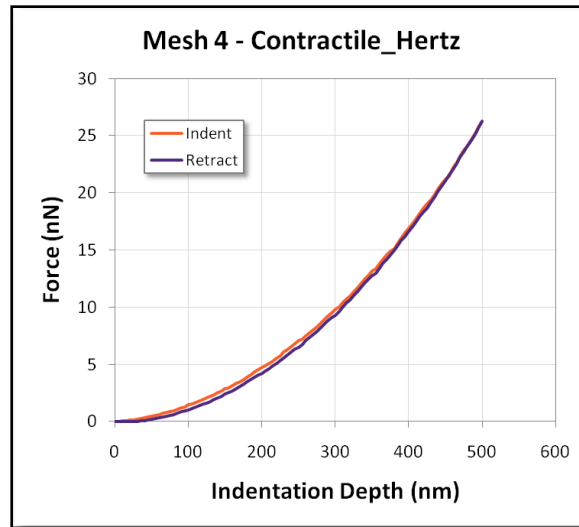
Figure C.23. Mesh 4 Indentation Curve

- ▪ 3.6% Hysteresis

C.1.5. MESH 5

- Created Quad8 Paver Mesh with no mesh seed

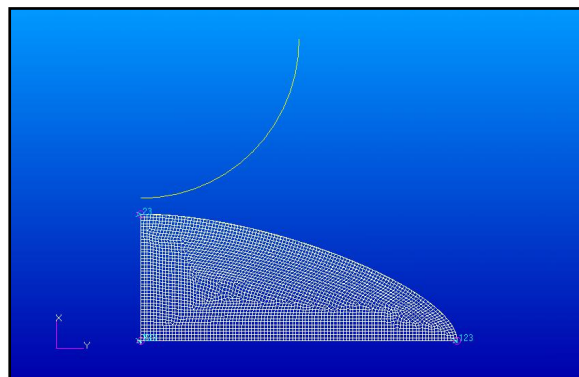 - o Global Edge Length = 0.05

  - o 3,055 Elements

Figure C.24. Mesh 5 Prior to Indentation

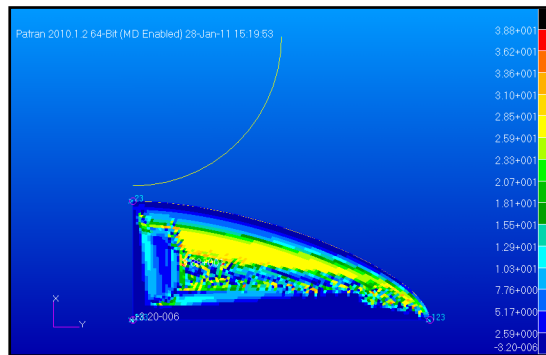- o 66 Elements Failed

  - ▪ Skew: 30 Failed

    - • Max = 38.8

Figure C.25. Mesh 5 Skew Element Quality Prior to Indentation
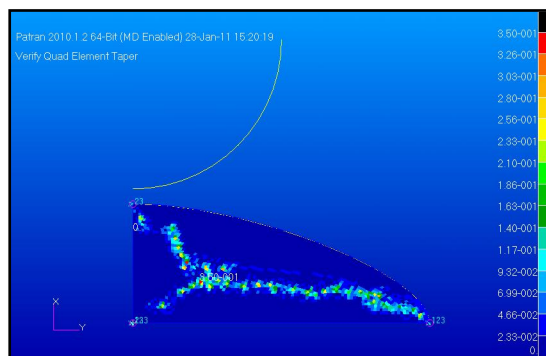
  - ▪ Taper: 36 Failed

    - • Min = 0.650

Figure C.26. Mesh 5 Skew Element Quality Prior to Indentation

- • Results

- o Would not solve past Cycle 5

    - ▪ Read Log file and noticed that Adaptive Meshing was set to remesh every 5 cycles (**under Increment Frequency**), and it was freezing the first time it tried to remesh

        - • Unchecked the **Increment Frequency** box

    - ▪ Changed remeshing criteria (under **Advanced**) to **Element Distortion**

        - • Did not need to remesh at all

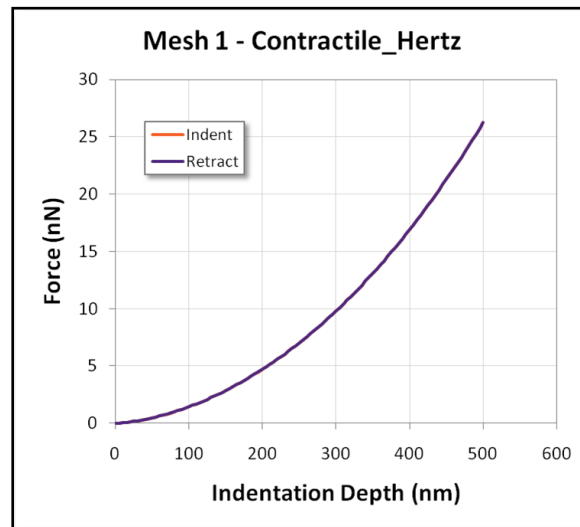- o Solution Time: 496 sec = 8 min 16 sec

- o Indentation Curve

Figure C.27. Mesh 5 Indentation Curve

    - ▪ No Hysteresis

C.1.6. ELEMENT SENSITIVITY RESULTS

- Based on Global Adaptive Remeshing

  o Remeshed based on **Increment Frequency** = 5 for Mesh 1 through 4

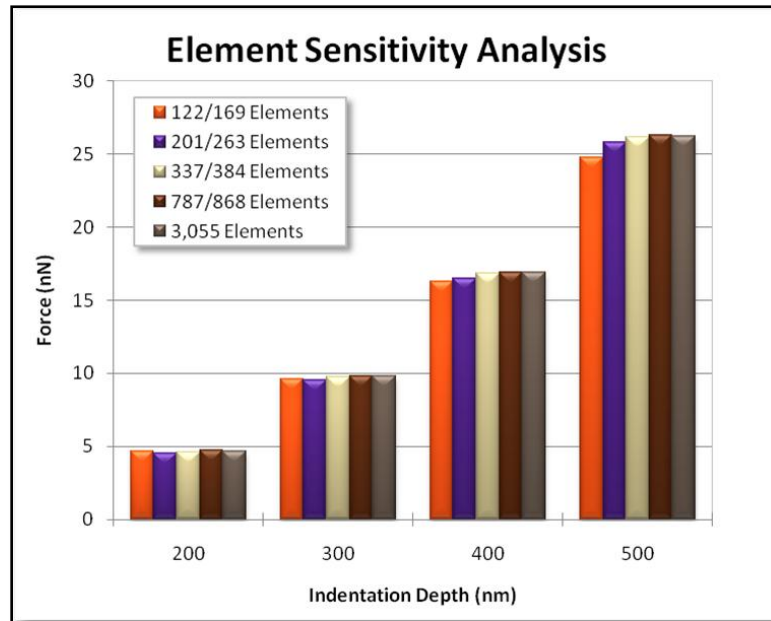 o Remeshed based on **Element Distortion** for Mesh 5 (did not remesh)

Figure C.28. Element Sensitivity Analysis Results

APPENDIX D

PROTOCOLS

D.1. Patran Protocols

D.1.1. RUNNING THE FINAL VERSION OF THE FINITE ELEMENT MODEL AS PRESENTED IN CHAPTER 6

- Select **File>Session>Play…** from the top menu

  - Uncheck **Commit Commands** check box

    - Leaving this box checked will result in very slow playing of the session file

  - Select the appropriate session file (e.g. build_cell6.ses) and click the **-Apply-** button

  - Patran will then reconstruct the geometry as written in write_patran_session.m from Appendix A

- When the session file stops playing, select **Group>Post…** from the top menu

  - Select the following groups: **cimport**, **cimport_base**, **nimport** and click **Apply**

- In the ribbon menu, select the **Meshing** tab

  - In the **Meshing** menu, select **Delete>Element**

- o Place the cursor in the **Element List** dialog box and then use the mouse to
  select all elements visible in the viewport (they should all be green)

- o Make a note of which elements are being deleted, then click **Apply**

- Select **Group>Post…** from the top menu again and post the group **ntet**

- In the ribbon menu, select the **Properties** tab

  - o In the Properties menu, select Create>3D>Solid

  - o In the **Property Set Name** dialog box, type a name for the nucleus (e.g.
    nsolid)

  - o Click the Input Properties … button

    - ▪ In the **Value Type** for the **[Formulation Options]** selection, click
      the drop menu that says **String** and select **Assumed Strain**

    - ▪ In the **Value Type** for the **Material Name** selection, click the
      button, select **nucleus_mat**, and click **OK**

  - o Click the Select Application Region … button

    - ▪ Click the **Tet element** button in the tool bar, then select all the
      elements visible in the viewport (they should be purple).

    - ▪ Make note of which elements are in the nucleus group (listed in the
      Select Members dialog box), then click the **Add**, **OK**, and **Apply**
      buttons

  - o Select **Group>Post…** from the top menu, post the group **ctet**, and repeat
    the procedure for the cytoplasm elements (making sure to note which
    elements are in this group as well)

- Make a note of which elements are in the **actin** group

    o The lowest element number will be one greater than the highest element number deleted above

    o The highest element number will be one less than the lowest element in the **ntet** group

    o The element numbers for the **actin**, **ntet**, and **ctet** groups will be used later to insert the actin elements into the solid elements

- In the ribbon menu, select the **Loads/BCs** tab

    o In the Load/Boundary Conditions menu, select Create>Displacement>Nodal

    o In the **New Set Name** dialog box, type a name for your fixed boundary condition (e.g. fixed)

    o Click the **Input Data…** button

        ▪ In the **Translations <T1 T2 T3>** dialog box, type <0,0,0> and click **OK**

    o Click the Select Application Region… button

        ▪ In the ribbon menu, select the **Home** tab

            • Click the **Bottom View** button

        ▪ In the **Select Application Region** menu, click the drop menu next to **Select:** and chose **FEM**

        ▪ Click in the **Select Nodes** dialog box, then select all of the bottom-most layer of nodes in the current group of elements in the

viewport (representing the points in contact with the glass

coverslip), then click **Add**, **OK**, **-Apply-**

- In the ribbon menu, select the **Loads/BCs** tab

  o In the Load/Boundary Conditions menu, click the Deformable button

  o In the **New Set Name** dialog box, give the deformable contact body a

  name (e.g. cell_contact)

  o Click the **Select Application Region…** button and then select all visible

  elements in the viewport for the **Select 3D Elements** dialog box, then

  click **Add**, **OK**, **-Apply-**

- In the ribbon menu, select the **Analysis** tab

  o In the **Analysis** menu, click the **Job Parameters…** button, then the

  Adaptive Meshing… button

  - For Adaptivity Type, select Global

  - Give the adaptive mesh a name (e.g. amesh) in the **Zone Name**

    dialog box

  - Select the deformable contact body that was just created in the

    Select a Deformable Contact LBC box

  - For Adaptive Mesh Criteria, select 3D

    - Uncheck the **Increment Frequency** check box

    - Click the **Advanced…** button

      o Uncheck the **Volume Control** check box

238

o Check the **Strain Change (Max)** check box and

   type the desired strain at which to remesh (e.g.

   0.25), then click **OK**, **OK**, **OK**

o If the solver type, analysis time, or number of increments for analysis are

   desired to be changed, do so in the **Load Step Creation…>Solution**

   Parameters…>Load Parameters… button menus

o In the Analysis menu, select Analyze>Entire Model>Analysis Deck, then

   click Apply

   ▪ This will write a "Job Name".dat file in the Patran directory

- Insert the actin elements into the solid elements

  o Open the file in the same directory named cellX_insert_card.dat in

     WordPad, where X is the id of the cell from reconstruct_whole_cell.m in

     Appendix A

     ▪ On the second line of the file, replace the first -1 term with the

        lowest element number of the nucleus group that was noted above

        and the second -1 term with the highest element number of the

        cytoplasm group

        • Be sure to pay attention to spaces, as they do matter to

           Marc. For every character inserted, be sure to delete the

           same number of spaces.

     ▪ Repeat this process on the fourth line of the file, this time using the

        lowest and highest element numbers of the actin group

239

- Press Ctrl-A to select all of the text in the file and press Ctrl-C to copy it

o Open the "Job Name".dat file in Notepad

- Press Ctrl-F to bring up the Find dialog box, type CONTACT in the Find dialog box, and press Enter

- Place the cursor directly in front of the first instance of the word and press Ctrl-V to paste the INSERT card into the file

- Save, then close the file

- To solve the model, open the Windows Command Prompt

  o Run cmd.exe for Windows Command Prompt prompt

  o Type: `cd C:\MSC.Software\Marc\2010.2\marc2010\tools`

  o Type: `run_marc.bat`

  o Type: `cd` working directory, where working directory is the directory that the "Job Name".dat file is located

  o In university assist folder,

    - Copy/paste marc_submit.bat to working directory

    - Right-click>Edit to change the model name after the `-j` parameter

    - Double click to submit

  o The model is now solving and can be monitored in Patran

    - In the **Analysis** menu, select **Monitor>Running Job** and click **Apply**

240

- After the model has successfully finished solving (**Exit Number: 3004**), results

  may be obtained by following the protocol in Appendix D.1.2.8.

D.1.2. GENERAL PATRAN INSTRUCTIONS FOR CREATING AND SOLVING A SIMPLE 2D AXISYMMETRIC AFM INDENTATION SIMULATION USING THE MARC NONLINEAR SOLVER

D.1.2.1. LEARNING THE BASICS

- Tutorial videos available at www.youtube.com/simulatemore

- Help files, Reference Manual, and MSC online forums (forums.mscsoftware.com)

  are useful resources

- The following exercises in the Marc help file documentation illustrate useful

  concepts:

  - Exercise 1 - Build a Cantilever Beam

  - Exercise 2 - A Simple Static Load

  - Exercise 5 - A Simple Contact Problem

  - Exercise 10 - Transient Dynamic Analysis

- Axisymmetry convention for Marc is listed in the forums as (I am currently

  unsure if this is still true for newer versions such as ours):

  - X-axis = Axial

  - Y-axis = Radial

D.1.2.2. GENERAL NOTES

- Patran doesn't like using units of 10^{-6} (e.g. micron-scale geometries in a model

  using standard SI units)

- Patran does not support units for conversion purposes, therefore the user must be very careful to keep units consistent throughout the analysis

- Since geometries must be modeled in microns, be sure to use microns in all other measurements (e.g. $1\ Pa = \dfrac{N}{m^2} = \dfrac{kg \cdot m}{s^2 \cdot m^2}\dfrac{1\ m}{1e6\ \mu m} = 1e^{-6}\dfrac{kg}{s^2 \cdot \mu m}$)

- When starting a new file:

  - Select Model Dimension = **10**

    - This tells Patran to make the viewport the appropriate size for a geometry with a max dimension size of 10 units

  - Select Analysis Code:>MSC.Marc

  - Click **OK**

D.1.2.3. GEOMETRY TAB

- Make a curve for the lower boundary of the cell body using **Create>Curve>Point**

- Make a curve for the upper boundary of the cell body using **Create>Curve>Conic**

  - Use the Sum of the Starting and Ending Point Lists for the Focal Point List, e.g. if the starting point is **[2,0,0]** and the ending point is **[0,5,0]**, the the focal point is **[2,5,0]**

  - Under Conic Section Classification, enter a value between 0 and 0.5

    - I use Conic Altitude for Ellipse = **0.33**

- Create the cell body surface using **Create>Surface>Curve>2 Curve**

- Create the AFM probe geometry using **Create>Curve>2D Arc2Point**

- Create a mesh seed on the upper boundary of the cell body to generate an increasing mesh size using **Create>Mesh Seed>One Way Bias>L1 and L2**
  - Pay attention to the arrow direction on the surface of interest
  - A good starting point, assuming the arrow points from the center of the cell outward and the geometry is in microns, is:
    - L1 = 0.05
    - L2 = 0.5
- Create the mesh using **Create>Mesh** and check the box for **Automatic Calculation** in the Global Edge Length section
- The resulting mesh should look similar to that below
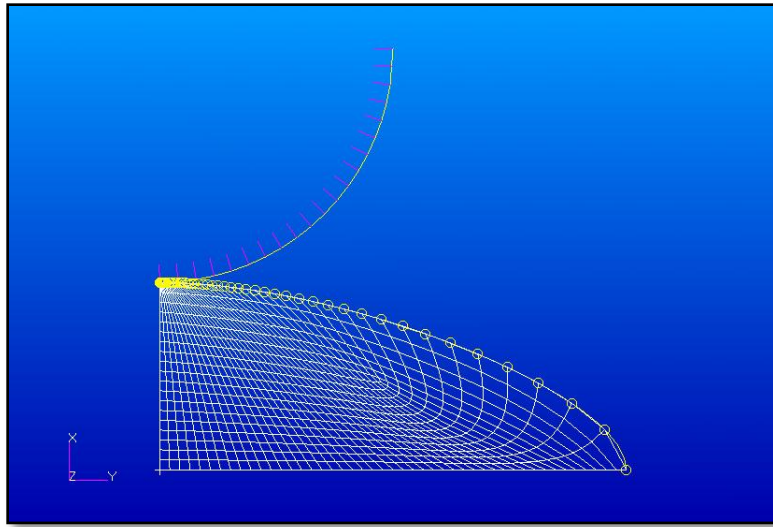
Figure D.1. Mesh of 2D Axisymmetric finite element model

D.1.2.5. PROPERTIES TAB

D.1.2.5.1. CREATING THE MATERIAL PROPERTIES

- Click the **Isotropic** button on the left-hand side of the toolbar ribbon

- Give the material a name, e.g. contractile_continuum

- Click Input Properties

    o Enter material properties

        ▪ 15.3 kPa = 1.53e-2 $\frac{kg}{s^2 \cdot \mu m}$

        ▪ 1.9 GPa = 1.9e3 $\frac{kg}{s^2 \cdot \mu m}$ (for actin filaments)

- Click **Apply**

D.1.2.5.2. ASSIGNING THE MATERIAL PROPERTIES

- Note: The following instructions apply to a simple linear elastic continuum model only.

- In the toolbar ribbon, click **2D Properties>2D Solid**

- Enter a name in the Property Set Name field, e.g. cell_body

- Select Options>Axisymmetric

- Click Input Properties

    o For [Formulation Options], select **Assumed Strain**

    o For Material Name, click the button and select a material name

    o Click **OK**

- Click Select Application Region

    o Make sure the cursor is in the Select Members field and click on the appropriate region of the geometry

    o Click **Add**

    o Click **OK**

- Once all material properties have been properly assigned, click **Apply**

D.1.2.6. LOADS/BCS TAB

D.1.2.6.1. CREATE THE BOUNDARY CONDITIONS

- Under Create>Displacement>Nodal, New Set Name = fixed

- Click Input Data

    o Translations <T1 T2 T3> = <0,0,0>

    o Click **OK**

- Click Select Application Region

  o Make sure the cursor is in the Select Members field and click on the

     appropriate region of the geometry (bottom boundary of the cell)

  o Click **Add**

  o Click **OK**

- Under Create>Displacement>Nodal, New Set Name = **axisymmetric**

- Click Input Data

  o Translations <T1 T2 T3> = **< ,0,0>**

  o Click **OK**

- Click Select Application Region

  o Make sure the cursor is in the Select Members field and click on the

     appropriate region of the geometry (axial boundary of the cell)

  o Click **Add**

  o Click **OK**

D.1.2.6.2. CREATE THE CONTACT PARAMETERS

- Select Create>Contact

  o Under Option, select **Deformable Body**

  o Under Target Element Type, select the appropriate number of dimensions

     for the cell body (e.g. **2D**)

  o Under New Set Name, give the contact parameter a name (e.g.

     cell_contact)

  o Click Select Application Region

- In the Application Region box, select the geometry for the cell

- Click **Add**

- Click **OK**

- In the LBC Fields section on the toolbar ribbon, click the **Create Non-Spatial**

  button 🖼️

  - In the Field Name box, type movement

  - In the Table Definition box, make sure that only the **Time check box** is

    selected, then click the **Input Data** button

    - Define the movement vs. time here: put each time measurement in

      the **t** column, and each movement measurement in the **Value**

      column, e.g.:

t	Value
0	0
x	Indentation depth
2x	0

Table D.1. AFM Probe Movement

    - Click **OK**

  - Click -Apply-

- Select Create>Contact

  - Under Option, select **Rigid Body**

  - Under Target Element Type, select the appropriate number of dimensions

    for the probe geometry (e.g. **1D**)

- o Under New Set Name, give the contact parameter a name (e.g.

  probe_contact)

- o Click Input Data

  - ▪ Under Motion Control, select **Position**

  - ▪ Under Displacement (vector), type <-1., 0., 0.,>

  - ▪ Click in the Displacement vs. Time field box to put the cursor

    there, then select movement from the Time-Dependent Fields box

  - ▪ Click OK

  - ▪ Make sure the lines that now appear on the probe face away from

    the contact side, as shown in Figure D.1.

  - ▪ If they are on the wrong side, click the **Input Data** button again

    and select the **Flip Contact Side check box**.

- o Click Select Application Region

  - ▪ In the Application Region box, select the geometry for the cell

  - ▪ Click **Add**

  - ▪ Click **OK**

- o Click -Apply-

D.1.2.7. ANALYSIS TAB

Note: The following instructions are for solving a simple linear elastic continuum

model with local adaptive meshing.

- Make sure Analyze>Entire Model>Full Run is selected

- Give the analysis a name in the Job Name field

248

- Click the **Job Parameters** button

  - Click the **Adaptive Meshing** button

    - Select Adaptivity Type:>Local

    - Give the adaptive mesh a name (e.g. amesh_loc)in the Zone Name box

    - Select the Snap to Geometry check box

    - In the Select a Group box, select **default_group**

    - Click **Apply**

    - Click **OK**

  - Click **OK**

- Click the Load Step Creation button

  - Click the Solution Parameters button

  - Select Linearity:>NonLinear

  - Select Nonlinear Geometric Effects:> Nonlinear Geometric Effects:>Large Displacement/Large Strains

  - Click the Load Increment Params button

    - Select Increment Type:>Fixed

    - Tell it the appropriate Number of Increments

      - I've been indenting a total of 0.75 μm and want measurements every 5 nm so I've been using 300 increments

    - Tell it the appropriate Total Time

- - Equal to the largest value in your movement table

- - - Click **OK**

- o Click **OK**

- o Click **Apply**

- o When the message pops up, click **Yes**

- Click **Apply** to solve the model

- Select **Monitor>Running Job** at the top of the right-hand menu, then click

  Apply

  - o If the Exit Number is 3004, the model has solved correctly

- Select Read Results>Result Entities>Attach

  - o Select the appropriate job from the Available Jobs box

  - o Click the **Select Results File** button and select the appropriate *.t16

    results file

  - o Click the Translation Parameters button

    - - Select the **Import Results check box** and make sure the

      increments you are interested in are selected in the Available

      Increments box

    - - Click **OK**

  - o Click **Apply**

- Select Read Results>Result Entities>Import

  - o Click the **Select Results File** button and select the appropriate *.t16

    results file

o   Click **Apply**

- The results are now ready to be viewed in the Results tab

D.1.2.8. RESULTS TAB

- After you attach the .t16 results in Patran, do the following:

- To Create a Graph of Results:

    o   Select **Group > Post** and pick all the desired groups named similarly to

    Mesh Set: A1-1 Incr 1:17

    ▪   Note here that the group name could be slightly different

    depending on the number of increments – in this example it is 17.

    o   From the Results tab, select Create > Graph > Y vs X

    o   In the Select Results menu

    ▪   Select all desired increments from the **Select Result Cases** field

    ▪   Y: Global Variable

        - Variable: Pick the deformable contact body, Force (or force

        or moment component that you want to plot)

            o   E.g. Body cell_contact, Force X

    ▪   X: Global Variable

        - Variable: Pick another "Global Variable"

            o   Choose Time, Increment, rigid contact body

            Position, etc.

                ▪   E.g. Body probe_contact, Position

251

o Format the graph axes in the Display Attributes [icon] menu

o In the Plot Options [icon] menu

- Input the appropriate Scale Factor

- **-1000** for all of my models so far

- Input a name for the plot if desired

- E.g. Save Graph Plot As: indent or retract

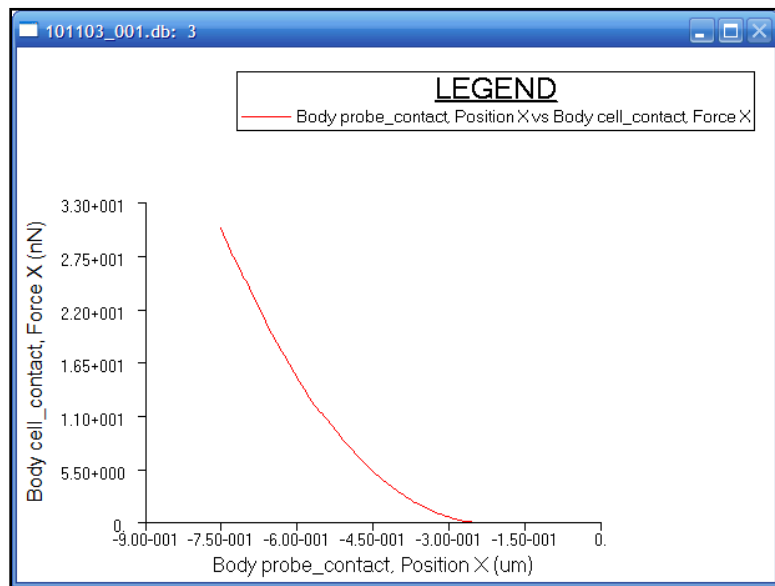o Click **Apply** – at this point you should see the graph of the X and Y

entities.

Figure D.2. Indentation Results of Finite Element Model

- To Export Results Data to ASCII file from Graph:

- o From the XY Plots box on the menu ribbon, Select Modify

- o Select Modify > Curve

- o Pick the curve to be exported (Usually the curves will be named as following "Default_graph30" or appended with Node number)

- o Click Data from Keyboard

    - ▪ In the menu that opens, select either **XY Pairs** or **Y Data** as the data type

        - • XY Pairs will export data from the X and Y axes

        - • Y Data will only export data from the Y axis

    - ▪ Check the Write XY Data to File box

    - ▪ Click **Apply** and enter a filename and optional title

        - • The default file type here is *.xyd, so end the file name with .txt to save as a *.txt file

            - o *.xyd and *.txt are both ASCII Files

D.1.3. MAKING IMPORTED .STL MESHES USABLE IN PATRAN

D.1.3.1. USEFUL INFORMATION

- • Search for "convert tria6 mesh to solid" on http://simcompanion.mscsoftware.com

    - o Find video: "how to convert a cylinder of tria elements to a solid with tet elements (matching the tria mesh)"

- o Saved as C:\Documents and Settings\finou\My

    Documents\Scott\Research\Image Conversion\Mesh

    Conversion\Convert Mesh To Solid (Patran).avi on lab desktop

    computer

- You can also find helpful tips at http://www.eng-

  tips.com/viewthread.cfm?qid=240225&page=1

  - o Forums > Engineering Computer Programs > General

    Engineering Programs > MSC.Software: Patran Forum

- To confirm element form, found good image showing node placement on each

  type of mesh element

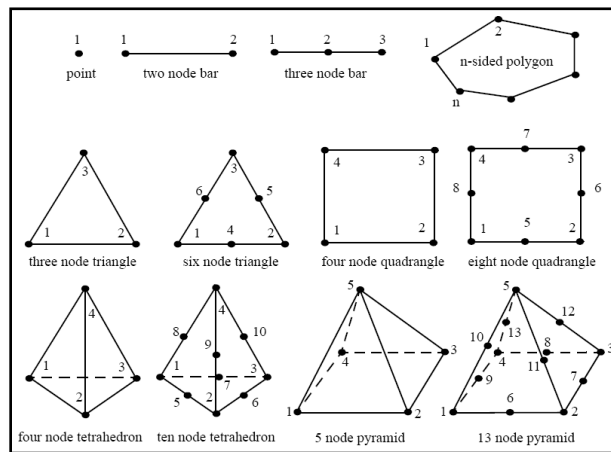 - o https://visualization.hpc.mil/wiki/EnSight_Gold_-_Geometry_Files

Figure D.3. Types of Elements Supported by Patran

D.1.3.2. PROCEDURE FOR PROCESSING IMPORTED .STL MESHES FOR USE IN PATRAN

- Import the mesh from .stl file

- o File > Import, Source: STL

- o Note: STL files are imported as 3 node triangle (tria3) elements, but Patran requires 6 node triangle elements (tria6) for converting to 10 node tetrahedral elements (tet10)

- Create a group for the imported elements by selecting **Group > Create** from the menu bar at the top

  - o Under New Group Name, give the new group a name (e.g. stl)

  - o Click the box for Entity Selection and then select the entire mesh and click **Apply**

  - o Select **Action: Post**, then select only **default_group** and click **Apply**

D.1.3.2.1. UNDER MESHING TAB

- Verify mesh quality using Verify > Element > Boundaries

  - o Select **Free Edges**, Click **Apply**

    - ▪ There should be nothing showing, indicating no free edges (i.e. completely closed geometry)

    - ▪ If there are any free edges at all, the mesh will fail

  - o Click **Reset Graphics**, then select **Free Faces** and click **Apply** again

    - ▪ All faces of the geometry should be highlighted (gold)

    - ▪ Click Reset Graphics again

IF MESH APPEARS TO BE OF GOOD QUALITY VISUALLY AND HAS NO FREE EDGES:

- Select Modify > Element > Edit

  - o Element Attributes: Select **Type**

255

- o New Topology: **Tria6**

- o Element List: Select entire mesh, click **Apply**

- Create > Mesh > Solid

  - o Select the **Tri Element** button ⬜ from the toolbar shown to the right

    - ▪ This allows the user to select the mesh

  - o Input List Select entire mesh

  - o Give an appropriate Global Edge Length and click **Apply**

- Select **Group > Create** from the menu bar at the top

  - o Enter a **New Group Name** (e.g. tet)

  - o Select the **FEM Entity** ⬜ **> Element** ⬜ **> Tet Element** ⬜

    button from the toolbar shown to the right

    - ▪ This allows the user to select only the newly created

      tetrahedral elements

  - o Select all of the mesh in the **Entity Selection** box and click **Apply**

  - o Select Action > Post

    - ▪ Select only the newly created group (e.g. **tet**) and click

      Apply

- The mesh is now ready for assigning material properties, loads, boundary

  conditions, etc.

IF MESH DOES NOT APPEAR TO BE OF GOOD QUALITY VISUALLY OR HAS FREE EDGES:

- Select **Group > Create** from the menu bar at the top

  - o Enter a New Group Name (e.g. stl)

- Select all of the mesh in the **Entity Selection** box and click **Apply**

- Select Action > Post

  - Select only **default_group** and click **Apply**

- Select **Create > Mesh > On Mesh** to create a new mesh over the old mesh

  - DO NOT select Delete Elements

    - Will cause unwanted random edge deletion

  - Element Shape: Select desired shape

    - **Tria**ngle or **Quad**rilateral

  - Seed Option

    - **Uniform**: The mesher will create new boundary nodes based on input global edge length.

    - **Existing Boundary**: All boundary edges on input mesh will be preserved.

    - **Defined Boundary**: The mesher will use all the nodes selected in the data box Boundary Seeds to define the boundary of the output mesh. No other boundary nodes will be created.

      - Boundary Seeds data box = **Boundary Hard Nodes** data box under **Feature Selection**

    - Both **Uniform** and **Existing Boundary** seem to work equally well for me so far

  - Check the Feature Recognition box

- If checked, the features on the input mesh will be defined automatically based on feature edge angles and vertex angles, and be preserved on the output mesh.
- Edge Angle
  - If Feature Recognition is on, an edge on the input mesh will be defined as a feature edge and be preserved if the angle between the normals of two adjacent triangles is greater than the feature edge angle.
- Vertex Angle
  - If Feature Recognition is on, a node on a feature line will be defined as a feature vertex and be preserved if the angle of two adjacent edges is less than the feature vertex angle.
- Mesh on Mesh does not preserve original shape without using feature recognition
  - Check the **Use Selection Values** box if using **Defined Boundary** or if otherwise needed, but so far it has not been necessary for me
  - Select all desired parts of the mesh in the **2D Elem List** box
  - Give an appropriate **Global Edge Length** and click **Apply**
- Select **Group > Post** from the menu bar at the top
  - Post only the group created above (e.g. **stl**)
  - Either delete the imported mesh or move it out of the way of the new mesh

- If the new mesh appears to be of good quality visually and has no free edges, follow the directions above, otherwise continue here

  o It may be more easily visualized using the **Hidden Line** ⬚ or **Smooth Shaded** ⬚ displays in the Home tab than in the default **Wireframe** ⬚ mode

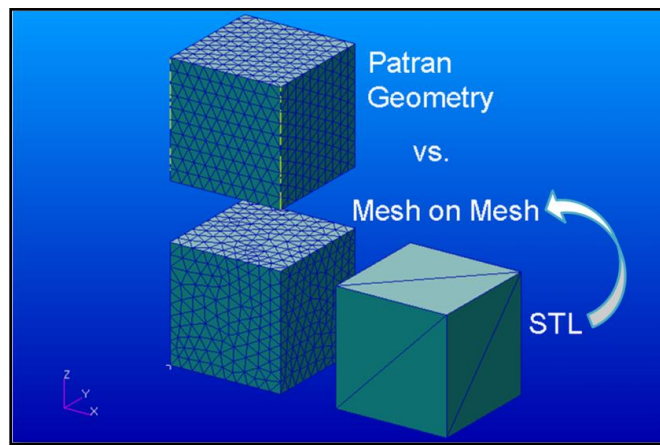 o Mesh on Mesh is sometimes not very good at creating efficient meshes, e.g.:

Figure D.4. Difference in Results between Using a Paver Mesher for Mesh on Mesh and Using the Default IsoMesh Mesher in Patran

  ▪ Mesh on Mesh appears to use the Advancing Front mesher, whereas native Patran geometry seems to be meshed using the Delauney Triangulation mesher

259

- See Marc® 2010 Volume A: Theory and User Information, Chapter 4 Introduction to Mesh Definition, pp. 92 – 93

- If the new mesh does not appear to be of good quality visually, it will need to be remeshed using Global Adaptive Remeshing during Analysis

D.2. ASYLUM AFM PROTOCOL

D.2.1. GETTING STARTED

1. Open the most recent version of Igor on the desktop

    o Click File>Load AFM Software

    o Close all the windows that open except the Master and Heater panels

2. In the Main tab of the Master Panel, **put the AFM in Contact Mode**

    o Should see the following:

        ▪ Sum

        ▪ Deflection

        ▪ Lateral

        ▪ Z Voltage

3. Make sure AFM is laterally level

4. Find the probe using the mirror knobs in the very back (and using focus wheel if necessary), find the laser, put the laser at the tip of the probe

5. Use the dials on the back and right side of the AFM to move the laser and **Maximize the Sum**

6. Use the dial on the left side of the AFM to **Zero out the Deflection**

7. **Hit Engage** and use the dial on the front of the AFM to move down toward the surface

8. It should 'ding' when the deflection hits one

   o Continue to move down *very slowly* and **center out the Z voltage**

D.2.2. APPROXIMATE SEPARATION DISTANCE

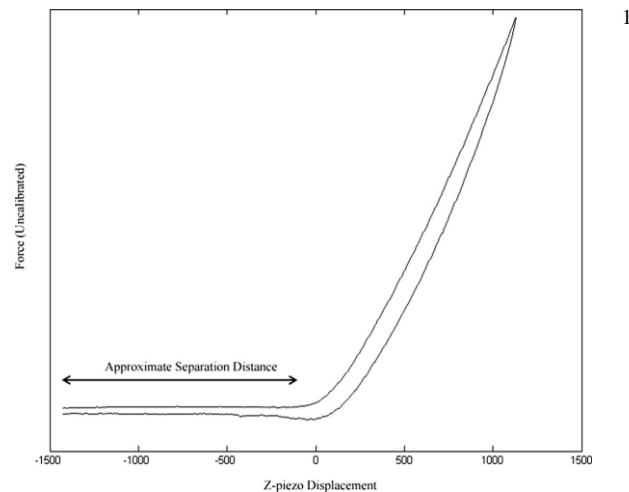- The distance between the tip and the top of the sample

Figure D.5. AFM Indentation Curve Demonstrating Approximate Separation Distance

D.2.3. CONTROL/FORCE CURVES

[1] Hemmer, J.D., et al., *Role of Cytoskeletal Components in Stress-Relaxation Behavior of Adherent Vascular Smooth Muscle Cells.* Journal of Biomechanical Engineering-Transactions of the ASME, 2009. **131**(4): p. 9.

- Go to the **Force Panel** of the Master Tab

- Set **Force Dist** = 10 μm

- Set **Velocity** = 5 μm/s

- In the Save tab

    o Uncheck Save to Disk

    o Give **Base Name** as "Control"

    o Click the **Path** button → Browse → Browse → Select folder for data →

      OK → Close with ❌

- In the Misc. tab

    o Set Trigger Channel to Deflection

    o Set **Trigger Point** = 100 nm

- Click Single Force

    o After it finishes, if it didn't find the surface slide the **red bar** on the left to

      try to find the surface

        ▪ Make sure neither axis is reversed

- Once the surface has been found, set **Trigger Channel** to **None** and keep

  tweaking the **red bar** and using **Single Force** until the curves look good

- Once a good curve has been obtained, click on the force graph, then press **Ctrl-I**

    o Drag the **A** circle to the bottom of the linear portion of the red line and the

      B square to the top
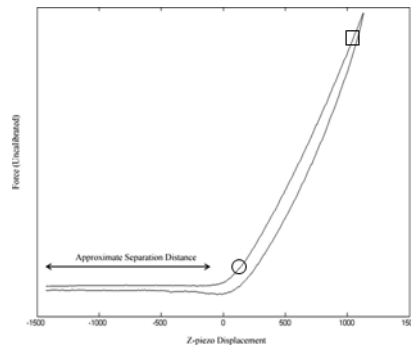
Figure D.6. Diagram of Deflection Sensitivity Calibration Markers

- In the Cal. Tab

    o Input the Spring Constant

    o Click Set Sensitivity → DeflInVOLS

- In the Save tab

    o Check Save to Disk

- Click Continuous

    o When suffix reaches 0004, click **Stop Forces**

    o Should have 5 control curves

- For Force Curves, change **Base Name** and, if needed, **Path**

D.2.4. STRESS RELAXATION

- Use **Ctrl-I** to see depth with circle and square (dX = depth)

- Dwell FB Z sensor

- Dwell Toward Surface

- Set Dwell Time

- Use checked box for Dwell Rate

- Trigger Channel: Raw Z Sensor

- Trigger Point = square x-position

D.3. Solution Preparations

D.3.1. VSMC MEDIA

10% FBS, 1% Anti/Anti (or Pen/Strep if antifungal agent must be avoided)

Into 500 mL High Glucose DMEM, add:

- 56.2 mL FBS

- 5.6 mL Anti/Anti

    o 2.8 mL Penicillin/Streptomycin

    o 2.8 mL Amphotericin B

D.3.2. SERUM-FREE VSMC MEDIA (FOR INDUCTION OF CONTRACTILE PHENOTYPE)

1% Anti/Anti (or Pen/Strep if antifungal agent must be avoided)

Into 500 mL High Glucose DMEM, add:

- 5.05 mL Anti/Anti

    o 2.525 mL Penicillin/Streptomycin

    o 2.525 mL Amphotericin B

D.3.3. COLLAGEN

50 µg/mL

From stock solution of 8.58 mg/mL: 5.83 µL per mL PBS

- To 5 mL PBS, add 29.14 µL stock solution

1 mg/mL

From stock solution of 8.58 mg/mL: 116.55 µL per mL PBS

- To 5 mL PBS, add 582.8 µL stock solution

D.3.4. CELLMASK™ DEEP RED PLASMA MEMBRANE STAIN

5 µg/mL – For Live Cells (let sit on cells at 37°C for 5 min)

From stock solution of 5 mg/mL: 1 µL per mL cell media

- *To 5 mL media, add 5 µL CellMask™ stock solution*

7 µg/mL – For Live Cells (let sit on cells at 37°C for 5 min)

From stock solution of 5 mg/mL: 1.4 µL per mL cell media

- *To 5 mL media, add 7 µL CellMask™ stock solution*

D.3.5. DAPI

25 µg/mL – For Live Cells (let sit on cells at 37°C for 1 hr)

From stock solution of 5 mg/mL DAPI: 5 µL DAPI stock *solution* per mL cell media

- *To 5 mL media, add 25 µL DAPI stock solution*

300 nM DAPI (1:50,000) – For Fixed Cells

From stock solution of 5 mg/mL DAPI: 0.02105 µL DAPI stock *solution* per mL PBS

- To 50 mL PBS, add 1.05 µL DAPI stock *solution*

- To 100 mL PBS, add 2.11 µL DAPI stock *solution*

Stock solution

5 mg DAPI powder per mL water

D.4. Staining Cells for Actin, Nucleus, and Microtubules

1. 30 min PBS/0.01 M Glycine/0.1% Triton-X

    - To make 50 mL: 50 mL PBS/0.0375 g Glycine/ 0.05 mL Triton-X

2. 15 min 5% BSA/PBS

3. 15 min 5% Normal Serum (1% BSA/PBS)

4. Overnight   Primary Antibody (1% BSA/PBS) @ 4°C (1:100)

    *************** DON'T THROW PRIMARY AWAY! ***************

5. 2 x 15 min   Rinse with 1% BSA/PBS

6. 15 min 5% Normal Donkey Serum (1% BSA/PBS)

    ********************* COVER WITH FOIL *********************

7. 2 hoursSecondary Antibody (1% BSA/PBS) @ 37°C (1:100)

8. 15 min Rinse with 1% BSA/PBS

9. 2 x   Rinse with PBS

10. 15 min 488 Phalloidin in PBS Shaking at RT (1:100)

11. 3 x   Rinse with PBS

9.

10. If not mounting for microscopy:

    12. 5 min   DAPI in PBS Shaking at RT (300 nM)

    13. 3 x   Rinse with PBS

11.

12. If mounting for microscopy

13. Mount with SlowFade® Gold antifade reagent with DAPI (Invitrogen: S36939)

APPENDIX E

ROLE OF CYTOSKELETAL COMPONENTS IN STRESS RELAXATION BEHAVIOR OF ADHERENT VASCULAR SMOOTH MUSCLE CELLS

E.1. Introduction

The results presented in this appendix were part of a study published in the Journal of Biomechanical Engineering [1]. The published study investigated the role of various cytoskeletal components play in the stress relaxation behavior of adherent VSMCs by treating VSMCs with various agents that either enhance or prevent polymerization of specific cytoskeletal filaments. The work presented in this appendix pertains specifically to the qualitative analysis of the effects of those cytoskeletal agents and is presented here directly from the published study.

E.2. Materials and Methods

Smooth muscle cells isolated from adult male Sprague-Dawley rat aortal explants were cultured in Dulbecco's Modified Eagle's Medium (DMEM) (Mediatech, Herndon, VA) supplemented with fetal bovine serum (FBS) (10 %) (Sigma, St. Louis, MO) and antibiotic/antimycotic (1 %) (Sigma). Cells were maintained in a humidified, 37 ℃, 5% CO_2, 95% air environment. Prior to AFM experiments, cells were seeded onto 22 x 22

mm glass coverslips coated with type I collagen (Vitrogen 100, Cohesion Technologies, Palo Alto, CA) at a density of 150,000 cells per coverslip. Seeded coverslips were incubated in 6-well plates with DMEM (10% FBS) at 37 ºC with 5% CO2 for 3 to 5 days prior to AFM experimentation. Cells were used in experiments between passages 5 and 8.

E.2.1. CYTOSKELETAL AGENTS

To assess the role of actin filaments in VSMC stress relaxation behavior, cells were treated with either 1 μM cytochalasin D (Sigma, St. Louis, MO) or 0.1 μm jasplakinolide (Fisher Scientific, Pittsburgh, PA) at 37 °C for 1 hour prior to tests. Cytochalasin D is an actin depolymerizing agent that caps the barbed end of F-actin, while jasplakinolide is an actin stabilizing agent that binds to both ends of actin filaments, preventing depolymerization. Likewise, to determine the role of microtubules in stress relaxation behavior, groups of cells were treated with either 20 μm nocodazole or 10 μM paclitaxel (both from Sigma) at 37 °C for 1 hour to induce microtubule depolymerization or hyperpolymerization, respectively. Both nocodazole and paclitaxel bind to β-tubulin; however, the former disrupts and the latter stabilizes microtubules. Concentrations of all cytoskeletal agents were chosen based on published research [2-4] or based on our own experience, as in the case of cytochalasin D, where we chose the maximum concentration that can be used without inducing cell detachment. Control groups for each experiment consisted of cells treated only with the equivalent amount of vehicle (DMSO) for these cytoskeletal agent treatments.

E.2.2. IMMUNOFLUORESCENCE.

Immunofluorescence staining was used to visualize actin filaments and microtubules. Cells were fixed in 4% paraformaldedyde at room temperature for 30 minutes following cytoskeletal-agent treatments at the same time points as the cells for the corresponding AFM experiments. The cells were then incubated with blocking solution consisting of PBS (90%) (Sigma), bovine serum albumin (3.8%) (Sigma), donkey serum (3.0%) (Sigma), and Triton-X (0.2%) (Sigma) for 30 minutes. This was followed by incubation with either Alexa Fluor 488 conjugated phalloidin (Sigma) at room temperature for 15 minutes for actin staining or alpha- and beta-tubulin primary antibodies (Hybridoma Bank, U. of Iowa) at 4°C overnight for microtubule staining. The microtubule-stained cells were further incubated with a TRITC-conjugated secondary antibody (Invitrogen, Inc., Carlsbad, CA) the following day for 2 hours and then with DAPI for 5 minutes (Invitrogen, Carlsbad, CA). All samples were viewed using an Olympus IX71 inverted microscope (Olympus, Tokyo, Japan); images were subsequently collected and processed using HCImage software (Hamamatsu Corp., Bridgewater, NJ).

E.3. Results

Untreated VSMCs exhibited normal actin (Figure E.1(a)) and microtubule structure (Figure E.1(b)). Immunofluorescence imaging of actin (Figure E.1(c)) and microtubules (Figure E.1(d)) in cytochalasin D-treated VSMCs revealed significant disruption of actin stress fibers and no identifiable changes to microtubule structure. Nocodazole-treated VSMCs showed significant microtubule disruption (Figure E.1(f)) without any changes
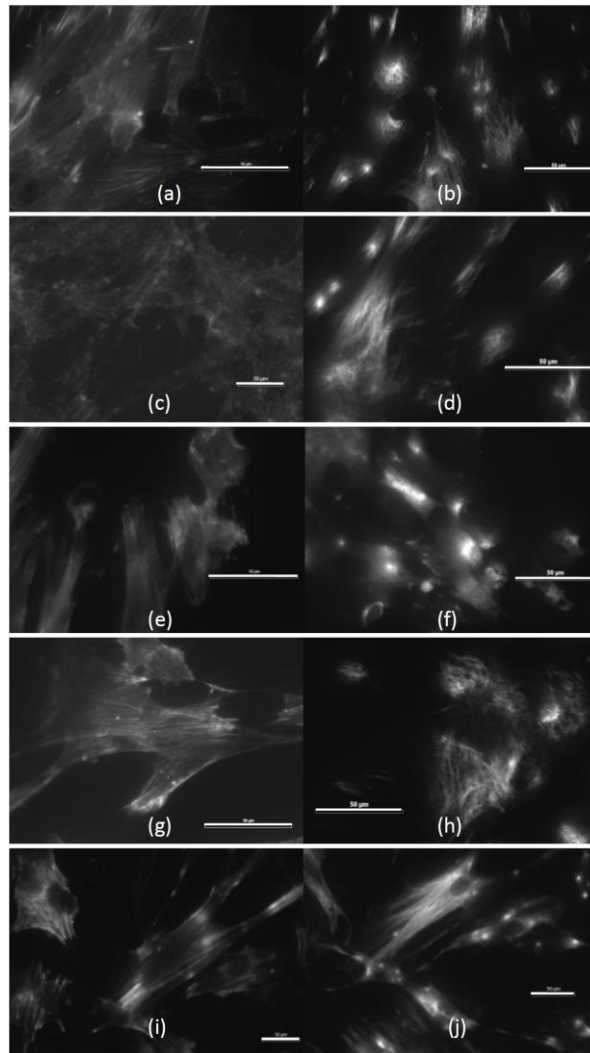
Figure E.1. Immunofluorescence images of untreated VSMC (a) actin and (b) microtubules; cytochalasin D-treated VSMC (c) actin and (d) microtubules; nocodazole-treated VSMC (e) actin and (f) microtubules; paclitaxel-treated VSMC (g) actin and (h) microtubules; jasplakinolide-treated VSMC (i) actin and (j) microtubules. Scale bars represent 50 μm.

to actin structure (Figure E.1(e)). No consistent visual differences were observed with

actin or microtubule structure in paclitaxel-treated VSMCs (Figure E.1(g) and 5(h)),

although some cells did appear to exhibit denser microtubule content with less free

tubulin. No visual differences were observed in actin or microtubules (Figure E.1(i) and

5(j)) of jasplakinolide-treated VSMCs.

E.4. References

1.   Hemmer, J.D., et al., *Role of Cytoskeletal Components in Stress-Relaxation Behavior of Adherent Vascular Smooth Muscle Cells.* Journal of Biomechanical Engineering-Transactions of the Asme, 2009. 131(4): p. 9.

2.   Collinsworth, A.M., et al., *Apparent elastic modulus and hysteresis of skeletal muscle cells throughout differentiation.* American Journal of Physiology-Cell Physiology, 2002. 283(4): p. C1219-C1227.

3.   Costa, K.D., *Single-cell elastography: Probing for disease with the atomic force microscope.* Disease Markers, 2003. 19(2-3): p. 139-154.

4.   Rotsch, C. and M. Radmacher, *Drug-induced changes of cytoskeletal structure and mechanics in fibroblasts: An atomic force microscopy study.* Biophysical Journal, 2000. 78(1): p. 520-535.